University of Wollongong

Research Online

University of Wollongong Thesis Collection 2017+

University of Wollongong Thesis Collections

2021

Phanerozoic evolution of mantle convection, long-wavelength dynamic topography and long-term sea level in a global tectonic framework

Alexander Young
University of Wollongong

Follow this and additional works at: https://ro.uow.edu.au/theses1

University of Wollongong

Copyright Warning

You may print or download ONE copy of this document for the purpose of your own research or study. The University does not authorise you to copy, communicate or otherwise make available electronically to any other person any copyright material contained on this site.

You are reminded of the following: This work is copyright. Apart from any use permitted under the Copyright Act 1968, no part of this work may be reproduced by any process, nor may any other exclusive right be exercised, without the permission of the author. Copyright owners are entitled to take legal action against persons who infringe their copyright. A reproduction of material that is protected by copyright may be a copyright infringement. A court may impose penalties and award damages in relation to offences and infringements relating to copyright material. Higher penalties may apply, and higher damages may be awarded, for offences and infringements involving the conversion of material into digital or electronic form.

Unless otherwise indicated, the views expressed in this thesis are those of the author and do not necessarily represent the views of the University of Wollongong.

Recommended Citation

Young, Alexander, Phanerozoic evolution of mantle convection, long-wavelength dynamic topography and long-term sea level in a global tectonic framework, Doctor of Philosophy thesis, School of Earth, Atmospheric and Life Sciences, University of Wollongong, 2021. https://ro.uow.edu.au/theses1/1131

Research Online is the open access institutional repository for the University of Wollongong. For further information contact the UOW Library: research-pubs@uow.edu.au

UNIVERSITY
OF WOLLONGONG
AUSTRALIA

Phanerozoic evolution of mantle convection, long-wavelength dynamic topography and long-term sea level in a global tectonic framework

Alexander Young

Supervisor:
Dr Nicolas Flament

This thesis is presented as part of the requirement for the conferral of the degree:
Doctor of Philosophy

This research has been conducted with the support of the Australian Government Research Training Program Scholarship

University of Wollongong
School of Earth, Atmospheric and Life Sciences

February 2021

Abstract

The changing pattern of convective circulation in the Earth's mantle induces slowly developing, vertical displacements of the crustal surface resulting in dynamic topography; which influences erosion, sedimentation, eustatic sea-level change and continental flooding. Given the importance of dynamic topography, attempts have been made to constrain its spatiotemporal pattern, wavelength and amplitude. Thus, tracking the influence of mantle flow over geologic time is one of the important scientific endeavours. To achieve this aim, geodynamic experiments of mantle convection can be coupled with plate tectonic reconstructions to predict upwellings and downwellings that in turn elevate or depress the Earth's surface.

The overarching aim of this thesis is to understand and quantify the effect of mantle dynamics on the Earth's surface throughout the Phanerozoic by combining global plate tectonic reconstructions, dynamic Earth models and geological observations.

In order to investigate the evolution of the plate-mantle system in deep geological time, I first created a global plate motion history model spanning 410-0 Ma. A new model is a necessity because kinematic analysis of previous plate motion models of pre-Cretaceous times exhibit fast plate velocities (11 cm/yr), high net-rotation (0.7 °/Ma) and pervasive trench advance (70% of trenches), all of which are geodynamically implausible and occur in those models because plate motion is determined relative to structures in the lowermost mantle which are assumed to be rigid and fixed through time. Thus, the first aim of this project was the development of a new model that does not assume fixed lowermost mantle structures. Kinematic analysis of the new model shows plate and trench velocities of the same order of magnitude observed at the present-day. Using the new plate motion model, mantle flow was reconstructed back to 410 Ma. The results of geodynamic modelling show a good match between the predicted and observed present-day lower mantle structure and challenge the proposed fixity of the structures on the core-mantle boundary.

Global sea level is a primary factor on sediment deposition, continental flooding, species migration, changes in Earth's climate and the evolution of life. The traditional approach to tracking the temporal evolution of eustatic changeover million-year time scales is sequence stratigraphy and over longer time scales (> 10 Myr) sea level change is inferred from models, though details and assumptions of such models are not widely accessible. Therefore, to quantify and analyse Phanerozoic first- (~100-200 Myr) and second- (~10-80 Myr) order eustatic cycles I coupled plate tectonic models with reconstructions of past mantle flow and develop a new open-access holistic method to model time-dependent sea level change. The model accounts for the

main solid Earth drivers of eustatic rise and fall and allows for investigation into how individual mechanisms effect eustatic change. The results demonstrate that dynamic topography is a dominant contributing factor to long-term global sea level change.

My newly developed tools a combination of plate motion history, mantle structure and dynamic topography models provide the opportunity to investigate how mantle flow has affected subsidence in sedimentary basins. To this end, I compiled and back-stripped well data for Paleozoic intercontinental basins in Australia to reconstruct the water-loaded subsidence history of these depocenters. The basins were selected because they were the most stable in Australia for the time period of interest; making them most suitable for an analysis of this type. A simple stretching forward model was fit to the backstripped well subsidence; the difference between the two was considered to be anomalous vertical motion. Mantle flow models are used to reconstruct time-dependent dynamic topography and anomalous motions are linked to the history of dynamic topography. The results suggest that long-wavelength dynamic topography can be invoked to explain aspects of the basins subsidence histories.

Finally, I integrated paleogeographic models which plate tectonics, dynamic topography and basin subsidence histories to evaluate the reliability of Australian stratigraphic sections as records of Paleozoic eustasy. My results suggest that Australia was tectonically and dynamically active during Ordovician and Devonian times when Western and Central Australia, and Eastern Australia, respectively, are used as reference stratigraphic sections for calculations of Paleozoic sea-level based on stratigraphic methods. Combining global maps of dynamic topography and paleogeography suggests a correlation between paleogeography and dynamic topography throughout the majority of Paleozoic times: positive continental dynamic topography is related to restricted continental flooding and negative continental dynamic topography is associated with extensive continental flooding.

This contribution presents a Paleozoic plate model with a large range of potential applications beyond the immediate outcomes of this project. It has revealed the effect of the solid Earth on global sea level twice as far back in time than has so far been possible and quantifies the effect of mantle flow on long-lived Australian onshore basins, thus providing the Australian Earth Science community with a new framework to understand episodes of anomalous vertical motion in Paleozoic basins and confounding paleo-depositional patterns. As a body of work, this thesis bridges the traditionally distinct fields of sedimentology and mantle convection. It suggests an intimate link between geodynamic processes and surface deformation from a scale of individual basins to continental platforms, to Earth's interior and global plate tectonics.

To my parents. Their love and support made this possible.

Acknowledgements

"Isn't it funny that day by day nothing changes, but when you look back, everything is different."

— C.S. Lewis

My PhD candidature at the University of Wollongong over the past four years has been one of the most enjoyable experiences of my life so far. For this, I owe many thanks to my parents and supervisor, Nico Flament.

Nico has provided me with his limitless energy, support, expertise, trust and above all else his patience. I am very thankful to have had a supervisor of Nico's quality. Nico is deserving of additional thanks for appointing me to demonstrating and marking duties, where I gained valuable teaching experience.

I thank my collaborators, in particular Dietmar Müller, Simon Williams and Andrew Merdith whose discussions regarding the contents of this thesis were invaluable. I would also like to thank Ömer Bodur for his revisions.

I am greatly appreciative of the editing by my Aunt, Nicola Young.

Lastly, I owe thanks to my family and friends for the laughs, the hugs and the good times.

CRediT author statement

Term	Definition
Conceptualization	Ideas; formulation or evolution of overarching research goals and aims
Methodology	Development or design of methodology; creation of models
Software	Programming, software development; designing computer programs; implementation of the computer code and supporting algorithms; testing of existing code components
Validation	Verification, whether as a part of the activity or separate, of the overall replication/ reproducibility of results/experiments and other research outputs
Formal analysis	Application of statistical, mathematical, computational, or other formal techniques to analyse or synthesize study data
Investigation	Conducting a research and investigation process, specifically performing the experiments, or data/evidence collection
Writing - Original Draft	Preparation, creation and/or presentation of the published work, specifically writing the initial draft (including substantive translation)
Writing - Review & Editing	Preparation, creation and/or presentation of the published work by those from the original research group, specifically critical review, commentary or revision – including pre-or post- publication stages
Visualization	Preparation, creation and/or presentation of the published work, specifically visualization/ data presentation
Supervision	Oversight and leadership responsibility for the research activity planning and execution, including mentorship external to the core team

From Brand, A., Allen, L., Altman, M., Hlava, M., & Scott, J. (2015). Beyond authorship: attribution, contribution, collaboration, and credit. *Learned Publishing*, **28(2), 151-155.**

This thesis is based on the following three articles:

Chapter 2

Young, A., Flament, N., Maloney, K., Williams, S., Matthews, K., Zahirovic, S., and Müller, R. D., 2019, Global kinematics of tectonic plates and subduction zones since the late Paleozoic Era: *Geoscience Frontiers*, **v. 10, no. 3, p. 989-1013**. doi: https://doi.org/10.1016/j.gsf.2018.05.011

Alexander Young: Conceptualization, Methodology, Software, Formal analysis, Investigation, Writing - Original Draft, Visualization **Nicolas Flament**: Conceptualization, Methodology, Software, Validation, Writing - Review & Editing, Supervision **Kayla Maloney**: Conceptualization, Methodology, Investigation, Writing - Review & Editing **Simon E. Williams**: Methodology, Validation, Writing - Review & Editing **Kara Matthews**: Conceptualization, Methodology, Investigation, Writing - Review & Editing **Sabin Zahirovic**: Conceptualization, Methodology, Writing - Review & Editing **R. Dietmar Müller**: Conceptualization, Validation, Writing - Review & Editing, Supervision

I confirm that the authorship attribution statement above is correct.

Alexander Young

I confirm that the authorship attribution statement above is correct.

Nicolas Flament

I confirm that the authorship attribution statement above is correct.

___

Kayla Maloney

I confirm that the authorship attribution statement above is correct.

Simon E. Williams

I confirm that the authorship attribution statement above is correct.

Kara Matthews

I confirm that the authorship attribution statement above is correct.

Sabin Zahirovic

I confirm that the authorship attribution statement above is correct.

_____

R. Dietmar Müller

Chapter 3

Young, A., Flament, N., Williams, S., Merdith, A., and Müller, R. D., *In review*, Long-term Phanerozoic sea level change from solid Earth processes: *Earth and Planetary Science Letters*.

Alexander Young: Conceptualization, Methodology, Software, Formal analysis, Investigation, Writing - Original Draft, Visualization **Nicolas Flament**: Conceptualization, Methodology, Software, Validation, Writing - Review & Editing, Supervision **Simon E. Williams**: Conceptualization, Methodology, Validation, Writing - Review & Editing **Andrew Merdith**: Methodology, Validation, Writing - Review & Editing **R. Dietmar Müller**: Conceptualization, Validation, Writing - Review & Editing, Supervision

I confirm that the authorship attribution statement above is correct.

Alexander Young

I confirm that the authorship attribution statement above is correct.

Nicolas Flament

I confirm that the authorship attribution statement above is correct.

Simon E. Williams

I confirm that the authorship attribution statement above is correct.

Andrew Merdith

I confirm that the authorship attribution statement above is correct.

R. Dietmar Müller

Chapter 4

Young, A., Flament, N., Hall, L., and Merdith, A., In review, The influence of mantle flow on intracontinental basins: three examples from Australia: *Basin Research*.

Alexander Young: Conceptualization, Methodology, Software, Formal analysis, Investigation, Writing - Original Draft, Visualization **Nicolas Flament**: Conceptualization, Methodology, Software, Validation, Writing - Review & Editing, Supervision **Lisa Hall**: Methodology, Investigation, Writing - Review & Editing **Andrew Merdith**: Methodology, Validation, Writing - Review & Editing

I confirm that the authorship attribution statement above is correct.

Alexander Young

I confirm that the authorship attribution statement above is correct.

Nicolas Flament

I confirm that the authorship attribution statement above is correct.

Lisa Hall

I confirm that the authorship attribution statement above is correct.

Andrew Merdith

I, the candidate, Alexander Jonathon Young, declare that the authorship attribution statements above are correct.

Alexander Young

As supervisor for the candidature upon which this thesis is based, I can confirm that the authorship attribution statements above are correct.

_____

Dr. Nicolas Flament

As Head of Postgraduate Studies for the School of Earth, Atmospheric and Life Sciences at the University of Wollongong, I can confirm that the authorship attribution statements above are correct.

Associate Professor Phillip Byrne

Certification

I, Alexander Jonathon Young, declare that this thesis submitted in fulfilment of the requirements for the conferral of the degree Doctor of Philosophy, from the University of Wollongong, is wholly my own work unless otherwise referenced or acknowledged. This document has not been submitted for qualifications at any other academic institution.

Alexander Jonathon Young
26th February 2021

Table of Contents

Chapter 1. Connecting plate tectonics, mantle flow and surface topography

There is a mystic aura, a sense of the common story of humanity, that drives our unending fascination with the underground. From industry to the arts, religion to science, cultures in every part of the world share a fascination with the mythic qualities of the subterranean. Perhaps it has to do with the safety and comfort provided by the caves which contain the footprints, stories and histories of our ancestors. Or, somewhat paradoxically, maybe it reflects a curiosity with our mortality; reaching out into the dark unknown to touch the one thing we have been designed to avoid. Indeed, our connection to the unknow beneath us may well be our most universal and deeply embedded curiosity. Stories throughout the world appeal to this inquisitiveness by evoking the transformative powers of the subterranean. From characters in Christian and Islamic religious texts, to the young girl named Alice who fell through a rabbit hole and the Italian writer Dante who journeyed through Hell, new wisdom has been found in the darkness deep beneath us.

In 1638, Athanasius Kircher, a Jesuit scholar drawn by a fascination for the mysterious subterranean world, ventured into the crater of Mt. Vesuvius to study the source of Earth's inherent physical power. Following a path that he believed would lead him to the very centre of the planet and reveal the secrets of its tectonic movements, Kircher came to experience the Earth's dynamism firsthand. The jagged and broken rock of the crater walls lead down into the volcano's chamber where Kircher observed boiling, sputtering magma; streaming smoke; and flames which burst with force and violence and cracked with deafening explosions. It was within this volcanic cavity that Kircher began to develop his thoughts on the processes operating within the Earth. Many years after visiting Mt. Vesuvius, he would set down his theories about Earth's interior in his famous scientific textbook, *Mundus Subterraneus*, published in 1664. Kircher proposed that the Earth's internal structure contained three interconnected systems of conduits, one for each of air, fire and water. The flow of elements through the channels was related to surface processes; the fire conduit, which was connected to an eternal flame in the centre of the Earth, was responsible for volcanoes, while the interaction between fire and air caused earthquakes and the interaction of water and fire was proposed to explain hot springs (Fig. 1.1). Though his ideas and observations about the Earth were advanced for the day they sound more like nonsense to present-day scientists, and yet, his idea of a dynamic Earth, in which heat transfer from the deep interior is the cause of major geological events, remains fundamental to the modern view of the interior and its relationship to the Earth's surface.

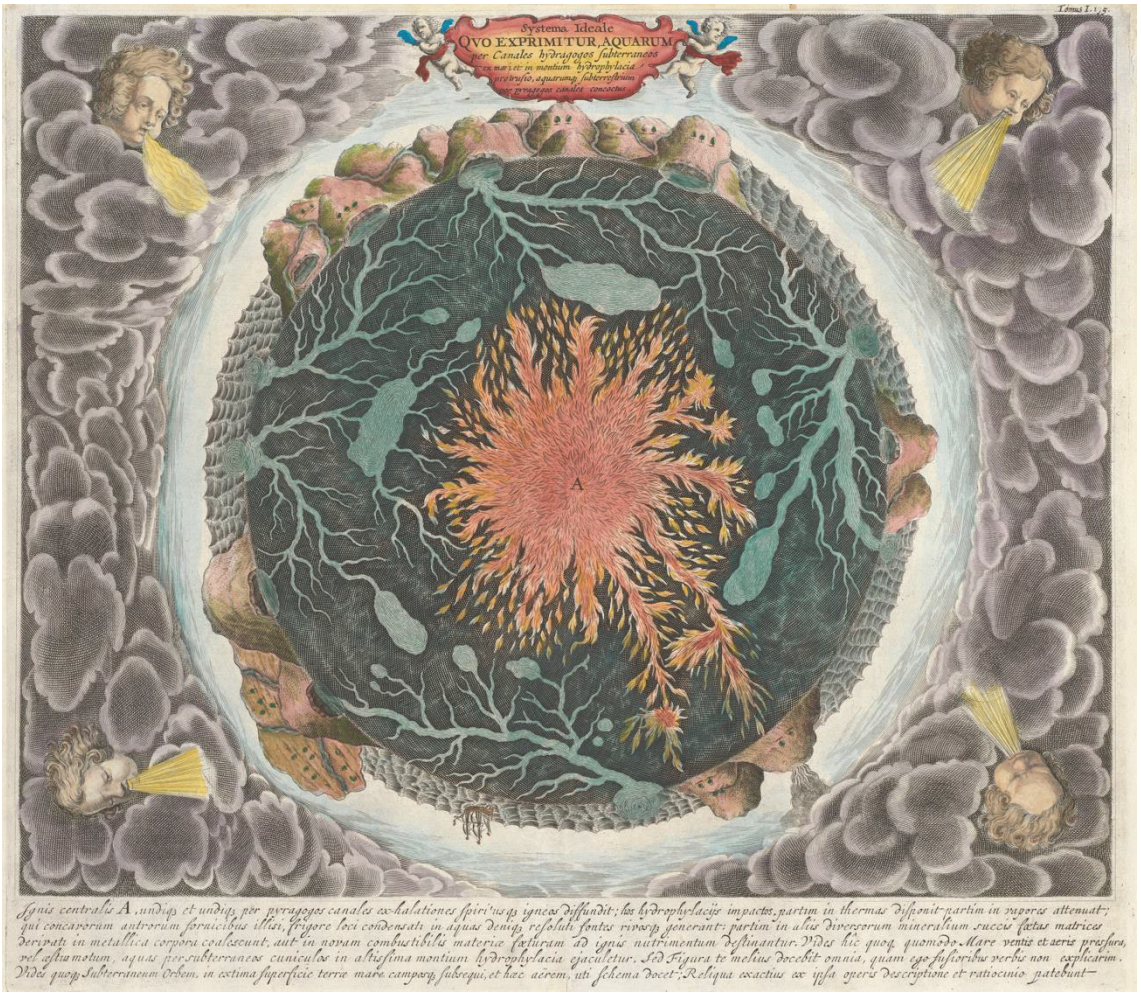

Figure 1.1: Athanasius Kircher (1668), "*Systema ideale quo exprimitur, aquarum per canales hydragogos subterraneos ex mari et in montium hydrophylacia protrusio, aquarumq[ue] subterrestrium per pyragogos canales concoctus*".
English translation: "*Schematic depiction showing how water is thrust from the sea and up to the hydrophylacia* of the mountains through water-carrying subterranean channels, and how subterranean water is boiled by fire-carrying channels.*"
*Hydrophylacia is a technical term of Kircher's, who theorised that there are great subterranean cavities containing liquid water.
This 17th-century, hand-drawn, colour map depicts Kircher's vision of Earth. Situated amongst dense clouds the Earth is depicted as a dynamic, fiery sphere. At the surface we can recognise the oceans, mountains, continents, rivers, whirlpools and even a ship. Within the centre is an eternal flame surrounded by a vascular like network of subterranean conduits and reservoirs.

1.1 The unifying theory of geology

Plate tectonics is the major paradigm for how the solid Earth works. Established in the 1960's, its inception began in 1912 with Alfred Wegener's theory of continental drift. Inspired by a map of the continents and intrigued by the fit of the South American and African coastlines, Wegener developed a theory, supported by paleontological and geological observations, to explain how the continents shift position on the Earth's surface. Wegener's theory was widely denounced by his peers (see Gracht et al., 1928 for a contemporary review); the key objection was an absence of a model to explain how the continents moved apart – i.e., there was no driving mechanism. Despite intriguing observational evidence that the continents had moved Wegener could not provide an explanation for how or why they had moved. Nevertheless, he was one of the first to realize Earth's surface has evolved over time, and he introduced the idea of large-scale crustal movement to the scientific community and laid the foundation for the development of modern plate tectonics.

The hypothesis of plate tectonics states that the Earth is divided into interlocking, internally rigid

plates in constant motion over hotter, more mobile asthenospheric mantle. It is fundamentally linked to the four major components that comprise the structure of the Earth: the crust, the mantle, the outer core, and the inner core; identified from the analysis of seismic waves propagating through the Earth (Dziewonski and Anderson, 1981). The idea of a lithosphere, which represents the rigid, brittle outer part of the Earth including the upper portion of the mantle was first presented by Barrell (1914). It was Holmes (1931) who realised that the shifting plates of the lithosphere not only form the thermal boundary layer of a convecting system (Fig. 1.2) but are the surface manifestation of this process. In the presence of a gravitational field, if material is heated from below or from within, and is cooled from above, it becomes gravitationally unstable; for example, a lava lamp – hot, buoyant material goes up and cold, dense material goes down. In the Earth, contrasting viscosities between the lithosphere and the deeper mantle precludes this simple analogy since greater viscosity in the deeper mantle results in less vigorous convection relative to the less viscous asthenospheric mantle; and yet, the slow creeping motion of Earth's mantle is caused by thermal convection carrying the hot mantle rocks from the interior to the surface, where they cool and descend back into the mantle. The ascent of mantle material at ocean ridges where new seafloor is created and pushed away from the axis of the ridge as it cools is part of this process, as is the descent of the colder lithosphere back into the mantle at subduction zones.

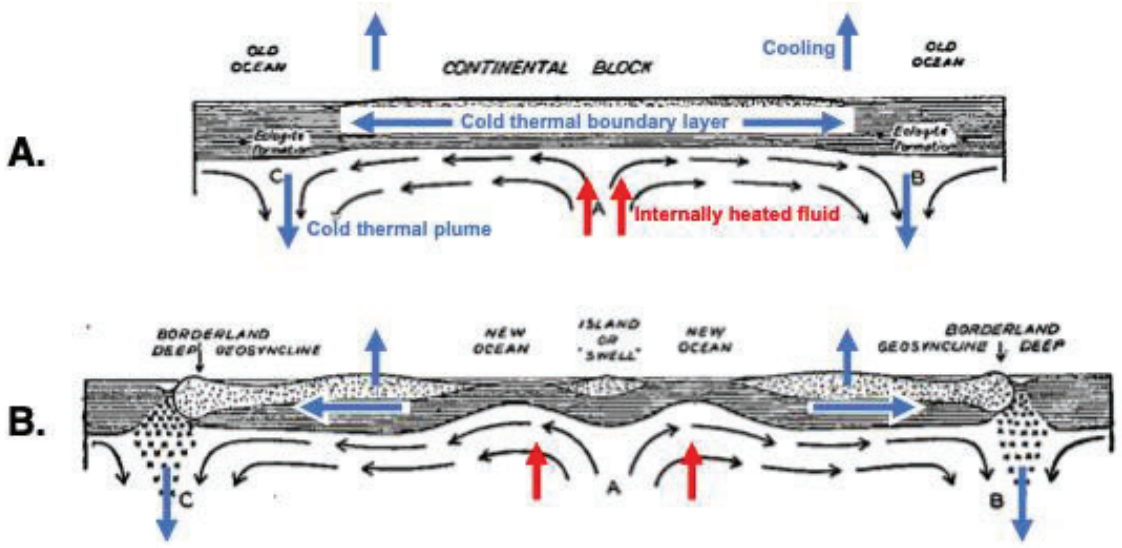

Figure 1.2: A; Holmes' (1931) 2D model for boundary layer thermal convection in a fluid layer heated from within and cooled from above. B; A "real world" application of Holmes' (1931) model.

An essential feature of plate tectonics is that low temperature, rigid layer of the outer Earth is separated into plates. The plates move over the surface without significant internal deformation over geological time scales. Their boundaries are contiguous between plates and fall into three categories: (i) divergent boundaries, (ii) convergent boundaries, and (iii) transform boundaries. The concept of a divergent boundary was introduced by Hess (1962) who proposed that seafloor was created and successively moved away from the axis of a ridge. McKenzie (1969) developed the idea that subduction zones were convergent boundaries where crust was recycled back into the Earth's mantle and Wilson (1965) established the concept of plates and transform faults, where crust is not created or destroyed but plates slide horizontally past each other.

The basic hypothesis of plate tectonics was given by Morgan (1968). Initially, the theory was supported by paleomagnetic studies (Runcorn, 1955) which demonstrated the North Magnetic Pole has drifted across the surface of the globe over time. Assuming Earth's magnetic field is a simple dipole, this meant that either the plates were in motion or, the typically static North Magnetic Pole was. Additional evidence was discovered in the form of patterned magnetic reversals on oceanic crust (Vine and Matthews, 1963). When new lava erupts on the sea flood, the magnetic minerals within the molten rock align themselves with the North Magnetic Pole. The Earth's magnetic field changes overtime, so that the positions of magnetic north and south are switched. The intermittent flipping of the magnetic field is thus recorded with the formation of new oceanic crust is positive proof that the lithosphere is in motion. A final break-through was revealed by global seismicity data that exposed a fundamental geological truth: active geological features – volcanoes and earthquakes – are predominantly aligned along distinct and continuous boundaries (Fig. 1.3) around the world that define the edges of Earth's tectonic plates (Isacks et al., 1968).

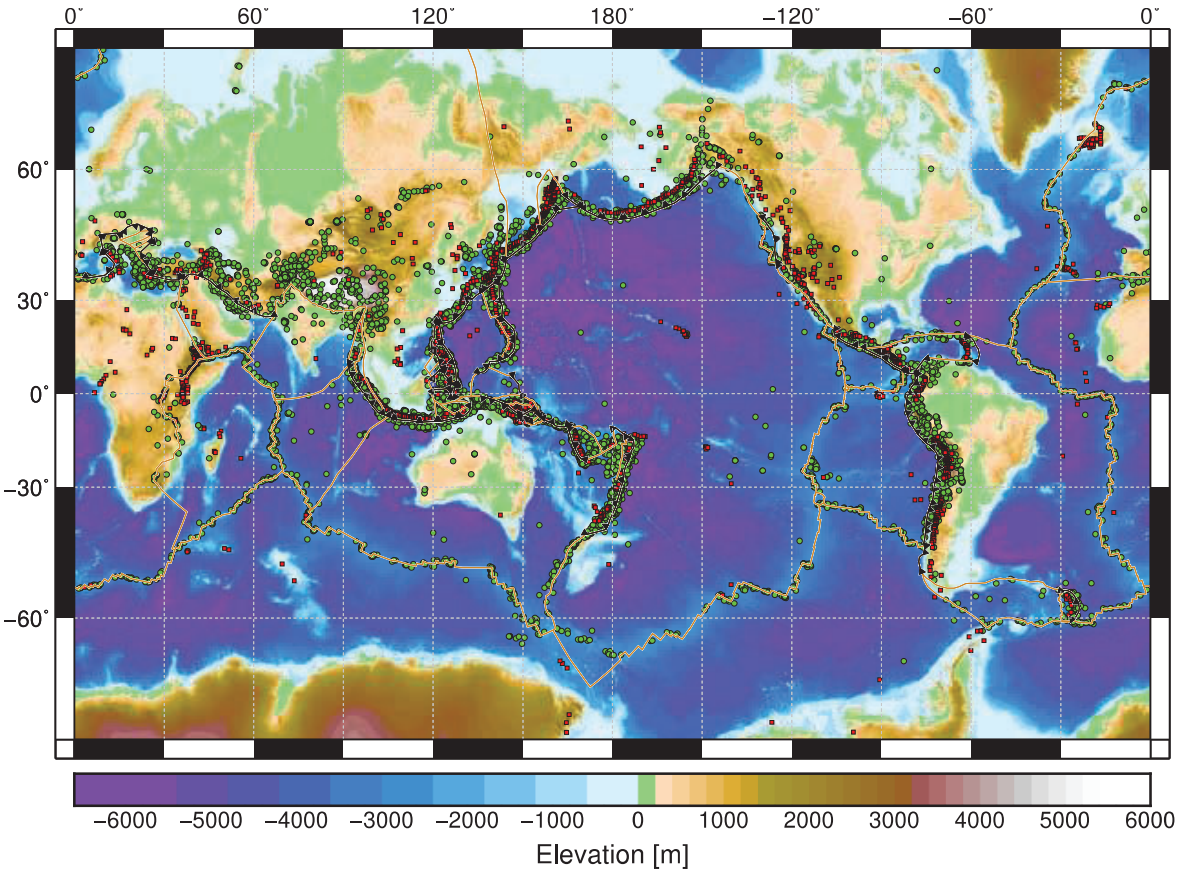

Figure 1.3: Global topography (Amante and Eakins, 2009) plotted with a catalogue of recorded earthquakes (green circles) since 1970 and volcanoes (red squares) thought to have been active in the last 10,000 years. Subduction zones shown as black lines with triangles on the overriding plate and mid-oceanic ridges and transform faults in khaki. Note the correlation between plate boundaries and active tectonism.

Considering the rejection of continental drift on the basis that there was no mechanism, is it somewhat unfair to Wegener that plate tectonics was accepted without a proven mechanism for plate motion. The belief that the plates move due solely to thermally driven mantle convection was lent stronger support when Tackley (1998) demonstrated self-consistent generation of tectonic plates using 3D

mantle convection models and while mantle convection certainly plays a role, it cannot explain why some plates move faster than the convective currents beneath them. The current view – that the plates move as part of a gravity driven system – is still controversial and the forces that act on the plates continue to be investigated. Presently, observational and theoretical inferences suggest plate boundary forces are the most significant (Forsyth and Uyeda, 1975; Carlson et al., 1983; Richardson, 1992), namely: slab pull and ridge push. The former predominates and originates from the negative buoyancy of down-going oceanic lithosphere at subduction zones. As the oceanic lithosphere moves away from an ocean-ridge, it cools, thickens, and increases in density. This results in a gravitational instability between the lithosphere and the underlying asthenosphere so that the lithosphere bends and sinks into the interior of the Earth at a subduction zone. The downward gravitational force on the sinking lithosphere pulls the plate and plays an important role in driving plate tectonics. The ridge push force is the result of a distributed pressure gradient that arises from the newly formed lithosphere cooling and slipping down the raised asthenosphere below mid-ocean ridges. At mid-ocean ridges the newly formed oceanic crust is hot and thus has a higher elevation than the older, colder and more dense plate material further away. The lateral gravitational force generated by the new lithosphere at higher elevations pushes the plate further from the ridge.

Although slab-pull is the primary candidate as the main driving force for plate motion, the force-balance driving plate motions remains a topic of debate and there are scenarios where mantle/asthenospheric drag could be a significant component of the force-balance. Indeed, Poiseuille flow – the component of mantle flow that is driven by horizontal pressure gradients (Turcotte and Schubert, 2002; Höink and Lenardic, 2010; Natarov and Conrad, 2012) – has been suggested to have driven 50% of the Pacific Plate motion since 15 Ma (Stotz et al., 2018).

1.2 Time-dependence and episodicity of tectonic processes

Prior to the introduction of plate tectonics, numerous Earth scientists had identified instances of long-term episodicity in tectonic processes (e.g., Umbgrove, 1940; Holmes, 1951; Sloss, 1963; Sutton, 1963) and, it was the landmark paper of Wilson (1966) that introduced the idea of cyclical continental drift to the mainstream. In particular, he explained – using geological evidence from North America and Europe – that ocean basins open and close; invoking the concepts of divergent and convergent plate boundaries and combining them into a conceptual model that matched geological observations. Inherent in Wilson's (1966) model of opening and closing oceans was Sutton's (1963) less famous argument for the episodic clustering of continents, however, together these two pioneers laid the groundwork for what would come to be known as the supercontinent cycle. Following the validation of plate tectonics by observations, the concept of its cyclicity was advocated to explain temporal patterns in fossil diversity, sea level, plutonism, sedimentation and climate (e.g., Valentine and Moores, 1970; Hallam, 1974; Fischer et al., 1984). Though, it was Worsley et al. (1982; 1984) who recognised that the long-term cyclicity of tectonic processes is the manifestation of supercontinent assembly and breakup and suggested a link between Earth's mantle convection system and the supercontinent cycle.

1.3 The deep-seated origin of Earth's topography

We have seen how the transfer of heat between the surface and inner Earth drives mantle convection, and how in combination with the gravitational forces acting on the lithosphere this drives horizontal plate motion. However, does convection have any effect on the Earth's surface?

Earth's surface topography is primarily supported by density contrasts within the lithosphere and is in isostatic balance (Molnar et al., 2015). These density variations are due to varying lithospheric thickness and composition and are mostly attributed to subduction and continental collision (Fig. 1.4A). Yet, there is another component of topography that is not isostatic and is driven by mantle convection. It is called dynamic topography that arises from density variations in the convective mantle. It was Pekeris (1935) who conceptualised the idea, hypothesising that the surface above a convecting mantle should be pushed upward over rising flow and pulled downward above sinking flow (Fig. 1.4B).

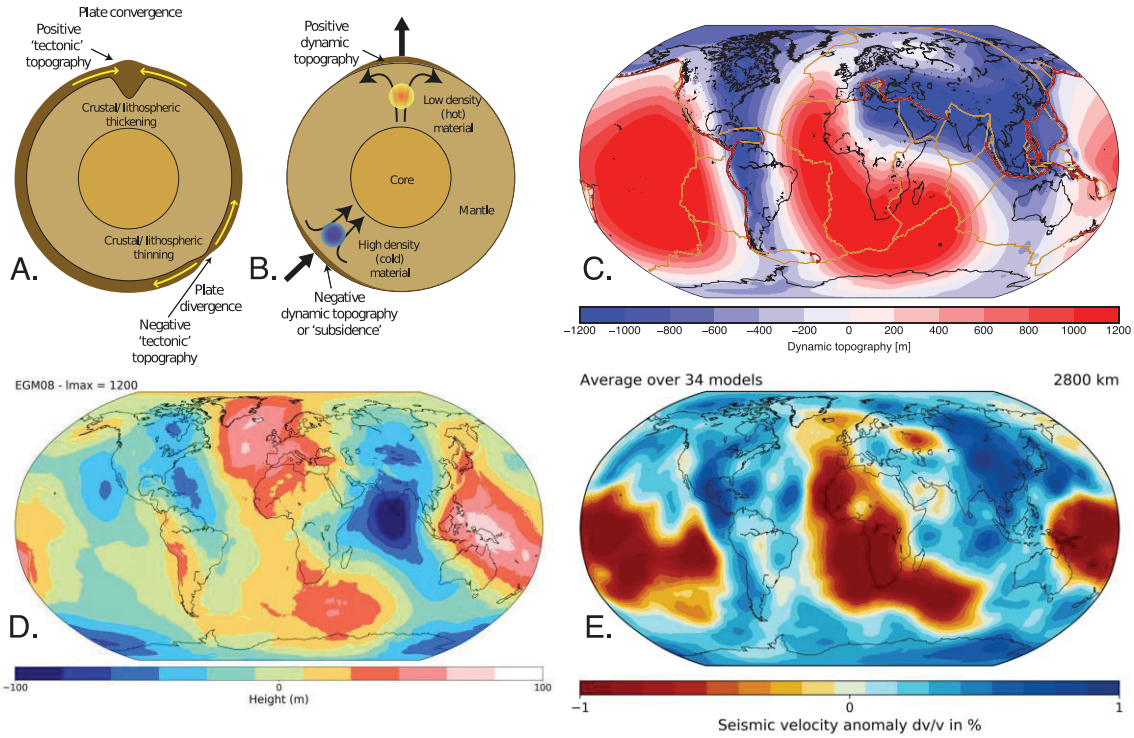

Figure 1.4: Surface expressions of mantle dynamics. A: A cartoon from Braun (2010) showing the normal, isostatically compensated, tectonic topography created by plate tectonics. Convergence results in orogeny and crustal thickening and divergence results in seafloor spreading. Surface topography and crustal thickness are highly exaggerated. B: Another cartoon from Braun (2010), this one illustrating how mantle flow produces dynamic topography at the surface. The red and blue circles represent low (hot) and high (cold) density anomalies in the mantle; the black arrows show the induced mantle flow. Note the resulting surface response. C: Global long-wavelength dynamic topography model from Cao et al. (2018) with subduction zones shown as brown lines with triangles on the overriding plate and mid-oceanic ridges and transform faults in khaki. D: Earth's geoid (Pavlis et al., 2012). E: Average seismic velocity anomalies at 2800 km depth from tomography P wave and S wave models currently supported in *SubMachine* – a web-based tool for interactive visualization, analysis and evaluation of global data sets of the Earth's interior (Hosseini et al., 2018).

Dynamic topography is transient and varies spatially, therefore its signal can be difficult to isolate. Indeed, constraining the present-day spatial pattern, wavelength and amplitude of dynamic topography remains an ongoing debate that has to do with methodology, the definition of the term and uncertainties about the rheology of the mantle (Molnar et al., 2015). There are two predominant methods for estimating present-day dynamic topography: (i) calculating the topography by removing the isostatic contribution of the sediments, ice, crust, and lithosphere from the observed topography which gives the residual

topography (e.g., Hoggard et al., 2017) and (ii) estimating deflection of the Earth's surface in response to the normal stresses predicted by time-dependent mantle flow models (e.g., Flament et al., 2013a). The former indicates dynamic topography occurs at short (~10^3 km) wavelengths with peak amplitudes 800-900 m (Davies et al., 2019; Flament, 2019a) while the latter suggests longer wavelengths (~10^4 km) and greater amplitudes (> 1,500 m; Fig. 1.4C). It has been suggested that the shorter wavelength component is determined by flow in the upper mantle and lithospheric structure while the long-wavelength component is principally controlled by mantle convection (e.g., Davies et al., 2019). A first-order correlation of long-wavelength geoid lows (Fig. 1.4D) and fast seismic anomalies (Fig. 1.4E) – indicating cold, dense regions in the lower mantle – imaged in global seismic tomography models demonstrates a powerful connection between the Earth's surface and density heterogeneities within the mantle; although the relationship between the mantle, geoid and dynamic topography is not straightforward (Hager et al., 1985).

Dynamic topography is also fundamental to understanding the Earth's gravitational field (Hager and Richards, 1989; Colli et al., 2016), it impacts erosion, sediment transport as well as deposition (Burgess and Gurnis, 1995; Petersen et al., 2010; Shephard et al., 2010) and drives eustatic change and continental flooding (Spasojevic and Gurnis, 2012; Conrad, 2013). Given its importance, constraining the spatio-temporal pattern, wavelength and amplitude of dynamic topography has become a focus of many earth scientists (Mitrovica et al., 1989; Lithgow-Bertelloni and Gurnis, 1997; Müller et al., 2000; Wheeler and White, 2002; Heine et al., 2008; Liu et al., 2011; Flament et al., 2013a; Czarnota et al., 2014; Hoggard et al., 2016; Vibe et al., 2018a, b). To track its evolution through geological time, geodynamic models of mantle convection are required. In the numerical models of mantle convection, the component of dynamic topography can be estimated by using the normal stresses produced by the upwellings and downwellings (Lithgow-Bertelloni and Silver, 1998; Steinberger, 2007; Flament et al., 2013a) – although other methods are also used (e.g., Rubey et al., 2017) – which can then be validated by comparison with the geological record. However, a numerical modelling approach can only be used to recover the time-dependent long-wavelength dynamic topography. To reconstruct short-wavelength dynamic topography back in time, details of the structure of the lithosphere are required (e.g., thickness, density, viscosity); which are poorly known for the present-day (Hirth and Kohlstedt, 2004), let alone in the past. Thus, in this work, predictions of the temporal evolution of dynamic topography are reliant on the long-wavelength component, which can be modelled back in time using mantle flow models and not the short-wavelength component which requires a knowledge of the thermochemical structure of the uppermost mantle; *a priori* unknown.

1.4 Reconstructing the past configuration of Earth's tectonic plates

Plate motion models are tools that describe the kinematics of Earth's tectonic plates in a spatial and temporal context. These models are utilised across the Earth sciences in studies of paleogeography (e.g., Scotese and Golonka, 1997; Blakey, 2011), paleoclimate (e.g., Boucot et al., 2013) and eustasy (e.g., Hays and Pitman, 1973; Müller et al., 2008). Critically, they can be used as a surface boundary condition in geodynamic experiments of mantle convection (e.g., Bunge et al., 1998; McNamara and Zhong, 2004; McNamara and Zhong, 2005; Zhang et al., 2010; Rudolph and Zhong, 2014; Flament et al., 2017a) and are fundamental to understanding the evolution of the Earth throughout geological time.

As we have seen from Wegener (1912), the practice of reconstructing the position of continents at different geological times is not new. However, since the early 1900's a wealth of new data, in particular marine geophysical (e.g., magnetic anomaly picks, fracture zones, extinct ridges, seamount trails and absolute sea floor ages from deep sea drilling) and paleomagnetic have significantly improved plate reconstruction models. Also, the progression of computer technology and the development of interactive desktop software (e.g., *PaleoGIS*, (Ross and Scotese, 2000); *PointTracker*, (Scotese, 2010a); and *GPlates* (Müller et al., 2018a)) that allow the visualisation of plate-tectonics has augmented the methods used to build plate motion models and led to the development of high-resolution reconstructions of past plate positions, shapes, and movements. Indeed, what began as a simple geometrical exercise (e.g., Wegener, 1912) later developed into more advanced, computer-generated reconstructions made using numerical methods (e.g., Bullard et al., 1965) and then into more geologically grounded approaches based on fitting magnetic anomaly and fracture zone data (Hellinger, 1981). Soon, tectonic models with comprehensive database of finite rotation poles based on the seafloor spreading record and paleomagnetic data were developed (e.g., Scotese, 1991; Golonka, 2007a; Müller et al., 2008; Fig. 1.5). Over the decades many plate tectonic models and related plate modelling software have been created in both academic institutions and private companies (see Vérard, 2019 for a recent review) however, a particular software is uniquely suited for investigating the feedback between plate motions and mantle flow: the open-source *GPlates* software (https://www.gplates.org/). The specificity of *GPlates* is its link to mantle convection software such as *CitcomS* (e.g., Zhong and Davies, 1999; Zhong et al., 2000; Tan et al., 2006; Zhong et al., 2008; Tan et al., 2010) and *TERRA* (e.g., Baumgardner, 1985; Bunge et al., 1996, 1997; Yang and Baumgardner, 2000; Davies et al., 2013). This is achieved through the implementation of "topological plate boundaries" (Gurnis et al., 2012); a continuous, fully closed network of time-dependent plate boundaries that are used to calculate plate velocities that can then be assimilated into *CitcomS* along with subduction zone geometries and polarities and the thermal structure of the lithosphere (Bower et al., 2015).

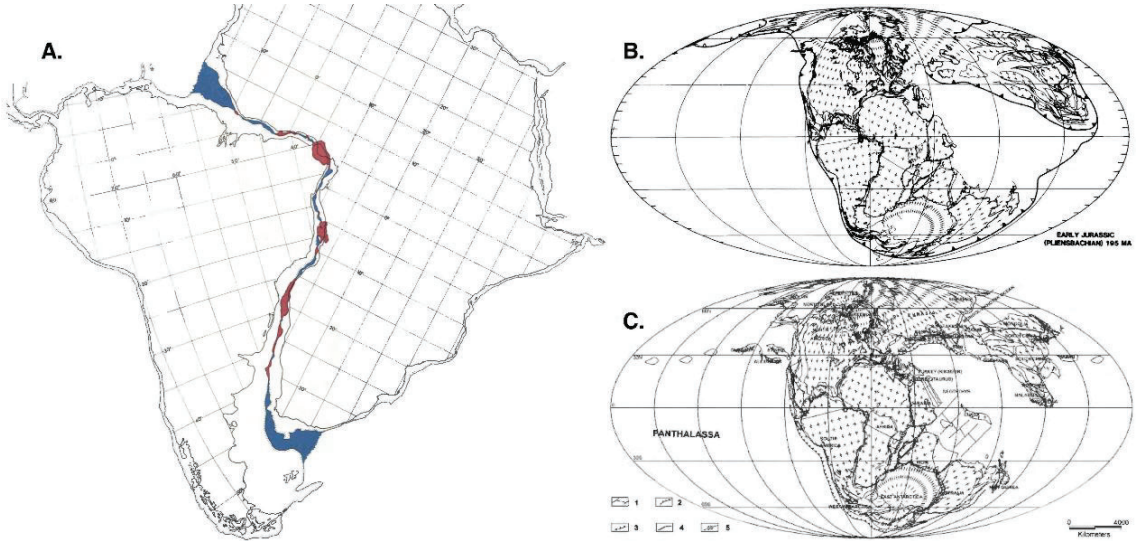

Figure 1.5: Examples of reconstructions according to different models. A: The plate reconstructions of Bullard et al. (1965), one of the first to use computational mathematics and to quantify the uncertainty of rotations. Red and blue areas indicate continental overlaps and gaps respectively. B: This global reconstruction from Scotese (1991) is a synthesis of numerous published regional plate tectonic models. C: A reconstruction from Golonka (2007). This map depicts the plate tectonic configuration inferred from paleoenvironment and lithofacies interpretations. Note the increasing number of continental blocks and inclusion of plate boundaries (subduction zones, mid-ocean ridges and transforms) as well as higher resolution continent-ocean boundaries and coastlines as the models become more modern.

Using *GPlates*, a new generation of tectonic reconstructions – coupled geodynamic-plate models – with plate boundary locations and continuously evolving whole plate topological polygons (Seton et al., 2012; Domeier and Torsvik, 2014; e.g., Matthews et al., 2016; Müller et al., 2016a; Merdith et al., 2017; Domeier and Torsvik, 2019) are being used to reconstruct mantle flow and predict past mantle structure (e.g., Müller et al., 2016b; Young et al., 2019, Chapter 2). These new models incorporate vast collections of geological and geophysical data compiled over decades of research and as such, the configuration of past plates is determined with high accuracy for the past 200 Myr; beyond which approximately 70% of the Earth's surface is unconstrained (Domeier and Torsvik, 2019). And yet, ever increasing amounts of paleomagnetic and geological evidence from continental regions provide plate modelers with the information they need to push tectonic reconstructions further back in time (e.g., Scotese et al., 1979; Dalziel, 1997; Meert and Torsvik, 2003; Li et al., 2008); though, these models only consider the positions of the continents and have no regard for the movement of oceanic plates.

Recently, Merdith et al. (2021) combined reconstructions of the Neoproterozoic (Merdith et al., 2017), early Paleozoic (Domeier, 2016, 2018) and late Paleozoic to present-day (Young et al., 2019, Chapter 2) into the first full-plate, global tectonic reconstruction model spanning continuously from 1 Ga. This model is built in *GPlates* with closed plate polygons so that a time-dependent description of plate boundaries and velocities can be extracted. This permits the investigation and analysis of plate kinematics and dynamics over long geological time scales and supercontinent reorganizations. When coupled with programs to generate synthetic seafloor age maps (Karlsen et al., 2020; Williams et al., 2021) and mantle convection code (e.g., *CitcomS*) plate tectonic reconstructions of this class become powerful tools with which to explore Earth's history (Fig. 1.6).

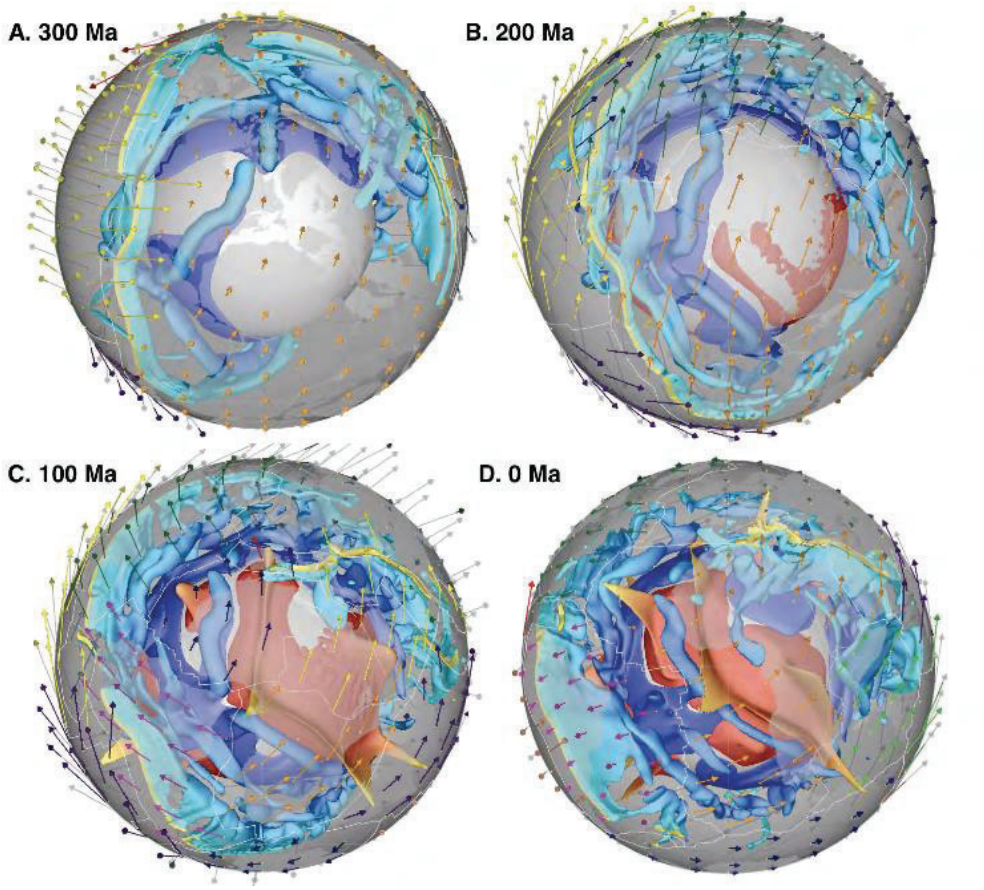

Figure 1.6: Coupled geodynamic-plate models of Young et al. (2019, Chapter 2) spanning 300 Ma to present-day in 100 Myr increments. Absolute plate velocity fields (arrows coloured by tectonic plate) reconstructed present-day coastlines in transparent grey and plate boundaries as white lines. Reconstructed mantle structure indicated by temperature isosurfaces. Isosurface 1 is represented by cooler colours and shows down-going slabs. Temperatures on isosurface 1 are 10% colder than ambient mantle and have values between -0.5 and +0.5. Here, the isovalue is -0.05. This value is non-dimensional and can be converted to temperature as $\Delta T=2825 \times -0.05= -141.25°C$ (i.e., 141ºC cooler than average at a given depth). Isosurface 2 shows hot mantle upwellings as warmer colours (lighter colours are shallower). Temperatures on isosurface 2 are 20% hotter than ambient mantle and have values between -0.5 and +0.5. Here, the isovalue is 0.01; $\Delta T=2825 \times 0.01= 282.5°C$ (i.e., 282.5ºC hotter than average at a given depth). These models demonstrate that as subduction girdles form around mature supercontinents (B) down-going slab material induces upwelling return flow below the supercontinent (C).

1.5 Numerical models of three-dimensional mantle convection

The earliest numerical models of mantle convection were two dimensional (e.g., Moore and Weiss, 1973; Richter, 1973) and while these models provide useful insights into the nature of mantle flow, they cannot replicate actual mantle convection; the fundamental features of which – subducting slabs, mantle plumes and toroidal motion – are three dimensional. More realistic pictures of the form of convection in the mantle began to emerge in the mid-late 1980's with the development of three-dimensional numerical models of thermal convection (e.g., Baumgardner, 1985; Machetel et al., 1986; Cserepes et al., 1988; Houseman, 1988). A major limitation of these early modes is that mantle flow is decoupled from the crust and lithospheric mantle. Considering that approximately 80% of the Earth's mantle surface is covered by these layers (the core mantle boundary covering the remaining 20%) the importance of the plates in geodynamic models of mantle flow becomes self-evident. Thus, relative plate motion history is one of the primary constraints that must exist in the mantle convection models (Ricard and Vigny, 1989; Bunge et al., 1998; Lithgow-Bertelloni and Richards, 1998).

In the early 1990's Louis Moresi wrote *Citcom* (California Institute of Technology Convection in the Mantle), a finite element code that was designed to solve thermal convection problems related to the

Earth's mantle. Originally used to investigate two dimensional convection (Moresi and Solomatov, 1995) *Citcom* was soon modified to solve equations of motion and continuity within three-dimensional Cartesian domains (Moresi and Gurnis, 1996) and later, a spherical version of the code – named *CitcomS* – in which thermal convection is governed by the equations for conservation of mass, momentum and energy was created (e.g. Zhong and Davies, 1999; Zhong et al., 2000; Tan et al., 2006; Zhong et al., 2008; Tan et al., 2010). An important development was made by Bower et al. (2015) who modified the *CitcomS* code to progressively assimilate both the lithosphere and slab history – including plate and upper mantle slab velocities as well as the thermal structure of the lithosphere and upper mantle slabs – from plate reconstruction models and consequently improved the agreement of geodynamic model outputs (dynamic topography, mantle structure) to observations (residual topography, seismic tomography). Now, with the advent of plate tectonic reconstructions spanning from Neoproterozoic times, the modified *CitcomS* code can be used to compute global time-dependent thermochemical mantle convection and model the evolution of mantle structure and dynamic topography (Fig. 1.7) over longer geological timescales (under various approximations).

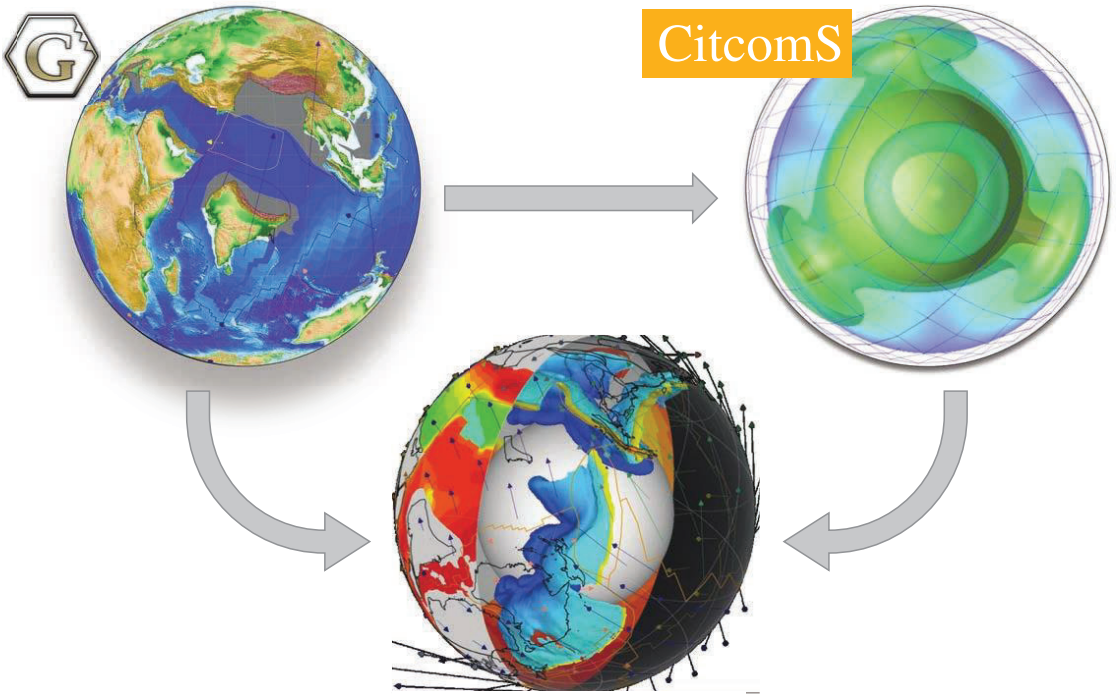

Figure 1.7: Development of forward global mantle flow models. Global reconstructions with continuously closing plate polygons are built using the *GPlates* software (upper left). Plate velocities and thermal structure of the lithosphere and shallow slabs from the tectonic reconstruction are progressively assimilated into the mantle convection code *CitcomS* (upper right). Visualisation of coupled geodynamic-plate models using *GPlates* provides insights into the evolution of mantle structure over long geological timescales (lower centre). Figure made by Dr. Sabin Zahirovic, University of Sydney and used with permission.

Of course, *CitcomS* is not the only mantle convection code and there are numerous alternatives equally capable of solving equations for the conservation of mass, momentum and energy; the governing parameters of thermal convection. For example, *StagYY* (e.g., Tackley, 2008) *TERRA* (e.g., Baumgardner, 1985; Bunge et al., 1996, 1997; Yang and Baumgardner, 2000; Davies et al., 2013). However, the difficulty in reconstructing mantle flow – specifically for investigations into the plate-mantle system – is not mostly about determining numerical solutions to thermal convection but is primarily due to

parametrising the rheological properties of the lithosphere and convecting mantle. Determining the appropriate conditions that reconcile plate boundary behaviour and interior dynamics of the mantle while simultaneously accounting for pressure, temperature and compositional uncertainties in the Earth is not straightforward (Liu and Gurnis, 2008)

Early numerical experiments of three-dimensional mantle flow showed that cold downwellings and hot upwellings dominate mantle dynamics, and these processes lead to long-wavelength lower mantle structures; as suggested by seismic tomography (Tackley et al., 1993). However, variable viscosity, plate tectonics and continental lithosphere are not included in such models and therefore, do not reproduce the present-day mantle structure for comparison with geological observations. Thus, more complex solutions are required.

Presently, three methods dominate studies of mantle flow modelling: forward, backward and adjoint numerical models. Since plate-tectonics and mantle flow are inherently time forward processes, arguably the most logical model is a forward model. In this approach, strategic integration of thermodynamics and plate motion history, is utilised to produce time-dependent reconstructions of mantle flow that are capable of explaining aspects of the geological record (e.g., Gurnis et al., 1998; Lithgow-Bertelloni and Silver, 1998; Flament et al., 2013a). The fundamental limitation of forward convection models is the parametrisation of a suitable initial condition (Bunge et al., 1998; McNamara and Zhong, 2005), since past mantle structure is unknown. Additionally, the choice of plate motion history model is known to have profound effect on the results (Zhang et al., 2010; Young et al., 2019, Chapter 2). Thus, present-day geophysical observables – e.g., the geoid, dynamic topography, mantle structure – can be different to solutions computed by forward models. Some of these limitations can be resolved through the use of a backward advection model.

Models run by using a backward advection approach solve in reversed time and utilise seismic tomographic models to estimate the initial structure of the mantle (e.g., Conrad and Gurnis, 2003; Moucha et al., 2008). This approach guarantees reasonable results for the present-day but is not so useful for investigations into the plate-mantle system in deep geological time (> tens of millions of years) due to complications that arise from time inversion; specifically, thermal diffusion. Since thermal diffusion is an inherently forward process, it is impossible to reconstruct heat to its previous thermal structure once it diffuses into a system. While this can be partially overcome by ignoring heat diffusion and just advecting density backward in time, this limits the validity of the results only back to ~70 Ma (Steinberger and O'Connell, 1998). Furthermore, backward-in-time convection models are unable to infer the generation of thermal buoyancy in boundary layers back in time (Bunge et al., 2003).

To account for the limitations inherent in forward and backward models, adjoint models – which iteratively solve the forward and backward equations – have been developed (e.g., Bunge et al., 2003; Colli et al., 2018; Colli et al., 2020). Results from conceptual studies suggest that adjoint models can constrain mantle flow back in time for approximately 100 million years, assuming past plate motions and the present-day mantle structure are well known (Bunge et al., 2003; Colli et al., 2018). Naturally, mantle flow models based on this approach are more likely to produce results consistent with the present-day mantle structure – since tomographic models are used as an input – thus, permitting detailed and complex comparisons to observations (Liu et al., 2008; Shephard et al., 2010). However, a downside is that adjoint

flow models are numerically intensive and therefore incur a significant computational cost. Also, a single model can take a few months to run (Coltice and Shephard, 2018) and poorly known model parameters (e.g., Rayleigh number, viscosity, thermal expansivity, etc.) as well as uncertain state estimations limit the inverse problem (Colli et al., 2020). Thus, despite substantial improvements, numerical convection modelling of the plate-mantle system remains challenging, and the approach one chooses depends on the problem at hand.

Herein *CitcomS* is used to model mantle flow. The specificity of *CitcomS* is: (i) it is currently the most adept at integrating tectonic reconstructions because plate velocities and thermal structure of the lithosphere are read in to ensure asymmetric subduction (Bower et al., 2015) (ii) it is a forward convection code and therefore capable of modelling mantle flow in deep geological time (>100 Ma), (iii) it is computationally efficient, (iv) the parameter space has been extensively explored (Flament et al., 2017a), (v) the convection model is independent from tomography so the results can be compared to tomographic images of the Earth's interior and (vi) the set up makes comparison to the geological record possible. Some limitations of *CitcomS* will be discussed in Chapter 6.

1.6 Problematic and outline

As established in the preceding sections, Earth's surface is fundamentally linked to flow within the mantle. Indeed, the most observable manifestation of this flow is one of Earth's defining characteristics: plate tectonics. That said, the convective flow in the mantle also produces differences in topographic relief at the Earth's surface (dynamic topography), the evolution of which profoundly impacts the geosphere.

The advent of powerful analytical tools (e.g., *GPlates*) and numerical models (e.g., *CitcomS*) in addition to ever increasing libraries of geological and geophysical data make it possible to quantitatively determine the impact of long-wavelength dynamic topography over long geological time scales (beyond ~100 million years ago). By coupling global plate tectonic reconstructions, dynamic Earth models and geological observations, the time-dependent effect of mantle flow can be analysed and quantified.

This thesis focuses on the impact of dynamic topography as a driver of global sea level change and aims to ascertain the contribution of mantle flow on the evolution of Australian onshore basins over the last 550 million years. To this end, I first create a Phanerozoic plate motion model; discussed and analysed in Chapter 2. The plate reconstruction was constructed with its future use in geodynamic modelling a fundamental consideration and optimising plate and trench kinematics was a primary motivation for this work.

Plate motion model parameters that describe the long-term state of the plate–mantle system (e.g., the balance between advance and retreat of subduction zones, plate velocities, and net-rotation) are useful in assessing the relationship between surface plate motions and Earth's deep interior and provide insights into what might be considered geodynamically reasonable plate behaviour. For example, Zahirovic et al. (2015) extracted time-dependent plate velocities from a plate tectonic reconstruction to suggest Earth's fastest tectonic plates move at a rate of ~9 cm/yr. Furthermore, Torsvik et al. (2010a) used a plate motion model to argue that over the past 150 Ma, rates of net rotation range from 0.1°/Myr to 0.3°/Myr, and following a similar approach, Williams et al. (2015) showed that net rotation values may range from

0.1°/Ma to 0.6°/Ma over the past 120 Myr. In addition to net-rotation considerations, Williams et al. (2015) computed subduction zone kinematics for the last 130 Myr and extended the presented-day findings of Schellart et al. (2008): that trench retreat should dominate over advance.

Previously published full-plate global models of plate motion history spanning Paleozoic times are characterised by fast plate speeds (mean = 11 cm/yr), high net-rotation (mean = 0.7 °/Ma) and widespread trench advance (70% of trenches) (Domeier and Torsvik, 2014; Matthews et al., 2016) which are implausible and also unfavourable for geodynamic modelling; since large plate speeds have been positively correlated with net rotation (Alisic et al., 2012) and high net rotation affects the results of geodynamic modelling (Rudolph and Zhong, 2014).

The aforementioned Paleozoic plate models are hampered by fast plate velocities, high net-rotation and pervasive trench advance because they link plate motion histories to structures in the lowermost mantle – large low shear velocity provinces (LLSVP) – and assume these structures are stable and fixed through time, due to the apparent correlation between the present-day margins of LLSVPs and the reconstructed eruption sites of large igneous provinces and kimberlites (Burke and Torsvik, 2004; Torsvik et al., 2010a); a correlation that is debated (Austermann et al., 2014; Davies et al., 2015) and an assumption that has been questioned by geodynamic modelling (Zhong and Rudolph, 2015; Flament et al., 2017a). The plate reconstruction presented here is devoid of geodynamic assumptions that are evident in other Paleozoic plate models, implements kinematically reasonable histories for the Paleozoic evolution of North and South China and the closure of the Rheic Ocean. When used as a boundary condition in geodynamic modelling, the new tectonic reconstruction produces a model of mantle flow that is consistent with the present-day structure of the deep mantle, challenging the proposed fixity LLSVPs.

Global sea level change causes the waxing and waning of inland seas, affects species migration, the evolution of life and the atmosphere and is fundamental in the deposition of sediment. However, the traditional approach to determining eustatic change – sequence stratigraphy – is only suitable for recovering the sea level signal on million-year time scales and importantly, assumes that tectonically quiescent regions are stable. In order to track eustatic change over longer time scales (> 10 Myr) the sequence stratigraphic approach is augmented by models, though details of such models are not widely accessible (Vail et al., 1977; Haq et al., 1987; Haq and Schutter, 2008). Thus, the development of an open-access, time-dependent method to quantify and analyse first- (~100-200 Myr) and second- (~10-80 Myr) order eustatic cycles is of interest to the entire scientific community.

In Chapter 3, I couple plate tectonic models with time-dependent models of flow within the Earth's mantle and develop a new open-access holistic method to model time-dependent sea level change, allowing me to investigate and quantify the impact of the solid Earth on long-term eustatic change. This work quantifies the evolution of sea level throughout Phanerozoic times, links eustatic fluctuations to the supercontinent cycle, and isolates and quantifies the individual solid Earth mechanisms of eustatic change. The results suggest that long-term sea level change is primarily driven by changes in the volume below mid-ocean ridges (460 m of sea level change), with secondary contributions from dynamic topography (250 m), mantle/ocean water exchange (230 m), marine sedimentation (170 m) and the volume capacity of subduction zones (130 m). Contrary to a published hypothesis, the outcomes of the study show that ocean basin volume change through time is not compensated by either the vertical motion

of continents (Rowley, 2017) or trench topography (Hager, 1980; Gurnis, 1990a).

With newly available plate history, mantle structure and dynamic topography models I am in a position to quantify the magnitude and time dependence of dynamic topography on the evolution of Earth's continental surface. This investigation is achieved by back-stripping well data from three Australian intercontinental basins. The basins selected were the Canning, Southern Carnarvon and Cooper basins specifically because during the time period of interest – the Paleozoic – they were the most stable in Australia. In Chapter 4, I quantify the magnitude and time dependence of dynamic topography on the evolution of Australia. By comparing backstripped and forward modelled tectonic subsidence histories of the three Australian intercontinental basins with models of dynamic topography I investigate how mantle flow has impacted the vertical motion of the Australian continent since Paleozoic times. The results suggest that mantle supported topography influenced the development and evolution of the Canning, Cooper and Southern Carnarvon basins.

Next, in Chapter 5 I integrate paleogeographic reconstructions with all the components of the previous chapters into a final investigation into the effects of mantle flow of depositional environments and an evaluation of the reliability of Australian sequence stratigraphic data as indicative of Paleozoic eustasy. My analysis suggests that during key time intervals – early Ordovician and Devonian – crucial Australian areas were tectonically active and undergoing topographic fluctuation due to mantle flow. These findings question the reliability of the Australian reference districts for eustatic reconstruction and suggest that tectonic and dynamic topography should be considered when selecting reference districts for Paleozoic sea level change. I then examine the correlation between global patterns of dynamic topography and depositional environment to show that dynamic topography may be a controlling factor in paleogeography.

Chapter 2. Global kinematics of tectonic plates and subduction zones since the late Paleozoic Era

Alexander Young[1*], Nicolas Flament[1], Kayla Maloney[2], Simon Williams[2], Kara Matthews[2], Sabin Zahirovic[2], R. Dietmar Müller[2,3]

[1] School of Earth and Environmental Sciences, University of Wollongong, Wollongong, NSW 2522, Australia

[2]EarthByte Group, School of Geosciences, The University of Sydney, Sydney, NSW 2006, Australia

[3]Sydney Informatics Hub, The University of Sydney, Sydney, NSW 2006, Australia

** Corresponding author*

Key words

Tectonic reconstruction**,** Paleozoic**,** plate velocities**,** subduction zone kinematics**,** lower mantle structure, South China

Abstract

Detailed global plate motion models that provide a continuous description of plate boundaries through time are an effective tool for exploring processes both at and below the Earth's surface. A new generation of numerical models of mantle dynamics pre- and post-Pangea timeframes requires global kinematic descriptions with full plate reconstructions extending into the Paleozoic (410 Ma). Current plate models that cover Paleozoic times are characterised by anomalously large plate speeds and trench migration rates because they assume that lowermost mantle structures are rigid and fixed through time. When used as a surface boundary constraint in geodynamic models, these plate reconstructions do not accurately reproduce the present-day structure of the lowermost mantle. Building upon previous work, we present a global plate motion model with continuously closing plate boundaries ranging from the early Devonian at 410 Ma to present day.

We analyse the model in terms of surface kinematics and predicted lower mantle structure. The magnitude of global plate speeds has been greatly reduced in our reconstruction by modifying the evolution of the synthetic Panthalassa oceanic plates, implementing a Paleozoic reference frame independent of any geodynamic assumptions, and implementing revised models for the Paleozoic evolution of North and South China and the closure of the Rheic Ocean. Paleozoic (410-250 Ma) root mean square (RMS) plate speeds are on average ~8 cm/yr, which is comparable to Mesozoic-Cenozoic rates of ~6 cm/yr on average. Paleozoic global median values of trench migration trend from higher speeds (~2.5 cm/yr) in the late Devonian to rates closer to 0 cm/yr at the end of the Permian (~250 Ma), and during the Mesozoic-Cenozoic (250-0 Ma) generally cluster tightly around ~1.1 cm/yr. Plate motions are best constrained over the past 130 Myr and calculations of global trench convergence rates over this period indicate median rates range between 3.2-12.4 cm/yr with a present-day median rate estimated at ~5 cm/yr. For Paleozoic times (410-251 Ma) our model results in median convergence rates largely ~5 cm/yr. Globally, ~90% of subduction zones modelled in our reconstruction are determined to be in a

convergent regime for the period 120-0 Ma. Over the full span of the model, from 410-0 Ma, ~93% of subduction zones are calculated to be convergent, and at least 85% of subduction zones are converging for 97% of modelled times. Our changes improve global plate and trench kinematics since the late Paleozoic and our reconstructions of the lowermost mantle structure challenge the proposed fixity of lower mantle structures, suggesting that the eastern margin of the African LLSVP margin has moved by as much as ~1450 km since late Permian times (260 Ma). The model of the plate-mantle system we present suggests that during the Permian Period, South China was proximal to the eastern margin of the African LLSVP and not the western margin of the Pacific LLSVP as previously thought.

2.1. Introduction

Plate motion models that describe the kinematics of Earth's tectonic plates in a spatial and temporal context are utilised in studies of paleogeography (e.g. Scotese and Golonka, 1997; Blakey, 2011), paleoclimate (e.g. Boucot et al., 2013), reconstructions of past sea levels (e.g. Hays and Pitman, 1973; Müller et al., 2008), mantle convection (e.g. Bunge et al., 1998; Zhang et al., 2010; Rudolph and Zhong, 2014; Flament et al., 2017a) and provide a framework for geophysical and geological data synthesis and analysis that help unravel the solid Earth's history. A new generation of models that reconstruct the continuous evolution of whole plates using continuously evolving topological polygons has been developed (Gurnis et al., 2012). Such global tectonic reconstructions (Torsvik et al., 2010b; Seton et al., 2012; Müller et al., 2016a) have mostly been developed for Mesozoic times. Recent advancements have, however, seen global reconstructions with continuously closing plates produced for late Paleozoic (Domeier and Torsvik, 2014; Matthews et al., 2016) and Neoproterozoic (Merdith et al., 2017) times.

Developing a global plate reconstruction model that extends back into the Paleozoic Period presents numerous challenges. Marine geophysical data (magnetic anomaly picks, fracture zones, extinct ridges, seamount trails and absolute sea floor ages from deep sea drilling) contribute a considerable component to the data assemblage used to constrain the motion of oceanic plates (Seton et al., 2012; Müller et al., 2016a). Due to the continuous destruction of oceanic lithosphere through subduction, data constraining ocean basin evolution become increasingly sparse back in time. Plate models preceding Mesozoic times are ever more dependent on data including paleomagnetic constraints, palaeontology, sedimentology, and episodes of significant magmatism, metamorphism and orogenesis. In combination, these data can be used to constrain the spatial and temporal distribution of plates through geological time. Paleomagnetic data represent the primary constraint on the paleolatitude of continental blocks prior to the Mesozoic, but due to the symmetry of Earth's rotation axis and the position of the time averaged geomagnetic field, paleolongitudes remain elusive (Butler, 1998).

An important feature of global plate motion models that incorporate closed plate polygons is the ability to extract a continuous description of plate velocities through time. Current published plate motion models for late Paleozoic times are characterised by large global plate speeds (Domeier and Torsvik, 2014; Matthews et al., 2016). It is generally recognised that removing unrealistically large speeds of partly- or entirely synthetic plates for Paleozoic times can improve the robustness of global plate reconstructions spanning these times. Furthermore, plate motion models analysed in terms of subduction

zone kinematics (Matthews et al., 2016) suggest that Paleozoic trench migration rates are inconsistent with Cenozoic estimates (Williams et al., 2015).

As modellers attempt to reconstruct Earth's plate configurations farther back in time, paleomagnetic data take on additional importance as other data become increasingly scarce. However, the difficulty in determining paleolongitude represents the fundamental limitation of paleomagnetic tectonic reconstructions. To supplement paleomagnetic constraints on plate motion in geological times, authors have sought to utilize the deep mantle structure as a reference frame for the surface movements of tectonic plates (Domeier and Torsvik, 2014; Torsvik et al., 2014). Inherent in this workflow is the assumption that the structure of the lowermost mantle has remained unchanged since Paleozoic times, a hypothesis that has been questioned by numerical modelling (Bunge et al., 1998; Zhang et al., 2010; Tan et al., 2011; Bower et al., 2013; Hassan et al., 2015; Zhong and Rudolph, 2015; Flament et al., 2017a). Anchoring past plate motions to the present-day mantle structure has implications for both relative and absolute plate velocities. Strict adherence to deep mantle constraints on the Devonian position of Laurussia (Domeier and Torsvik, 2014; Matthews et al., 2016) produces fast relative plate motions (~30 cm/yr) with respect to adjacent plates (Africa) and fast absolute speeds (>15 cm/yr) with respect to the spin axis for this plate. The absolute speed of Laurussia during the Devonian exceeds tectonic speed limits (~15 cm/yr) suggested for plates with large continental area (Zahirovic et al., 2015).

Reducing global plate speeds was the principal objective of this study, which we achieved by using an alternative Paleozoic reference frame and refining the relative plate motion model. We qualitatively assessed our reconstruction by applying it as a surface boundary condition for geodynamic modelling and comparing the resulting reconstructions of Earth's lowermost mantle with vote maps for present day tomography models (Lekic et al., 2012). Building upon the foundation provided by previous studies (Domeier and Torsvik, 2014; Matthews et al., 2016) we present a global plate model that spans from late Paleozoic times to the present day (410-0 Ma). We modify the late Paleozoic (410-251 Ma) behaviour of the synthetic Panthalassa Ocean plates, and implement alternative scenarios for the Devonian-Carboniferous closure of the Rheic Ocean and the amalgamation of Eastern China at ~200 Ma to reduce plate speeds over the interval. Using the new plate reconstruction as a surface boundary condition, we model mantle convection from 410 Ma to present day and analyse the behaviour of lowermost mantle structures since late Permian times.

We have endeavoured to create a plate model that is consistent with key geological data, follows the principles of plate tectonics and satisfies geodynamic criteria including plate and subduction zone kinematics (Williams et al., 2015; Zahirovic et al., 2015).

2.2. Geodynamic and geological motivations for plate motion models

Our work uses the late Paleozoic to present-day global plate model of Matthews et al. (2016) as a primary framework, which itself was constructed from two published models (Domeier and Torsvik, 2014; Müller et al., 2016a). In the reconstruction of Domeier and Torsvik (2014), the motions of some continental blocks (e.g., Africa, Laurentia, South China) are defined directly with respect to the spin axis based on their own apparent polar wander paths. Alternatively, the plate model of Matthews et al. (2016) describes the motion of any given plate relative to an adjacent plate using a finite Euler rotation. In this

way, all plates in the reconstruction of Matthews et al. (2016) move relative to the African continent, which is linked, via a true polar wander (TPW) correction (Torsvik et al., 2014), to Earth's spin axis. Africa is considered the top of the plate hierarchy because in post Pangea times it has undergone little longitudinal movement and has been surrounded by passive margins (Torsvik et al., 2008).

Our reconstruction was built using the software *GPlates*, and as with the input model, utilises a global plate hierarchy with Africa at its top. Therefore, the model we present is a relative plate motion model tied to Earth's spin axis via a reference frame describing Africa's motion relative to the spin axis.

2.2.1 Plate motion model

An important component of any global plate motion model is the method used to link (relative) plate motions to the Earth's spin axis. Constraining plate motion reference frames into the geological past can involve incorporating volcanic hot spot tracks (for the last ~130 Ma) and paleomagnetic data to produce a hybrid reference frame (Torsvik et al., 2008). A key uncertainty associated with the paleomagnetic component (for ages before ~70 Ma) of the hybrid reference frame is the unconstrained nature of paleolongitude. Aiming to improve paleomagnetic reference frames in Paleozoic times, a number of studies have used the apparent correlation between the present-day margins of large low shear velocity provinces (LLSVPs) and the reconstructed eruption sites of large igneous provinces (LIPs) and kimberlites (Burke and Torsvik, 2004; Burke et al., 2008; Torsvik et al., 2010a; Torsvik et al., 2014) to constrain paleolongitudes. Such reference frames assume both that LLSVPs are stable and rigid, and that plumes arise from their edges. Alternatively, Mitchell et al. (2012) identified that the centres of successive supercontinents (corresponding to Earth's axis of minimum moment of inertia, I_{min}) since Nuna (~1.7 Ga; Hawkesworth et al., 2009) are offset by ~90°. Mitchell et al. (2012) proposed fixed points for the determination of paleolongitude deep in geological time by tracing the trajectory of consecutive supercontinents centres with respect to the present-day I_{min}.

Inherently, the paleomagnetic poles used to describe absolute plate motions record the signal of two sources of motion: motion of the plate relative to the spin axis and the rotation of the entire mantle relative to the spin axis. The latter is called true polar wander (TPW) and is caused by the spin of the Earth driving a redistribution of mass anomalies, such as supercontinents or large-scale mantle density anomalies, which form as a result of plate tectonic processes (Evans, 2003). In a stable state, Earth's largest moment of inertia is aligned to the spin axis, so that geoid highs are placed near the equator and geoid lows are at the poles (Steinberger and Torsvik, 2010). When this is not the case, TPW occurs, rotating the mantle and plates as a single unit with respect to the core.

TPW can be quantified by measuring the relative motion of hotspots to the paleomagnetic reference frame (Besse and Courtillot, 1991; Evans, 2003) assuming slow moving, deep-mantle hotspots. For times before ~130 Ma, an absence of well-defined hotspot tracks (Müller et al., 1993) precludes the calculation of TPW in this way and alternative methods for measuring pre-Cretaceous TPW are required (Evans, 2003; Steinberger and Torsvik, 2008). However, estimates of TPW produced by these methods are rather uncertain as they rely on continental Apparent Polar Wander (APW) paths in isolation and consequently make estimates of TPW without knowledge of oceanic plate motion. Despite the relatively limited available data, authors have examined the pre-Cretaceous paleomagnetic record and there is

consensus that TPW occurred in these times (Van der Voo, 1994; Kirschvink et al., 1997; Marcano et al., 1999; Meert, 1999; Evans, 2003). Recently, advanced continental plate models have been used to investigate pre-Cretaceous TPW following the methods of Steinberger and Torsvik (2008). Assumptions regarding the fixity of the I_{min} axis about which TPW occurs result in very different reconstructions (Mitchell et al., 2012; Torsvik et al., 2014). Torsvik et al. (2014) assumed that LLVPs are stable and fixed I_{min} in its present-day position at 0°N, 11°E during Paleozoic times. Alternatively, Mitchell et al. (2012) proposed a model of supercontinent orthoversion and shifted the location of I_{min} 90° from its present-day position to 0°N, 100°E in the earliest Paleozoic. Domeier and Torsvik (2014) implemented the reference frame and accompanying TPW correction of Torsvik et al. (2014) in their plate reconstruction, reducing global plate speeds and net rotation in Paleozoic times by only 4% on average compared to a non-TPW corrected reconstruction.

As the paleolongitude of continental blocks cannot be constrained in pre-Mesozoic times without making assumptions, we applied the purely paleomagnetic reference frame of Torsvik and Van der Voo (2002). This paleomagnetic reference frame is the spherical spline apparent polar wander path (APWP) of Gondwana, derived from reliable paleopoles and calculated assuming a geocentric axial dipole field. Considering the uncertainties and assumptions implicit in distinguishing TPW from plate motions and the negligible impact it appears to have on global surface kinematics, we decided not to correct absolute plate motions for TPW.

2.2.2. Geological evidence of past relative plate motions

2.2.2.1. China

Modern China is a composite ensemble of tectonic blocks, most of which were separate from the major continental masses of Gondwana, Laurussia, and Siberia during Paleozoic times (McElhinny et al., 1981; Stampfli and Borel, 2002; Scotese, 2004; Golonka, 2007b; Cocks and Torsvik, 2013; Domeier and Torsvik, 2014; Torsvik et al., 2014). The North China Block (NCB) and the South China Block (SCB) represent two of the larger tectonic units in Eastern Asia and are separated by the Qinling Orogenic belt (Fig. 2.1) (McElhinny et al., 1981; Mattauer et al., 1985; Lerch et al., 1995; Xue et al., 1996; Meng and Zhang, 1999, 2000; Dong et al., 2011a; Wu and Zheng, 2013). Within the Qinling Orogenic belt are three ophiolite zones and four main tectonic divisions, from north to south these are: The Southern North China Block (S-NCB), the Erlangping ophiolite zone, the North Qinling Belt (NQB), the Shangdan suture zone, the South Qinling Belt (SQB), the Mianlue suture zone, and the SCB (Fig. 2.1B) (Dong et al., 2011a).

Historically, the prevailing tectonic model for the growth of the orogen was a simple model of collision between the NCB and the SCB, however, the timing of the collisional event has been disputed. Post-collisional granitoid plutonism, deformation and metamorphism in the northern part of the NQB led Xue et al. (1996) to propose the Erlangping ophiolite zone as the main suture zone between the NCB and the SCB in the Late Ordovician. Alternatively, the Shangdan suture zone has been advocated as the site of a long and complicated collision between the NCB and SCB that spans the Late Paleozoic; this is deduced from stratigraphic analysis of the Devonian section, and geochronology and geochemistry of intrusive magmatic rocks, ophiolite suites, granites, and volcanic and sedimentary rocks (Mattauer et al., 1985; Benren et al., 1994; Lerch et al., 1995; Zaiping and Qingren, 1995). Also, a Mesozoic aged collision is

supported by paleomagnetic data, paleobiogeography, stratigraphic data and geochronology of subduction-related intrusive volcanics (Sengor, 1985; Lin and Fuller, 1990; Huang and Opdyke, 1991; Yin and Nie, 1993). In the following, we review each of the three suture zones between NCB and SCB and clarify the role of each in the tectonic evolution of the Qinling Orogenic belt.

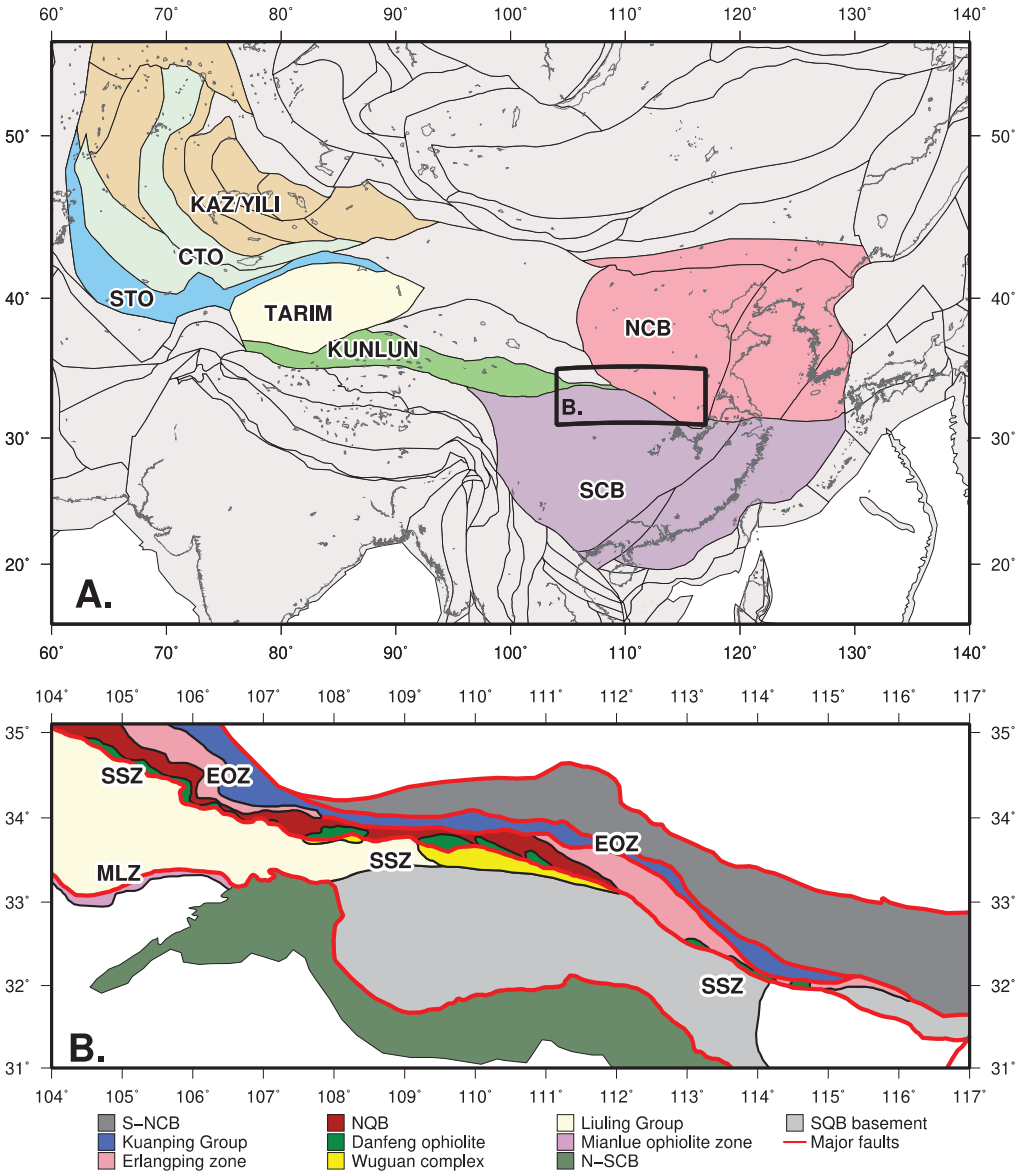

Figure 2.1. (A) Tectonostratigraphic blocks of China discussed in the text. KAZ/YILI, Kazakhstan-Yili (brown); CTO, Central Tianshan block (light green); STO, South Tianshan block (blue); Tarim block, (yellow); Kunlun block, (green); NCB, North China block (pink) and; SCB, South China block (purple). (B) A simplified tectonic map of the Qinling orogenic belt showing the tectonic divisions. EOZ, Erlangping ophiolite zone; SSZ, Shangdan suture zone and; MLZ, Mianlue suture zone. Modified from Chen et al. (2014), Dong and Santosh (2016) and Liao et al. (2017).

The Erlangping ophiolite zone (Fig. 2.1B) in the North of the Qinling belt consists of a mélange unit of pillow lavas and massive basalts interlayered with deep water Ordovician to Silurian radiolarian cherts (Benren et al., 1994; Meng and Zhang, 2000; Dong and Santosh, 2016). The prevailing interpretation for the geodynamic affinity of the Erlangping volcanics, based on geochemical characteristics, is that these rocks formed in a back-arc setting (Benren et al., 1994; Sun et al., 1996; Yan

et al., 2007; Dong et al., 2011b). Middle-Late Ordovician granites that crosscut the Erlangping mélange constrain the timing of back arc closure (Wang et al., 2016) and they mark terminal collision between the NQB with NCB.

Cambrian and Ordovician paleomagnetic data from sedimentary rocks in the NCB indicate that the block was located in the tropical zone (between 30°-15°) of the southern hemisphere during early Paleozoic times, which is consistent with sedimentary facies analysis (Zhenyu et al., 1998). A late Ordovician paleomagnetic pole reconstructs the SCB to a similar position (Han et al., 2015a).

The Shangdan suture zone (Fig. 2.1B), which consists of an ophiolite mélange composed of mafic and ultra-mafic rocks and radiolarian cherts (Meng and Zhang, 2000; Dong et al., 2011a), separates the NQB from the SQB and is commonly thought to represent the principal site of the collision and subduction events that preceded the consolidation of the NCB and the SCB (Mattauer et al., 1985; Guowei et al., 1989; Enkin et al., 1992; Meng and Zhang, 1999; Dong et al., 2011a; Li et al., 2015). Subduction-related intrusive rocks in the Shangdan suture zone yield Silurian-early Devonian zircon ages, and indicate subduction during this time (Kröner et al., 1993; Lerch et al., 1995; Yan et al., 2008; Dong et al., 2011a; Dong et al., 2013).

An early Paleozoic sedimentary wedge, occasionally referred to as the Wuguan complex (Yan et al., 2016; Liao et al., 2017), and the middle to late Devonian Liuling Group are located in the SQB to the south of the Shangdan suture zone (Fig. 2.1B) and record the subduction of Shangdan oceanic lithosphere (Mattauer et al., 1985; Zaiping and Qingren, 1995; Dong et al., 2011b; Dong et al., 2011a; Dong et al., 2013). The youngest age of detrital zircons from the meta-clastic rocks in the western Wuguan complex indicate deposition after 455 Ma, and magmatic zircons from a cross-cutting dike are dated at ~435 Ma, constraining deposition between these times (Dong et al., 2013). The youngest age of detrital zircons in the eastern part of the wedge constrains time of sedimentation to after ~420 Ma (Chen et al., 2014; Yan et al., 2016). A fore-arc basin setting has been suggested as the depositional environment for sedimentary rocks of the western Wuguan complex (Qingren et al., 1994; Zaiping and Qingren, 1995) and the uniform age spectrum of detrital zircons supports this model, as it indicates provenance of sediment is consistently from erosion of the NQB island arc (Dong et al., 2013).

Fossil evidence and regional correlations suggest the Liuling Group (Fig. 2.1B) is middle to late Devonian in age (Yan et al., 2012). A correlation between the Liuling Group and both the NQB and SQB is evidenced by analogous Cambrian-Devonian peaks in detrital zircon age spectra (Ratschbacher et al., 2003; Dong et al., 2013; Liao et al., 2017), similar stratigraphic profiles (Meng and Zhang, 2000), and sediment providence trends indicated by La/Th ratios (Benren et al., 1994; Gao et al., 1995), suggesting closure of the Shangdan Ocean preceded the deposition of the Liuling Group in the middle Devonian. Interpretation of stratigraphic sections has led to the classification of the Liuling Group as a flysch unit (Ratschbacher et al., 2003) therefore, a foreland basin setting has been proposed as the depositional environment (Dong et al., 2013). The north-directed subduction of the Shangdan Ocean beneath the southern margin of the NQB is suggested by WNW-trending, sinistral transpressive wrench zones in Northern Qinling and ~N-S shortening within the Liuling Group (Ratschbacher et al., 2003) as well as: the continuous deposition of middle Devonian to early Triassic successions in the SQB (Meng and Zhang, 2000), the exhumation of the NQB, as suggested by amphibole geochronology (Dong and Santosh, 2016),

metamorphic zircon overgrowths (403 ± 7 Ma) obtained from the northernmost Liuling Group (Ratschbacher et al., 2003), and widespread occurrence of subduction-related intrusive volcanic rocks in the NQB (Dong et al., 2011a). Northward subduction of the Shangdan oceanic crust at the southern margin of the NQB resulted in the collision between the SQB and the NCB before the end of the Silurian. Paleomagnetic poles place the SCB in a position in the equatorial domain (~8°N) during the Silurian evolution of the Shangdan Ocean (Opdyke et al., 1987; Huang et al., 2000).

The Mianlue suture (Fig. 2.1B) in the south of the SQB consists of broken ophiolite sequences containing ultramafic rocks, gabbros, oceanic tholeiites and radiolarian cherts (Zhang et al., 1995; Meng and Zhang, 1999; Dong and Santosh, 2016). The discovery of the Mianlue suture (Zhang et al., 1995) led to a revision of the tectonic model for the development of the Qinling Orogenic belt, implying that it is a multiple-phase orogeny characterised by the subduction and collision of several plates at several suture zones (Li et al., 1996; Xue et al., 1996; Meng and Zhang, 1999; Ratschbacher et al., 2003; Lai et al., 2004; Xu et al., 2008; Dong et al., 2011a; Liao et al., 2017).

Silurian continental rifting along the northern margin of the SCB, resulting in the opening of the Mianlue Ocean, is evidenced by extensive basalts of the Lanjiafan Group (Yunpeng et al., 1999) and supported by zircon geochronology from anorogenic A-type granitoids (439 ± 6 Ma, Ma et al., 2005). The geochemical characteristics of the Mianlue ophiolite complex and its associated volcanics are consistent with oceanic crust (LREE depleted N-MORB) generated during Carboniferous through Permian times (Dong et al., 1999; Lai et al., 2004). Triassic ages have been derived from whole rock Sm-Nd and Rb-Sr isochron dating of metavolcanic rocks from the Mianlue Ophiolite Zone and are interpreted to represent the metamorphic age of the rocks, thus providing an upper limit for the initiation of ocean basin closure (Li et al., 1996). U-Pb zircon dating from igneous rocks within the Mianlue Ophiolite Zone suggest a 300 ± 61 Ma subduction event beneath the SQB (Li et al., 2004). Orogenic granites in South Qinling yield zircon U-Pb ages that indicate Triassic collision between NCB and SCB (Sun et al., 2002; Qin et al., 2008), an event that reactivated Devonian shear zones and caused north-south shortening by folding and thrusting throughout the Qinling belt (Ratschbacher et al., 2003). High-Mg andesites and adakitic andesites recognised within the Mianlue Ophiolite Zone are characteristic of melts generated in an island arc setting (Xu et al., 2000), suggesting northward subduction of the Mianlue Ocean. Analysis of pre-Jurassic paleomagnetic poles from the NCB and SCB are significantly different, whereas post-Jurassic poles are indistinguishable, leading to the prevailing interpretation that the two blocks were joined by ~170 Ma (Enkin et al., 1992; Gilder and Courtillot, 1997; Van der Voo et al., 2015). Paleomagnetic data from the SCB show that it drifted progressively north though the late Paleozoic before colliding with the NCB in the Jurassic and amalgamating into Eurasia (Hanning et al., 1998; Han et al., 2015a). Permian paleomagnetic poles place both blocks in near equatorial positions, with the NCB at ~10°N and the SCB at ~2°N (McElhinny et al., 1981). The Permo-Triassic history of the SCB is characterised by a period of rapid northward drift (Ma et al., 1993). Paleomagnetic data show that the NCB underwent a slight northward motion accompanied by counterclockwise rotation during Jurassic times (Van der Voo et al., 2015). In summary, age data from the Mianlue ophiolite and associated volcanics indicate that the Mianlue Ocean was initially opened during Silurian times, formed and expanded mainly during Devonian-Carboniferous times, and was closed by Jurassic times.

These data suggest that through the Devonian and Carboniferous, the Mianlue Ocean developed into a large, wide ocean separating the NCB-NQB-SQB collage from the SCB. Subduction of the Mianlue oceanic plate beneath the southern margin of the SQB began in early Permian times and continued until the SCB collided during the Jurassic Period. Coeval subduction on the northern margin of the NCB closed the Paleo-Asian Ocean (PAO) and joined Amuria to the NCB in the early Triassic (Domeier and Torsvik, 2014), so that by earliest Jurassic times the SCB, NCB and Amuria had amalgamated and formed a single tectonic plate. During the Jurassic the Sino-Amuria plate and Siberia approached each other as the Monghol-Okosk Ocean was subducted beneath the eastern margin of Siberia and was sutured together during early Cretaceous times (Van der Voo et al., 2015). Subduction beneath eastern Siberia is based on a structural analysis of the Central Asian Orogenic Belt (Lehmann et al., 2010) and supported by numerical modelling and seismic tomography (Fritzell et al., 2016).

2.2.2.2. Tarim block

The Tarim block (TRM) (Fig. 2.1A) rifted off Gondwana during late Ordovician-Silurian times (Zhao et al., 2014) and was probably a solitary continent throughout Devonian and Carboniferous times, similar to the NCB and SCB. During this period, TRM experienced several important tectonic events, including continental collision with the Kunlun block (Fig. 2.1A) at its southern margin (Matte et al., 1996; Yang et al., 1996; Zhihong, 2004) and the Central Tianshan block (CTO) (Fig. 2.1A) at its northern margin (Gao et al., 2011; Han et al., 2011; Wang et al., 2011). Igneous rocks of middle Silurian to Devonian age found on the northern margin of TRM indicate subduction during this time (Ge et al., 2012; Han et al., 2015b; Zhao et al., 2015). Reactivated ENE-trending thrust faults and wide erosional surfaces caused by uplift of the periphery of the Tarim Basin are further indications of convergence along the northern margin of TRM during middle Paleozoic times (He et al., 2016).

At present, the South Tianshan Orogenic belt separates TRM from the Central Tianshan Block to the north (Fig. 2.1A), but corresponding peaks in complied radiometric ages and similar Hf isotope signatures from magmatic rocks in these adjacent terranes suggest that that during emplacement, these areas together formed a broad magmatic arc along the northern margin of a united TRM/CTO before the opening of the Southern Tianshan Ocean (Charvet et al., 2011; Wang et al., 2011; Han et al., 2015b). Zircon grains younger than ~400 Ma are distinctively absent from Carboniferous strata in northern TRM, an observation that, in combination with a regional unconformity separating Silurian from early Devonian strata, and a coeval gap in magmatism, is interpreted to represent a shift from an active to passive margin during this period (Han et al., 2015b).

Whole-rock geochemical data, zircon U-Pb ages and Lu-Hf isotopes, and Sr-Nd isotope composition of gabbros in the South Tiashan Orogenic (Fig. 2.1A) belt indicate they were likely produced in a back-arc environment during Silurian times (Zhao et al., 2015), and this extensional event separated the CTO from the TRM. Growth index calculations suggest late Silurian-early Carboniferous ages for extensional structures interpreted on Tarim Basin seismic data; adding support to the back-arc model (Li et al., 2014).

Back-arc spreading in the Southern Tianshan Ocean is constrained to late Silurian-middle Devonian times by zircon U-Pb ages for gabbro and biostratigraphic data from the Heiyingshan ophiolite

mélange in the CTO (Wang et al., 2011). Abundant geochronological data from HP-LT rocks in the Tianshan metamorphic belt indicate that closure of the ocean occurred through late Devonian-Carboniferous times (Gao and Klemd, 2003; Klemd et al., 2005; Su et al., 2010; Wang et al., 2010). A zircon U-Pb age of 285 Ma obtained from a dike that crosscuts the belt provides an upper age limit for collisional metamorphism, thus the amalgamation of the CTO and TRM must have been completed before the end of the Paleozoic Era (Gao et al., 2011). The northern margin of the CTO remained active until the terrane collided with Kazakhstan-Yili during late Devonian-early Carboniferous times (Charvet et al., 2007; Charvet et al., 2011). Intense Carboniferous calc-alkaline magmatism in the CTO records the northward subduction of the Southern Tianshan oceanic lithosphere (Han et al., 2015b).

The information discussed here stipulate a passive northern margin for the TRM craton during late Paleozoic times. During this period, back arc rifting opened the Southern Tianshan Ocean between the CTO and the northern margin of the TRM craton. The northern margin of the Central Tianshan was active from at least the late Silurian to Latest Devonian, and subduction along this margin closed the ocean basin separating this block from the Kazakhstan-Yili terrane. After the amalgamation of CTO and the Kazakhstan-Yili terrane, subduction of the Southern Tianshan Ocean commenced at the southern margin of the CTO. This margin was active until collision with TRM occurred during late Carboniferous times.

The Kunlun terrane (Fig. 2.1A) developed on the southern margin of TRM when an early Paleozoic arc was accreted during Ordovician times (Yuan, 1999). Intense, widespread magmatism indicate that north-dipping subduction was continuous along this margin from late Ordovician until Carboniferous times (Yuan, 1999; Liu et al., 2005). The early Carboniferous magmatic record of TRM is characterised by a cessation of igneous activity (Yuan, 1999; Yin and Harrison, 2000) and the widespread deposition of shallow marine carbonates and clastic sediments (Youngun and Hsü, 1994; Mattern et al., 1996; Yin and Harrison, 2000; Zhihong, 2004). This information has led some authors to propose that a back-arc basin developed during this time (Mattern et al., 1996; Yin and Harrison, 2000; Zhihong, 2004). Interestingly, geochemical analysis of lavas from the Kudi ophiolite belt in northwestern Kunlun fall exclusively in the volcanic arc field (Yang et al., 1996), and radiolarian-bearing deposits in the upper part of the ophiolite sequence have early Carboniferous-Permian ages (Mattern et al., 1996). An early Carboniferous age for the ophiolite is supported by Rb-Sr isochron geochronology of basaltic rocks (Jiang, 1992; Mattern et al., 1996), whereas other authors suggest Neoproterozoic-early Paleozoic ages (Wanvming, 1995; Xiao et al., 2003). In any case, indications are the southern margin of TRM was passive through much of late Paleozoic. Intense late Carboniferous folding and Permian magmatism in the central part of the Western Kunlun Mountains are interpreted to represent basin closure by southward subduction beneath Southern Kunlun (Yang et al., 1996).

Late Paleozoic paleomagnetic data for TRM are sparse, but paleomagnetic poles have been reported for early-middle Devonian times (Fang et al., 1996), late Devonian times (Bai et al., 1987; Li et al., 1990), late Carboniferous times (Bai et al., 1987; Dajun et al., 1998; Sun et al., 2014) and early Permian times (Bai et al., 1987; Sharps et al., 1989; Gilder et al., 1996). These data indicate that through most of the Devonian Period TRM was located at mid-low latitudes in the northern hemisphere (~18°). From late Devonian to late Carboniferous times the block experienced a significant northward drift to

~25°N accompanied by a clockwise rotation. From late Carboniferous to Permian times the TRM poles become relatively stationary implying TRM did not experience considerable movement during this period, which is consistent with geochronological data (Gao et al., 2011) that suggest TRM and the CTO/KAZ were amalgamated during this time.

2.2.2.3. Laurussia and Gondwana

The Rheic Ocean, which separated Laurussia and Gondwana prior to the assembly of Pangea, represents one of the major Paleozoic ocean basins. Abundant lithostratigraphic, paleontological, paleomagnetic and geochronological data have led to a model in which the inception of the Rheic Ocean began with the rifting of the peri-Gondwana terranes Avalonia, Carolina and Ganderia from northern Gondwana in the late Cambrian-early Ordovician (Cocks and Torsvik, 2002; Hibbard et al., 2002; Murphy et al., 2006; Murphy et al., 2010; Nance et al., 2010; van Staal et al., 2012; Weil et al., 2013), and that its closure occurred during Devonian-Carboniferous times with the terminal collision between Laurussia and Gondwana during the Variscian-Alleghanian-Ouachita orogeny (Hibbard and Waldron, 2009; Murphy et al., 2010; Nance et al., 2010; Weil et al., 2013; Hopper et al., 2017). As the ocean developed through the early Paleozoic Era, Laurussia and Gondwana became increasingly separated, however, their positions relative to each other remain largely unresolved. Numerous reconstructions, primarily based on paleomagnetic data, with contributions from palynology and lithofacies associations, place Laurussia in an equatorial-low southerly position north of the northwestern Gondwana margin during the Silurian and Devonian (Fig. 2.2) (McKerrow et al., 2000; Cocks and Torsvik, 2002; Stampfli and Borel, 2002; Lewandowski, 2003; Scotese, 2004; Veevers, 2004; Golonka, 2009a). In an alternative group of reconstructions, Laurussia is placed so that its eastern margin is facing the western margin of Gondwana, along present-day western South America (Fig. 2.2) (Domeier and Torsvik, 2014; Torsvik et al., 2014; Domeier, 2015; Matthews et al., 2016). These models reconstruct Laurussia to a low southerly latitude over the eastern arm of the Pacific LLSVP based on a combination of paleomagnetic data and the occurrence of kimberlites in western Laurentia and northern Baltica. These reconstructions require Laurussia to undergo ~8,500 km of relative dextral transform motion at speeds of ~30 cm/yr with respect to Gondwana to reach its position during final Pangea assembly (Matthews et al., 2016). Dextral structures that indicating a couple of hundred kilometres displacement are well documented along the south-eastern margin of Laurentia (Arthaud and Matte, 1977; Adams et al., 1994; Nance and Linnemann, 2008; Hibbard and Waldron, 2009; Murphy et al., 2011; Waldron et al., 2015), and suggest a component of transcurrent convergence. However, the low-angle structure of the Appalachian/Alleghanian suture precludes extensive strike-slip motion accommodated on the fault zone, instead requiring a more orthogonal collision (Hopper et al., 2017). The structure of the suture thus places an important kinematic constraint on the relative plate motions between Gondwana and Laurussia during their amalgamation and is incompatible with models that invoke extensive strike-slip motion. Based on this geologic constraint, and to reduce plate speeds, we reconstruct Laurussia to a position north of Gondwana and implement an alternative plate motion path for Laurentia (Fig. 2.2) to model a more orthogonal collision during closure of the Rheic Ocean.

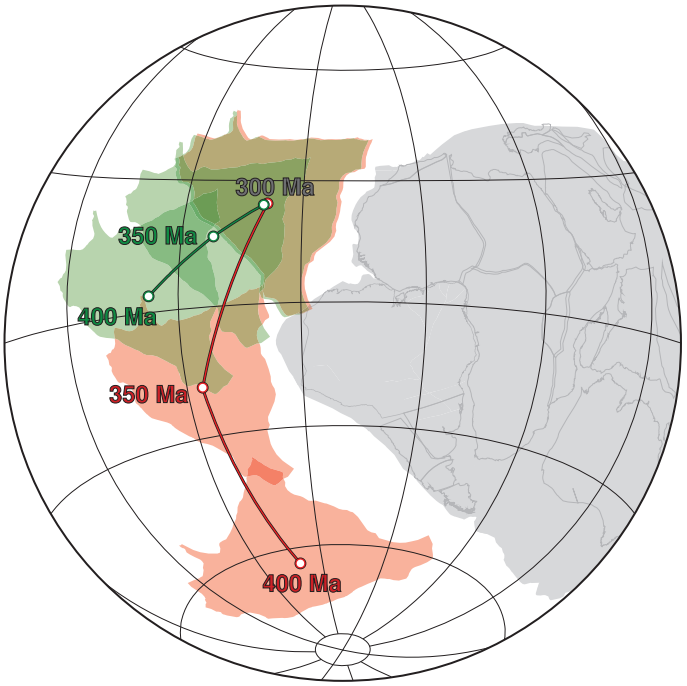

Figure 2.2. Continental reconstructions from Matthews et al. (2016) (red) and this study (green) at 400 Ma, 350 Ma and 300 Ma showing the motion of Laurentia relative to fixed Gondwana (grey).

2.2.2.4. Variscan orogeny

Early Devonian transpressive convergence of Armorica (Fig. 2.3) with Laurussia is recorded by a strain event in the sedimentary rocks of SW Ireland (Meere and Mulchrone, 2006), implied by low-grade metamorphism of Silurian slate beds in England and Wales (Soper and Woodcock, 2003), and interpreted to mark the beginning of the Variscan orogeny (Kroner and Romer, 2013). Orogeny associated with the late Silurian-Devonian northward-directed subduction of the Rheic Ocean beneath Laurussia is evidenced by a rich collection of geological data spanning from the northern Appalachians to the eastern European Variscides (Murphy et al., 1999; Catalán et al., 2007; Kroner et al., 2007; Woodcock et al., 2007). The subduction of the Rheic Ocean along the south Baltic Laurussian margin is implied by the late Silurian-early Devonian magmatic arc of the Mid-German Crystalline Zone (MGCZ) (Fig. 2.3) (Zeh and Will, 2010), which contains metasedimentary rocks with Gondwanan/peri-Gondwanan sourced detrital zircon spectra in the south, and southwest Baltica-derived detrital zircon spectra from units in the north (Zeh and Gerdes, 2010). The strata of the Rheno-Hercynian Basin (Fig. 2.3), which include clastic rocks sourced from the arc (Langenstrassen, 1983) and record a history of sedimentation spanning late Ordovician through early Carboniferous times (Dallmeyer et al., 2013), are located to the north of the MGCZ. The formation of the Rheno-Hercynian basin in a back arc setting has been proposed (Floyd, 1982; Leeder, 1982; Kroner et al., 2007; Salamon and Königshof, 2010; Zeh and Gerdes, 2010), a model in which the Lizard ophiolite, which has a mid-ocean ridge (MOR) like chemical signature (Floyd, 1995), represents the development of sea floor spreading and the establishment of a narrow ocean (Stampfli et al., 2002). Compressive structural features mark the onset of basin closure in the early Devonian (Oncken, 1988) and have been linked to the beginning of the Variscan Orogeny (Zeh and Gerdes, 2010). A late Devonian flip in subduction polarity, so that Laurussia was subducting beneath the Armorican margin of Gondwana, is indicated by the presence of early Carboniferous gabbros that are

interpreted to have been generated as part of a magmatic arc (Altherr et al., 1999) as well as combined U-Pb and Lu-Hf isotope analysis of detrital zircons (Zeh and Gerdes, 2010) from the MGCZ, and is coeval with closure of the Rheic Ocean (Barreiro et al., 2007; Arenas et al., 2014).

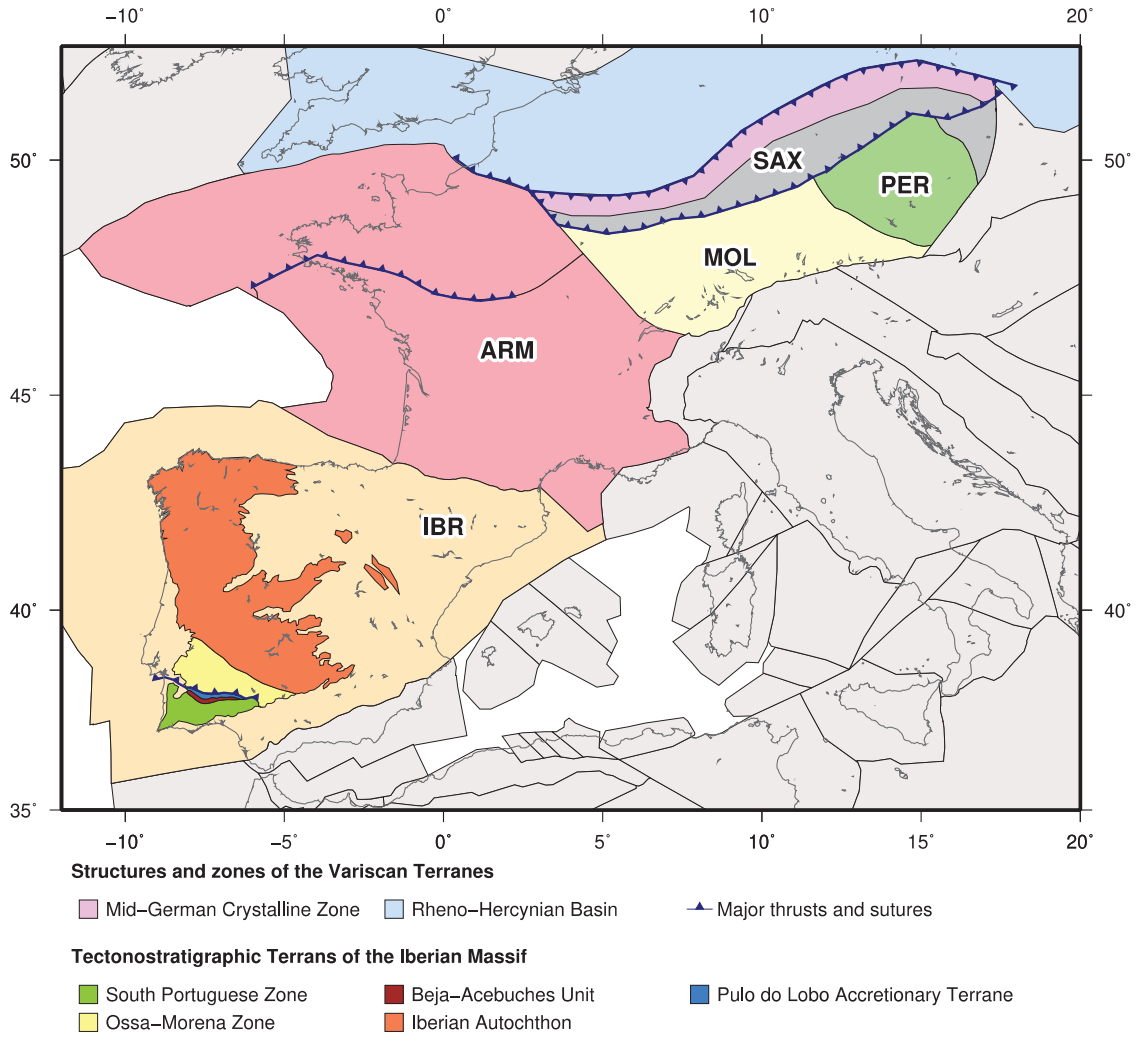

Figure 2.3. Main structures, zones and tectonostratigraphic units of the Variscan orogeny in Europe. ARM, Armorica (red); IBR, Iberia (light orange); MOL, Moldanubia (yellow); PER, Perunica (green); and SAX, Saxo-Thuringia (dark grey). Light grey indicates the extent of continental crust in surrounding regions. Modified from Eden and Andrews (1990), Franke (2000); Pin et al. (2008); Hartley and Otava (2001).

The Beja Igneous Complex (BIC) (Pin et al., 2008) located in the southwestern most region of the Iberian peninsula separates the northern Ossa Morena Zone (OMZ) from the South Portuguese Zone (SPZ) to the south (Fig. 2.3) and has long been recognised as having an oceanic affinity and is often considered to be the continuation of the Rheic suture to the west of the MGCZ (Crespo-Blanc and Orozco, 1991; Fonseca and Ribeiro, 1993; Castro et al., 1996; Pin et al., 2008; Pin and Rodríguez, 2009; Braid et al., 2011; Kroner and Romer, 2013). The boundary zone features the scattered and discontinuous mafic/ultramafic rocks of the Beja-Acebuches ophiolite/amphibole unit and middle-late Devonian mélange deposits in the Pulo do Lobo unit (Pin et al., 2008). The designation of the BIC as the Rheic suture zone has been questioned by U-Pb zircon geochronology which indicate Mississippian ages for the unit, too young to be considered Rheic oceanic crust (Azor et al., 2008). Instead, rocks of the Beja-

Acebuches unit have been attributed to MOR spreading and the development of a narrow ocean between the OMZ and SPZ following the closure of the Rheic Ocean (Azor et al., 2008). However, the geochemical and geochronological data that constitute the basis for this model have been challenged (Pin and Rodríguez, 2009). Considering the characterisation of the BIC as a post-collisional magmatic event (Pin et al., 2008), it has also been suggested that the Mississippian aged rocks of the Beja-Acebuches unit are not of oceanic origin but are instead related to the latter magmatic episode (Pin and Rodríguez, 2009). In any case, paleontological dating, structural mapping, and stratigraphic analysis of mélange blocks in the Pulo do Lobo unit (Fig. 2.3) clearly place the development of these deposits in a middle-late Devonian accretionary setting (Eden and Andrews, 1990; Eden, 1991). Detrital zircon spectra from the Pulo do Lobo strata contain dominant Mesoproterozoic and late Paleoproterozoic populations that are characteristic of both Baltica and Laurentia. In contrast, the dominance of Neoproterozoic and Paleoproterozoic ages in zircon from the SPZ are typical of derivation from West Africa, supporting the model for Rheic Ocean suturing along the BIC (Braid et al., 2011). Final suturing of the Rheic Ocean is indicated by the mixing of Gondwanan and Laurussian sources in BIC flysch deposits, implying juxtaposition of the SPZ and OMZ between 347 and 330 Ma, the latter age indicating the maximum deposition of the flysch and emplacement of the Gil Márquez pluton that crosscuts the sedimentary deposits (Braid et al., 2011). The Iberian portion of the Rheic suture records sinistral transpression (Quesada, 1997; Braid et al., 2010), which is consistent with a component of dextral motion of Laurussia during collision and is also reflected in the curvature of the suture zone. Compressional tectonics ended in the Laurussian Variscides at ~300 Ma (Kroner et al., 2008), although transpressional deformation continued in the Moroccan Variscides until ~290 Ma (Feroni et al., 2010).

South of the Rheic suture is a collage of tectonostratigraphic units including Iberia, Armorica, Saxo-Thuringia, Moldanubia and Perunica (Fig. 2.3), which are collectively termed the Variscan Terranes (Domeier and Torsvik, 2014). The geological history of the Variscan Terranes during Silurian and Devonian times is controversial. The characterisation of the units as individual or collective microplates (a plate tectonic term) or microcontinents (a paleogeographic term) and their paleoposition relative to Gondwana and Laurussia during the closure of the Rheic Ocean (Servais and Sintubin, 2009; Pastor-Galán et al., 2013) are both debated. Perunica and Armorica have been considered as both separate microcontinents on the basis of endemic faunal assemblages (Havlíček et al., 1994; Fatka and Mergl, 2009), and separate microplates, as suggested by paleomagnetic data for Perunica (Tait et al., 1994; Tait, 1999) that imply large scale rotation between the two blocks larger than expected in an intraplate setting (Tait, 1999). However, the reliability of these paleomagnetic data is low (Robardet, 2003; Van der Voo, 2004), the ages of magnetization present large uncertainties, and deformation during the Variscan orogeny precludes the paleomagnetic declinations required for large scale crustal rotation (Krs et al., 2001). Regardless of this debated point, paleomagnetic poles for Armorica (Tait, 1999), Perunica (Krs, 1968; Tait et al., 1994; Patočka et al., 2003) and Iberia (Van der Voo, 1967; Tait et al., 2000) indicate that these terranes occupied the same latitudinal belt (~20°S) in close proximity to Gondwana during late Silurian-early Devonian times, an arrangement supported by faunal assemblages (Paris, 1993; Cocks and Torsvik, 2002; Robardet, 2003; Torsvik and Cocks, 2004) and distributions of lithofacies (Robardet and Doré, 1988; Golonka, 2007b, 2009). Zircon spectra found in NW Iberia (Pastor-Galán et al., 2013;

Fernández-Suárez et al., 2014), north Armorica (Miller et al., 2001; Samson et al., 2005) suggest a close relationship between these terranes and West African Gondwana. Similarly, detrital zircon U-Pb ages from Saxo-Thuringia indicate a consistent West African source for the entire period of Cambrian to early Carboniferous times, interpreted to reflect no difference in position between the two domains over this interval (Linnemann et al., 2004). Nd isotopic analysis of Saxo-Thuringia sedimentary rocks indicates an absence of any significant contribution from a young mafic source from Cambrian-early Carboniferous times, precluding the formation of new oceanic crust between Gondwana and Saxo-Thuringia during this period (Linnemann et al., 2004). Geochemical data from Paleozoic detrital rocks suggest that NW Iberia was a passive margin from Ordovician to late Devonian times, supplied with a stable source of sediment from Gondwana (Pastor-Galán et al., 2013). Based on this evidence, we model the Variscan Terranes in permanent, close connection with Northwest Africa and a part of the Gondwana plate through the late Paleozoic (Fig. 2.4A-D).

2.2.2.5. Western Margin of Gondwana

Following the Cambrian-Ordovician Famatinian orogen, the western (South American) margin of Gondwana is characterised by a late Paleozoic record lull in magmatism, metamorphism and deformation in southern Central Andes (Bahlburg and Hervé, 1997; Lucassen et al., 2000; Büttner et al., 2005; Bahlburg et al., 2009), northern/Peruvian Andes (Chew et al., 2007; Cardona et al., 2009) and southern Andes (Fortey et al., 1992), which has been interpreted to reflect the rifting off of a western part of the Arequipa-Antofalla terrane, an event that lasted ~100 Myr until the late Carboniferous period (Fig. 2.4C-D) (Bahlburg and Hervé, 1997). Crystallization ages of Peruvian plutons demonstrated by zircon U-Pb dating (Mišković et al., 2009) suggest that arc activity resumed during early Carboniferous times along the South American margin of Gondwana; it has continued uninterrupted to the present.

The location of the Patagonian terrane (Fig. 2.4) in the western Gondwana during the Paleozoic remains poorly understood. Its basement has traditionally been subdivided into two tectonic blocks, the Deseado Massif in the south and the Somún Cura/North Patagonian Massif in the north (Ramos, 2008; Pankhurst et al., 2014). In southern Argentina, a late Paleozoic magmatic belt trending dominantly NW-WNW has been taken to represent a convergent margin along which the allochthonous/parautochthonous Patagonia terrane accreted to South American Gondwana during late Paleozoic times (Bahlburg and Hervé, 1997; Ramos, 2008), a model supported by NE-SW trending compressional structures located to the north of the North Patagonian Massif (Von Gosen, 2003; Rapalini et al., 2010). However, Cambrian granites (Pankhurst et al., 2014), provenance analysis of detrital zircons (Augustsson et al., 2006) and Devonian paleomagnetic data (Rapalini, 2005) suggest that the Patagonia terrane has remained proximal to, if not part of, South America since early Paleozoic times (Pankhurst et al., 2003). This alternative is reinforced by the lack of direct evidence of an ophiolitic belt between Gondwanan South America and the Patagonian terrane (Ramos, 2008). While the autochthonous relationship of Patagonia to South America is debated, evidence in the form of magmatic, metamorphic and detrital zircon geochronology suggest that the Deseado and Somún Cura/North Patagonian Massifs were involved in the major Neoproterozoic-Jurassic orogenic events of western Gondwana (Pankhurst et al., 2003; Ramos, 2008; Gregori et al., 2016), precluding any reconstructions that model Patagonia as an exotic terrane (e.g. Domeier and Torsvik, 2014; Matthews et al., 2016). Considering the complex and contentious history of Patagonia, we

reconstructed its late Paleozoic position (Fig. 2.4A-F) following a simplified model accounting for the main episodes of convergence during mid-Ordovician and late Paleozoic times, and Silurian-late Carboniferous rifting (Bahlburg and Hervé, 1997; Ramos, 2008).

2.3. Overview of a new global tectonic reconstruction

Our plate model is based on the work of Matthews et al. (2016), Domeier and Torsvik (2014), and Müller et al. (2016a) but includes a number of regional updates (Section 2.2.2.) aimed at improving kinematics during late Paleozoic to Mesozoic times. In this section, we present and discuss the major tectonic events associated with our changes. The global tectonic reconstruction is shown in 20 Myr intervals in the paleomagnetic reference frame (Fig. 2.4). For the descriptions that follow, all directions and orientations are expressed relative to the reconstructed model unless explicitly stated otherwise.

2.3.1. Devonian Period (419-359 Ma)

Our reconstruction (Fig. 2.4) commences at 410 Ma during the early Devonian, shortly after the amalgamation of Laurentia, Baltica and Avalonia to form Laurussia. This time interval was characterised by the distribution of continental lithosphere into two large landmasses, Laurussia and Gondwana, and a number of smaller isolated continents. Laurussia and Gondwana were separated by the Rheic Ocean where MOR spreading was already underway when our model begins (Fig. 2.4A). Subduction of Rheic oceanic lithosphere at the eastern active margin of Baltic Laurussia produced the Mid-German Crystalline Zone (MGCZ) magmatic arc (Fig. 2.4A-E) and induced back arc spreading east of the Avalonia terrane (Fig. 2.4A, B). Rifting in the back arc continued into middle Devonian times and ultimately developed into the Lizard Ocean basin. During this period, Laurussia drifted eastward toward its Pangea position at an average rate of ~9 cm/yr (this study), thereby closing the Rheic Ocean at ~380 Ma – although closure may have been initiated earlier, at 400 Ma (Wu et al., 2020). Subduction of the Rheic MOR and cessation of spreading in the Lizard Ocean at the onset of early Devonian times (Oncken, 1988) marked the end of active divergence in the region. According to our kinematic scenario, subduction in the southern Rheic Ocean continued along the eastern margin of Laurussia until middle Devonian times when the basin in this region closed and a period of continent-continent collision begun. The MGCZ arc accreted to the western Variscan margin at a similar time. Gondwana was in a dominantly south polar position during the Devonian Period, and incipient rifting at its northeastern margin opened the Paleo-Tethys Ocean (von Raumer and Stampfli, 2008). To model the development of a passive margin setting along both the northeast and northwest margins of Gondwana in Devonian times (Domeier and Torsvik, 2014) we reconstructed spreading in the Rheic and Paleo-Tethys Oceans via a ridge-ridge-ridge triple junction. Paleo-Tethys oceanic crust drifted northward and was subducted along the southern active margins of Siberia and Kazakhstan. East of the Paleo-Tethys, a mosaic of small plates were scattered in the realm of the Paleoasian Ocean. In this region subduction of the Paleo Tianshan Ocean at the western margin of Central Tianshan (CTO) triggered back-arc extension in the South Tianshan Ocean (STO) to the east. Rifting in the STO separated the CTO from Tarim (TRM) and continued throughout Devonian times (Fig. 2.A-C). The CTO drifted westward, closing the Paleo Tianshan Ocean and eventually colliding with Kazakhstan at the beginning of the Carboniferous (Fig. 2.4C, D). Subduction along the eastern margin of

TRM, which began in Ordovician times, continued through to the end of the Devonian (Fig. 2.4C, D). Continental rifting along the northern margin of SCB commenced in Silurian times and opened the Mianlue Ocean basin where spreading continued uninterrupted throughout the Devonian (Fig. 2.4A-C). At the Gondwana western margin, subduction, which was active from early Paleozoic times, was suspended in middle Devonian times, when all evidence of magmatism along the periphery of South America ceases at this time. This period of magmatic quiescence along the South American continental margin is modelled by the opening of a back-arc basin. As the magmatic arc retreated NW, a rift between the Arequipa-Antofalla and Patagonia terranes, and western Gondwana, where a passive margin is modelled (Fig. 2.4B, D). From the beginning of the model, the developing Panthalassa Ocean dominates the proto-Pacific realm. Subduction of this ocean occurred largely along the southern, eastern and western margins of Gondwana.

2.3.2. Carboniferous Period (359-299 Ma)

During latest Devonian times, along the western margin of the Variscan Terranes, the provenance of detrital zircons within the MGCZ record a reversal of subduction polarity (Zeh and Gerdes, 2010) (Fig. 2.4C, D). Convergence along this margin continued into Pennsylvanian times, then ceased at 319 Ma, by which time Pangea was fully amalgamated. During the middle-late Carboniferous times, the Gondwana plate underwent a pulse of northward motion as its African core transitioned from a south polar position to a mid-low latitude (~40°) position (Fig. 2.5) in the southern hemisphere (Stampfli and Borel, 2002; Collins, 2003; Scotese, 2004; Golonka, 2007b; Mitchell et al., 2012; Torsvik et al., 2014). Subduction of the Paleo-Tethys Ocean along the Baltic margin of Laurussia persisted for the entirety of the Carboniferous. The collision of the CTO with Kazakhstan occurred at the end of the Devonian, coeval with cessation of spreading in the STO. Following the unification of the CTO and Kazakhstan, subduction initiated along the eastern margin of Kazakhstan plate, drawing TRM westward and closing the STO (Fig. 2.4D-F). Subduction of the STO throughout the Carboniferous was contemporaneous with the evolution of the Kazakhstania orocline and the consolidation of Kazakhstan and Siberia into Pangea. Towards the end of the Carboniferous the amalgamation of TRM and Pangea marks the terminal closure of the STO. Following collision with Kazakhstan, late Carboniferous paleomagnetic data from TRM imply a phase of northward drift. To accommodate this motion, a major sinistral strike-slip event must have occurred in the region. Deformation features consistent with a sinistral tectonic activity are found in the Tianshan Orogen, and although late Paleozoic ages are anticipated, no definitive geochronological data are available to constrain the age of the deformation (Laurent-Charvet et al., 2002; Laurent-Charvet et al., 2003). The end of the Devonian marks a shift from a convergent to divergent regime at the TRM eastern boundary. Long-lasting subduction at the margin initiated back-arc extension in the Kunlun terrane, and the resulting basin expanded the basin during Carboniferous times (Fig. 2.4D, E). The start of basin closure in the latest Carboniferous was coeval with the onset of subduction along the western margin of South Kunlun. Along the western Gondwana plate boundary, back-arc extension ceased in the Mississippian as the passive margin collapsed and subduction resumed along the proto-Andean margin. With the closing of the Arequipa-Antofalla basin in late Carboniferous times (Fig. 2.4D, E), Patagonia amalgamated with the rest of Pangea. Following the accretion of Patagonia, subduction along the western margin of the Patagonia plate resumed.

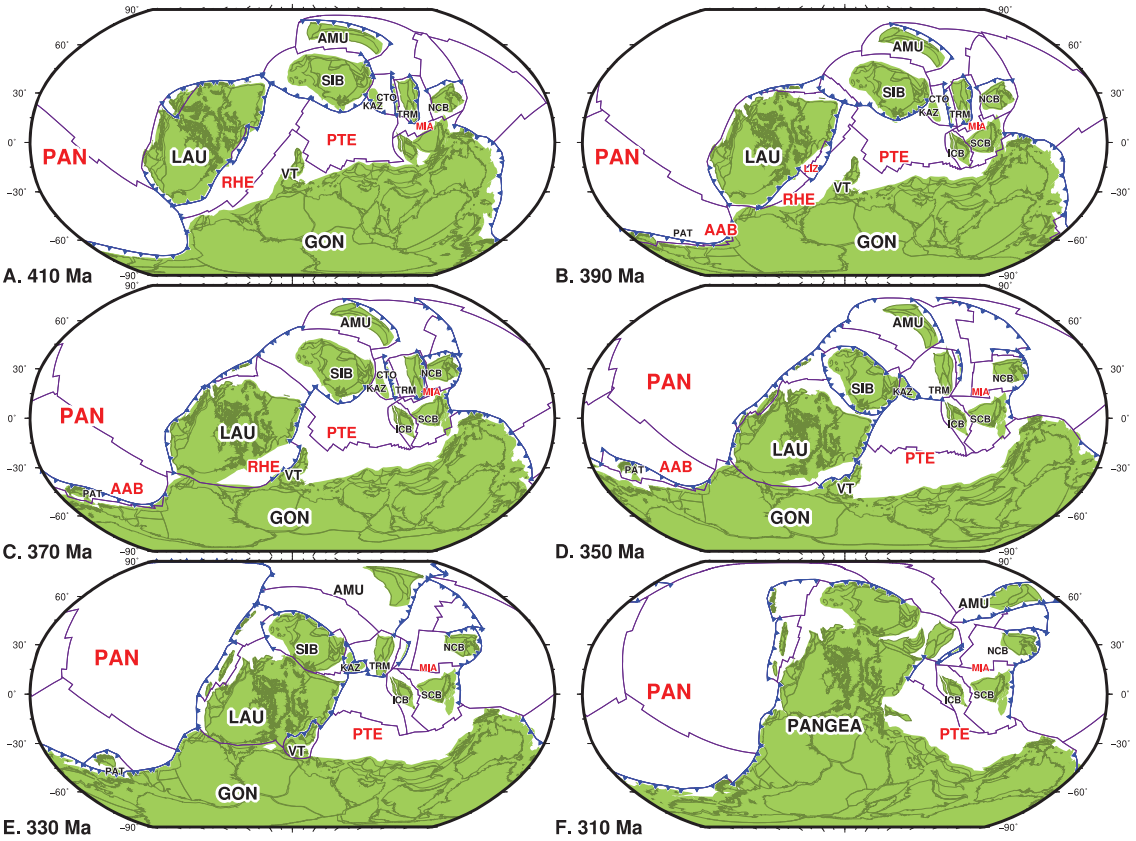

Figure 2.4. Global plate reconstructions between 410-310 Ma at 20 Myr intervals showing the distribution of major ocean basins and continental plates. An approximation for the extent of the continents is shaded green. Blue lines with triangles on the overriding plate indicate subduction zones, and purple lines denote mid-ocean ridges and transform faults. Abbreviations (red, oceanic; black, continental): PAN, Panthalassa Ocean; RHE, Rheic Ocean; PTE, Paleo-Tethys Ocean; AAB, Arequipa-Antofalla Ocean, MIA, Mianlue Ocean; LIZ, Lizard Ocean; LAU, Laurussia; GON, Gondwana; VT, Variscan Terranes; SIB, Siberia; AMU, Amuria; KAZ, Kazakhstan; CTO, Central Tianshan; TRM, Tarim; NCB, North China; SCB, South China; ICB, Indochina and; PAT, Patagonia. (A-C), Devonian aged reconstructions and (D-F), Carboniferous aged reconstructions.

2.3.3. Permian Period (299-252 Ma)

After drifting north during Carboniferous times, Pangea underwent a period of relative stability as the core of its landmass settled at low southerly latitudes (~40°) during early Permian times (Fig. 2.5). Convergence at both the western and eastern active margins of South Kunlun continued in the early Permian (Yang et al., 1996; Yuan, 1999; Liu et al., 2005). In the mid-Permian we model a kinematic scenario in which the eastern Kunlun margin evolved into a transform boundary. The change in kinematics at this margin coincided with a significant plate reorganisation due to the subduction of the Paleotethys Paleo-Tethys MOR and cessation of spreading in the Mianlue Ocean (Fig. 2.4H). Subduction at the western margin of South Kunlun persisted throughout Permian times, gradually closing the basin that had opened outboard eastern TRM in the Carboniferous Period. The southern margin of NCB, which faced the slow spreading Mianlue Ocean, was passive through most of late Paleozoic times. During mid-Permian times, the passive margin collapsed (which is one of the proposed modes of subduction initiation; Stern, 2004), and closure of the Mianlue ocean basin commenced by north directed subduction beneath the NCB (Fig. 2.4H). The subduction of the Paleo-Tethys MOR (275 Ma) was coeval with the opening of the Neotethys ocean and the subsequent detachment of the Cimmerian terranes from the

Arabia-India-Australia margin of eastern Pangea (Domeier and Torsvik, 2014). The PAO was a large ocean that existed in the Sino-Siberian region for most of late Paleozoic times. The terminal closure of the PAO by double-vergent subduction along the southern margin of Amuria and the northern margin of NCB occurred near the end of Permian times (Chen et al., 2000; Chen et al., 2009) and consolidated these two terranes into a united Mongol-Okhotsk (MOO) plate (Fig. 2.4I). In the early Permian, the eastern passive margin of Annamia failed and developed into an active subduction zone (Fig. 2.4G). Convergence at this boundary closed the Song Ma basin separating the SCB from Annamia, and the two units collided during the late Permian-early Triassic to form an amalgamated unit (Domeier and Torsvik, 2014). We modelled the timing of this collisional event differently to Matthews et al. (2016), who initiated closure of the ocean basin at 279 Ma, with SCB and Annamia joining at 244 Ma. We initiated basin closure at 300 Ma and preferred an end Permian terminal collision at 250 Ma, as allowing extra time for the Song Ma basin to close avoids unreasonably large plate speeds while remaining consistent with timing estimates.

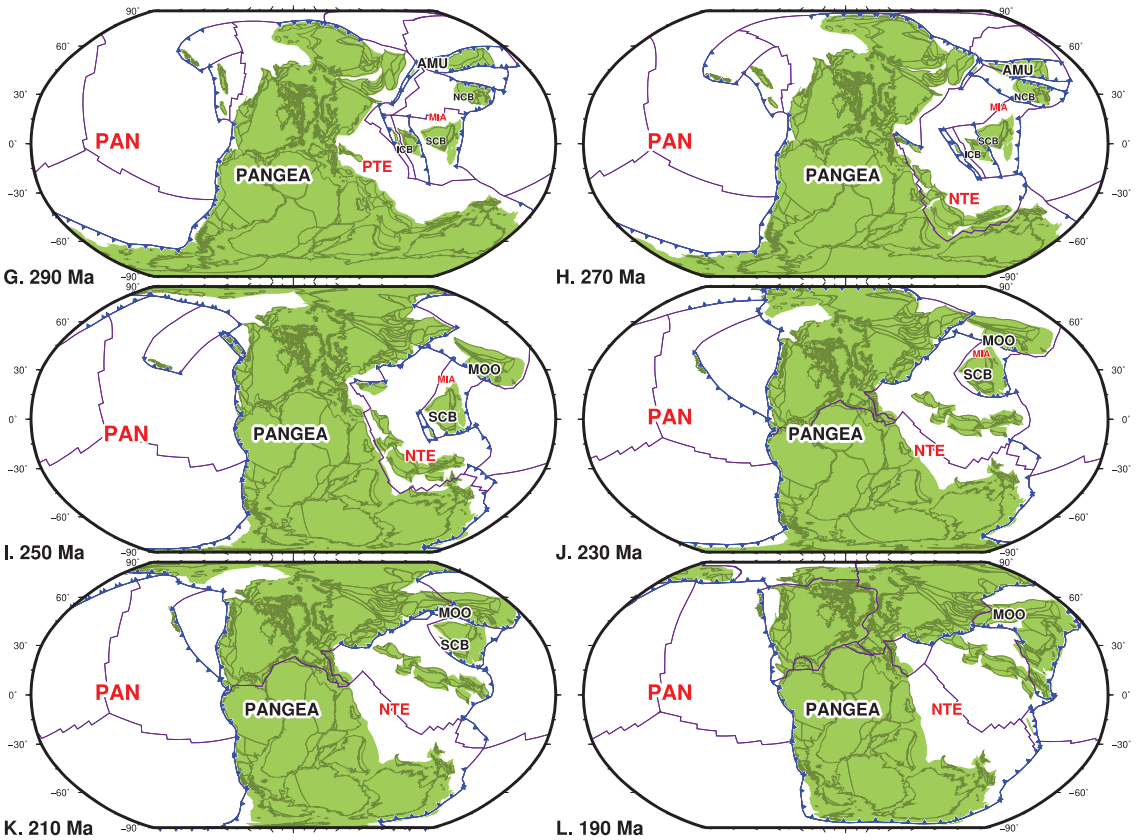

Figure 2.4 ***(continued).*** Global plate reconstructions between 290-190 Ma at 20 Myr intervals showing the distribution of major ocean basins and continental plates. An approximation for the extent of the continents is shaded green. Blue lines with triangles on the overriding plate indicate subduction zones, and purple lines denote mid-ocean ridges and transform faults. Abbreviations (red, oceanic; black, continental): PAN, Panthalassa Ocean; PTE, Paleo-Tethys Ocean; NTE, Neotethys Ocean; MIA, Mianlue Ocean; AMU, Amuria; NCB, North China; SCB, South China; ICB, Indochina and; MOO Mongol-Okhotsk plate. (G-H), Permian aged reconstructions; (I-K), Triassic aged reconstructions and (L), early Jurassic reconstruction.

Subduction along the western margin of Annamia gave rise to the short-lived Jinghonh-Nan-Sra Kaeo basin that developed behind the Sukhothai Arc during latest Carboniferous-late Permian times (Sone and Metcalfe, 2008). Back-arc rifting detached the Sukhothai Arc from the Annamia plate, so we modelled the latter as an independent unit beginning in earliest Permian times. The eastern margin of Sukhothai and the western margin of Annamia were passive during early Permian times as the Jinghonh-

Nan-Sra Kaeo basin developed. During middle Permian times, the eastern passive margin of Sukhothai failed and west directed subduction developed at the boundary, initiating basin closure. From middle to late Permian times Pangea (represented by South Africa) underwent a period of northward drift (Fig. 2.5), accompanied by a minor counterclockwise rotation, so that by the end of the Paleozoic Era the African core was in an equatorial position.

2.3.4. Mesozoic Era (252-130 Ma)

Our global reconstruction transitions between Paleozoic and Mesozoic reference frames during early Triassic times, causing Pangea (here represented by South Africa) to drift to the southwest (Fig. 2.5). East directed subduction of the Jinghonh-Nan-Sra Kaeo basin lithosphere beneath Sukhothai continued during early Triassic times (Fig. 2.4I). By middle Triassic times this basin was closed and the Sukhothai terrane collided with Annamia (Singharajwarapan and Berry, 2000), integrating into the SCB. Continuous subduction of the Mianlue Ocean occurred along the southern active margin of the NCB throughout Triassic times, leading to the continental collision between the NCB and the SCB at the end of the period (200 Ma). After 200 Ma the MOO plate, now composed of all the major Sino-Siberian terranes, was pulled towards the northeastern Siberia active margin of Pangea. The Mongol-Okhotsk Ocean, which separated Siberia from northern Amuria throughout Paleozoic times and much of Mesozoic times, was continuously subducted along this plate boundary until the early Carboniferous. By this time the ocean basin had been closed, and northern Amuria collided with Siberia (Van der Voo et al., 2015) to form the Eurasian plate. After the complete subduction of Mongol-Okhotsk oceanic lithosphere at 130 Ma the relative plate motions in our reconstruction are similar to those of Matthews et al. (2016), with the exception of the minor adjustments discussed in Section 2.4.4.

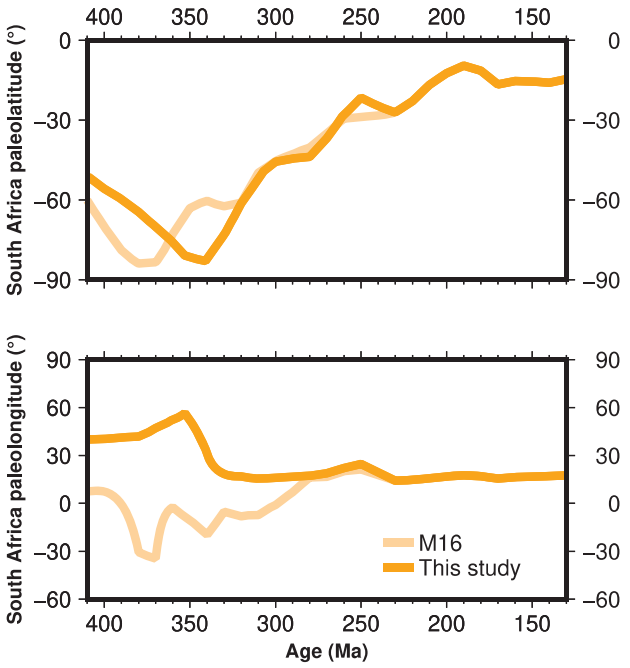

Figure 2.5. Paleolatitude and paleolongitude of the South African plate (measured from a point at present day 8°S, 28°E) during the late Paleozoic/early Mesozoic as described by the reference frame used in the model of Matthews et al. (2016) (light orange) and this study (orange).

2.4. Reconstruction analysis and discussion

It has become common practice to quantify global plate speeds produced by reconstruction models (Lithgow-Bertelloni and Richards, 1998; Zhang et al., 2010; Domeier and Torsvik, 2014; Domeier, 2015; Zahirovic et al., 2015; Matthews et al., 2016; Müller et al., 2016a; Merdith et al., 2017). Beyond providing a standardised means to compare and validate global plate reconstruction models, plate speeds constitute a critical consideration when plate motion models are incorporated as boundary conditions of mantle flow models. Modelling studies suggest that plate speeds positively correlate with lithospheric net rotation (Alisic et al., 2012), which subsequently affects the predicted lower mantle structure produced by geodynamic modelling (Rudolph and Zhong, 2014). Cognizant of the impact plate speeds have on geodynamic models, we were motivated to create a model in which Paleozoic plate kinematics were more similar to estimates for more geologically recent times.

To analyse plate speeds in our reconstruction, we extracted time dependent plate velocities from which root mean square (RMS) speeds were computed following the methods of Zahirovic et al. (2015). Over the modelled interval, the magnitude of global plate speeds has been greatly reduced in our reconstruction (Fig. 2.6). Average plate speeds calculated for our model are larger in the Paleozoic (410-251 Ma) compared to the Mesozoic-Cenozoic (250-0 Ma): ~8 cm/yr and ~6 cm/yr, respectively. Overall, our reconstruction results in plate speeds that are generally >6 cm/yr, and increase back in time, reaching maximums of ~12 cm/yr during the late Carboniferous (~320 Ma). After the breakup of Gondwana ~100 Ma, there is a significant decrease in speed, and the profile trends distinctly down, reaching a minimum of ~4 cm/yr at ~40 Ma. From ~25 Ma to the present-day global plate speeds are typically ~5 cm/yr.

2.4.1 Reference frame and true polar wander

The reference frame implemented in Matthews et al. (2016), hereafter referred to as M16, is a hybrid model that combines a moving hotspot frame from 70-0 Ma (Torsvik et al., 2008) with two paleomagnetic frames, one from 230-100 Ma (Domeier et al., 2012) and the other from 410-250 Ma (Torsvik et al., 2014). Due to the uncertainty constraining paleolongitude in pre-Mesozoic times (Section 2.2.1), we implemented an alternative reference frame of Torsvik and Van der Voo (2002) (TV02) for Paleozoic times (410-251 Ma).

M16 implemented, via the African plate circuit, the TPW corrected paleomagnetic frame of Torsvik et al. (2014) (T14). Alternatively, our reconstruction uses the uncorrected paleomagnetic frame of TV02 and, similarly, links it to the spin axis via Africa. Both models are implemented in African coordinates, so comparing the velocities of the African plate through the late Paleozoic makes it possible to quantify the rate of motion given by the different reference frame in models (T14 and TV02). African plate speeds during the period 410-251 Ma range between ~1 and ~14 cm/yr in both of the models, however, they are ~12% less on average for TV02.

The reduction in African plate speed led us to adopt reference frame TV02 in our reconstruction. However, contrary to expectations, applying the paleomagnetic reference frame TV02 to the relative plate motion model of M16 increased global plate speeds (by ~7% on average between 410-251 Ma), particularly over the interval from 370-320 Ma (Fig. 2.6A, B, red and orange curves). This increase in plate speeds is due to the relative plate motion (RPM) model of M16. In M16, during the Carboniferous,

Laurussia is reconstructed to a position near the Gondwana western margin (Fig. 2.1; Section 2.2.2.3). To reach its position during final Pangea assembly, Laurussia is required to undergo significant transform motion with respect to Gondwana, at relative plate speeds in excess of 30 cm/yr in Carboniferous times. Over the same period, the reference frame used in M16 describes a significant, ~60° counter clockwise, rotation of Africa, whereas the reference frame of TV02 specifies only ~1° of clockwise rotation. The large clockwise rotation that describes the relative motion Laurussia with respect to Gondwana in M16 is balanced by counter clockwise rotation defined by the reference frame so that the absolute velocity of Laurussia during the Carboniferous is between 10-20 cm/yr. Conversely, the Carboniferous motion of Gondwana given by reference frame TV02 does not oppose the Laurussia motion, thereby exposing the unreasonably high relative plate speeds, which manifest as an overall increase (~7%) in global RMS plate speeds (Fig. 2.6A, B, red and orange lines).

Isolating the continental component of plate motion (Fig. 2.6C, D, green and red lines), reveals that average continental RMS plate speeds for the Paleozoic (410-251 Ma) are ~7 cm/yr in our reconstruction and ~9 cm/yr in M16. The continent-only RMS plate speeds are useful to evaluate the effect of implementing the paleomagnetic TV02 reference frame. The profile for our plate reconstruction is characterised by a Carboniferous (340-300 Ma) peak, a Permian trough (300-280 Ma) and a Permian (280-260 Ma) peak all of which can be related to the choice of reference frame. Because our model is organised as a relative plate motion model with Africa at the base of the hierarchy, any motion of Africa propagates along the plate circuit. In this way peaks and troughs described by the TV02 reference frame (implemented through the African plate) are amplified on all the plates that move with Africa. Indeed, large RMS continental plate speeds in the Carboniferous and Permian Periods are consistent with accelerations in the Gondwana APWP as described by the reference frames used in both this study and M16 (Torsvik and Van der Voo, 2002; Torsvik et al., 2014), however, the Permian trough is unique to TV02.

Continental RMS plate speeds are ~1 cm/yr in our reconstruction and ~9 cm/yr in M16 for early Permian times (300-280 Ma). Notably, this discrepancy is not related to the paleolatitudinal component of plate motion, that is well constrained by paleomagnetic data, but by the paleolongitudinal component. The paleolatitudes of a point (presently at 8°S, 28°E) on the African plate are similar at 300 Ma; 45.6°S and 45.4°S, and at 280 Ma; 43.8°S and 40.3°S between the reference frame of TV02 and M16 respectively (Fig. 2.5), reflecting very little north-south motion during these times and a consistent implementation of Gondwana paleomagnetic poles. Conversely, between 300 and 280 Ma the reference frame TV02 results in ~1° of west-east motion of Gondwana while during the same interval the reference frame of M16 invokes ~17° of west-east Gondwana motion (Fig. 2.5) to adhere to LLSVP constraints (Torsvik et al., 2014). In the reference frame of M16, negligible north-south motion of Gondwana during the early Permian is compensated by significant west-east motion, so during this interval continental RMS plate speeds do not significantly deviate from background (Fig. 2.6). Paleolongitudes are unconstrained in reference frame TV02, resulting in minimal palaeolongitudinal motion of Gondwana in our reconstruction (Fig. 2.5). Between 300-280 Ma, when the north-south drift of Gondwana decelerates, reference frame TV02 does not assume any longitudinal motion of the plate, resulting in an early Permian standstill which manifests as a distinctive drop in continental RMS plate speeds (Fig. 2.6).

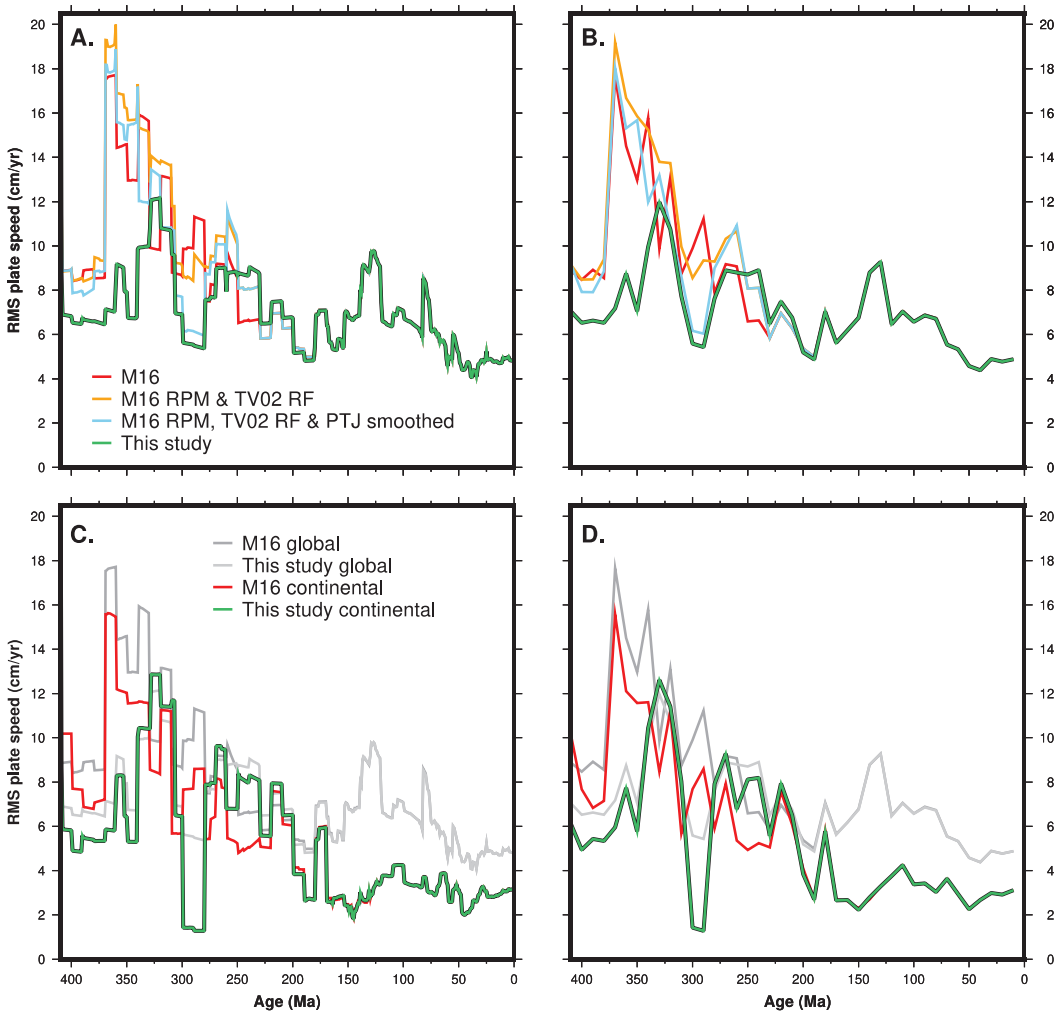

Figure 2.6. RMS plate speeds sampled at 1 Myr intervals. "M16"; Matthews et al. (2016), "M16 RPM + TV02 RF"; Matthews et al. (2016) relative plate motion model with the Paleozoic paleomagnetic frame of Torsvik and Van der Voo (2002) implemented, "M16 RPM + TV02 RF and PTJ smoothed"; Matthews et al. (2016) relative plate motions in the Torsvik and Van der Voo (2002) frame with a smoothed motion path for the Panthalassa triple junction, and this study. (A) Global plate speeds at 1 Myr intervals; (B) Global plate speeds averaged over a 10 Myr moving window; (C) Continental (coloured profiles) compared to global (grey scale profiles) plate speeds; (D) Continental (coloured profiles) compared to global (grey scale profiles) plate speeds averaged over a 10 Myr moving window.

2.4.2 Panthalassa

Oceanic lithosphere is recycled into the mantle as it is consumed at subduction zones. The complete recycling of the oceanic lithosphere within Earth's mantle may occur over ~200-250 Myr (Butterworth et al., 2014), making it difficult to reconstruct global tectonic configurations before the Mesozoic. Due to the subduction of most ancient oceanic lithosphere, oceanic realms that existed during late Paleozoic need to be represented by synthetic plates. Three major ocean basins are represented in reconstructions of late Paleozoic times: the Rheic, Paleo-Tethys and Panthalassa oceans (Stampfli and Borel, 2002; Scotese, 2004; Golonka, 2009a; Domeier and Torsvik, 2014; Torsvik et al., 2014; Matthews et al., 2016), combining to cover majority of Earth's surface. The largest of the oceans is Panthalassa and, because of its significant size, the kinematics of the topological plates that make up the ocean can have a dominating effect on global plate speeds, as can be seen by isolating continental speeds (Fig. 2.6). In the model that underpins our reconstruction (Matthews et al., 2016), the motions of the Panthalassan plates are tied, via plate motion chains, to a triple junction that is subsequently linked to the base of the mantle

via a TPW correction. This triple junction has a complex motion path described by stage poles at 10 Myr intervals from 410-250 Ma. Periods of large global plate speeds can be explicitly linked to the different phases of rotation in the motion path of Panthalassa triple junction (PTJ) (orange versus blue profiles, Fig. 2.6A, B). To minimise the influence that the largely unconstrained kinematics of oceanic plates have on global RMS speeds, we smoothed the PTJ path by removing intermediate stage poles between 410-250 Ma, allowing motion to be linearly interpolated between these times. This decreased global time-averaged RMS speeds in the Paleozoic from 11.8 cm/yr to 11 cm/yr, a reduction of ~6% (Fig. 2.6A, B).

Smoothing the motion path of the PTJ reduced overall global plate speeds, however, a period between 370-310 Ma remains marked by larger RMS plate speeds (Fig. 2.6A, B) that can be traced to rapid eastward drift of Laurussia and a counter clockwise rotation of Gondwana during the closure of the Rheic Ocean. During these times, western Laurussia and southeastern Gondwana were bounded by subduction zones (Domeier and Torsvik, 2014; Matthews et al., 2016). Therefore, to uphold plate tectonic principles and ensure convergence along these margins the speeds of Panthalassan plates are required to increase. Our reconstruction, in which we have implemented alternative models for western Gondwana (Section 2.2.2.5.) and the closure of the Rheic Ocean (Section 2.2.2.3.), reduced continental RMS plate speeds during late Devonian-Carboniferous times (Fig. 2.6C, D), resulting in a reduced speed of Panthalassan oceanic plates. As previously mentioned, the destruction of the oceanic lithosphere necessitates that global plate reconstructions develop synthetic motions for oceanic plates, therefore, we find it reasonable to fit the motions of these synthetic plates to the comparatively well constrained kinematics of continental plates.

2.4.3. Global plate kinematics

Our reconstruction results in reduced Paleozoic plate speeds through the simplification of the kinematic model for the Panthalassa Ocean and implementation of an alternative model for the closure of the Rheic Ocean (Sections 2.2.2.3. and 2.2.2.4.). Despite these changes, a period of high global RMS speeds persists from ~350-300 Ma (Fig. 2.6). The source of this Carboniferous peak can be traced to the paleomagnetic reference frame TV02 that we chose for the Paleozoic component of our reconstruction. As mentioned in the previous section, during Carboniferous times, Gondwana rapidly (~12 cm/yr) drifted north from a south polar position to a mid-low southern latitude (Fig. 2.5). This motion is dictated by the reference frame and is an artefact that affected all plates.

In their study of Mesozoic-Cenozoic tectonic speed limits, Zahirovic et al. (2015) suggested that plates with a significant portion of continental and/or cratonic area exceeding RMS speeds of ~15 cm/yr for more ~10 Myr may represent reconstruction artefacts. While the Carboniferous plate speeds of Gondwana approach without surpassing the aforementioned thresholds, it is unlikely that a continental plate composed almost entirely of ancient continental lithosphere and bounded by rifted margins and subduction zones (since slab pull does not affect the overriding plate), would move so fast for such a prolonged period of time. Perhaps plate speeds were high during the Carboniferous because of TPW (Torsvik et al., 2014) or, as proposed by Zahirovic et al. (2015), greater RMS speeds in the past may be a surface manifestation of more vigorous mantle convection; however, this effect is expected to be small over the last 300 Ma, since the solid Earth currently cools down at a rate between 53-190 K/Gyr (Jaupart

et al., 2007). Another possibility for faster plate speeds is that Gondwana moved toward a mantle downwelling generated by a period of extensive subduction. An accumulation of cold material in the mantle would generate a localised cold spot and thereby create the necessary buoyancy for velocities to increase by 10 cm/yr or more (Gurnis and Torsvik, 1994). Throughout much of Devonian and early Carboniferous times, Laurussia was located at equatorial positions and contemporaneous subduction of Panthalassic and Rheic oceanic lithosphere occurred along the western and eastern margins of the continental block, respectively (Fig 4A-E). This long-lived subduction of cold, dense oceanic lithosphere into the mantle via convergence along the periphery of Laurussia would have created a pile of cold material over which a dynamic topographic low would have formed. A significant rise in regional relative sea level would have occurred as the continent settled over the dynamic topographic low, after the peak in its rate of motion. Although ~3,500m of topographic relief (Fluteau et al., 2001) might have been generated by the Carboniferous Alleghanian-Variscan orogenic events (precluding the complete inundation of Laurussia), paleogeographic maps (Golonka, 2007b) indicate that Laurussia did experience a period of marine sedimentation between 350-300 Ma, providing support to this concept. Alternatively, an acceleration of the Gondwana plate between 350-300 Ma may be an artefact of increased data uncertainty, since paleomagnetic data coverage of Gondwana is poor to non-existent for the Carboniferous Period (Torsvik and Van der Voo, 2002).

2.4.4. Subduction zone kinematics

Because our global reconstruction incorporates closed plate polygons and provides a continuous description of plate boundaries and velocities, we are able to calculate global characteristics of subduction zone kinematics through time. In particular, we focused on convergence orthogonal to subduction zones and subduction zone migration rates (Fig. 2.7A, B), and use these metrics to further evaluate the plate motion model. We followed the workflow of Williams et al. (2015) to extract subduction zone segments from the reconstruction at 1 Myr intervals and resampled them at regularly spaced intervals of 1 arc degree. The rate of convergence and velocity of migration of subduction zones was then calculated for each point, using the local orientation of the subduction zone and the plate kinematics. Subduction zone migration rate is defined as the portion of absolute subduction zone velocity that is orthogonal to the subduction zone line segment. The subduction zone convergence rate is the orthogonal component of the velocity difference between the overriding plate and the subducting plate. We used the global plate model of M16 as a benchmark against which to interpret the results of our analysis. This reconstruction was selected as it covers the same temporal range as ours work, allowing us to make a continuous comparison.

Global median trench migration rates for both our reconstruction and M16 over the past 410 Myr are calculated and compared (Fig. 2.7A). For the extent of the modelled interval, the median value of trench motion remains closely distributed (standard deviation $\sigma = 0.82$ cm/yr) around ~1 cm/yr, indicating a preference towards trench retreat. During the Paleozoic component of the model (410-251 Ma), the global standard deviation of trench migration is large before ~250 Ma, indicating that some trenches migrate rapidly but it is low after ~250 Ma, indicating a more consistent behaviour of trenches. The two populations (advancing and retreating trenches) evident in the Paleozoic median migration rate data reflect a global kinematic adjustment to supercontinent assembly. Overall, median trench migration rates

during the Mesozoic-Cenozoic cluster tightly around ~1.1 cm/yr, excluding the period from ~120-100 Ma during which Gondwana was in a mature stage of dispersal. During this event, global trench migration rates peaked at ~3.8 cm/yr. Characteristic of the data presented in Fig. 2.7A is the variability of migration rates in Paleozoic times. From 250-0 Ma trench migration rates are contained within ±12 cm/yr whereas, from 410-251 Ma the error envelope for migration rates ranges within ±18 cm/yr. This distinction could be representative of the uncertainty associated with reconstructing plate motions in pre-Mesozoic times, as controls on plate motions are increasingly poorly constrained back in geological time due to an absence of robust surface data, such as seafloor spreading anomalies and hotspot trails (Müller et al., 1993). Alternatively, it is possible that the large variation in subduction zone migration rates during the late Paleozoic is not a model artefact, but is instead an expression of supercontinent assembly, as the closing of large interior oceanic basins may have forced periods of rapid trench motion.

A noticeable feature of the subduction zone migration analysis is the relatively narrow error envelope of our reconstruction for the period from 300-275 Ma. During this time, although median rates of migration are approximately the same in both models, M16 is characterised by more variable rates of trench migration (Fig. 2.7A). We attribute this contrast to the different reference frames used in the reconstructions. The reference frame implemented in M16 is that of Domeier and Torsvik (2014), which imposes a major (~15°), dominantly eastward, drift of the lithosphere during early Permian times (Fig. 2.5). This motion corresponds to a marked increase in the global RMS plate speeds (Fig. 2.6). Meanwhile, the contemporaneous rotation in our model prescribes a sluggish northeastward drift (Fig. 2.5), manifest in the RMS speeds as a prominent trough (Fig. 2.6). A similar instance of distinctive difference between the trench migration error envelopes occurs during early Triassic times (Fig. 2.7A). However, in this case subduction zone migration rates are greater for our reconstruction. The time interval from 250-230 Ma is a period in which both models transition from Paleozoic to Mesozoic reference frames. The 250 Ma Gondwana paleomagnetic pole calculated by Torsvik and Van der Voo (2002) is located south east (present day orientation) of the coeval pole of Domeier and Torsvik (2014), so that when these paleopoles are used to constrain the Triassic position of Gondwana the former reference frame reconstructs the continent to higher latitudes compared to the latter (Fig. 2.5). We followed M16 and implement the reference frame of Domeier et al. (2012) after 230 Ma. This required shifting southern Africa (the top of the plate hierarchy) from its position at 250 Ma to its position at 230 Ma. This shift is larger in our reconstruction compared to M16, resulting in augmented plate velocity and subduction zone migration rates for 250-230 Ma (Fig. 2.6 and Fig. 2.7).

Our model includes alternative reconstructions for the closure of the Rheic Ocean (Sections 2.2.2.3. and 2.2.2.4.), and the Paleozoic evolution of China (Section 2.2.2.1.). These changes impact subduction zone migration rates calculated between ~370-340 for the two studies, to the effect that subduction zone retreat is the dominant regime in our model, whereas subduction zone advance dominates M16 (Fig. 2.7). Two subduction zones in M16 have particularly rapid trench migration rates (>10 cm/yr), and therefore have a strong influence on global trench speeds include the Kunlun-Qinling subduction zone that bounds the southern margin of North China and Tarim, and the Paleo-Tethys intra-oceanic arc.

Adopting the reconstruction of Domeier and Torsvik (2014), M16 implemented north-dipping

subduction of the Shandang Ocean beneath the Kunlun-Qinling active margin during late Devonian and Carboniferous times. Cessation of subduction along this margin corresponded with the collision between the Qinling unit and North China at 320 Ma (Domeier and Torsvik, 2014). The kinematics driving this collision also resulted in advancement of the Proto-Japan subduction zone outboard of eastern South China. We implemented an alternative scenario in which the NCB and Qinling collision occurred in late Silurian times, prior to the start of our reconstruction. In our reconstruction, for most of late Paleozoic times the southern margin of North China was passive, facing the Mianlue Ocean, and it only became active in late Permian times when the margin collapsed and subduction commenced (Fig. 2.4A-H). The rotations we applied to satisfy the spreading history in the Mianlue Ocean resulted in the Proto-Japan subduction zone retreating during the Paleozoic.

The other major instance of subduction zone advance during late Paleozoic times begins in M16 at 369 Ma, when a lengthy intra-oceanic subduction zone forms in the Paleo-Tethys Ocean. This long subduction zone spans the length of the Paleo-Tethys Ocean from northwest Gondwana to southern Kazakhstan (~12,000 km) and represents the eastern and southern boundary of the large western Paleo-Tethys oceanic plate. From late Devonian-early Carboniferous times, the Paleo-Tethys intra-oceanic subduction zone advanced rapidly westward with the western Paleo-Tethys plate to subduct at the east Variscan and southeast Baltic margins (Domeier and Torsvik, 2014). We modelled the Variscan margin facing the western Paleo-Tethys Ocean as passive in late Devonian-early Carboniferous (Fig. 2.4A-E) times following Golonka (2007), precluding convergence at this margin.

Aligning Paleozoic subduction zone migration trends with Cenozoic estimates was a key motivation of our study, and to this end, we focused our attention on the closing of the Rheic Ocean and the Variscan Orogeny as well as the Paleozoic evolution of China. While we were able to reduce episodes of dominant subduction zone advance, overall, larger rates of subduction zone migration persisted during late Paleozoic times (Fig. 2.7A), precluding favourable comparisons with Cenozoic times. The absolute positions of reconstructed subduction zones (Fig. 2.9) give a spatial and temporal indication of trench mobility. Paleozoic subduction zones are more stable in our reconstruction compared to M16 (Fig. 2.9A, B), which is a reflection of how each study treats the present-day structure of LLSVPs as a constraint on plate motion. We note that while subduction zones are mostly directed away from present-day LLSVPs inferred from tomography for the period 250-0 Ma (Fig. 2.9A, C), there is significant overlap between subduction zones and present-day LLSVPs for the period 410-250 Ma (Fig. 2.9B, D). Overall, the Paleozoic subduction history appears difficult to reconcile with the hypothesis of fixed and rigid LLSVPs (Torsvik et al., 2010a).

For the period 70-0 Ma, we implemented the modified relative plate motion model of Müller et al. (2016a) and the moving hotspot reference frame of Torsvik et al. (2008). Various components of the Müller et al. (2016a) model were adjusted for the period 83-55 Ma and these changes are detailed below. Here, we make some first order observations about the subduction zone convergence rates implied by our reconstruction. The results for the Cenozoic Era are best constrained, however, this time period is relatively short. Extending our investigation back to 120 Ma in the Early Cretaceous provides an opportunity to evaluate subduction zone dynamics since the breakup of Gondwana while simultaneously retaining a relatively low level of geological and geophysical uncertainty.

The global median convergence rate drastically decreased after peaking during the breakup of Gondwana and plateaued at ~5 cm/yr in Cenozoic times (Fig. 2.7B). Over the past 130 Myr, 90% of global median convergence rate is between 3.5-11.7 cm/yr, with a full range between 3.2-12.4 cm/yr. For recent times (~70-0 Ma), global median convergence rates cluster about ~4 cm/yr. Both our reconstruction and M16 are within these ranges during Paleozoic times. Globally, our model calculates that median convergence rates are largely ~6 cm/yr (standard deviation σ = 1.85 cm/yr) in Paleozoic times. During the breakup of Gondwana between ~155-100 Ma, median global convergence rates peaked, reaching rates in excess of 12 cm/yr.

The convergence rate is defined as the orthogonal component of relative velocity between the overriding plate and the subducting plate. Therefore, any point on the line segment with negative convergence is representive of a divergent system, indicating an inconsistency within the model. About 93% of subduction zones are converging for our reconstruction and the interval 410-0 Ma (Fig. 2.7C). Counterintuitively, this metric drops to ~91% for the interval 130-0 Ma (Fig. 2.7C), which possibly reflects the increasing complexity of the reconstruction for younger ages. The Mesozoic and Cenozoic eras are characterised by a larger number of plates that have been implemented to capture regional complexities. However, with increased spatial resolution comes greater opportunity for inconsistencies to be recognised. The component of global subduction zone segments not in a convergent regime is represented temporally in Figure 7C. We note that >85% of global subduction zones are convergent for 97% of times for our reconstruction during 410-0 Ma, with departures occurring at ~400 Ma, ~220 Ma, ~80 Ma and ~50 Ma. These transient departures involve isolated subduction zone segments and are probably not indicative of wholesale problems with the reconstruction.

Convergence at subduction zones is most problematic at 82 Ma, in M16 (Fig. 2.7C). The low fraction of converging subduction zones from 82 Ma to 77 Ma is a reflection of several issues spread out through space over a short-term interval. We modified the relative plate motion model of Müller et al. (2016a) to improve the percentage of global converging subduction zones by 15% for this interval (Fig. 2.7C). We endeavoured to limit our changes to oceanic plates and boundaries, as these features are least constrained. Our changes, which are presented graphically in Supplementary Fig. 2.1, include: (i) cessation of western Mesotethys subduction at the NE African margin at 83 Ma instead of 75 Ma; (ii) modification of stage rotations to increase spreading rate in the of the proto-South Loyalty back arc basin (outboard eastern Australia) between 85-55 Ma; (iii) modification of stage rotations to increase spreading rate in an unnamed back arc basin near the Coral Sea between 85-70 Ma; (iv) modification of stage rotations to slow the subduction of the Caribbean plate from 83-73 Ma and; (v) changing the 85-80 Ma plate boundary along the western margin of the Antarctic Peninsula from a subduction zone to a transform boundary. These limited changes to the model improved the fraction of converging subduction zones by ~15% for the period ~90-70 Ma (Fig. 2.7C).

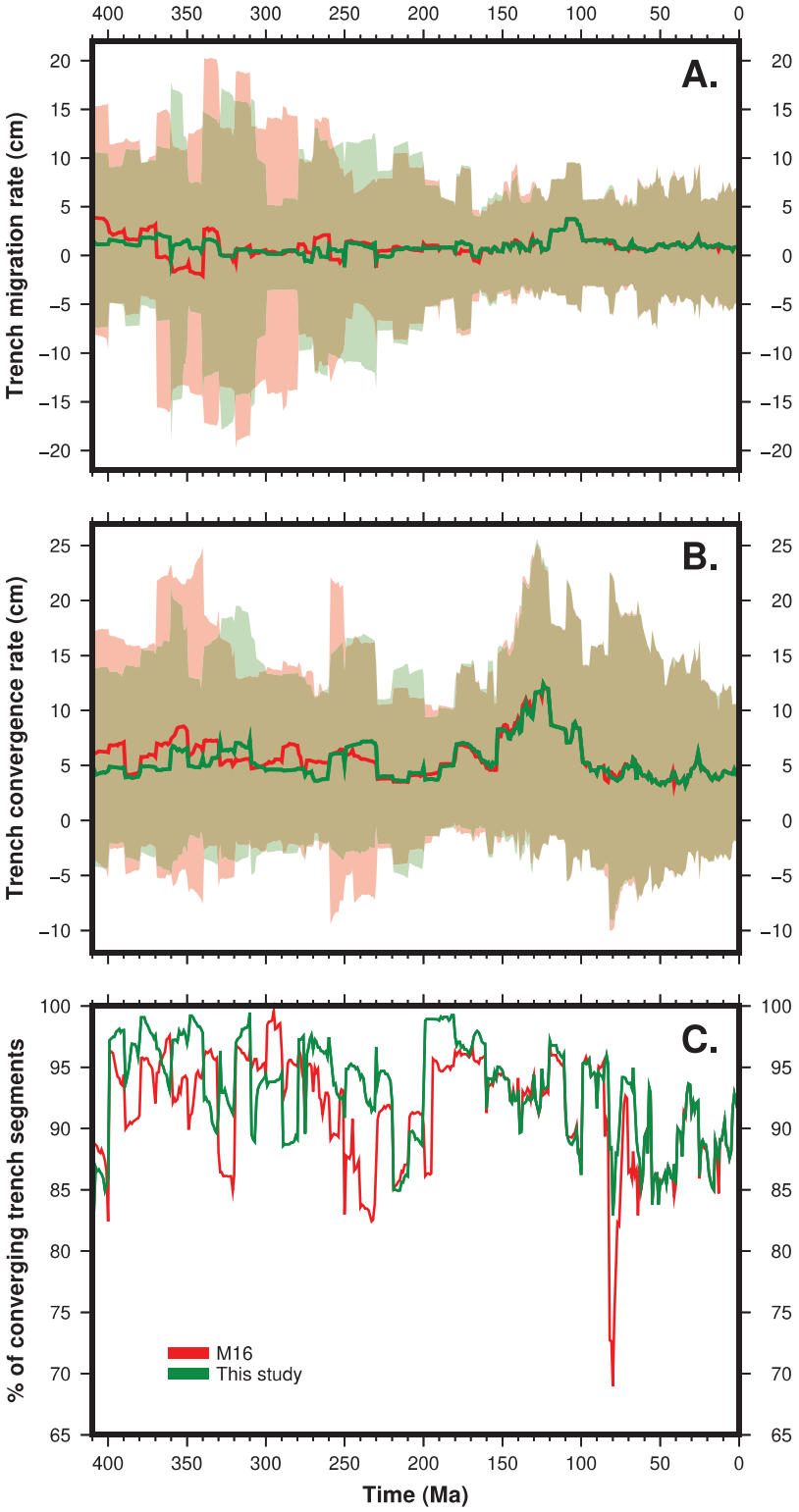

Figure 2.7. Global subduction zone kinematic statistics for the reconstruction of Matthews et al. (2016) and the reconstruction presented in this study. (A); Median value of subduction zone motion with error envelopes (2 standard deviations) shaded. (B); Median value of subduction zone convergence rate with error envelopes (2 standard deviations) shaded. (C); Percentage of subduction zones for which convergence rates are positive.

2.4.5. Geodynamic implications

To further gauge our reconstruction, we compared the present-day geometry of thermal structures in the lowermost mantle predicted by forward global mantle flow models to the location of LLSVPs from tomography models. In geodynamic models constrained by global plate reconstructions, the lower mantle structure is shaped by subducting slabs (Rudolph and Zhong, 2014). When these cold, dense slabs sink into the deep Earth, they deform the structure of the hot lowermost mantle, here assumed to be initially laterally uniform. Such flow models allow us to explore the role of tectonic configurations in shaping the structure of the deep mantle back to Paleozoic times.

2.4.5.1. Reconstructing mantle flow since the early Paleozoic Era

We use the mantle convection code *CitcomS* (Zhong et al., 2008), modified (Bower et al., 2015) to assimilate tectonic reconstructions with continuously closing plates (Gurnis et al., 2012) in one million-year increments. The model consists of 129 x 129 x 65 x 12 ≈ 13 million nodes which, with a radial mesh refinement, gives average resolutions of ~50 x 50 x 15 km at the surface, ~28 x 28 x 27 km at the CMB, and ~40 x 40 x 100 km in the mid-mantle. The initial condition at 410 Ma consists of an adiabatic temperature profile between two thermal boundary layers. The basal layer is initially laterally uniform (225 km thick) and includes a 113-km thick layer (2% volume of Earth's mantle; Hernlund and Houser, 2008) of material 4.24% denser than ambient mantle. Slabs are initially inserted to 1,200 km depth, with an angle of 45º down to 425 km depth, and vertically between 425 km and 1,200 km depth. Slabs are initially twice as thick in the lower mantle than in the upper mantle to account for advective thickening (Ricard et al., 1993). In subsequent steps, the thermal structure of slabs is assimilated down to 350 km depth, and subduction zones that appear during the model run are progressively inserted into the mantle. The model is entirely dynamic below 350 km depth.

The vigour of convection is defined by the Rayleigh number $Ra = \frac{\alpha_0 \rho_0 g_0 \Delta T h_{\mathrm{M}}^3}{\kappa_0 \eta_0}$, where $\alpha_0 = 3 \times 10^{-5}$ K^{-1} is the coefficient of thermal expansion, $\rho_0 = 4000$ kg m^{-3} is the density, $g_0 = 9.81$m s^{-2} is the gravity acceleration, $\Delta T = 2825$ K is the temperature change across the whole mantle, $h_{\mathrm{M}} = 2867$km is the thickness of the whole mantle, $\kappa_0 = 1 \times 10^{-6}$ m^2 s^{-1} is the thermal diffusivity, $\eta_0 = 1 \times 10^{21}$ Pa s is the viscosity, and the subscript "0" indicates reference values. With the values listed above, $Ra = 7.8 \times 10^7$. We consider the extended-Boussinesq approximation of mantle convection, as in Hassan et al. (2015), with a decrease in the coefficient of thermal expansion by a factor of three over the thickness of the mantle. The dissipation number $Di = \frac{\alpha_0 g_0 R_0}{C_{P_0}} = 1.56$, where $C_{P_0} = 1200$ J kg^{-1} K^{-1} is the reference heat capacity. We consider that 33.5 TW of heat originate from within Earth's mantle due to radioactive elements and primordial sources of heat dissipated by secular cooling of the solid Earth, in line with available constraints (Jaupart et al., 2007).

We approximate Earth's mantle as a Newtonian fluid in which viscosity varies with temperature and depth following $\eta = \eta_0(r)(1 + \eta_c C) \exp\left\{\frac{[E_\eta + Z_\eta(R_0 - r)]}{[R(T+T_{\mathrm{off}})]} - \frac{[E_\eta + Z_\eta(R_0 - R_c)]}{[R(T_{\mathrm{CMB}}+T_{\mathrm{off}})]}\right\}$, where $\eta_0(r)$ is the reference viscosity for four layers: it is equal to 2×10^{19} Pa s above 160 km, to 2×10^{18} Pa s between 160–310 km depth, to 2×10^{19} Pa s between 310–660 km depth and to 2×10^{20} Pa s below 660 km depth, in the lower mantle. *C* is the composition field, and η_c is the compositional viscosity pre-factor equal to 10 in

the subcontinental asthenosphere, in order to offset the lower viscosity in that layer to couple the continental lithosphere with the deep mantle and reduce the net rotation induced to the lower mantle (Rudolph and Zhong, 2014). r is the radius, R_C = 3504 km is the radius of the core and R_0 = 6371 km is the radius of the Earth. $E_\eta = 258\,\text{kJ mol}^{-1}$ is the activation energy, $Z_\eta = 1.9 \times 10^{-6}\,\text{m}^3\,\text{mol}^{-1}$ is the activation volume, R = 8.31 J mol^{-1} K^{-1} is the universal gas constant, T is the dimensional temperature, $T_{\text{off}} = 452\text{K}$ is a temperature offset and T_{CMB} is the temperature at the core-mantle boundary. The temperature offset is a constant that was adjusted together with the activation energy and activation volume to obtain variations in viscosity by three orders of magnitude over the range of considered temperatures and pressures. Horizontal averages of present-day mantle temperature and viscosity are shown in Fig. 2.9.

We consider two model cases: Case 1 based on the global tectonic reconstruction of Matthews et al. (2016), and Case 2 based on the global tectonic reconstruction presented in this study.

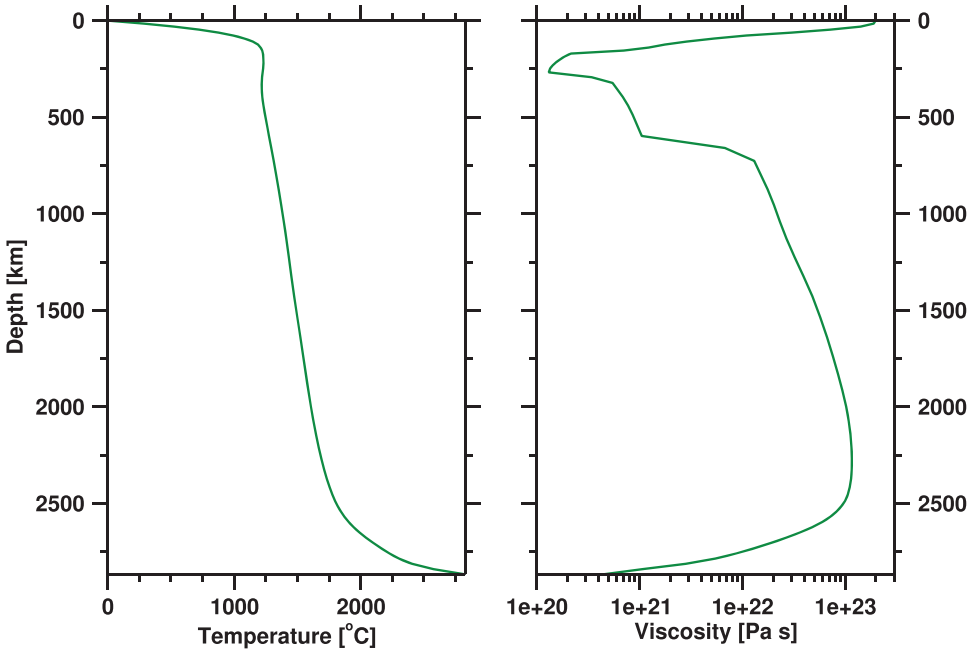

Figure 2.8. Horizontally averaged present-day mantle temperature (left hand side) and viscosity (right hand side) for Case 2.

2.4.5.2 Predicted evolution of lower mantle structures

We first verify that the predicted present-day CMB heat flow (4.3 TW for Case 1; 5.5 TW for Case 2) and surface heat flow (40.4 TW for Case 1; 41 TW for Case 2) are consistent with constraints (Jaupart et al., 2007). As in Flament et al. (2017a), we next use cluster analysis to quantify the match between the predicted present-day location of model lowermost thermochemical structures and the location of LLSVPs inferred from seven S-wave tomography models: SAW24B16 (Mégnin and Romanowicz, 2000), HMSL-S (Hernlund and Houser, 2008), S362ANI (Kustowski et al., 2008), GyPSuM-S (Simmons et al., 2010), S40RTS (Ritsema et al., 2011), Savani (Auer et al., 2014), SEMUCB-WM1 (French and Romanowicz, 2014). We find that Case 1 reproduces the structure of the lower mantle as imaged by these seven tomography models with average accuracy of 0.60, and Case 2 with average accuracy of 0.66. The accuracy for which both cases reconstruct the structure of the

lowermost mantle is less than that of reconstructions from flow models constrained to the past 230 Myr (Flament et al., 2017a). The reduced accuracy could be a reflection of the longer tectonic history and/or less well constrained plate motions in the Paleozoic used as boundary condition in Cases 1 and 2.

We then use the predicted thermal and compositional fields ~200 km above the core mantle boundary (Zhong and Rudolph, 2015; Flament et al., 2017a) as an indicator of the location of model lowermost thermochemical structures (Fig. 2.10) in comparison to the present-day tomography vote map of Lekic et al. (2012). The present-day spatial extent of the thermal and composition fields predicted by both model cases are in first-order agreement with the position and geometry of the African LLSVP and the Perm Anomaly from the tomography vote map (Fig. 2.10). However, we note that the western part of the Pacific LLSVP is not predicted well by either Case (Fig. 2.10), where a cold structure is predicted instead. That cold structure is linked to late Paleozoic subduction along the margins of Tarim and North China (Fig. 2.4A-E). In addition, Case 1 predicts a cold structure around the middle of the African LLSVP that is not suggested by tomography (Fig. 2.10C). This cold structure, which formed before 260 Ma (Fig. 2.10A), is due to intra-oceanic subduction at the northern margin of the Variscan assemblage in the early stages of M16 (Fig. 2.9B). That subduction zone does not exist in our reconstruction (Fig. 2.9D). Our reconstruction of the present-day lower mantle thermal structure is characterised by a homogenous, large wavelength, hot anomaly in the region of the African LLSVP. In the flow model, this feature develops from late Permian times (259 Ma) to the present as subduction along the western margin of the proto-Pacific causes mantle downwelling and introduces cold material into the mantle, displacing hotter material and moving the structure west. The outline of the basal thermochemical structures can be defined either using the composition or the temperature field (Fig. 2.10). We note that the Pacific thermo-chemical pile is compositionally less than 190 km high at 260 Ma in Case 2, which is consistent with the relatively weak temperature anomaly (Fig. 2.10D), and different to the Pacific thermo-chemical pile predicted at 260 Ma by Case 1 that uses on the plate reconstruction of M16.

We sampled three locations along the eastern margin and two locations along the western margin of the African thermochemical structure and traced the motion of these points from 260 Ma to present day (Fig. 2.10). Results for Case 1 suggest that the eastern margin of the African LLSVP has drifted ~1700 km west at an average rate of ~0.65 cm/yr and the western margin has moved west ~190 km at an average rate of ~0.07 cm/yr since late Permian times. Case 2 results suggest the eastern margin of the African LLSVP has drifted ~1500 km west at an average rate of ~0.58 cm/yr and the western margin has moved west ~870 km at an average rate of ~0.33 cm/yr since late Permian times. In both Cases, most of the motion occurred along the eastern margin of the African LLSVP over the last 130 Myr (average rates for Case 1 eastern margin: 260-130 Ma, ~0.31 cm/yr; 130-0 Ma, ~1 cm/yr and western margin: 260-130 Ma, ~0.25 cm/yr; 130-0 Ma, ~0.1 cm/yr, and average rates for Case 2 eastern margin: 260-130 Ma, ~0.18 cm/yr; 130-0 Ma, ~1.27 cm/yr and western margin: 260-130 Ma, ~0.4 cm/yr; 130-0 Ma, ~0.26 cm/yr) (Fig. 2.10). Minor movement along the western margin of the African LLSVP in Case 1 is associated with the model for the closure of the southern Rheic Ocean implemented in the plate reconstruction of M16. Closure of the ocean involves a series of subduction zones (Fig. 2.9A) along the margins of eastern Laurentia and western Gondwana during Devonian times. This subduction zone configuration results in significant material sinking into the mantle beneath western Gondwana during the late Paleozoic, which

pushes the western margin of the African LLSVP east, so that by late Permian times a cold mantle anomaly exists between the western margin of the LLSVP and the west Pangea convergent margin (Fig. 2.10A). This cold mantle anomaly then reduces the influence of the western Pangea subduction zone on the geometry and position of the western margin of the African LLSVP that remains stable (Fig. 2.10B, C). Alternatively, in Case 2 based on the reconstruction in this study, closure of the Rheic Ocean was dominated by subduction at the eastern margin of Laurentia until 380 Ma (Fig. 2.4A-D). This results in less subduction reaching the lowermost mantle along the western margin of Pangea (Fig. 2.10A). In this scenario, the western margin of the African LLSVP is in close proximity to the west Pangea convergent margin during late Permian times, where the introduction of subducted material pushes the southern part of the African LLSVP east by ~1500 km over the last 260 Myr.

The results from Case 1 and Case 2 suggest that lowermost mantle structures could be mobile rather than fixed, which is broadly consistent with the findings of Zhong and Rudolph (2015), who concluded from kinematically-driven models that the African LLSVP is unlikely to have been stable since early Paleozoic times, and that the presently dominant degree-two structure was established before 200 Ma (Fig. 2.10). The predicted mobility of the eastern margin of the African LLSVP is consistent with SKS–SKKS splitting measurements that reveal anisotropy with a fast east–west direction in the lowermost mantle within 150 km of the eastern boundary of the African LLSVP (Lynner and Long, 2014). The presented models, in which the basal layer thickens and becomes hotter over time (Fig. 2.10), are known to depend on initial conditions, physical parameters and tectonic reconstructions used as boundary conditions (Zhong and Rudolph, 2015; Flament et al., 2017b). A full model sensitivity study is beyond the scope of this study and will be the object of a separate study.

The plate motions for South China implemented in our model reconstruct the block to a location ~35° farther west of the coeval position of M16 in late Permian times. The reconstructed position of the SCB in M16 is dependent on the interpretation that South China should be at the western margin of the Pacific LLSVP during the 260 Ma eruption of the Emeishan LIP (Domeier and Torsvik, 2014). To satisfy this interpretation and prevent overlap with the Cimmerian terranes at 250 Ma, while simultaneously preventing rapid subduction zone advance at the eastern margin of the SCB/western margin of Panthalassa, M16 implemented the opening of an intermediate, model-dependent back-arc basin. Between 260-250 Ma, the SCB moves at up to ~40 cm/yr, which is tectonically unreasonable (Zahirovic et al., 2015). Geodynamic models constrained by the M16 plate motions show that the late Permian reconstructed position of the SCB is not reconstructed directly above a plume generation zone at the margin of either deep model thermochemical structure (Fig. 2.10). Conversely, flow models constrained by our tectonic reconstruction show that at ~260 Ma the SCB is positioned above the eastern margin of the model African deep thermochemical structure.

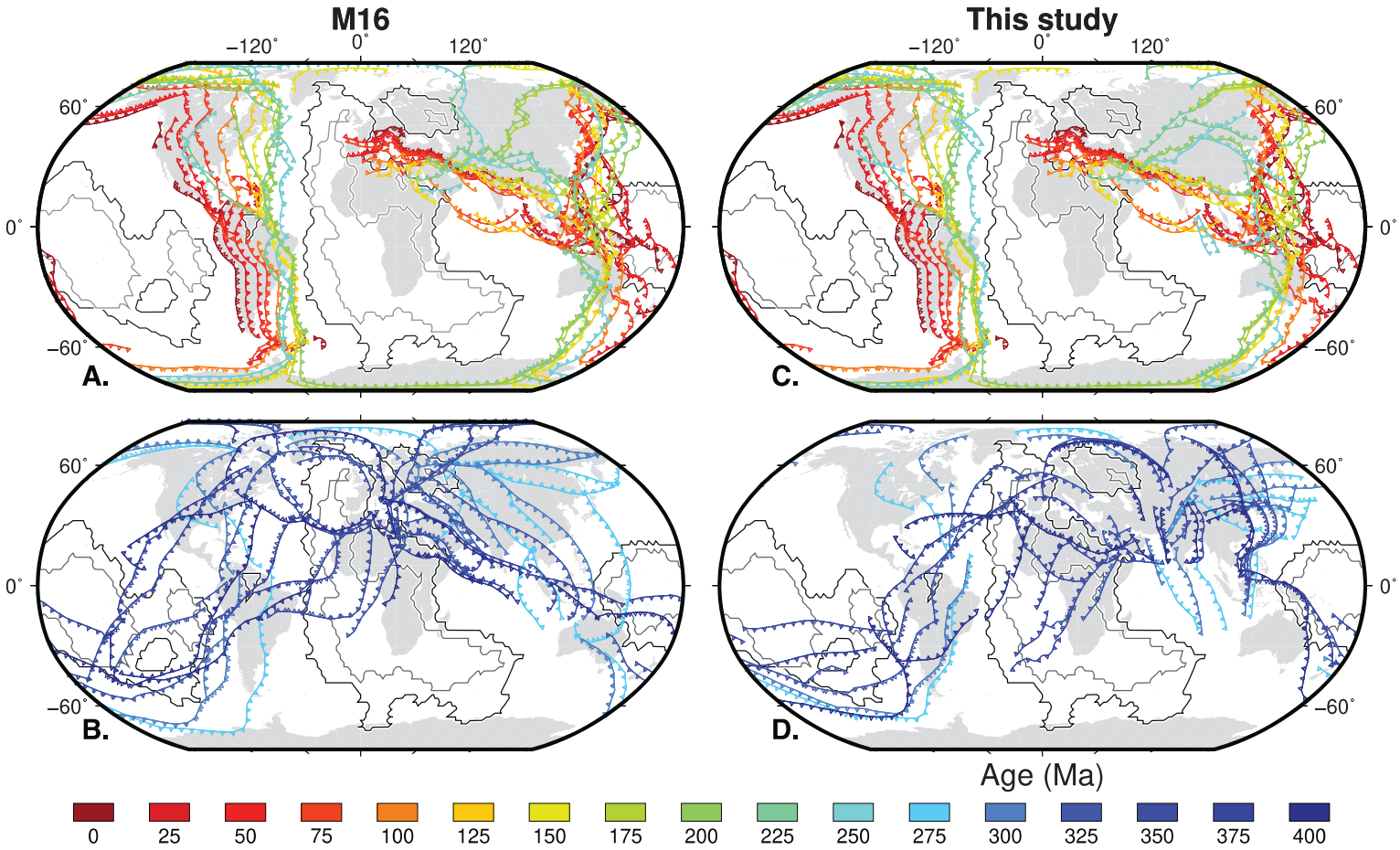

Figure 2.9. Subduction locations through time at 25 Myr intervals, for the period 0-240 Ma above (A, C) and 260-400 Ma below (B, D). (A, B). Reconstructed subduction locations from Matthews et al. (2016). (C, D). Reconstructed subduction locations from this study. The black contour represents a value of one and grey contour a value of five in vote maps for present day tomography models (Lekic et al., 2012).

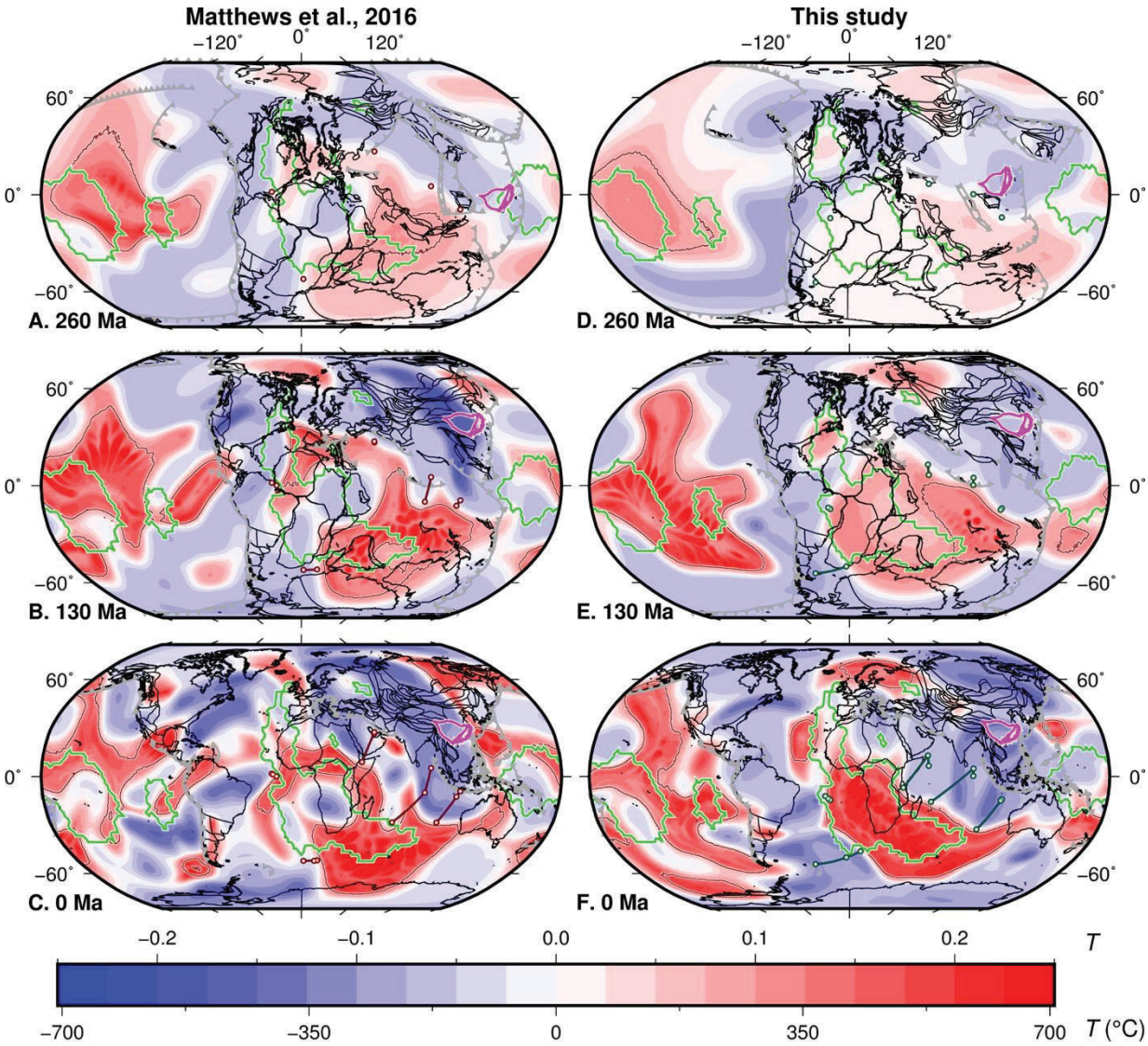

Figure 2.10. Mantle temperature anomalies at 2677 km depth predicted by mantle flow models driven by M16 (Case1, left) and this study (Case 2, right). The brown contours indicate 50% concentration of dense material. The green contour represents a value of five in vote map for tomography models (Lekic et al., 2012). Reconstructed locations of present-day coastlines are in black with the South China block show in magenta. Reconstructed subduction zone locations are shown as grey lines with triangles on the overriding plate. Trace points at the eastern and western margins and their motion paths are shown in 130 Myr intervals (Case 1, red and Case 2, green).

2.5. Conclusions

We have presented a global plate reconstruction model that builds upon and extends the pioneering models of Domeier and Torsvik (2014) and Matthews et al. (2016). We have implemented regional improvements to the relative plate motion model and an alternative absolute plate motion model to reduce global RMS plate speeds compared to M16. New regional models are implemented for the late Paleozoic closure of the Rheic Ocean and the tectonic evolution of the Qinling Orogenic Belt in China. Our model does not strictly follow theoretical models (Mitchell et al., 2012; Torsvik et al., 2014) to constrain the reconstructed longitudinal positions of Paleozoic plates. The new reconstruction produces Paleozoic plate RMS speeds (~8 cm/yr) that compare favourably to Mesozoic-Cenozoic rates (~6 cm/yr).

We analysed the global model for trends in subduction zone convergence and migration rate through time, demonstrating improvements in subduction zone kinematics throughout the considered period compared to the reconstruction of Matthews et al. (2016). In our reconstruction, median global convergence rates over the

past 410 Myr peaked at ~13 cm/yr during the break-up of Gondwana and have plateaued to rates of ~5 cm/yr over the past 100 Myr. In the Paleozoic component of our model, median convergence rates are tightly distributed around ~5 cm/yr, consistent with recent times. We calculate that over the modelled interval (410-251 Ma) ~93% of reconstructed subduction zones are in a convergent regime. The fraction of reconstructed subduction zones where convergence is not occurring are isolated trench segments. Globally, over the span of the model median rates of trench migration are largely clustered around ~1 cm/yr with median speeds trending to ~2.5 cm/yr in the late Devonian. In the reconstructions, subduction zones are more mobile in Pre-Carboniferous times than at other times, which may be characteristic of super continent assembly or, alternatively, could reflect increasingly poorly constrained plate motions in time.

Using our reconstruction as a time-dependent surface boundary condition for mantle convection modelling, we compared the predicted present-day thermal structure of the lower mantle to vote maps of tomography models and established a correlation between the two. Our model predicts a present-day structure at the CBM that is in first order agreement with the geometry of African LLSVP and Perm Anomaly from tomography vote maps. Geodynamic models driven by plate kinematics provide another means with which to gauge the geodynamic implications of global tectonic reconstructions. The significant motion of lower mantle thermochemical piles since late Permian times predicted by our models suggests that deep mantle structures are mobile and deformable, as opposed to fixed and rigid.

2.6. Supplementary material

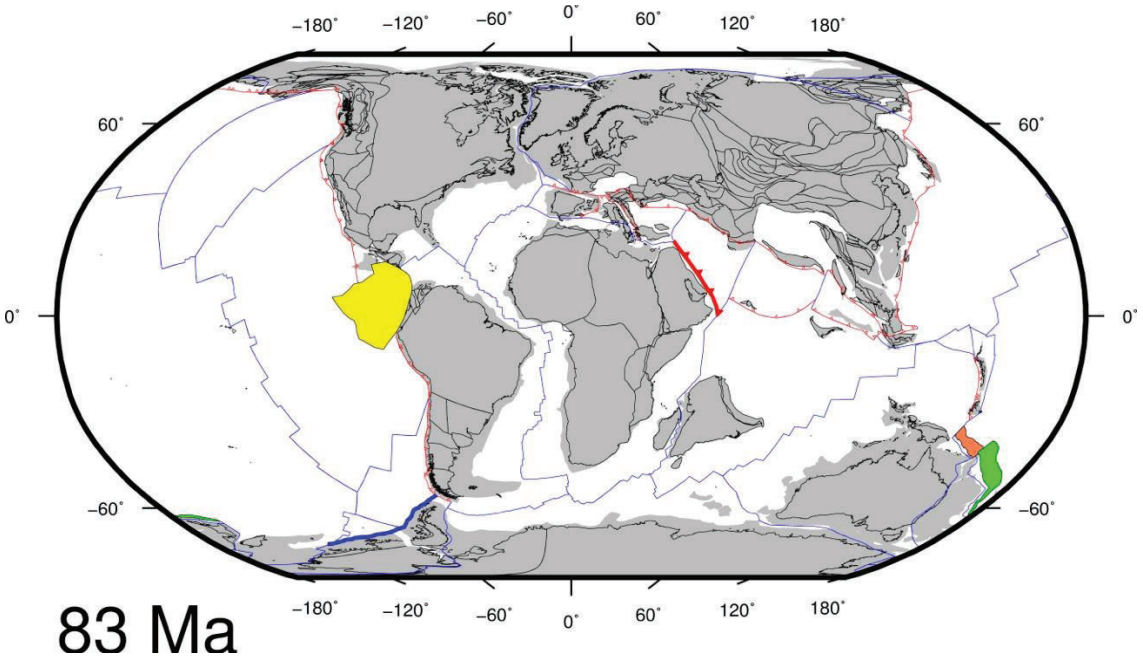

Supplementary Figure 2.1: Global reconstruction at 83 Ma highlighting changes made to improve subduction zone convergence. Present day reconstructed coastlines and continental polygons are represented in black and grey respectively. Red lines with triangles on the overriding plate indicate subduction zones, and blue lines denote mid-ocean ridges and transform faults. The thick red line with triangles is the Mesotethys subduction at the northeast African margin; the green polygon is the proto-South Loyalty back-arc basin (outboard eastern Australia); the orange polygon is a back-arc basin near the Coral Sea; the yellow polygon is the Caribbean Sea and; the thick blue line is a transform fault at the western margin of the Antarctic Peninsula.

Acknowledgments

This research was undertaken with the assistance of resources from the National Computational Infrastructure (NCI), which is supported by the Australian Government. This research has been conducted with the support of the Australian Government Research Training Program Scholarship. NF was supported by Australian Research Council grant DE160101020. SZ and RDM were supported by Australian Research Council grant IH130200012 and DP130101946. Figures were constructed using Generic Mapping (Wessel et al., 2013), GPlates (www.gplates.org) and ArcGIS. We are thankful for the constructive suggestions of two anonymous reviewers and the Editor that considerably improved the original manuscript. The digital files for viewing our reconstruction can be downloaded via the webdav link: https://www.earthbyte.org/webdav/ftp/Data_Collections/Young_etal_2018_GeoscienceFrontiers/Young_etal_2018_GeoscienceFrontiers_GPlatesPlateMotionModel.zip

Chapter 3. Long-term Phanerozoic sea level change from solid Earth processes

Alexander Young[1*], Nicolas Flament[1], Simon E. Williams[2], Andrew Merdith[3], R. Dietmar Müller[4]

[1]GeoQuEST Research Centre, School of Earth, Atmospheric and Life Sciences, University of Wollongong, Northfields Avenue, NSW 2522, Australia

[2]Department of Geology, Northwest University, Xi'an China

[3] Laboratoire de Géologie, Université of Lyon 1, France

[4]EarthByte Group, School of Geosciences, The University of Sydney, Sydney, NSW 2006, Australia

** corresponding author*

Abstract

The sedimentary record suggests that global sea levels may have fluctuated by hundreds of meters throughout Phanerozoic times. Stratigraphic methods are used to estimate sea level change over 1-10 Myr with the assumptions that tectonically quiescent regions are stable. Long-term (10-80 Myr) sea level change can be computed from plate tectonic methods that utilise paleogeographic reconstructions to calculate eustatic change. Plate tectonic reconstructions and mantle flow models make it possible to isolate, quantify and evaluate the contribution of different solid Earth mechanisms to sea level change, including: the volume below MORs, mantle-driven dynamic topography, marine sedimentation, oceanic large igneous province emplacement, deep water cycling, the volume above subduction zones and changes in continental area. Despite intrinsic links between these processes, their impact on sea level change is rarely studied in combination, and time-dependent models of long-term eustasy from tectonic and geodynamic processes are in their infancy. We couple plate tectonic reconstructions with time-dependent models of past mantle flow and develop a new holistic framework to model sea level change that accounts for the main solid Earth drivers of eustatic rise and fall. For the first time, we jointly quantify and analyse the effect of individual solid Earth mechanisms on Phanerozoic eustatic change, in particular the effects of mantle flow on continental and oceanic topography, the volumetric capacity above trenches and the changing shape of continents. Our results show that the dominant factor contributing to long-term global sea level change is the fluctuating volume below MORs (460 m) with secondary contributions from dynamic topography (250 m), the deep-water flux (230 m), marine sedimentation (170 m) and the volume capacity of trenches (130 m). We demonstrate that changes in ocean basin volume due to changes in the crustal age-area distribution are not balanced by a compensating equal but opposite volume change above subduction zones or by large-scale dynamic vertical motion of the continents. Additionally, we show that fluctuations in sea-level correlate with episodic patterns of supercontinent assembly and breakup; chiefly, variations in ridge volume and dynamic topography cause eustatic fall during supercontinent assembly and eustatic rise during dispersal.

Keywords

Phanerozoic, solid Earth, eustasy, mantle convection, dynamic topography, supercontinent cycle

3.1. Introduction

Eustatic change shifts coastlines and causes the waxing and waning of inland seas (Langford et al., 1995; Smith et al., 2004), modifies the composition of the oceans and atmosphere (Flament et al., 2008, 2013b), affects Earth's climate (Miller et al., 2005) and impacts the evolution of life (McKerrow and Cocks, 1976; Hallam, 1989). Studies of Phanerozoic eustasy (Vail et al., 1977; Hallam, 1984; Algeo and Seslavinsky, 1995; Snedden and Liu, 2010; Vérard et al., 2015; Van der Meer et al., 2017) show that sea level fluctuations follow cycles, with periods ranging from one to tens of million years. First order fluctuations in global sea level (10^7-10^8 years) are related to plate tectonics, correspond to continental flooding cycles (Golonka et al., 1994; Scotese and Golonka, 1997; Blakey, 2008) and have fluctuated throughout Phanerozoic times, exceeding present-day sea level by up to ~100-400 m (Algeo and Seslavinsky, 1995, Hallam, 1992).

Two prevailing methods exist to reconstruct past sea level; a stratigraphic method (Vail et al., 1977; Hallam, 1984; Algeo and Seslavinsky, 1995; Snedden and Liu, 2010) and a plate tectonic method (Müller et al., 2008; Vérard et al., 2015). The former utilises established criteria for sequence stratigraphic interpretations as well as lithological and paleontological data to interpret stratigraphic architecture, identify system tracts and quantify sea level change (e.g. Haq, 2014). This approach assumes that tectonically quiescent regions are stable; which has been shown to be invalid since mantle convection drives transient long wavelength vertical displacements of the Earth's surface (Gurnis, 1990b, 1993; Moucha et al., 2008; Spasojevic and Gurnis, 2012; Flament et al., 2013a). This process, called dynamic topography precludes attempts to reconstruct sea level from the rock record alone.

Sea level estimates derived from plate tectonic models focus on changes in first- (~100-200 Myr) and second- (~10-80 Myr) order eustatic cycles driven by solid Earth processes (Fig. 3.1). These processes alter sea level by: (i) changing the volume below mid-ocean ridges (MOR) (Hays and Pitman, 1973; Kominz, 1984; Worsley et al., 1984; Müller et al., 2008); (ii) mantle flow driving large scale vertical changes in topography (Spasojevic and Gurnis, 2012); (iii) marine sedimentation and oceanic large igneous province (O-LIP) emplacement (Harrison, 1999; Müller et al., 2008); (iv) deep water cycling (Karlsen et al., 2019); (v) changing topographies above subduction zones (Gurnis, 1990a; Husson and Conrad, 2006; Conrad, 2013), and; (vi) the expansion of continental area (Kirschner et al., 2010). Despite intrinsic links between these processes, their effect on sea level change is typically studied in isolation and there is no systematic understanding of how tectonic and geodynamic processes have jointly influenced sea level globally over long geological timescales (beyond ~100 million years ago; Spasojevic and Gurnis, 2012; Conrad, 2013). Linking plate tectonic to time-dependent models of past mantle flow makes it possible to quantify long-term eustatic variations based on large scale tectonic and dynamic mechanisms.

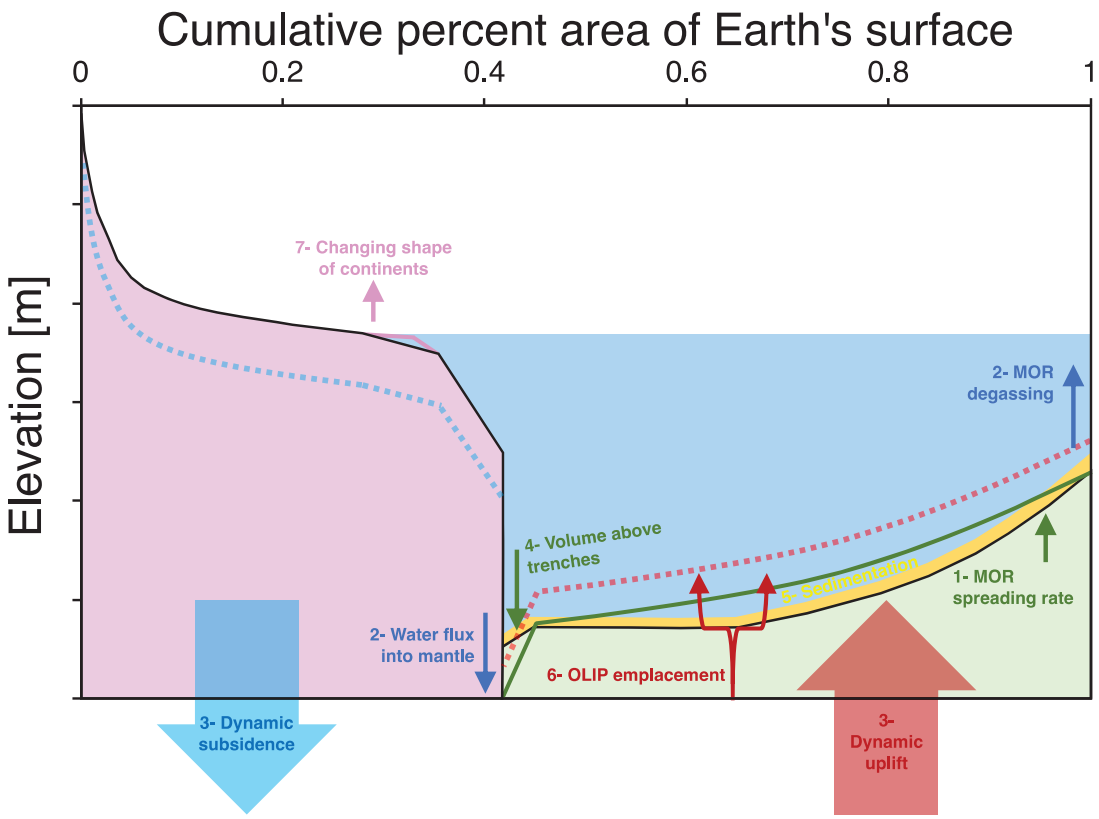

Figure 3.1: Mechanisms by which major solid Earth processes increase long-term sea level, overlain with a cartoon depiction of Earth's hypsometric curve, with elevation on the Y-axis and cumulative area above the corresponding elevation on the X-axis. Processes are numbered from 1 to 7. Pink area is continental lithosphere, green is oceanic lithosphere and blue fill is the ocean volume. Blue and red dashed lines represent continental and ocean elevations respectively, as they would appear having been modified by dynamic topography. MOR: Mid-ocean Ridge. O-LIP: Oceanic Large Igneous Province.

Recent advances in plate tectonic modeling (Domeier, 2016; Merdith et al., 2017; Domeier, 2018; Young et al., 2019, Chapter 2) have made it possible to extend models of the age of the ocean floor beyond the last 230 million years (Karlsen et al., 2020; Williams et al., 2021), unlocking the ability to quantitatively analyse Paleozoic eustatic trends using plate tectonic methods. Here, we jointly quantify the time-dependent impact of individual solid Earth mechanisms on first- and second-order sea level change and investigate their relationship to the Phanerozoic history of the solid Earth. In particular, dynamic deflections above subduction zones and the effects of mantle flow on average continental and oceanic topography have not previously been quantified over such time scales. The integrated nature of our workflow allows us to test alternative hypotheses for the driving forces of eustasy. We investigate whether changes in ocean basin volume due to variations in plate-tectonic spreading rates and ridge length are compensated by trench topography (Hager, 1980; Gurnis, 1990a), large-scale dynamic vertical motion of the continents (Rowley, 2017), or not compensated by either one of these mechanisms.

3.2. Methods

We develop a framework to model the main solid-Earth drivers of long-term sea level change over the past 560 Myr. The age of the ocean floor is reconstructed using a state-of-the-art tectonic reconstruction (Merdith et al., 2021) and workflow (Williams et al., 2021). Sea floor age maps are used to generate paleobathymetry models, continental shelf slopes (Algeo and Wilkinson, 1991), and to determine the amount of water being exchanged between the oceans and mantle (Karlsen et al., 2019). The tectonic reconstruction is used

as boundary condition to model past mantle flow, dynamic topography and the topography of oceanic trenches. We model Phanerozoic oceanic sedimentation and O-LIP emplacement. Past changes in topography and ocean volume are unified in time-dependent hypsometric curves from which historical sea levels are computed.

3.2.1. Plate tectonics and the volume below MORs

The foundation of our sea level model is a plate tectonic reconstruction. We use a reconstruction extending back to Neoproterozoic times (Merdith et al., 2021) that is modified to remove net lithospheric rotation, a standard practice in geodynamic modelling (Coltice et al., 2017). The reconstruction brings together the published models of Merdith et al. (2017), Domeier (2016, 2018) and Young et al. (2019, Chapter 2), and relies predominantly on paleomagnetic and geological evidence from the continents. Thus, the location and velocity of ancient oceanic plates is inferred; though the velocities are, by design, of the same order of magnitude present-day (~2-20 cm/yr). Furthermore, the high preservation potential of volcanic arcs, continental more so than oceanic (Safonova et al., 2017), provides some confidence in the reconstructed locations of past subduction zones (Cao et al., 2017a; Merdith et al., 2019).

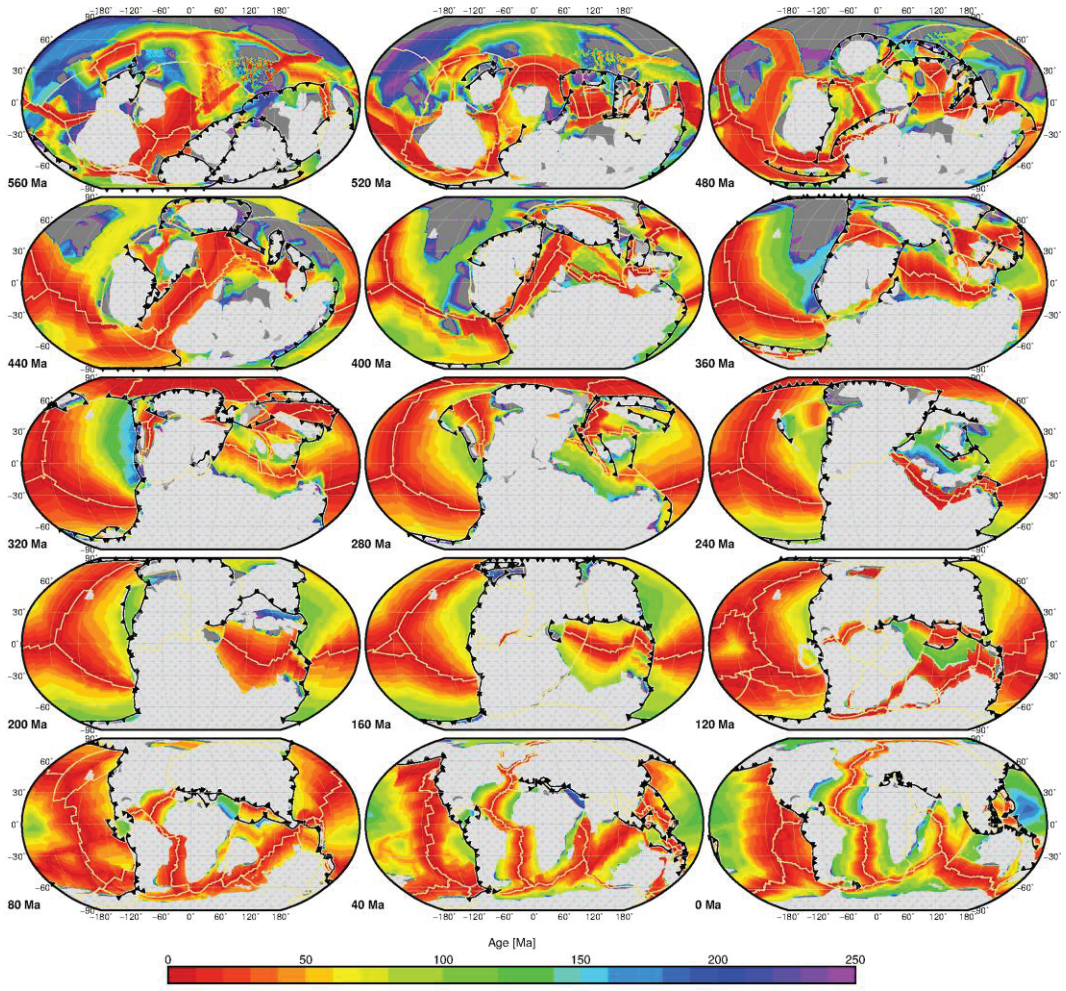

Figure 3.2: Past seafloor ages from 560-0 Ma for the reconstruction of (Merdith et al., 2021) in the no-net-rotation frame, illustrated in 40 Myr intervals. The colour scale indicates the paleo-age of the ocean crust; with dark grey as foreground colour. Reconstructed subduction locations are shown as black lines with triangles on the overriding plate, reconstructed mid-oceanic ridges and transform faults are in khaki, and reconstructed cratons (before 400 Ma) and continents (since 400 Ma) are show in grey with pattern fill.

Time dependent seafloor age maps are generated (Fig. 3.2) by applying a new open-source workflow (Williams et al., 2021) which utilizes topological plate reconstructions (Gurnis et al., 2018) and is used to calculate paleobathymetry (Fig. 3.3). Before 200 Ma approximately 70% of the Earth's surface is unconstrained (Domeier and Torsvik, 2019) so age estimates derived from the reconstruction are uncertain. Additionally, assumptions in the plate configuration, timing and extent of back-arc basins, and symmetrical spreading influence the distribution of ocean floor ages.

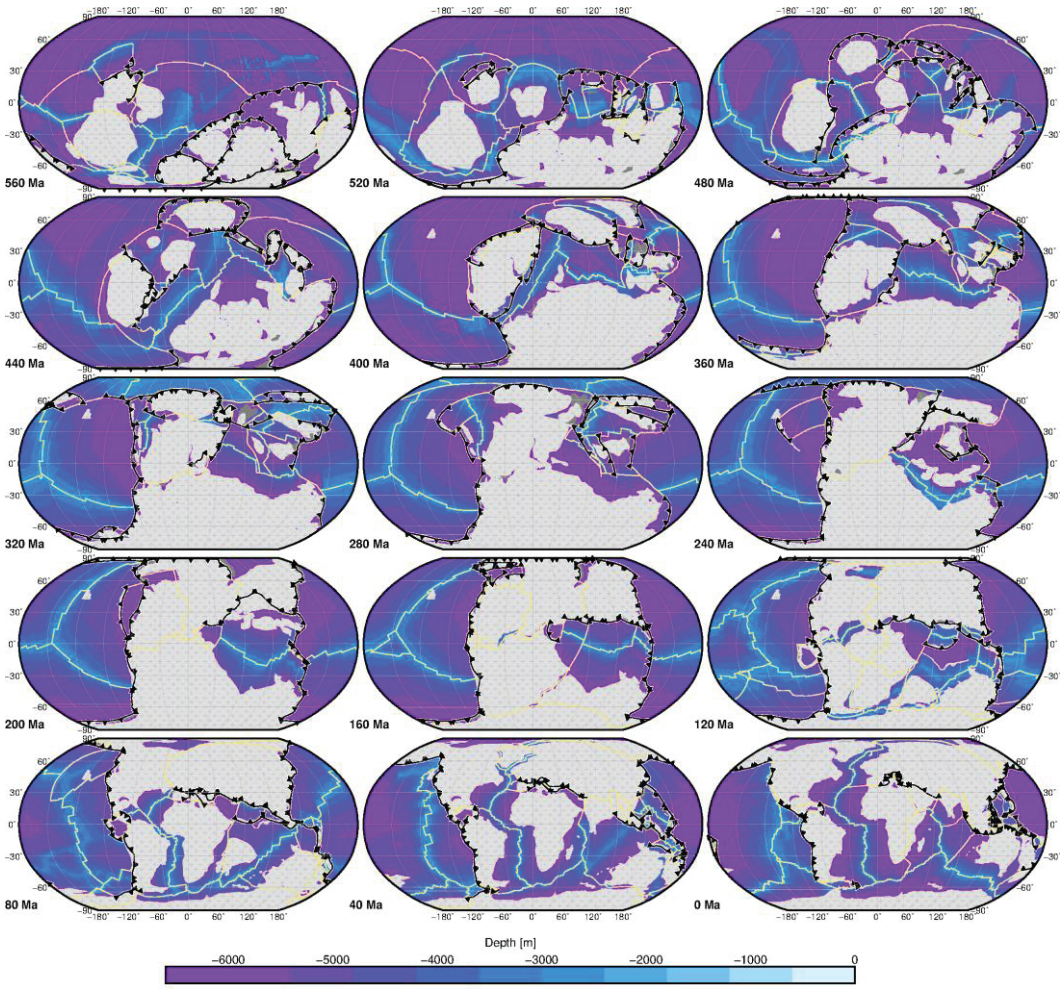

Figure 3.3: Reconstructions of paleobathymetry from 560-0 Ma, shown in 40 Myr increments and using the age-depth relationship of Richards et al. (2018). Reconstructed subduction locations are shown as black lines with triangles on the overriding plate, reconstructed mid-oceanic ridges and transform faults are in khaki, and reconstructed cratons (before 400 Ma) and continents (since 400 Ma) are show in grey with pattern fill.

Analysing the volume below MORs as a cause for sea-level change is a straightforward process since the depth of the ocean floor is primarily a function of its age (Parsons and Sclater, 1977). Younger lithosphere is warmer, thinner and less dense than older lithosphere and as a result, fast spreading ridges occupy more volume than slower ones (Fig. 3.1, process 1). Two principal models for the cooling of oceanic lithosphere exist: a half-space model, in which the lithosphere cools and thickens indefinitely as a function of age, and a plate model, in which the lithosphere cools until it reaches a maximum thickness. We use a plate model developed by Richards et al. (2018) to calculate paleobathymetry.

3.2.2. Deep water cycling

The subduction of sediments and hydrated oceanic lithosphere transports water from the oceans into the mantle (regassing), whereas MOR volcanism returns water to the surface (degassing). This deep-water cycle (Fig. 3.1, process 2) changes the volume of water in the ocean (Korenaga, 2017; Peslier et al., 2017). Changes in glaciation and groundwater storage also affect ocean water volumes however, our focus is on long-term eustasy, therefore we do not consider these processes which modulate change over short time scales (less than ~ 10 kyr).

Karlsen et al. (2019) recently parameterized subduction and MOR water flux to produce a history of deep water cycling and the resulting sea level change over the past 230 Myr. We apply their workflow to calculate deep-water flux from 560-0 Ma. First, subduction zone and MOR segments are extracted from the tectonic reconstruction at 10 Myr increments and resampled at regularly spaced 1 arc degree intervals. For each subduction zone point, plate age is extracted from the seafloor age map and convergence rate and segment length are calculated. Thickness of the subducting plate and its ability to retain water (ϵ) to depth are determined and the initial bulk water content of the plate (α) is set. The deep mantle water flux (kg/Myr) for a given time is calculated by summing over the product of ϵ, α, convergence velocity, density and plate thickness (Steinberger and Becker, 2018) for all subduction zone points. Then, spreading rate and ridge length are calculated for the MOR segments. The amount of water returning to the oceans at MORs is computed from a global degassing factor, spreading velocity and crustal thickness of all ridge segments. The change in ocean volume over time is the difference between regassing and degassing fluxes. We test two of the alternative scenarios presented by Karlsen et al. (2019) for differing ranges of present-day degassing and regassing rates; one in which regassing dominates (RD) and one in which the net water flux over the past 230 Myr is 0 kg/yr (long-term balance or LB). The details of this workflow are provided in Supplementary Section 3.7.1.

3.2.3. Dynamic and total topography

Mantle convection drives slow vertical displacements of Earth's surface leading to dynamic topography (e.g. Flament et al., 2013a). The long-wavelength component of dynamic topography evolves over millions of years and affects eustatic change (Husson and Conrad, 2006; Spasojevic and Gurnis, 2012; Conrad, 2013; Guillaume et al., 2016). For every mantle upwelling or downwelling there is a corresponding return flow that supports opposing topography. Therefore, the global average of dynamic topography from sources of buoyancy below a given depth should be zero. However, the average dynamic topography differs between emerged and submerged areas because of the evolving location of continents (Conrad and Husson, 2009; Spasojevic and Gurnis, 2012); thus, affecting eustasy. For example, dynamically uplifted seafloor and subsided continents lead to eustatic rise (Fig. 3.1, process 3), whereas dynamically uplifted continents and subsided seafloor lead to eustatic fall.

To model the evolution of dynamic topography we compute global time-dependent thermochemical mantle convection using a modified version of the finite element code *CitcomS* (Zhong et al., 2008) to solve equations for the conservation of mass, momentum and energy under the extended Boussinesq approximation (Christensen and Yuen, 1985) with time-dependent boundary conditions derived from a tectonic reconstruction (Bower et al., 2015). The whole mantle is modelled as a spherical shell with depth-, temperature and composition-dependent viscosity and an initial temperature condition including an adiabatic profile between two thermal boundary layers (see Supplementary Section 3.7.2 for details). The input parameters used in our forward

flow models are taken from the preferred model of Flament (2019b), who investigated the sensitivity of mantle flow models to factors relevant for the prediction of dynamic topography and mantle structure. The initial condition and properties of the basal layer are modified over a series of three cases to assess the sensitivity of sea level change to mantle flow. Our reference case C1 (from 1000 Ma) included a warm-up phase (1200-1000 Ma), case C2 starts at 750 Ma and case C3 starts at 1000 Ma. The basal layer is less dense in case C2 (Supplementary Table 3.2).

We consider two types of air-loaded model topography, which we compute in 20 Myr intervals: the total topography (Flament et al., 2014) which results from all sources of buoyancy, and the long-wavelength dynamic topography (Fig. 3.4) which results from sources of buoyancy below 350 km, with lateral viscosity variations preserved above this depth (Flament, 2019b). Both quantities are computed with a free-slip boundary condition. The long-wavelength dynamic topography is used to calculate the mean dynamic topography of the oceanic and continental domains as defined by ocean floor age maps and the total topography is used to calculate the volume above oceanic trenches (Section 2.4). We scaled modelled trench volumes because the modelled present-day trench volume is ~8% less than the equivalent volume calculated using ETOPO1 (Amante and Eakins, 2009).

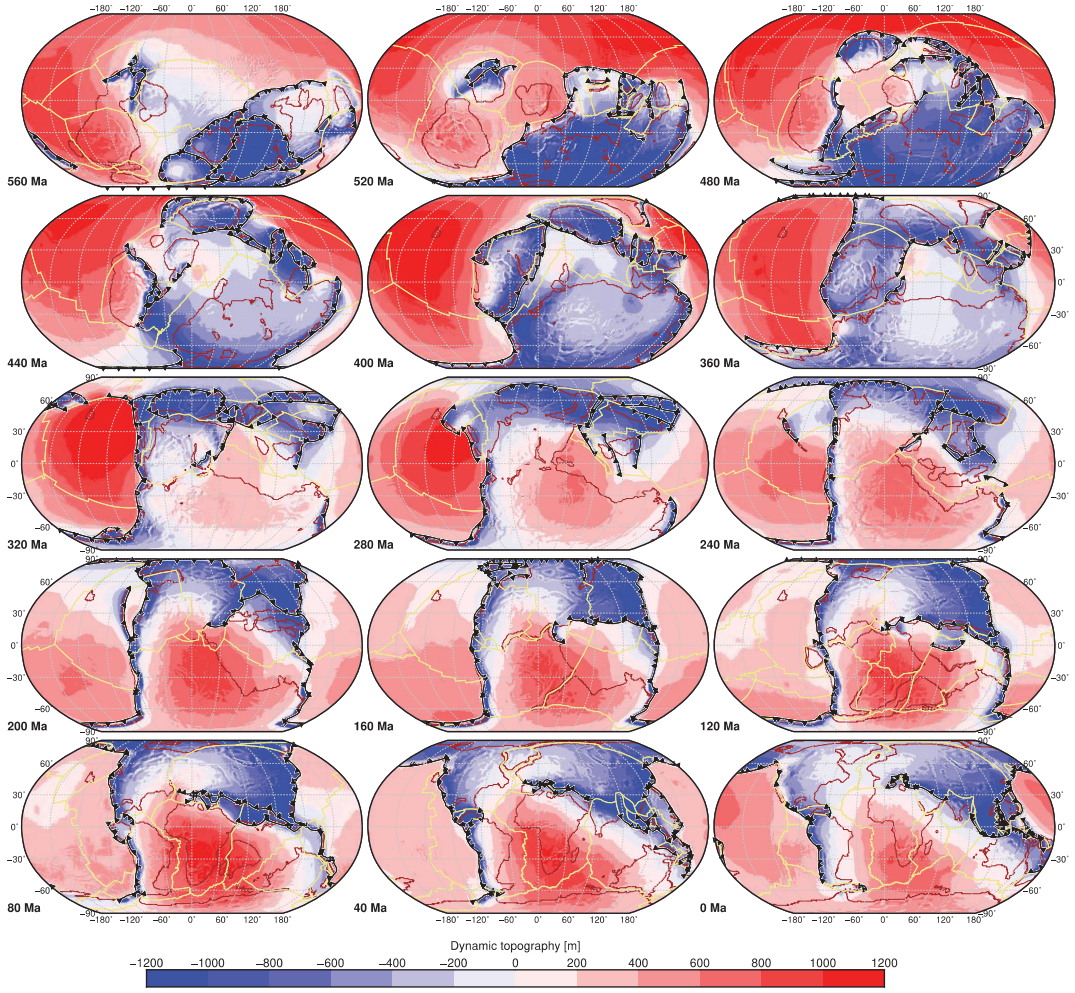

Figure 3.4: Modelled dynamic topography for flow model C1 from 560-0 Ma in 40 Myr increments, for sources of buoyancy deeper than 350 km, fee-slip boundary conditions and preserving lateral viscosity variations at all depths. Reconstructed subduction locations are shown as black lines with triangles on the overriding plate, reconstructed mid-oceanic ridges and transform faults in khaki, with continent-ocean boundary in brown.

3.2.4. Trench volume

To preserve mantle mass, Gurnis (1990a) proposed that changes in plate-tectonic spreading rates should be compensated at subduction zones. An increase in spreading rate forces old, thick oceanic lithosphere to subduct more rapidly, which enhances mantle downwelling and increases the negative topography above subducting slabs (Guillaume et al., 2016) (Fig. 3.1, process 4). In this way, the dynamic volume above trenches alters ocean basin capacity and may partially oppose the effect of ridge volume on eustasy (Husson and Conrad, 2006). However, numerical models demonstrate that a sustained increase in spreading velocity results in thinner, more buoyant subducting oceanic lithosphere and therefore shallower topography above the slab, resulting in sea level rise (Husson and Conrad, 2006). We investigate the time-dependent effect of trench volume on eustatic change by computing the reservoir capacity of the total model topography within 100 km, 300 km and 600 km of reconstructed trench locations.

3.2.5. Marine sedimentation

The accumulation of sediment on the continental shelves and deep ocean floor affects eustasy by altering the container volume of the ocean basin (Fig. 3.1, process 5). Modelling the evolution of marine sedimentation through time has previously been done by calculating sediment thickness as a function of oceanic crustal age and latitude (Müller et al., 2008) with recent studies incorporating the proximity to passive margins (Dutkiewicz et al., 2017). However, these methods tend to underestimate terrigenous sediment flux and sediment thickness on continental margins. Here, we use geostatistical modelling to estimate mean oceanic sediment thickness through time.

Assuming that (i) sediment accumulation has been greatest on continental shelves adjacent to passive margins (Fig. 3.5A) throughout time and (ii) that the present-day probability distributions of passive margin and abyssal plain sediment thickness (Fig. 3.5B) are representative of ancient sediment deposition patterns, a stochastic sedimentation model can be created for the time-dependent submarine area (Fig. 3.5C). This simple approach (described in detail Supplementary Section 3.7.3) will not account for the changing area of flooded continental shelves nor will it incorporate latitudinal sediment thickness variation, carbonate compensation depth or regional changes in terrigenous flux, yet it is a simple solution for estimating mean oceanic sediment thickness through time (Fig. 3.5E). Dutkiewicz et al. (2017) showed that the present-day river system contributes an anomalously large volume of sediment to the ocean; thus, the aforementioned approach may overestimate past sediment thickness on continental shelves. Therefore, we consider an alternative case in which maximum sediment thickness is constrained to 5 km (Fig. 3.5E).

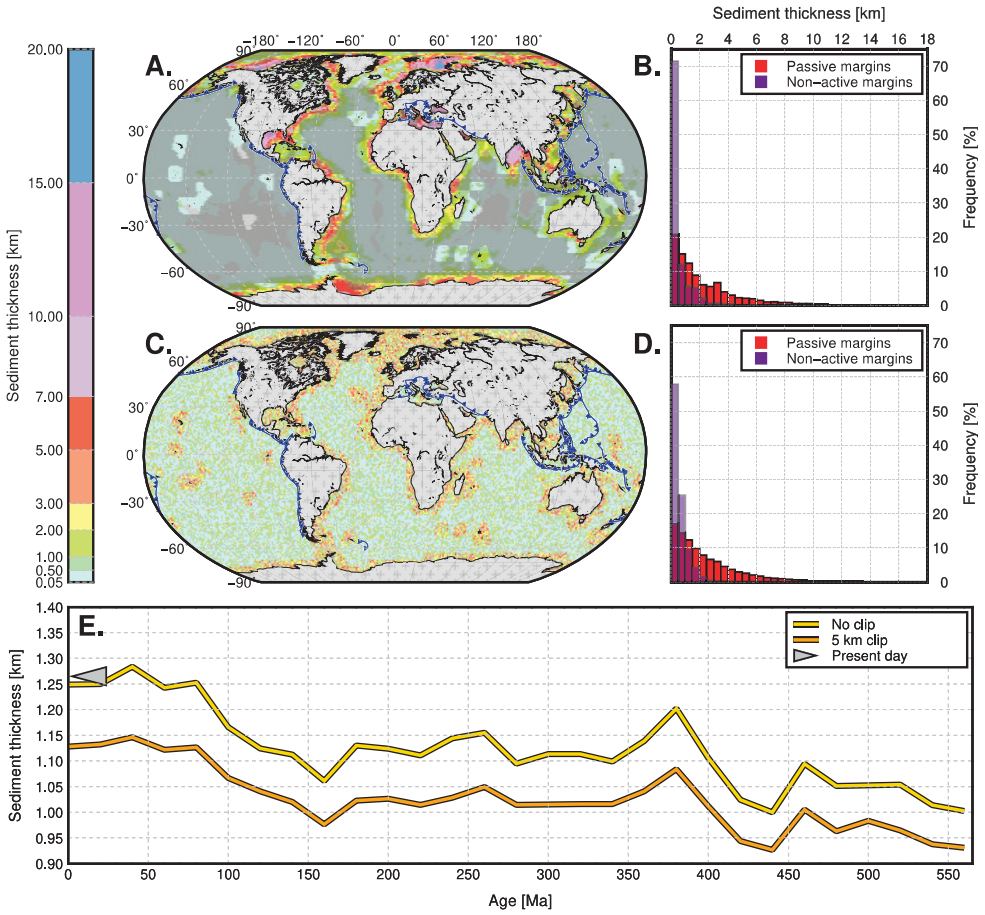

Figure 3.5: A: Present-day marine sediment thickness map (Straume et al., 2019) with subduction locations shown as blue lines with triangles on the overriding plate. The shading indicates sea floor that is not adjacent to a passive margin, whereas highlighted areas are within 400 km of passive margins. B: Frequency histograms of observed present-day sediment thickness from A; passive margin areas (highlighted areas in A) in red and non-active margins (shaded areas in A) in purple. C: Geostatistical model of submarine sediment for present day; colouring as in B. D: Modelled sediment thickness frequency histogram. Note the similarity between the frequency histograms of observed (B) and modelled (D) sediment thickness. E: Time-dependent modelled sediment thickness from 560-0 Ma. The grey triangle indicates present-day mean thickness from Straume et al. (2019).

3.2.6. Oceanic large igneous province emplacement

The emplacement of O-LIPs also changes the volume capacity of the ocean basin and thus impacts sea level (Fig. 3.1, process 6). To estimate this impact through time we calculate the present-day mean volume of individual O-LIPs > 0.1 Mkm^2 (Bryan and Ernst, 2008) using the databases of Whittaker et al. (2015) and Johansson et al. (2018). The average height of individual O-LIPs is determined as the difference between the modal depth to basement of the oceanic plateau and surrounding sea floor (Schubert and Sandwell, 1989) (Fig. 3.6).

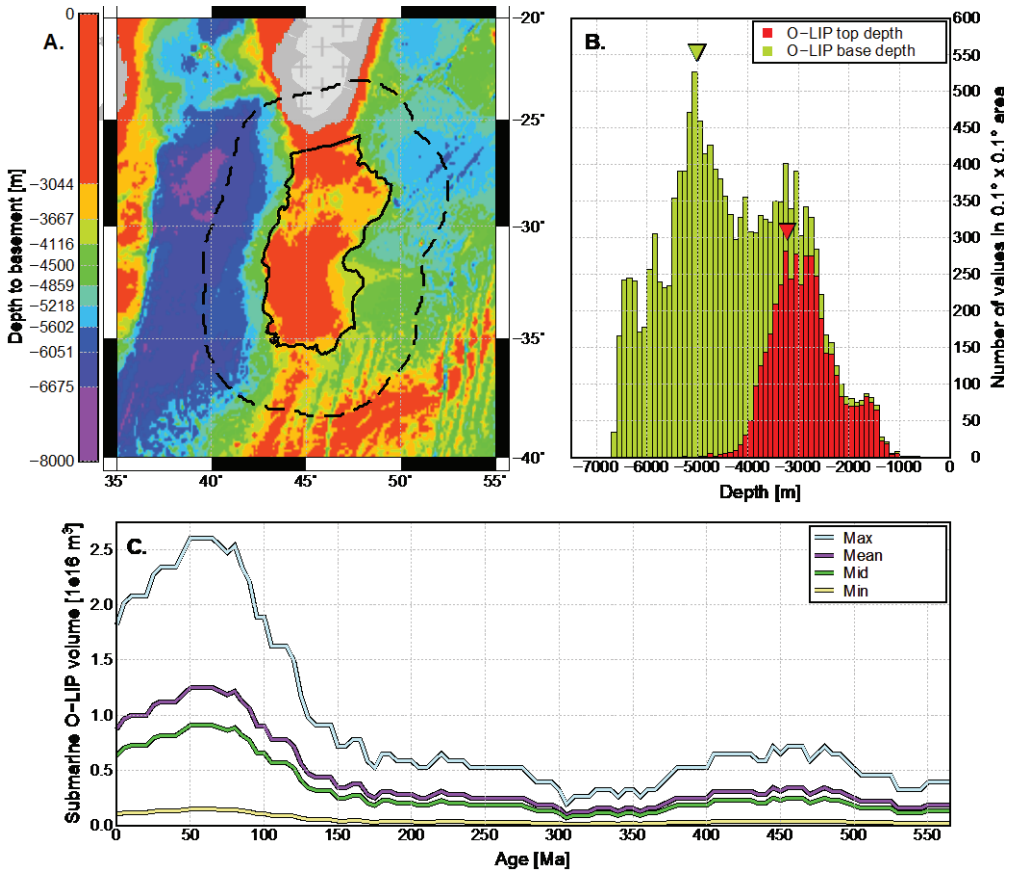

Figure 3.6: A: Present-day depth to basement surrounding the Madagascar O-LIP. B: Histogram showing elevation in 0.1° by 0.1° bins of the Madagascar O-LIP and surrounding seafloor within 300 m of the O-LIP. The peaks in the histograms, marked by the triangles, represent the top and base depth. C: Time dependent count of submarine O-LIPs on from 560-0 M, produced by performing a 120 Ma sliding window summation of the number of oceanic plume events from Doucet et al. (2020).

We build a time-dependent model of O-LIP volume using the Doucet et al. (2020) oceanic mantle plume occurrence record by summing plume occurrences over a 120 Myr sliding window so that the number of O-LIPs at a given time is equal to:

$$OLIP_n(t) = \sum_{t}^{t-120\text{Ma}} OLIP_n$$

where t is time. A cumulative distribution function of the present-day O-LIP volumes is used to determine minimum, maximum and middle volume estimates which are then multiplied by the O-LIP count in the record to give a total volume. This method (detailed in Supplementary Section 3.7.4) does not account for transient and/or permanent uplift of the seafloor associated with O-LIP emplacement (Wright et al., 2017) or for the influence of non-LIP submarine volcanism (Conrad, 2013).

3.2.7. Ancient hypsometries

Earth's hypsometry curve, which shows cumulative elevations of global topography by aerial distribution (Fig. 3.1), can be used to calculate the volume of water contained within the ocean basins. Any changes in this volume must be redistributed across the oceans and continental shelves. Indeed, if one assumes that Earth's ancient hypsometry was similar to present-day, the curve can be inundated with time dependent water volumes and changes in sea level estimated (Van der Meer et al., 2017).

Naturally, Earth's hypsometry changes during courses of tectonic cycles. Changes in the production

rate of ocean floor, in the type and age of continental margins, as well as uplift, erosion and the rifting and suturing of landmasses affect the shape of the hypsometry and play a role in determining sea level (Algeo and Wilkinson, 1991). Assuming a constant ocean water volume, if the slope of the continental hypsometry steepens, continental flooding would decrease and conversely, a flatter continental slope would increase continental flooding (Fig. 3.1, process 7). However, the absence of a record of ancient area-elevation distributions precludes the study of hypsometry evolution through time; therefore, hypsometric investigations of past sea level rely on proxy indicators.

Given that most models of Paleozoic sea level imply variations within a few hundred meters (+100 m to +400 m) relative to present day, the low-elevation portion of the continental hypsometric curve is most relevant to eustatic studies. We use the method of Algeo and Wilkinson (1991) – based on the principles of lithospheric cooling (old margins are steeper than young ones) – to determine the global hypsometric slope of the continental shelf since 560 Ma. The controlling parameters in the workflow (detailed in Supplementary Section 3.7.5) are the seafloor age at the continent-ocean boundary (COB), total continental area, and COB length, all of which are determined from the tectonic model and synthetic seafloor age maps.

We produce time-dependent global hypsometry models (Fig. 3.7) in 20 Myr increments by calculating area-elevation histograms of model air-loaded sea floor bathymetry (Fig. 3.3), which are scaled to match the present-day area of oceanic lithosphere. From the top of the ridge to the base of the continental shelf, the continental slope is modelled as a linear segment designed to fit present-day hypsometry from ETOPO1 (Eakins and Sharman, 2012). The hypsometric slope is used to model the low-elevation portion of the continental hypsometric curve from the top of the continental shelf to +200 m. The present-day hypsometry is used for elevations greater than +200 m. The modelled curve is a good match with the ETOPO1 hypsometry on the continental slope and shelf and into the high-elevation portion of the curve (Fig. 3.7). The mismatch between the modelled and observed bathymetry is expected because the simple plate cooling model (Richards et al., 2018) excludes anomalously thick and shallow crust such as oceanic plateaus and seamounts. We consider the half-space cooling model and the complex plate cooling model (Richards et al., 2018) as other scenarios for paleobathymetry.

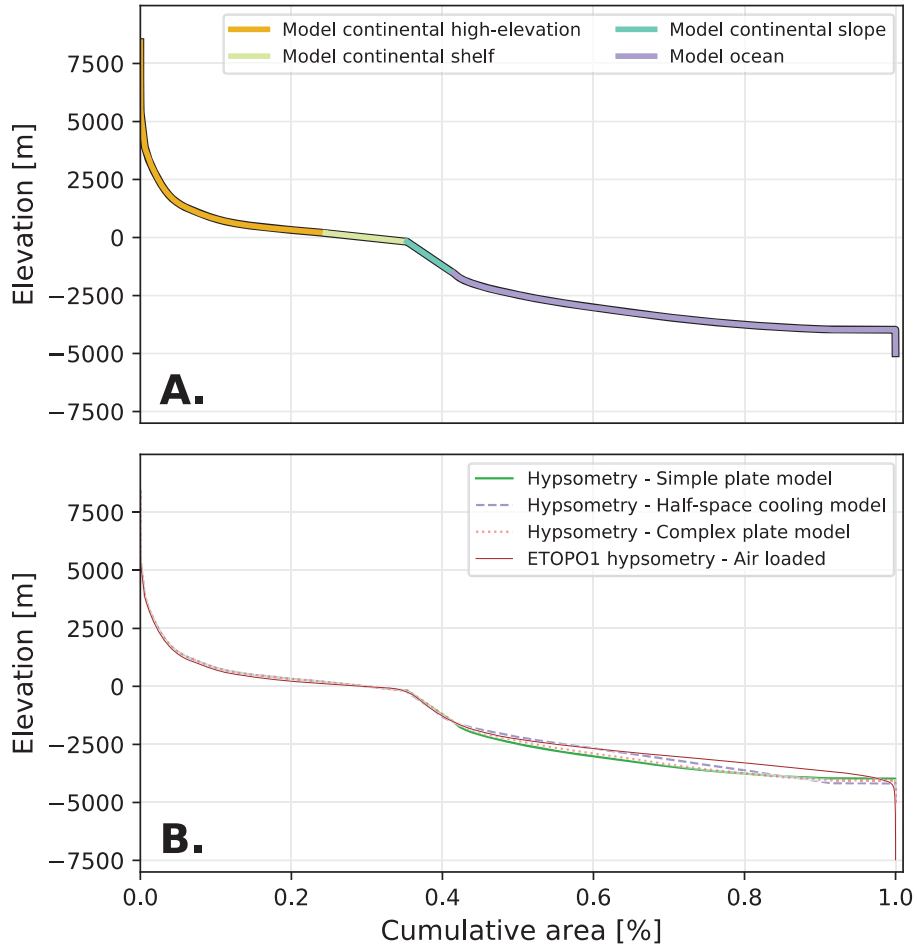

Figure 3.7: A: Example present-day air-loaded model hypsometry depicting its different components: high-elevations (>200m); the model shelf between 200 m and -140 m with slope determined using the method of Algeo and Wilkinson (1991); the continental slope modelled as a linear segment to the top of the MOR (-1533 m) and for depths greater than the ridge depth, the bathymetry model. B: comparison between model air-loaded hypsometry using: Pm; plate cooling model and HSCm; half-space cooling model paleobathymetry and Earth's present-day air-loaded hypsometry from ETOPO1 (Eakins and Sharman, 2012).

3.2.8. Water loading

We determine eustatic change in 20 Myr intervals. To do this, air-loaded dynamic topography at time t is used to modify the elevation of the oceanic and continental domains of the corresponding air-loaded hypsometric curve. The reconstructed topography is then iteratively flooded (Flament et al., 2008) to compute sea level for a target volume of water; V_t, which is the present-day capacity of the ocean augmented by contributions from deep-water cycling, sedimentation, volcanism and trench capacity. In this process, the volume of the time dependent oceanic reservoir is calculated using:

$$V_h = \int_{A_f}^{1} z \; dA$$

where A_f is the cumulative area of emerged continents and z is depth. If V_h is greater than V_t an alternative contour below 0 m is used to find A_f and V_h is recalculated. Sea level was determined by isostatically compensating (Parsons, 1982) the contour that gives $V_t = V_h$ (Fig. 3.8).

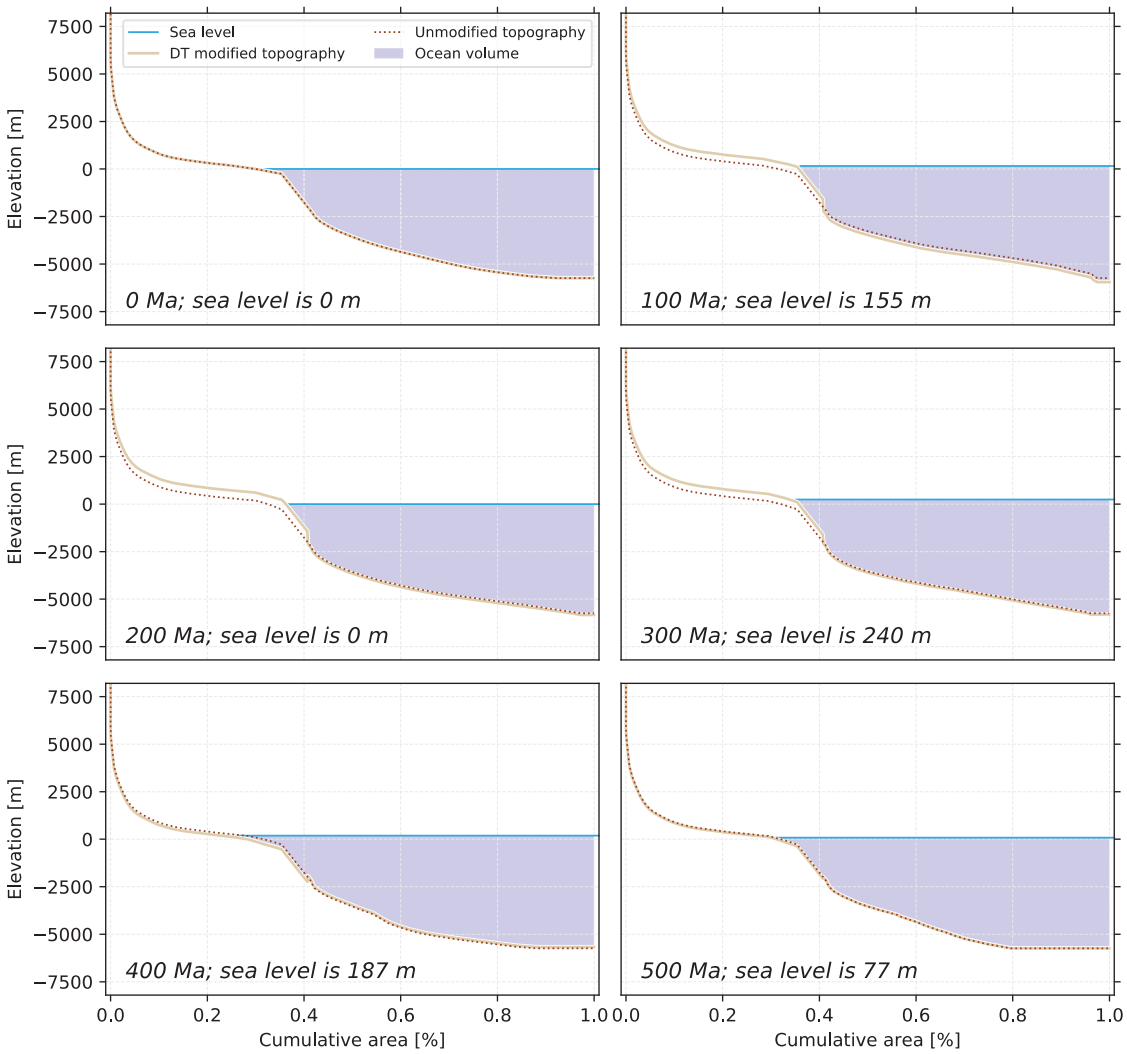

Figure 3.8: Results for hypsometry and sea level in 100 Myr increments. Note the comparison between model and ETOPO1 hypsometry at 0 Ma (Eakins and Sharman, 2012). For each timestep the modelled isostatic topography is modified by dynamic topography, flooded and water loaded with the present-day water volume corrected for volumes from the deep-water cycle, trench topography, sediment and O-LIPs. Global sea level is the intersection between the ocean surface (light blue) and the topography (khaki).

3.4. Results: Global sea level estimates

We compute sea level since 560 Ma using the approach outlined above. The results suggest that global sea level fluctuated between -200 m and 300 m throughout Phanerozoic times (Fig. 3.9A). The curve displays the Cretaceous and Devonian sea level highs and the Triassic low which are characteristic of first-order sea level reconstructions and well recognised in paleogeographic studies (Golonka et al., 1994; Scotese and Golonka, 1997; Blakey, 2008). Our results lie in the low range of published sea level estimates from present day to Triassic times as well as during Early Paleozoic times, and are approximately midway between previous estimates for Late Paleozoic times (Fig. 3.9A).

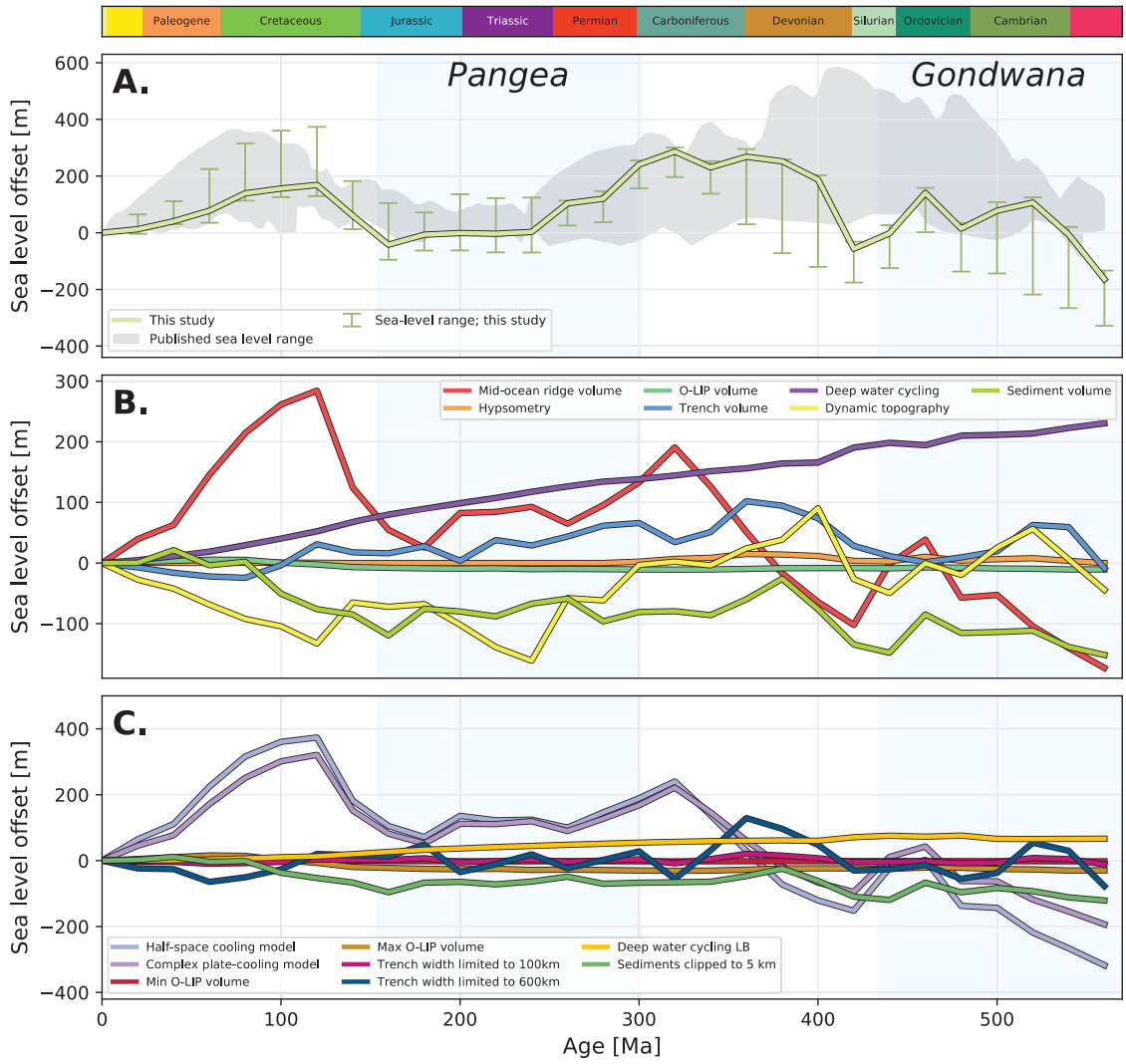

Figure 3.9: A: Model sea level fluctuations with respect to present-day compared to several previous studies (Vail et al., 1977; Hallam, 1984; Algeo and Seslavinsky, 1995; Kominz et al., 2008; Müller et al., 2008; Snedden and Liu, 2010; Vérard et al., 2015; Van der Meer et al., 2017) shown collectively as a grey envelope. B: Breakdown of the major sea level changing mechanisms and their estimated effect on sea level. C: alterative scenarios, half-space cooling model: paleobathymetry calculated using a half-space cooling model as opposed to a plate model; O-LIP min and max volume: sea level offset calculated using time dependent minimum and maximum O-LIP volume models (Fig. 3.6c); trench width limited to either 100 km or 600 km: sea level offset if trench volume is determined from model total topography within 100 km and 600 km of reconstructed trench locations; deepwater cycling LB: long-term balance scenario in which the net water flux to the ocean over the past 230 Myr is 0 kg/yr. Maximum sediment thickness 5 km: modelled sediment thickness is limited to a maximum of 5 km (Fig. 3.5e).

As part of our analysis, we isolate the time-dependent contributions of the major solid Earth mechanisms related to sea-level change (Fig. 3.9B). The results demonstrate the eustatic cycle is primarily driven by volumetric changes to the reservoir below the MOR system (460 m), with secondary contributions from dynamic topography (250 m), deep-water flux (230 m), marine sedimentation (170 m) and the volume capacity of trenches (130 m) (Fig. 3.9B). The first-order cycles recognised in our sea level curve have time durations > 100 Myr and appear to be associated with the break-up and amalgamation of supercontinents.

During both Pangea assembly (~420-300 Ma) and break-up (~160-0 Ma) modelled global spreading rates increased, the ocean floor shallowed, sediment thickness increased, and sea level rose (Fig. 3.9). The Devonian-Carboniferous eustatic high was significantly amplified by dynamic topography, trench volume and sedimentation (Fig. 3.9). During these times, the effects of mantle flow on continental and oceanic topography offset sea level by approximately 100 m and a decrease in the volumetric capacity above trenches augmented

sea level rise by 100 m. A sedimentation influx associated with an increase in rifting during middle Paleozoic times resulted in an additional 120 m of sea level increase (Fig. 3.9B).

After the low point during the Early Devonian, continental dynamic topography rose steadily through Late-Paleozoic, lowering sea level. However, increased modelled global spreading rates – inferred from elevated continental plate velocities (constrained by paleomagnetic data) at these times (Young et al., 2019, Chapter 2) – offset this eustatic sea level fall. Between ~300-160 Ma sea level decreased by 230 m due to declining rates of new oceanic lithosphere production, increased continental dynamic topography and trench volume (Fig. 3.10). In the modelled tectonic scenario, increases in the length of the spreading ridge system and seafloor production during the Gondwana break-up (~160-140 Ma) shallowed the oceanic bathymetry. Increased seafloor spreading created passive margins and additional accommodation space resulting in greater volumes of submarine sediment. In combination, these mechanisms overcame 100 m of eustatic fall due to dynamic topography during the break-up event (Fig. 3.9B). Global sea-floor production rates declined during the Late Cretaceous resulting in a large amplitude sea level fall. Contemporaneously, dynamic topography uplifted the seafloor by 90 m and subsided continents by 380 m (Fig. 3.10C), partially offsetting the eustatic fall.

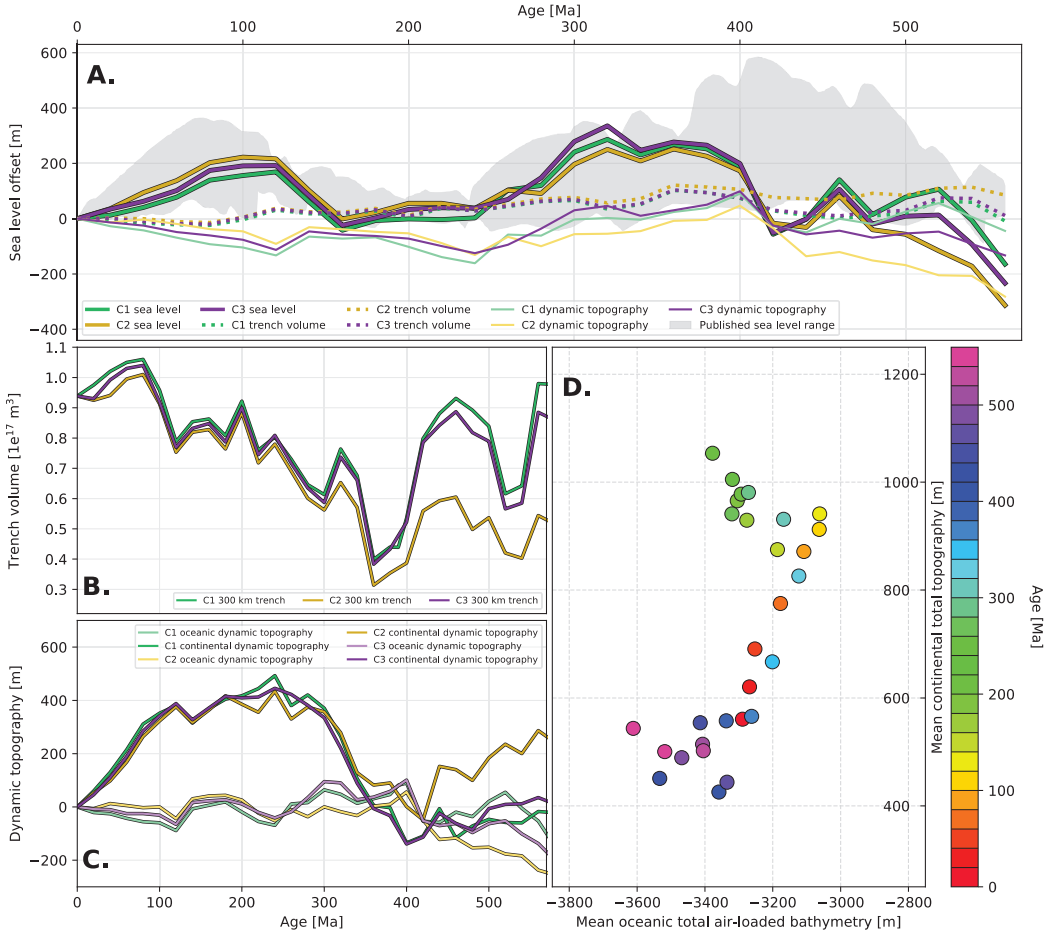

Figure 3.10. A: Comparisons of predicted sea levels from alternative flow models; C1, case 1 (reference); C2, case 2 and C3, case 3 (see Supplementary Table 3.2). B: Different trench volumes computed from the three flow models. Volumes calculated within 300 km of trench locations and have been scaled to present-day observations using ETOPO1 (Amante and Eakins, 2009). C: Average continental and oceanic dynamic topography computed with respect to present day for all flow model cases. D: Scatter plot of the mean continental total topography (isostatic and dynamic component) and mean oceanic total bathymetry coloured by age for flow model C1. Note that although ocean basin shallowing is not associated with continental subsidence, the sea level rise produced by increasing spreading rates and/or MOR length corresponds to periods of elevated continental topography (Fig. 3.10a).

The evolution of continental hypsometry throughout the Phanerozoic results in up to 20 m of eustatic rise. During times of dispersal, rifting intensifies resulting in a lengthening of passive margins, resulting in a gentler global slope of continental shelves which enhances continental flooding and thus raises sea level. In the assembly phase, rifting is less common and continental collisions destroys existing passive margins; the global hypsometric slope steepens, decreasing continental flooding and causing sea level to fall (Fig. 3.9). During the late Paleozoic (~300 Ma) the steepening of the global hypsometric slope resulted in 10 m of eustatic fall. During the Triassic the breakup of Pangea resulted in a flattening of the global hypsometric slope causing 10 m of eustatic rise.

Through the Phanerozoic changes to oceanic volume caused by the emplacement of O-LIPs resulted in 20 m of eustatic fluctuation (Fig. 3.9B). From 560-140 Ma O-LIP activity uniformly lowers sea level by ~10 m. After 140 Ma an increase in O-LIP activity resulted 20 m of eustatic rise. A decrease in submarine volcanism from 60 Ma to present-day corresponds to 10 m of sea level fall.

By applying the workflow of Karlsen et al. (2019) to our tectonic reconstructions, we calculate the time-dependent magnitude of sea level change related to the deep-water flux from 560-0 Ma (Fig. 3.9B). If, as Karlsen et al. (2019) established, regassing dominates over degassing, the sea level drop caused by ocean-mantle water exchange may have be as large as ~230 m since Cambrian times.

3.5. Discussion

3.5.1 Comparison with other sea level models

We have developed a new model of solid Earth contributions to long-term sea level change utilising time-dependent hypsometry models. The workflow allows us to isolate and quantify the amount of sea level change contributed by individual solid Earth mechanisms since 560 Ma, including, for the first time: time-dependent dynamic topography, the volumetric capacity of trenches and the changing shape of continents. Our results are similar in trends and magnitude changes compared to published sea level reconstructions from Devonian times to present day, with discrepancies occurring in older periods.

Numerous published sea level models have established the first-order eustatic paradigm: sea level highs in Cretaceous and majority of Paleozoic times are bound by lowstands in the Cambrian, Triassic and at present day (Fig. 3.9A). Our model demonstrates close alignment with the Cretaceous high and Triassic low as well as the later stages of the Paleozoic high and the earliest Paleozoic low. However, between 440-400 Ma our results are at odds with previous studies. In our reconstructed sea level curve, three solid earth mechanisms combine to drive a eustatic fall during Silurian times. In order of descending impact these mechanisms are changes in marine sedimentation (-200 m), MOR volume (-100 m) and dynamic topography (-40 m) (Fig. 3.9B).

Our model follows a tectonic scenario in which Late Silurian MOR length and spreading rates were low, causing the production of new oceanic lithosphere to slow down and the ocean basins to age and subside, increasing ocean basin volume and lowering sea level. The cause of decreased ridge length and spreading rates is four-fold. Firstly, spreading velocities in the large Panthalassa Ocean were low during Late Silurian times to align global Paleozoic plate kinematics with estimates for recent times (Young et al., 2019, Chapter 2). Secondly, the Late Silurian northward-directed subduction of the Rheic Ocean beneath Laurussia consumed part of a spreading ridge. Thirdly, the cohesion and unity of continental blocks during the Late Silurian resulted in

fewer passive margins and less marine sedimentation (Bradley, 2008). Fourthly, our mantle flow model suggests global mean oceanic dynamic topography was lower than at present.

A fundamental outcome of this work is the isolation and quantification of sea level change contributed by individual solid Earth mechanisms since 560 Ma, allowing us to evaluate how these processes have impacted eustasy over the evolutionary cycle of supercontinent Pangea. The relationship between eustasy and supercontinents has been contemplated since the early 1980's (Fischer et al., 1984; Worsley et al., 1984), the aggregation and dispersal of which is thought to particularly affect ridge volume and dynamic topography (Worsley et al., 1984; Conrad and Husson, 2009; Conrad, 2013). However, until now, it had not been possible to model the relationship, since time-dependent tectonic reconstructions, seafloor age distributions and mantle flow models did not exist over such timescales. Our results confirm the ideas of Worsley et al. (1984), Conrad and Husson (2009) and Conrad (2013) that: (i) during supercontinent assembly, seafloor aging and subsidence leads to eustatic fall while during fragmentation, increased rifting decreases the average age of the oceanic crust leading to shallower ocean basins and higher sea level and, (ii) that dynamic topography causes sea-level rise during supercontinent aggregation and dispersal, and sea-level drop for the time period over which a supercontinent is assembled (Fig. 3.9B).

3.5.2. Continental hypsometry, trench volume, dynamic topography, and sea level

Previous studies have investigated the effects of continental hypsometry (Algeo and Wilkinson, 1991; Rowley, 2017), trench volume (Husson and Conrad, 2006) and dynamic topography (Spasojevic and Gurnis, 2012) on eustasy; however, the impact of these mechanisms has not yet been considered in combination. An integrated approach using geologically and geophysical constrained inputs, such as ours, provides significant insights regarding the time-dependent impact of these mechanisms.

Firstly, through the course of the assembly and dispersal of a supercontinent, we find that the global mean hypsometric slope changes by approximately 50 percent, somewhat less than proposed by Algeo and Wilkinson (1991) who developed a theoretical model to examine the changes in coastal hypsometry over a 300 Myr plate tectonic cycle and found that hypsometric slope changes by a factor of 2-3. Despite differing magnitudes, our hypsometry model matches theirs in describing the evolution of hypsometric slope through a plate tectonic cycle: increase in hypsometric slope during initial rifting, progressive decreases during the rift-drift phase and then return to the pre-rift value (Fig. 3.9B). We thus confirm that the potential of a landmass to flood is greater at the end of a rift-drift phase than at the beginning (Algeo and Wilkinson, 1991).

A concept originally proposed by Hager (1980) and later developed by Gurnis (1990a) is that increased negative topography above more rapidly subducting slabs might compensate or overcome the effect of increased ridge volume associated with faster spreading rates. Husson and Conrad (2006) developed a dynamic model based on boundary layer theory (Bercovici et al., 2000) in order to evaluate this hypothesis. They showed that variations in trench topography due to plate motions typically alters ocean basin volume by <10% and may cause up to 80 m of sea level change. Additionally, they determined that sea level rise due to an increase in plate velocity will be augmented, not compensated, by the accompanying variation to trench topography. Our model agrees with the findings of Husson and Conrad (2006): the results suggest that since 560 Ma the topography above subducting slabs has altered the reservoir capacity of the oceans by 6-22 percent (average 13%), causing > 120 m of sea level change. We also find that as average ridge spreading velocity increases, trench volume

decreases, supporting the conclusion of Husson and Conrad (2006) that changes to ocean basin volume due to faster spreading rates are not compensated by increased trench volumes above more rapidly subducting slabs.

To counteract the effect of increased ridge volume associated with faster spreading rates, Rowley (2017) proposed an alternative hypothesis: that changes in the mean elevation of the oceans must be balanced by an opposite change in large-scale continental dynamic topography. Our workflow, which combines sea floor bathymetry, trench topography and dynamic topography of the oceanic and continental regions makes it possible to test this hypothesis back to 560 Ma. We computed the mean air-loaded continental total topography (dynamic and isostatic components) and the mean air-loaded oceanic total bathymetry. If the aforementioned hypothesis is valid, a strong negative correlation would be expected between mean continental total topography and mean total oceanic bathymetry.

Our results indicate the opposite: when continents are in a dispersed state (e.g., between 500-400 Ma and in the last 100 Ma) the average age of the ocean floor is relatively old, and the oceans are deep (Fig. 3.10D). In this state of dispersal, many parts of the continents have overridden "slab burial grounds" associated with subduction that occurred around the perimeter of a supercontinent; thus, there is a net subsidence of the continents between supercontinent assembly and mature dispersal. Contrary to the hypothesis of an increase in continental dynamic subsidence when seafloor spreading is faster (Rowley, 2017), our results suggest that shallow oceans are related to relatively high (~900 m) continental elevations (Fig. 3.10D). This is because ridges speed up when supercontinents start breaking-up, and that supercontinents are generally underlain by large-scale upwellings that generate positive dynamic topography (Li and Zhong, 2009; Conrad, 2013)

There are two recognised mechanisms by which dynamic topography can change sea level (Conrad and Husson, 2009). Firstly, mantle flow controls dynamic topography: e.g., as a slab sinks deeper in the mantle, the associated negative dynamic topography decreases over time, resulting in surface uplift and sea level fall. Secondly, plate motions can redistribute dynamic topography; a continent moving laterally over a region of negative dynamic topography causes continental subsidence and relative sea level rise: e.g., Australia's motion over a dynamic topographic low resulted in widespread subsidence and continental flooding during Cretaceous times (Gurnis et al., 1998). To model the time dependent contribution of dynamic topography on eustasy Conrad (2013) used a plate motion model to move continental blocks over a present-day map of dynamic topography and found that sea level could have increased by ~190 m since 140 Ma. This approach ignores fluctuations in dynamic topography due to changes in mantle flow. Spasojevic and Gurnis (2012) used a series of instantaneous mantle flow models linked to plate reconstructions to calculate oceanic and continental dynamic topography and ocean floor bathymetry at given ages, which they combined with isostatic topography to compute continental flooding and global sea level. Our approach shares similarities to the method developed by Spasojevic and Gurnis (2012) in that it considers changes in mantle flow, however it differs in being a forward, time-dependent method whereas theirs was a method combining backward advection of tomography and slabs imposed from tectonic reconstructions back to 90 Ma. Our model predicts approximately 100 m of sea level rise due to dynamic topography since 100 Ma, which is consistent with the 100-200 m of eustatic rise since 90 Ma estimated by Spasojevic and Gurnis (2012).

3.5.3. Model limitations and uncertainties

Our sea level calculations are subject to significant uncertainties. Indeed, all of the sea level mechanisms investigated here use a tectonic reconstruction and the associated seafloor ages as input. The uncertainties inherent to the reconstruction model (e.g., spatial and temporal distribution of spreading ridges, subduction zones and continental blocks, plate and mid-oceanic ridge spreading velocities, and presence of back-arc basins and passive margins) are propagated throughout the workflow. Due to a paucity of marine geophysical evidence, there is large uncertainty in the age distribution of the ocean floor for times before 180 Ma (Rowley, 2002; Müller et al., 2016a). Consequently, plate and spreading velocities rely on paleomagnetic data as well as: episodes of volcanism and metamorphism; correlations of palynology and paleogeography data and, geodynamic criteria including tectonic speed limits and trench kinematics (Williams et al., 2015; Zahirovic et al., 2015). Williams et al. (2021) investigated how changes in ridge spreading velocities may affect sea level by forcing the mean velocity in of synthetic oceanic plates within Panthalassa to maintain constant values between 50 mm/yr and 200 mm/yr. Their results suggest that changes in the kinematics of synthetic oceanic plates could change sea level by up to 300 m over the past 400 Myr. Furthermore, the destruction of ancient sea floor means that past spreading asymmetries and back-arc basins are unconstrained. Wright et al. (2020) showed that past spreading asymmetries and back-arc basins could have changed sea level over the past 200 Myr by ~150 m and ~120 Myr, respectively.

Temporal changes in ocean basin volume are the main uncertainty. In addition to the substantial uncertainty inherent to tectonic reconstructions of destroyed seafloor, the reservoir capacity of ocean basins varies significantly based on which cooling model is used to calculate bathymetry from sea floor age (Fig. 3.9C). To ascertain how this decision may impact sea level calculations, we ran two alternative cases in which seafloor depths were calculated using a half-space cooling model and a complex plate model (Richards et al., 2018). We find that sea level calculated using the half-space model is typically ~30 m higher than determined using the simple plate cooling model (Fig. 3.9C), and ~20 m higher for the complex plate cooling model. For ages younger than ~60 Myr there is no difference in the ridge volume predicted by the half-space cooling model and plate model. Therefore, during Cretaceous times, when the seafloor age distribution was skewed towards younger ages, the ridge volume calculated using the alternative scenarios is similar. However, at present day, the seafloor age distribution is skewed towards older ages and the half-space cooling model predicts greater ridge volume than the plate model. Therefore, the relative difference between Cretaceous and present-day ridge volume is greater for the half-space cooling model and so the calculations yield a greater eustatic rise.

When compared to the simple plate model, initial subsidence rate of the complex model is smaller while at older times the sea floor is deeper and subsidence rates are greater. The complex model therefore produces a present-day ocean basin volume that is deeper than that computed using the simple plate cooling model but, less than that computed using the half-space cooling model. Thus, although the complex model produces shallower seas in the Cretaceous the eustatic change is compensated by deeper seas at present day resulting in a relative difference that is between the half-space cooling model and the simple plate model.

Given the substantial uncertainty regarding the time dependence of mantle flow patterns and the absolute motions of continents relative to the deep mantle, dynamic topography is also uncertain. Key input parameters include model start time, preservation of lateral viscosity variations and depth above which sources of buoyancy are ignored (Flament, 2019b). We compute long-wavelength dynamic topography from sources of

buoyancy deeper than 350 km, despite the uppermost mantle contributing to the present-day dynamic topography (Hoggard et al., 2016; Davies et al., 2019). Reconstructing asthenospheric mantle flow and the associated dynamic topography back in time remains a challenge, although recent models of the thickness of the continental lithosphere (Richards et al., 2018) provide opportunities for future work in that space. We note that the present-day dynamic topography (Fig. 3.4) calculated from the flow model is consistent with previous work which shows a pattern of long wavelength negative dynamic topography in Southeast Asia, the Mediterranean and South America as well as positive dynamic topography in the Pacific Ocean and over Africa (Conrad and Husson, 2009; Spasojevic and Gurnis, 2012). In experimenting with the flow model initial conditions, we find that the resultant dynamic topography is primary controlled by the model start age (Fig. 3.10). A 750 Ma start age in Case 2 results in lower trench volume (Fig. 3.10B), and higher continental and lower oceanic dynamic topography (Fig. 3.10C) with respect to present day. This discrepancy is because the flow models take ~200 Myr to reach a dynamic equilibrium; therefore, the buoyancy forces that drive the flow model and produce the dynamic topography are less developed relative to the alternative cases (with older start times). Lower trench volumes predicted by Case 2 produce greater sea level rise in the early Paleozoic compared to the other cases, however, dynamic elevation of the continents and oceans offsets this rise (Fig. 3.10A). The total topography model used to calculate trench volume is obtained using the consistent boundary flux method (Zhong et al., 1993) for a rigid surface. The computed volume above trenches is withing 8% of the observed volume, which is reasonable and could be further refined by implementing a free surface algorithm (e.g. Kramer et al., 2012).

Considering its impact on sea level change since 560 Ma, temporal changes to the average thickness of marine sediments represents another major uncertainty. We tested an alternative case in which maximum sediment thickness is equal to 5 km to assess some of the uncertainty in our sedimentation model. This scenario changes sea level by up to ~30% (Fig. 3.9C). Additional uncertainty applies to controls on sedimentation which we have not considered here including: tectonic, chemical, biological, and climatic drivers; although constraining these for past times is a challenge. Despite its relative simplicity, our sedimentation model produces a first order trend in good agreement with previous studies (Müller et al., 2008; Conrad, 2013; Dutkiewicz et al., 2017).

3.6 Conclusion

We have developed a new holistic method to model sea level change that accounts for the main solid Earth drivers of eustatic rise and fall. Using our workflow, we forward modelled, for the first time, time-dependent sea level change driven by the changing shape of continents, volume of trenches and dynamic topography back to 560 Ma. Additionally, we isolated and quantified the component of first order sea level change attributed to variations in MOR volume, deep water recycling, dynamic topography, submarine sedimentation and OLIP emplacement.

Our reconstructed sea level curve predicts sea level highstands in the Cretaceous and late Paleozoic and lowstands in the early Mesozoic and early Paleozoic. Our results suggest that first-order volumetric changes to the ocean basins driven by changes in spreading rate and ridge length may have resulted in sea level fluctuations by up to 460 m over Phanerozoic times. Dynamic topography (250 m), the deep-water cycle (230 m), marine sedimentation (170 m) and the volume capacity of trenches (130 m) represent the dominant secondary contributors to eustasy. Additionally, we demonstrate that changes to ocean basin volume due to faster

spreading rates and/or ridge extent are not compensated by increased trench volumes above more rapidly subducting slabs or by large-scale dynamic subsidence of the continents. Temporal changes to continental shelf slope and isostatic topography have a negligible (~20 m) effect on the long term eustatic cycle. We find that Phanerozoic sea-level trends correlate with supercontinent tectonics and demonstrate a relationship between higher sea levels during supercontinent dispersal and sea level fall during periods of supercontinent assembly.

3.7 Supplementary material

The following details of the workflow previewed in the main text and provides some context to the workflow code and data which we have made available as Python Jupyter Notebooks https://doi.org/10.5281/zenodo.3924869. The version of *CitcomS* used in this research, described in Bower et al. (2015), is available from https://github.com/EarthByte/citcoms.

3.7.1. Deep water cycling

The time dependent ocean mass of water was calculated using the workflow of Karlsen et al. (2019). To calculate the deep-water flux, subduction zone and mid-ocean ridge (MOR) segments were extracted from the plate reconstruction at 10 Myr increments and were resampled at regularly spaced 1 arc degree intervals. Convergence rate, spreading rate, plate age and segment length were then calculated for each point.

In order for water to be recycled in the mantle, a slab must retain water at large depths (> 200 km). Water retention is dependent on the thermal structure of the subduction zone, which is controlled by the descending slabs initial temperature profile and the kinematics of subduction. To model subduction water flux, relative slab water retention ϵ was described as a function of the slab thermal parameter Φ, which is equal to the plate convergence rate time the plate age. Following Karlsen et al. (2019) ϵ was calculated as:

$$\epsilon = \max\left(0, a + b(1 - e^{-c\Phi})\right)$$

Karlsen et al. (2019) determined a = -0.1, b = 0.5 and c = 0.0023 by fitting the fraction of water retained at > 200 km depth following the slab dehydration study of Rüpke et al. (2004).

Karlsen et al. (2019) considered three scenarios for deep water recycling and used the net water flux into the mantle to determine the initial bulk water content of plates, α (nondimensional). Karlsen et al. (2019) constructed the cases by fixing the degassing parameter, γ (nondimensional), to obtain a present-day degassing rate equal to $2.0 \cdot 10^{11}$ kg/yr. In our study we considered a long-term balance (LB) defined as:

$$\int_0^{230\ \mathrm{Ma}} R(t) - D(t)\ \mathrm{d}t = 0$$

and a regassing dominated (RD) scenario, defined as:

$$R(0\ \mathrm{Ma}) = 3.5 \cdot 10^{11}\ \mathrm{kg/yr}, \mathrm{D}(0\ \mathrm{Ma}) = 2.0 \cdot 10^{11}\ \mathrm{kg/yr}$$

where R is the rate of water entering the mantle, D is the rate of water leaving the mantle and t is time. For the long-term balance scenario $\alpha = 2.28 \times 10^{-3}$ and for the regassing dominated scenario $\alpha = 1.07 \times 10^{-3}$ In each case $\gamma = 3.15 \times 10^{-3}$.

The volume of water entering the mantle at each subduction zone point was calculated by multiplying α with ϵ, upper mantle density (3,200 kg/m^3), plate thickness, subduction velocity and segment length. Global water subduction flux was then calculated by summing over the segments. The amount of water expelled at mid-ocean ridges was calculated by multiplying γ by upper mantle density, mean oceanic crust thickness (7 km),

ridge spreading velocity and segment length and summing over all the segments. Time-dependent ocean mass is the difference between the water subduction flux and the water expelled at mid-ocean ridges.

The major assumptions in this workflow are (i) that the degassing rate at mid-ocean ridges is proportional to the sea floor production rate, (ii) the melting zone beneath all the mid-ocean ridges contains the same amount of water, and (iii) that at present day, there is a significant net flux of water into the mantle (Karlsen et al., 2019). The model does not explicitly consider chemical reactions or transfers.

The notebooks *Make_SubZone_and_MOR_stats.ipynb* and *Calculate_DeepWaterFlux.ipynb* were used to calculate the time dependent ocean mass of water; see https://doi.org/10.5281/zenodo.3924869.

3.7.2. Past mantle flow and dynamic topography

We ran 3-D numerical models of past global mantle flow using the convection modelling code *CitcomS* (Zhong et al., 2008). Global plate velocities, subducting slabs and lithospheric variations were extracted from the no-net-rotation tectonic reconstruction and applied as the surface boundary conditions in 1 Myr increments (Bower et al., 2015). At the base the model boundary condition was free slip. We solved equations for the conservation of mass, momentum and energy under the Extended-Boussinesq approximation. The governing equations were the same as in Hassan et al. (2015). Slab geometries were progressively assimilated in 1 Myr increments according to the location and polarity of subduction zones on the surface (Bower et al., 2015). In the initial condition slabs were inserted down to a depth z_{slab}^{i} (initial slab depth) with a dip equal to 45°.

The mantle was modelled globally as a spherical shell consisting of $129 \times 129 \times 65 \times 12 \approx 13 \times 10^6$ nodes, which gives a resolution of $\sim 50 \times 50 \times 15$ km at the surface, $\sim 40 \times 40 \times 100$ km in the mid-mantle and $\sim 28 \times 28 \times 27$ km at the core-mantle boundary (CMB). The Rayleigh number which determines the vigour of mantle convection is defined by:

$$Ra = \frac{\alpha_0 \rho_0 g_0 \Delta T h_M^3}{k_0 \eta_0}$$

where α is the coefficient of thermal expansivity; ρ, density; g, acceleration of gravity; ΔT, temperature change across the mantle; h_M, mantle thickness; κ, thermal diffusivity; η, viscosity. and the subscript "0" indicates reference values listed in Supplementary Table 3.1. The effect of viscous dissipation was considered in the conservation of energy, and the dissipation number was set equal to 1.56 as in Flament (2019b). The dissipation number is defined as $Di = \alpha_0 g_0 R_0 / C_{P_0}$ where C_p is heat capacity and R_0 is the radius of the Earth.

We used depth-dependent temperature, viscosity and rheology. Mantle viscosity varied with temperature and depth following:

$$\eta = \eta(r)\, \eta_0 (1 + \eta_C C) \exp\left\{ \frac{\left[E_\eta + Z_\eta (R_0 - r)\right]}{\left[R + \left(T + T_{off}\right)\right]} - \frac{\left[E_\eta + Z_\eta (R_0 - R_c)\right]}{\left[R\left(T_{CBM} + T_{off}\right)\right]} \right\}$$

where $\eta(r)$ is a viscosity pre-factor for four layers equal to 0.02 above 160 km depth, 0.002 between 160-310 km depth, 0.02 between 310-660 km depth and 0.2 below 660 km depth (lower mantle); $\eta_0 = 1.1 \times 10^{21}$ Pa s is the reference viscosity, C is the composition field and η_C is the compositional viscosity pre-factor equal to 100 in the continental lithosphere and to either 10 (cases C1 and C3) or 1 (case C2) in the basal layer (Supplementary Table 3.2). r is the radius; $R_C = 3504$ km is the radius of the core and; $R_0 = 6371$ km, the Earth's radius. $E_\eta = 275$ kJ mol^{-1} is the activation energy; $Z_\eta = 1.9 \times 10^{-6}$ m^3 mol^{-1}, activation volume; $R = 8.31$ J mol^{-1} K^{-1}, universal gas constant; T, the dimensional temperature; $T_{off} = 452$ K, a temperature offset

and $T_{CBM} = 3380$ K, the CMB temperature. Horizontal averages of present-day mantle temperature and viscosity are shown in Supplementary Fig 3.1.

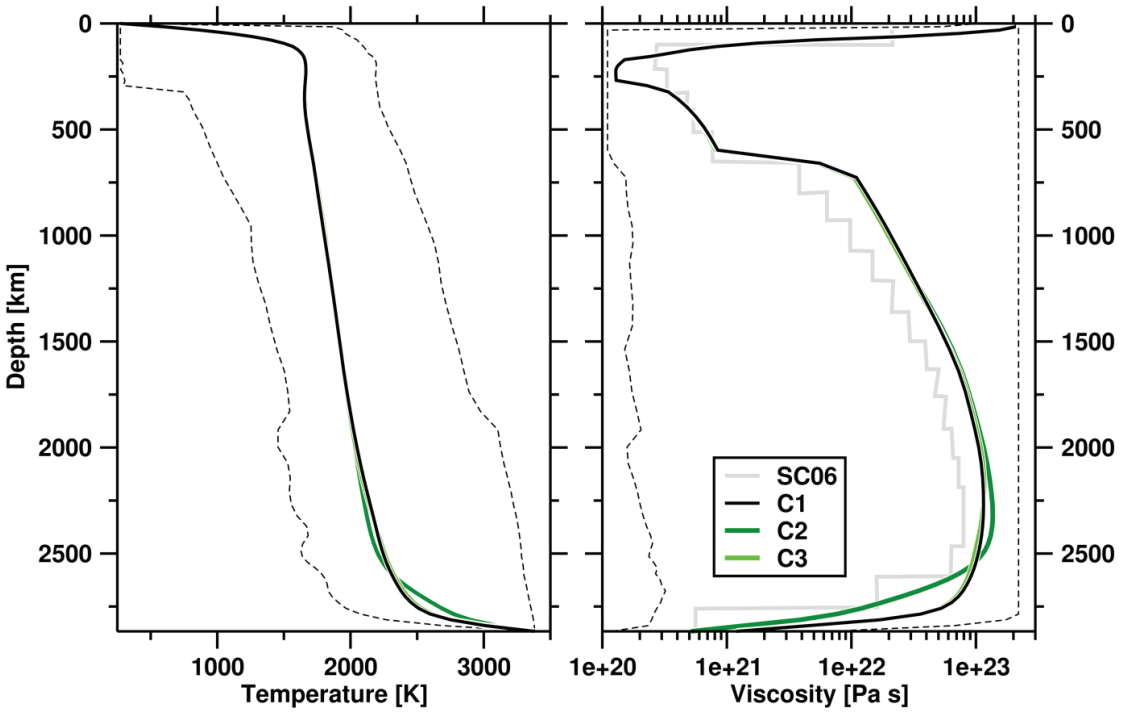

Supplementary Figure 3.1: Horizontally averaged present-day mantle temperature (left) and viscosity (right) for cases C1-3. The dashed lines show the temperature and viscosity minima and maxima for case C1. A viscosity profile from Steinberger and Calderwood (2006; SC06) is shown for reference.

The initial temperature condition includes an adiabatic profile between two thermal boundary layers; the basal thermochemical layer is initially uniformly 226 km thick thermally and includes a 113 km thick chemically-distinct layer just above the core mantle boundary (Supplementary Fig. 3.2). The density of the chemically-distinct layer is either +2.3% (cases C1 and C3) or +4.6% (case C2) greater than ambient mantle (Supplementary Table 3.2).

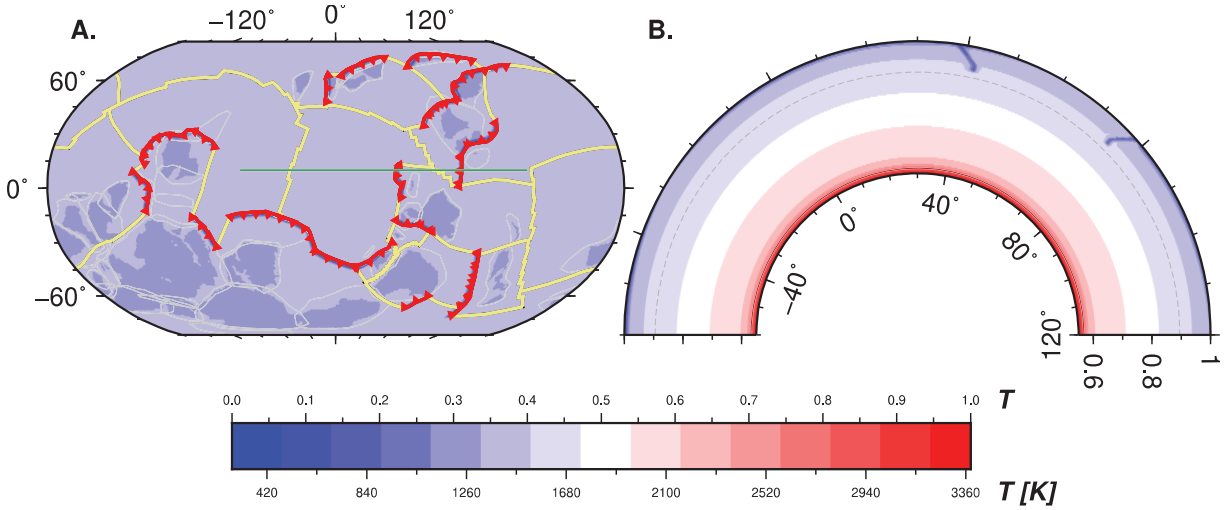

Supplementary Figure 3.2: Initial condition of mantle flow model C1 at 1200 Ma (A) Mantle temperature at 124 km depth. Reconstructed subduction locations are shown as red lines with triangles on the overriding plate, reconstructed mid-oceanic ridges and transform faults are shown as yellow lines, and reconstructed COB outlines are shown in grey. Model C1 included a "warm-up" phase in which the tectonic reconstruction at 1000 Ma was imposed for 200 Myr between 1200-1000 Ma; therefore, the reconstructed geometries are shown at 1000 Ma. The green line is the location of the cross-section shown in (B). (B) Mantle temperature along the cross-section shown in (A). The apparent dip along the cross-section is different from the dip of slabs in the direction perpendicular to the trench, which is 45º down to 425 km depth. The dashed grey line is the upper–lower-mantle boundary and the brown line outlines the chemically-distinct basal layer. Numbers above the color palette refer to the non-dimensional temperature, and numbers below the color palette to the dimensional temperature.

Model parameter	**Symbol**	**Value**	**Units**
Thermal expansion coefficient	α_0	3×10^{-5}	K^{-1}
Density	ρ_0	4000	kg m^{-3}
Gravity acceleration	g_0	9.81	m s^{-2}
Temperature change	ΔT	3100	K
Mantle thickness	h_M	2867×10^3	m
Thermal diffusivity	κ_0	1×10^{-6}	m^2 s^{-1}
Viscosity	η_0	1.1×10^{21}	Pa s

Supplementary Table 3.1: Parameters common to all mantle convection model cases. Subscript "0" indicates reference values.

Case	**Start age (Ma)**	**Initial slab depth (km)**	**Basal layer viscosity pre-factor**	**Basal layer density**
C1	1,000*	550	10	+2.3%
C2	750	550	1	+4.6%
C3	1,000	1,200	10	+2.3%

Supplementary Table 3.2: Input parameters varied across model cases. * model C1 included a "warm-up" phase in which the tectonic reconstruction at 1,000 Ma was imposed for 200 Myr between 1,200-1,000 Ma.

Models of past mantle flow were used to compute dynamic topography 20 Myr intervals using free-slip boundary conditions and ignoring temperature and lateral viscosity variations above 350 km depth; total topography included all sources of buoyancy and lateral viscosity variations (as in Flament et al., 2014). Topography was computed as:

$$h = \frac{\sigma_{rr}}{\Delta\rho g_0}$$

where σ_{rr} is the total normal stress, $\Delta\rho$ the density difference between the mantle and the surface load (air).

The initial conditions and properties of the basal layer were modified over a series of three cases to assess the impact of the mantle flow models on sea level change (Supplementary Table 3.2). The dynamic topography predicted for cases C2 and C3 is shown in Supplementary Figures 3.3 and 3.4.

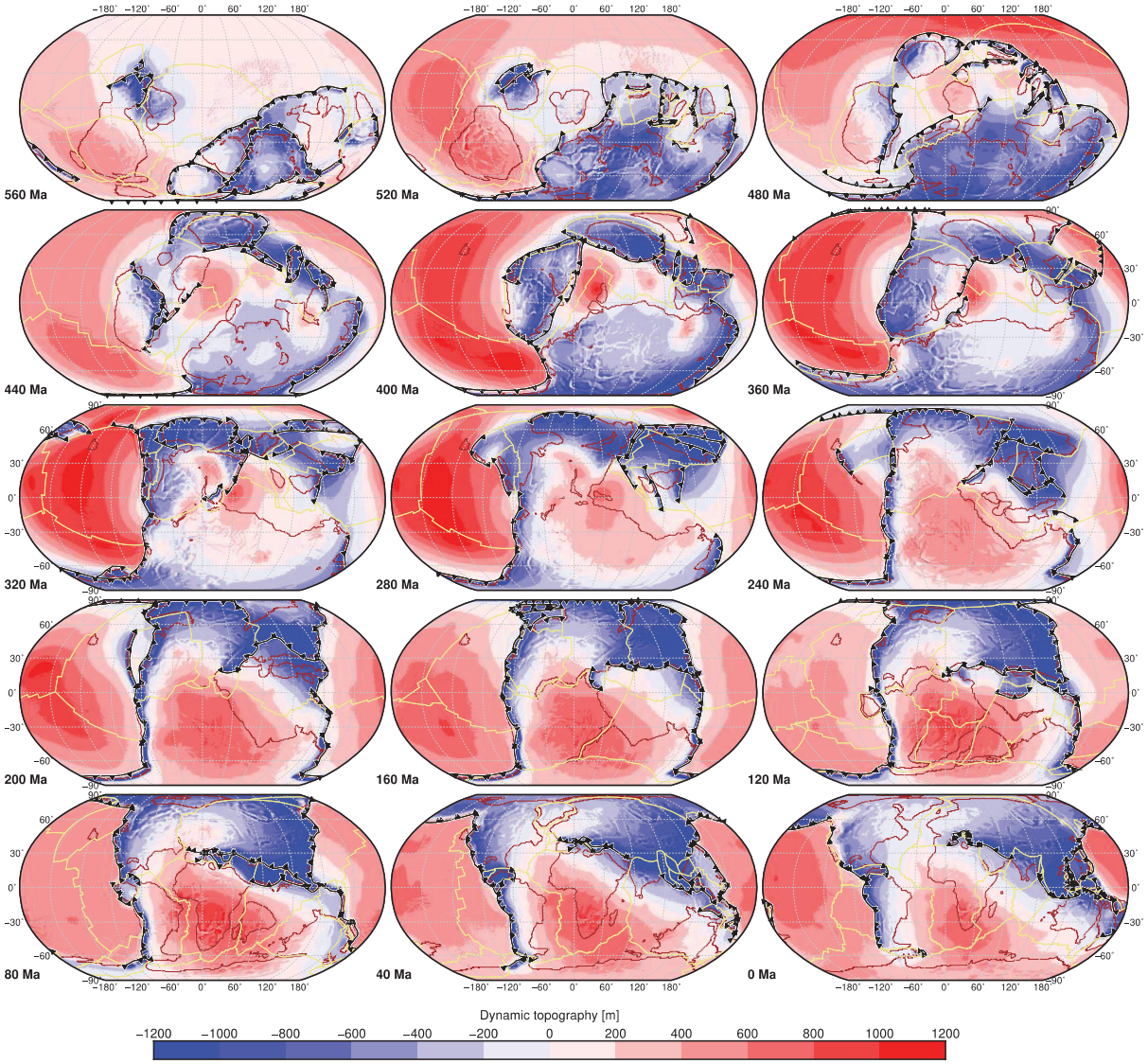

Supplementary Figure 3.3: Modelled dynamic topography for C2 from 560–0 Ma in 40 Myr increments. Reconstructed subduction locations shown as black lines with triangles on the overriding plate, reconstructed mid-oceanic ridges and transform faults in khaki, with continent-ocean boundary in brown.

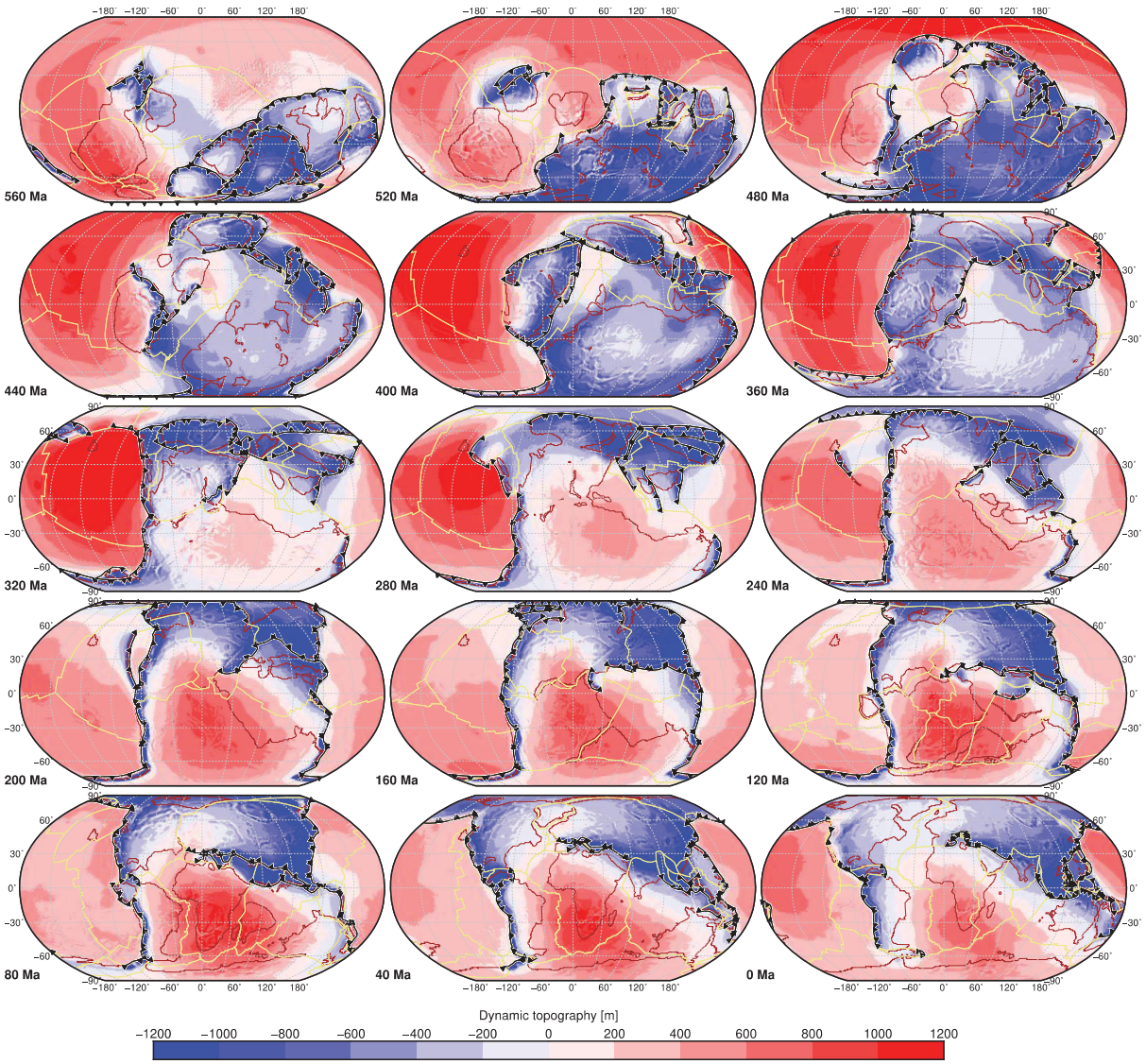

Supplementary Figure 3.4: Modelled dynamic topography for C3 from 560–0 Ma in 40 Myr increments. Reconstructed subduction locations shown as black lines with triangles on the overriding plate, reconstructed mid-oceanic ridges and transform faults in khaki, with continent-ocean boundary in brown.

3.7.3. Marine sedimentation

To model marine sediment thickness through time we extracted coastline and subduction zone segments from the tectonic reconstruction in 10 Myr increments. We used the Generic Mapping Tools (Wessel et al., 2019) and these geometries to create NetCDF rasters of areas ("masks") within 400 km of the reconstructed coastline and subduction zone locations, respectively. The subduction zone mask was then used to clip the coastline mask so that coastline points within 400 km of a subduction zone were removed (Supplementary Fig. 3.5). Thus, all coastlines that were not adjacent to a subduction zone were characterised as a passive margin. We then inverted this NetCDF raster to make a non-passive margin mask (Supplementary Fig. 3.6). The present-day masks were used to extract the passive and non-passive margin sediment thicknesses from the Straume et al. (2019) sediment thickness model. An exponential probability density function was fit to the present-day passive and non-passive margin sediment thickness data, and we verified how the distributions changed for 500 km and 600 km stencils (Supplementary Fig. 3.7). Using these distributions, the time-dependent masks were stochastically populated (Supplementary Fig. 3.8 and 3.9). The passive and non-passive

margin maps were then combined (Supplementary Fig. 3.10) and the mean sediment thickness was calculated. Because the mask width was kept constant over time, the method does not account for the changing area of flooded continental shelves. The notebook *Sediment_thickness_model.ipynb* can be used to run this model; see https://doi.org/10.5281/zenodo.3924869.

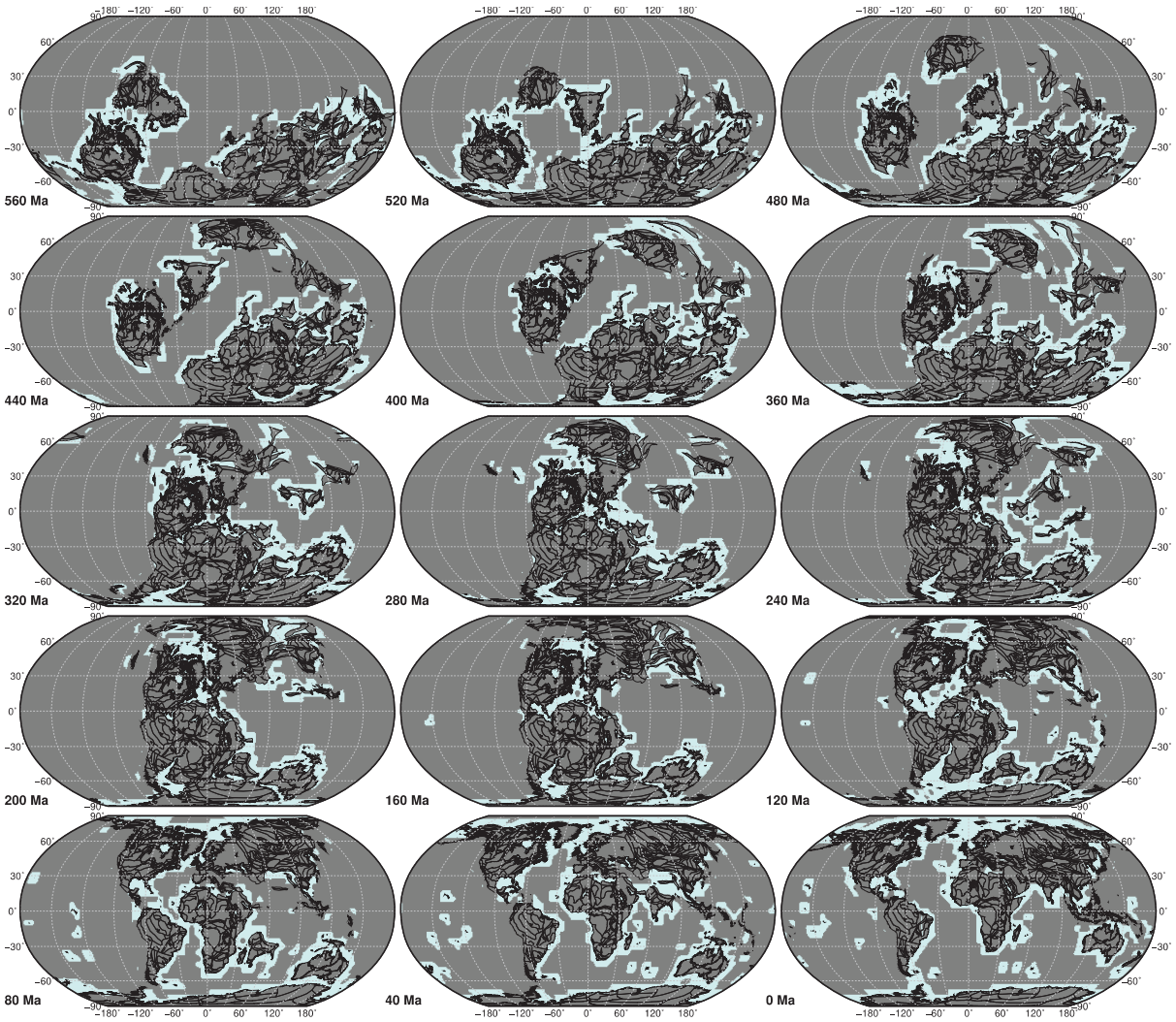

Supplementary Figure 3.5: Maps of coastline masks used in sediment thickness modelling between 560-0 Ma in 40 Myr increments. Blue fill is the 'mask' area, coastlines are in black.

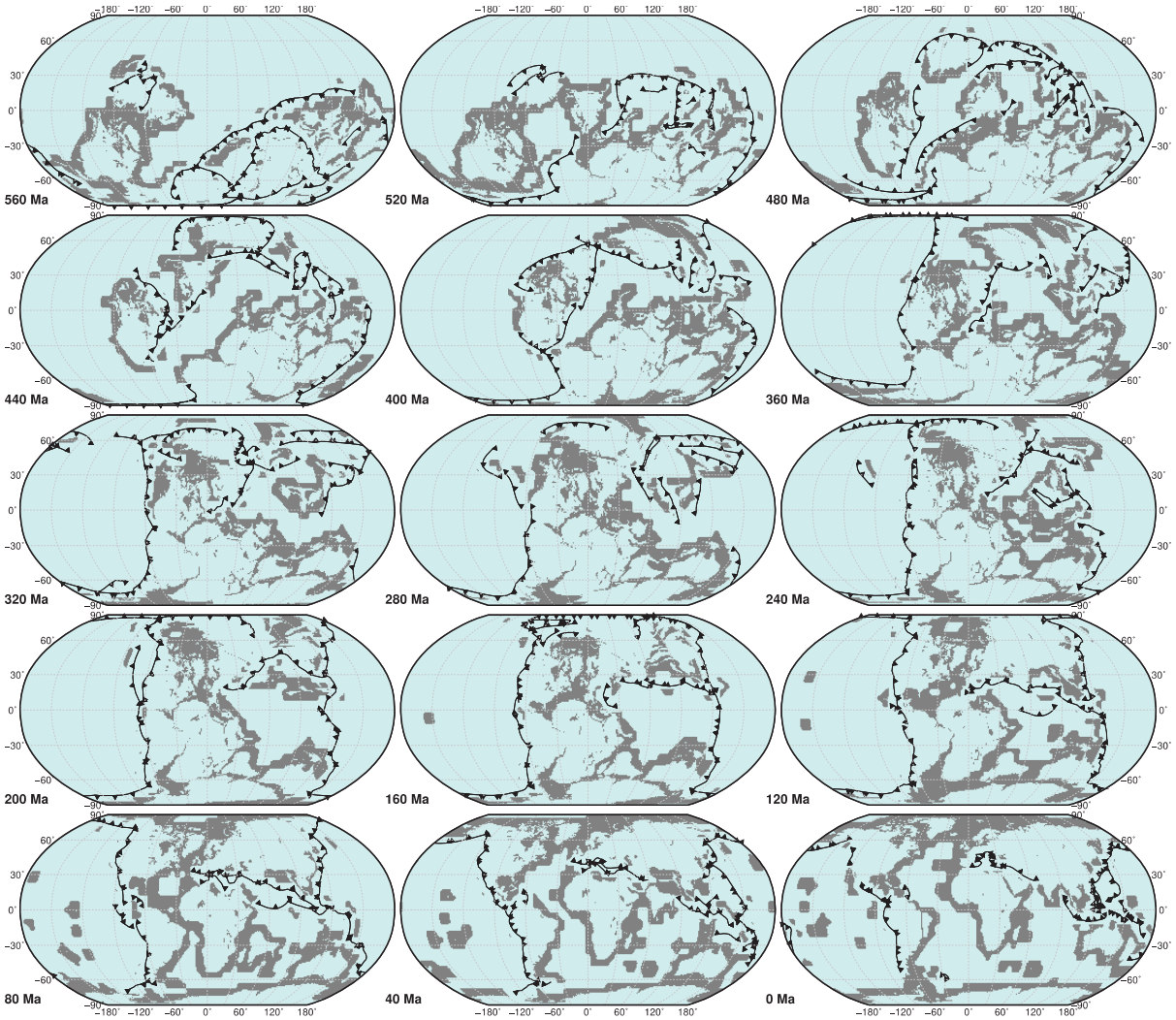

Supplementary Figure 3.6: Maps of non-passive margin masks used in sediment thickness modelling between 560-0 Ma in 40 Myr increments. Blue fill is the 'mask' area, subduction zones are in black.

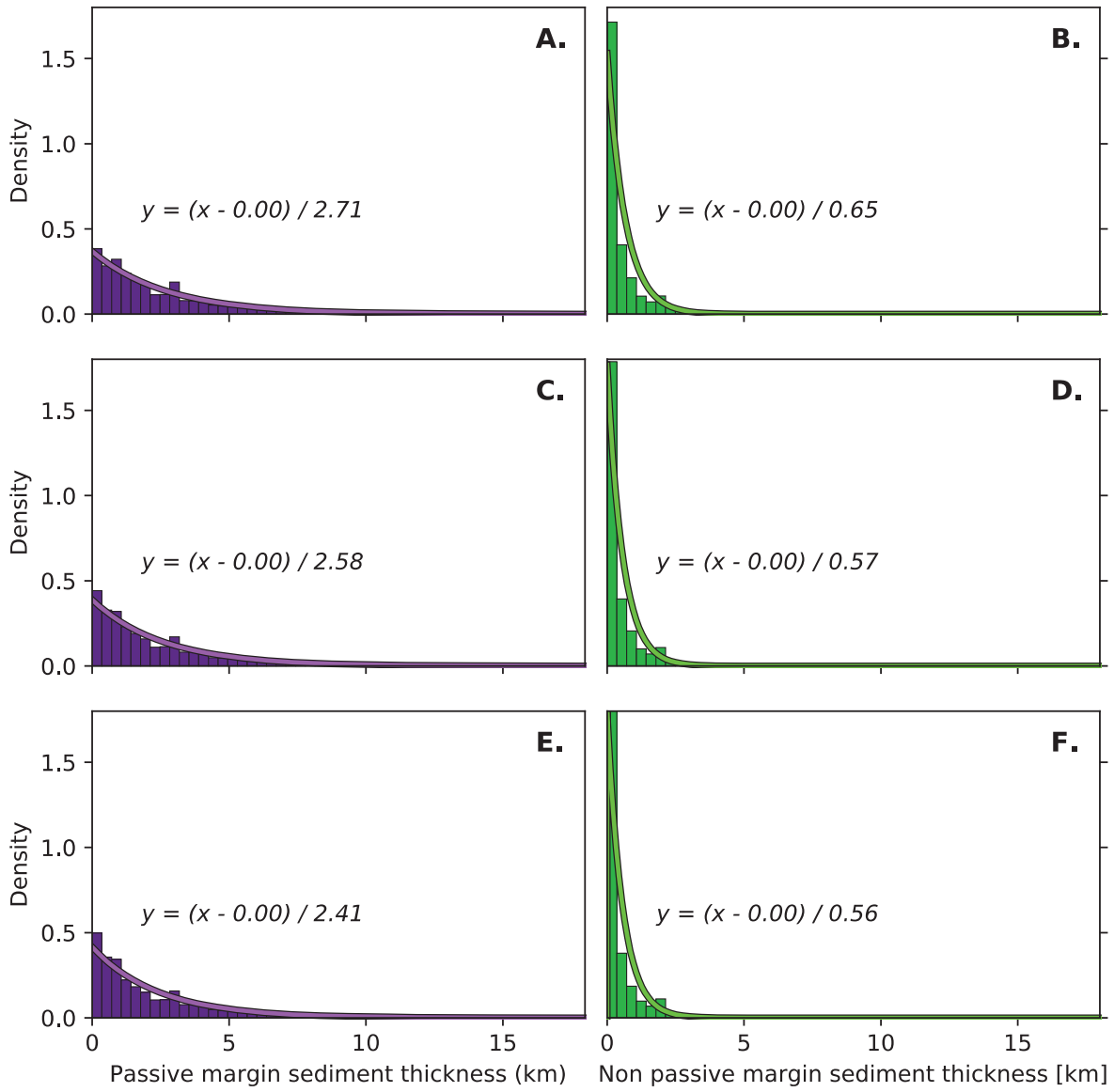

Supplementary Figure 3.7: Exponential probability density function (line, with equation) fit to present-day passive (purple) and non-passive (green) margin sediment thickness data using a 400 km stencil (A, B), 500 km stencil (C, D) and a 600 km stencil (E, F).

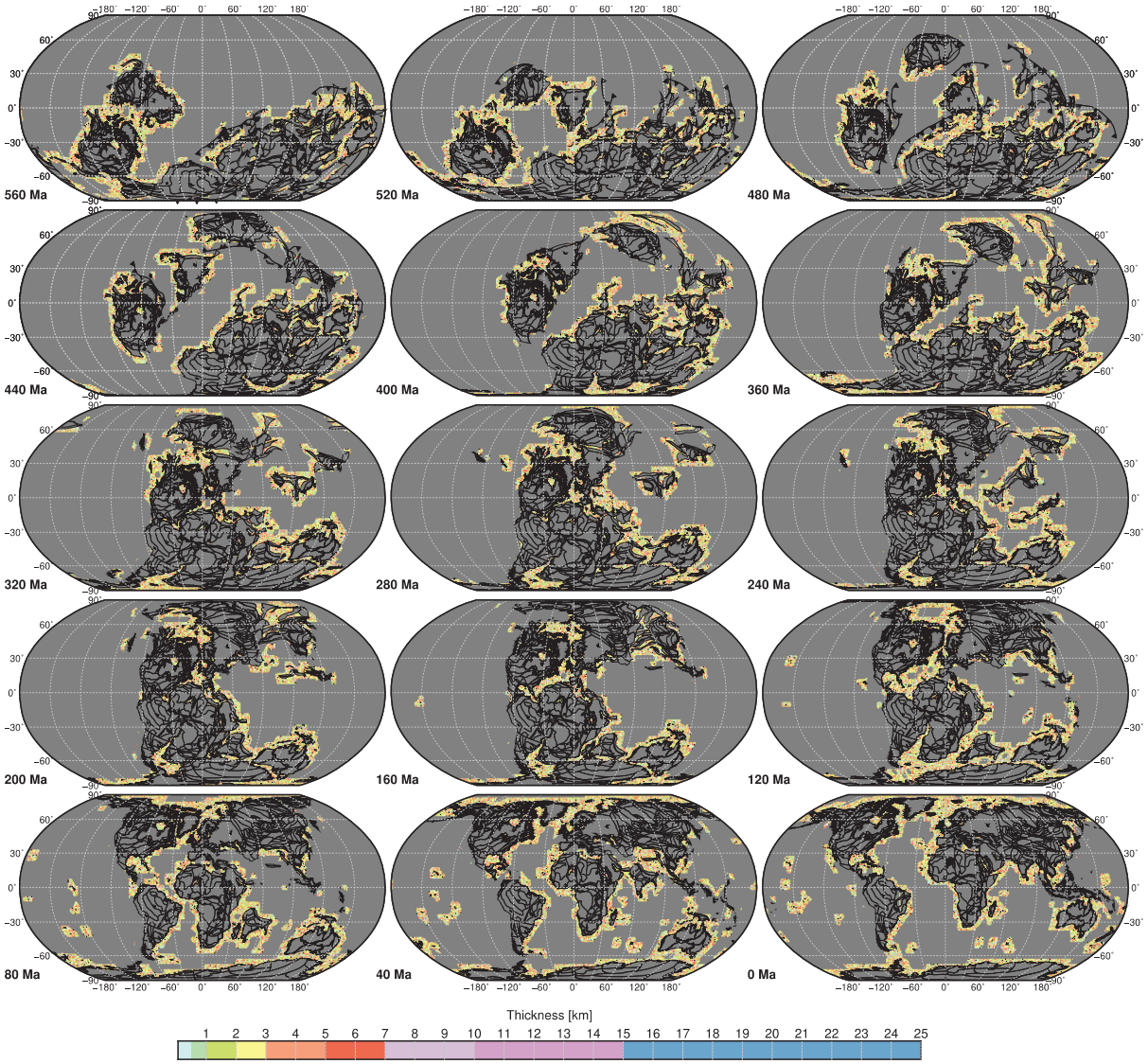

Supplementary Figure 3.8: Example passive margin sediment thickness model for 560-0 Ma in 40 Myr increments. Reconstructed coastlines are shown in black.

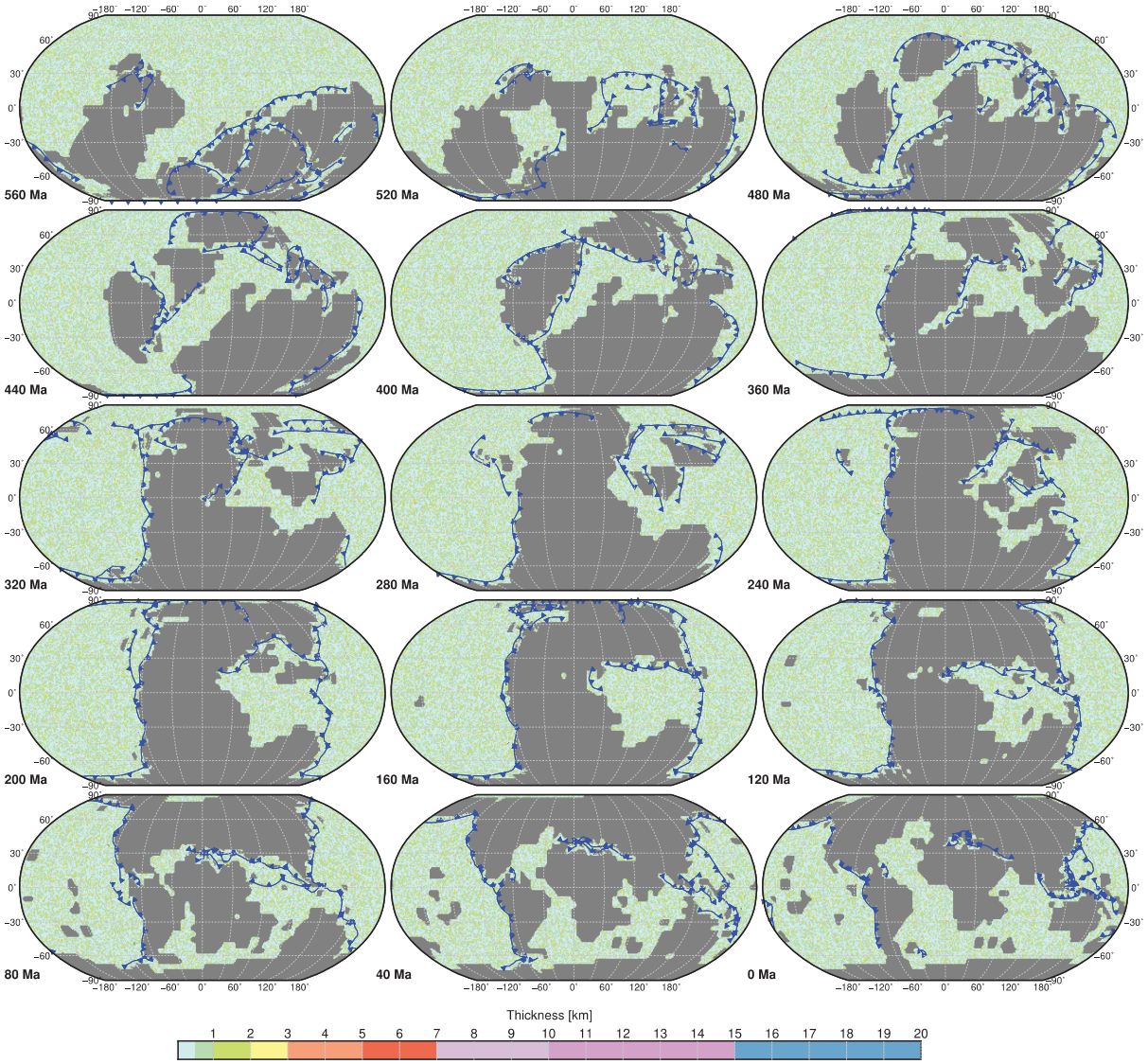

Supplementary Figure 3.9: Example non-passive margin sediment thickness model for 560-0 Ma in 40 Myr increments. Subduction zones are shown in blue. Sediment in subaerial areas has been removed.

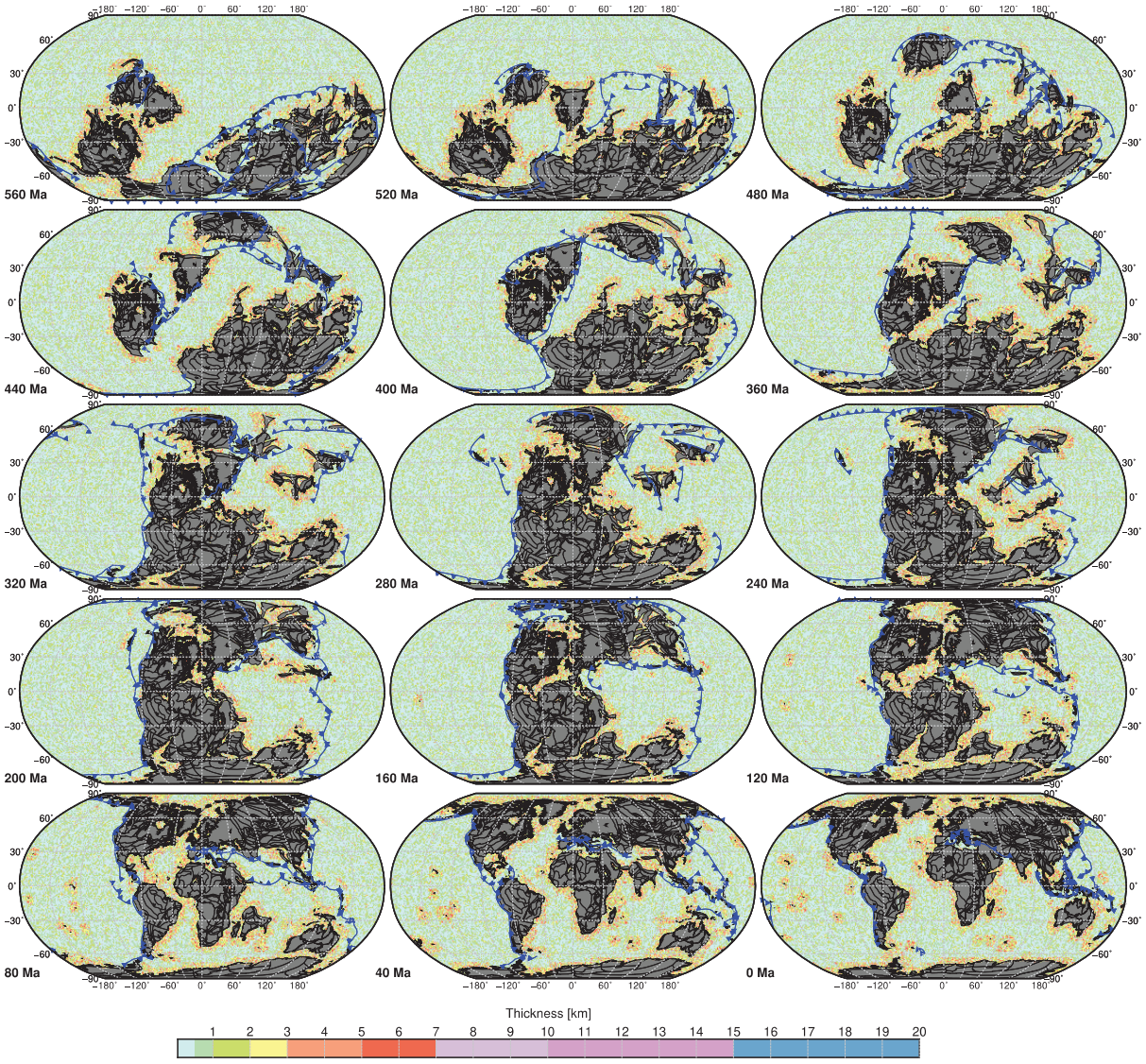

Supplementary Figure 3.10: Total sediment thickness model for 560-0 Ma in 40 Myr increments. Reconstructed coastlines are shown in black and subduction zones in blue.

3.7.4. O-LIP volume

To model O-LIP volume through time we first calculated the volume of present-day O-LIPs using the method of Schubert and Sandwell (1989). We merged the O-LIP catalogues of Whittaker et al. (2015) and Johansson et al. (2018) and removed O-LIPs with areal extent < 0.1 Mkm^2 (Bryan and Ernst, 2008). The volume of each O-LIP was determined using a depth to basement grid (Supplementary Fig. 3.11A), calculated as the difference between topography (Amante and Eakins, 2009) and sediment thickness (Straume et al., 2019). To calculate O-LIP volume we computed the modal depth to basement of individual O-LIP polygons. The modal depth to basement of the surrounding sea floor was determined in the same way, using a polygon 300 km wider than the original O-LIP outline. The difference between the modal depths of the O-LIP and the surrounding seafloor was the O-LIP height, which we multiplied by the area to give volume (Appendix 1); the empirical distribution function (EDF) of present-day O-LIP volumes is shown in Supplementary Fig. 3.11B. We then summed over the Doucet et al. (2020) oceanic mantle plume occurrence record in 120 Ma sliding intervals (Supplementary Fig. 3.11C). Time-dependent total O-LIP volumes were calculated by multiplying the number of O-LIPs (Supplementary Fig. 3.11C; 120 Ma running count) by minimum (10% of the empirical distribution

function; EDF), mid-point (50% of EDF) and maximum (90% of EDF) present day O-LIP volumes (Supplementary Fig. 3.11B). The notebook *Volumes_of_submarine_LIPs.ipynb* can be used to run this model; see https://doi.org/10.5281/zenodo.3924869.

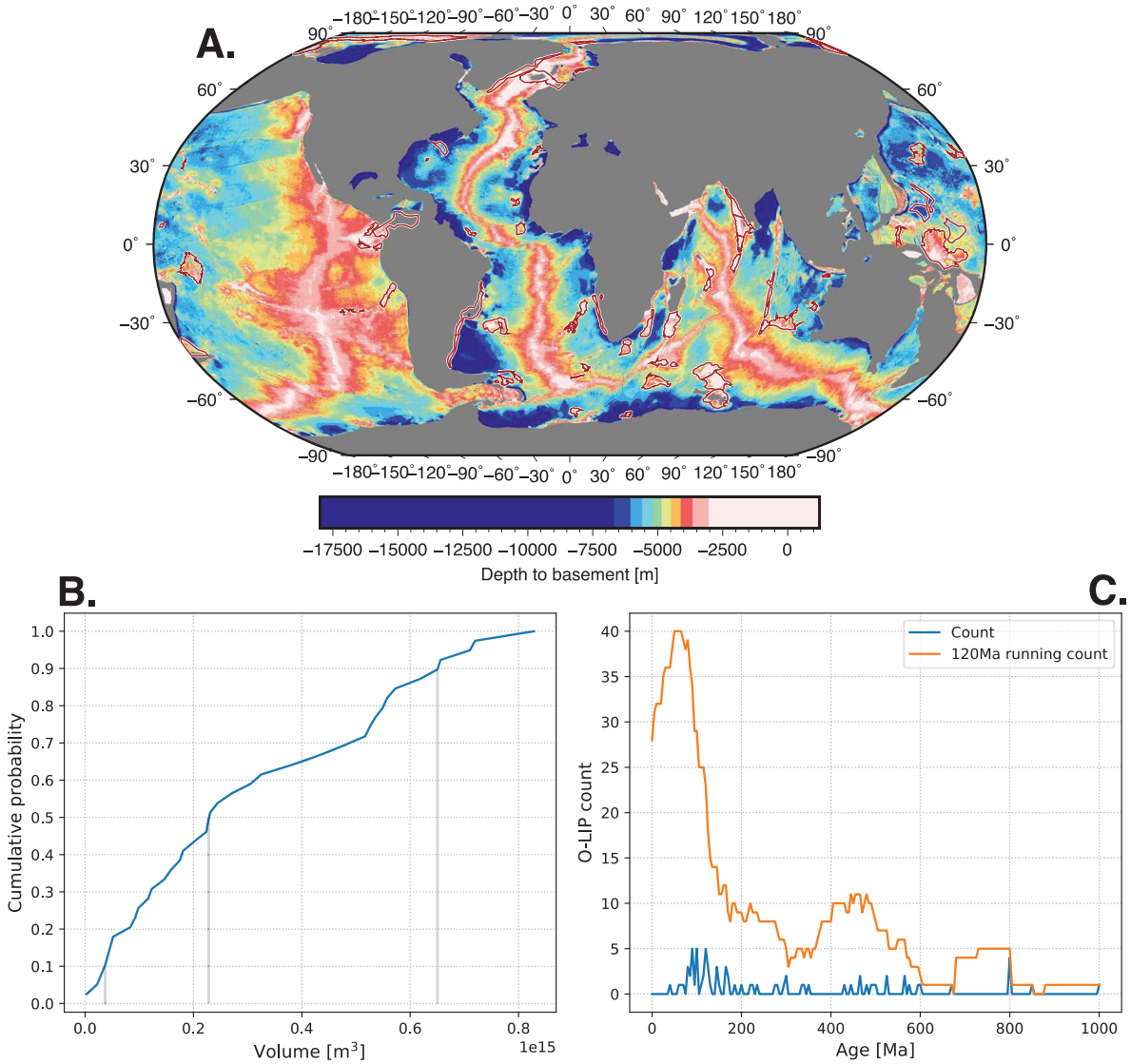

Supplementary Figure 3.11: (A) Global depth to basement map with O-LIPs used in this study outlined in brown. (B) Empirical distribution function of present-day O-LIP volumes with drop lines showing volumes for 10%, 50% and 90% of LIPs. (C) Doucet et al. (2020) oceanic mantle plume occurrence record (blue) and O-LIP count summed over 120 Ma sliding intervals (orange).

3.7.5 Ancient hypsometry

Algeo and Wilkinson (1991) showed that the slope of continental hypsometries (Harrison et al., 1983) is relatively uniform in the 'coastal zone' between -50 m and +200 m, which motivated them to develop a paleo-continental hypsometry model that uses the tectonic setting and age of continental margins to estimate past hypsometric slopes. Their model was based on the principles of lithospheric cooling so that coastal gradients are shallow for mature passive margins and steep for active and young margins. To model time-dependent hypsometry, we first used the method of Algeo and Wilkinson (1991) to determine the global hypsometric slope of the continental shelf. The controlling parameters in this workflow: margin age, total continental area, and

margin length were extracted from the reconstruction model in 10 Myr increments. Margins were divided into two classes: non-passive margins (defined as within 300 km of a reconstructed active margin: subduction zone or transform margin) and passive margins (defined as not within 300 km of a reconstructed active margin). Segments were resampled at regularly spaced 1 arc degree intervals and for each point margin age was obtained from past seafloor age maps (Supplementary Fig. 3.12A). Total continental area was also determined from the sea floor age maps. For each segment point a coastal gradient (*GC*) was calculated using:

$$CG = -0.0062\,\boldsymbol{\tau} + 1.28$$

where τ is the age of the plate (taken equal to 0 Ma for active and transform margins). The hypsometric slope (*HS*) (Supplementary Fig. 12B) was calculated as:

$$HS = \frac{A}{\sum \frac{SL}{CG} \times 100}$$

where *A* is total area and *SL* is segment length.

Once the hypsometric slope of the continental shelf was determined we constructed the time-dependent hypsometric curve by combining model bathymetry, the model hypsometric shelf slope, a linear function for the continental slope and present-day ETOPO continental elevations. The linear function used to fit the continental slope was:

$$y = 1.7 \times 130 \cdot x$$

where *y* is elevation (m), *x* is the cumulative fraction of Earth's surface area and 1.7×130 is the slope in m/fraction area. The notebook *Model_timedependent_AL_hypsometry.ipynb* can be used to run this model; see https://doi.org/10.5281/zenodo.3924869.

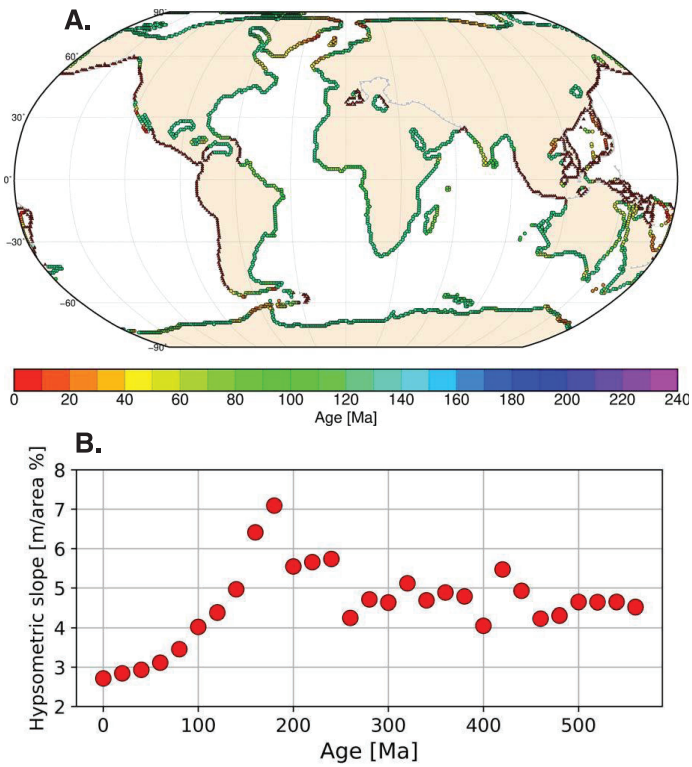

Supplementary Figure 3.12: (A) Present-day example of margin ages extracted from the global seafloor age map. Circles represent the passive margin segment points and triangles the non-passive margin points. Subduction zones are shown in grey and continental areas in light brown. Margin points are coloured by age. (B) Modelled time-dependent global hypsometric slope of the continental shelf.

Acknowledgments

This research has been conducted with the support of the Australian Government Research Training Program Scholarship. AJY and NF were supported by Australian Research Council grant DE160101020. RDM and SEW were supported by Australian Research Council grant IH130200012. ASM is supported through the Deep Energy Community of the Deep Carbon Observatory. This research was undertaken with the assistance of resources from the National Computational Infrastructure (NCI), which is supported by the Australian Government. The version of CitcomS used in this research, described in Bower et al. (2015), is available from https://github.com/EarthByte/citcoms. The workflow code and data used in this study are available at https://doi.org/10.5281/zenodo.3924869. Figures 2, 3, 4, 5, and 6 were constructed using Generic Mapping Tools (Wessel et al., 2019).

Chapter 4. The influence of mantle flow on intracontinental basins: three examples from Australia

Alexander Young[1*], Nicolas Flament[1], Lisa Hall[2], Andrew Merdith[3]

[1] GeoQuEST Research Centre, School of Earth, Atmospheric and Life Sciences, University of Wollongong, Northfields Avenue, NSW 2522, Australia

[2] Geoscience Australia, GPO Box 378, Canberra ACT 2601, Australia

[3] Laboratoire de Géologie, Université of Lyon 1, France

** corresponding author*

Abstract

During the Paleozoic, sedimentary basins developed within Gondwana without evolving to diverging plate boundaries. Such intracontinental basins present long subsidence histories with multiple phases of accelerated subsidence that are not always easily explained by far-field tectonic forces, and may be driven by processes other than rifting and thermal subsidence.

Here we investigate the subsidence of Paleozoic Australian intracontinental basins by comparing one-dimensional backstripped tectonic subsidence histories from the western Australian Canning and Southern Carnarvon Basins and the central Australian Cooper Basin to forward subsidence models for pure shear lithospheric thinning. We make the hypothesis that differences between observed and model subsidence may be explained by mantle-flow driven topography, in addition to tectonic forces. To test this hypothesis, we compute dynamic topography from the first geodynamic models of mantle flow spanning the entire Phanerozoic Eon, and we analyse the relationship between dynamic topography and anomalous basin subsidence to dynamic topography and mantle flow.

Although reconstructions of mantle flow in deep geological times are uncertain, our results suggest that long-wavelength dynamic topography could explain aspects of the complex tectonic histories of intracontinental basins. In the presented reconstruction of mantle flow, topographic rebound following the sinking of a Cambrian aged slab resulted in a minor phase of dynamic uplift in the Cooper Basin in middle Permian times.

Throughout Carboniferous-Triassic times Australia was positioned above a mantle upwelling driven by a hot structure at the base of the mantle. Structural uplift in the Canning and Southern Carnarvon basins during the Triassic-Jurassic interval was augmented by dynamic uplift produced by that large-scale upwelling, and possibly augmented by a focused active mantle plume during the Permo-Triassic. In Late Jurassic-Cretaceous times, Australia drifted east away from the mantle upwelling, resulting in a period of subsidence in the Canning and Southern Carnarvon basins. During the Cretaceous the Cooper Basin moved over a downwelling produced by long-lived subduction along the east Australian margin, resulting in a period of accelerated subsidence.

Keywords

Mantle flow, Dynamic topography, Paleozoic, Australia, Basin subsidence

4.1. Introduction

Intracontinental basins are formed between cratonic blocks on continental lithosphere away from active plate boundaries. Their subsidence histories typically display less initial subsidence than those observed in conventional rift basins and generally follow the shape and magnitude of the subsidence of the ocean floor; although with significant deviations (Xie and Heller, 2009); e.g., the Michigan Basin (Bond and Kominz, 1991; Kominz and Bond, 1991; Hamdani et al., 1994; Naimark and Ismail-Zadeh, 1995; Kaminski and Jaupart, 2000). Several tectonic and geodynamic mechanisms have been proposed to explain deviations between expected and observed tectonic subsidence including: intraplate stresses and reactivation of inherited structures (Bond and Kominz, 1991), plume-lithosphere interaction (Kaminski and Jaupart, 2000), deep crustal metamorphism (Middleton, 1980), lower crustal phase transition (Hamdani et al., 1994) and mantle downwelling (Kominz and Bond, 1991). The hypothesis that intracontinental basins are affected by dynamic topography has been analysed by Heine et al. (2008) for a global set of basins and Heine et al. (2010) for the Cenozoic of Australia. Here, we make the hypothesis that the complex subsidence histories of Paleozoic intracontinental basins have been impacted by mantle flow, and that the contribution of mantle flow to basin subsidence may be preserved in the geological record.

Dynamic topography, the topography due to flow in the mantle, which drives transient, long-wavelength, low amplitude vertical motion of Earth's surface (Pekeris, 1935; Parsons and Daly, 1983; Richards and Hager, 1984; Cazenave et al., 1989; Hager and Richards, 1989; Braun, 2010; Flament et al., 2013a), has been invoked to explain both subsidence and uplift of continental plates (Gurnis, 1990b; Pysklywec and Mitrovica, 1999; Liu et al., 2008). Geological expressions of long-wavelength dynamic topography are most likely to be found in continental interiors where the effects of plate boundary forces are subdued and preservation potential is high. For instance, continental burial depth and unroofing histories, inferred from apatite (U-Th)/He and apatite fission-track thermochronology (AFTA) studies have been used to test predictions of dynamic topography based on global mantle convection models for the last 400 Myr (Flowers et al., 2012; Zhang et al., 2012). Additionally, studies have been conducted to investigate the effect of dynamic topography on sedimentary basins (Mitrovica et al., 1989; Pysklywec and Mitrovica, 1999; Xie et al., 2006; Sutherland et al., 2010; Flament et al., 2014; Shephard et al., 2014; Vibe et al., 2018a, b). These studies focus on the post-Jurassic for which tectonic models, used to generate time-dependent mantle flow and dynamic topography models, were presently available.

Tectonic models are currently being developed for the past billion years (Merdith et al., 2021), allowing us to test the hypothesis that mantle convection contributed to the subsidence of three Australian Paleozoic basins: the Cooper, Canning and Southern Carnarvon Basins (Fig. 4.1). These basins were selected because (i) they were the most stable in Australia for the time period of interest and (ii) data are publicly available due to past hydrocarbon exploration. We first backstrip well data to determine the tectonic subsidence of the basins. We then compute the expected tectonic subsidence for the wells using a pure shear model (Jarvis and McKenzie, 1980) that fits the backstripped data, and identify episodes of anomalous vertical motion (calculated as the difference between backstripped and modelled subsidence). Finally, we compute the first time-dependent reconstructions of mantle flow spanning the Phanerozoic Eon and use these models to examine the relationship between dynamic topography and anomalous basin motions.

4.2. Geological context

4.2.1 Cooper/Eromanga Basin

The Cooper Basin in central Australia (Fig. 4.1) contains up to 2,400 m of Pennsylvanian-Middle Triassic stratigraphy (Hall et al., 2015). It unconformably overlies the lower Paleozoic sedimentary and volcanic rocks of the Warburton Basin and is disconformably overlain by the Jurassic-Cretaceous Eromanga Basin and the Cenozoic Lake Eyre Basin (Alexander et al., 1998). Subsidence in the Cooper Basin initiated during the late Carboniferous-early Permian (Moussavi Harami, 1996; Deighton and Hill, 1998; Deighton et al., 2003; Hall et al., 2015; Hall et al., 2016). The Daralingie compressional event at ~260 Ma produced regional anticlines, uplift and erosion, and reactivated basement structures (Battersby, 1976; Kuang, 1985; Apak et al., 1997; Gravestock and Jensen-Schmidt, 1998; Hall et al., 2015); after which, subsidence resumed and continued uninterrupted until ~235 Ma (Moussavi Harami, 1996; Deighton et al., 2003; Hall et al., 2016).

The Eromanga Basin succession is marked by localised Late Triassic deposition (Hall et al., 2016). Subsidence, in the absence of crustal extension, increased drastically during the Late Cretaceous (Zhou, 1989; Gallagher, 1989; Deighton and Hill, 1998; Mavromatidis, 2006; Hall et al., 2016) and has been linked to subduction-related tilting (Russell and Gurnis, 1994; Gurnis et al., 1998; Matthews et al., 2011).

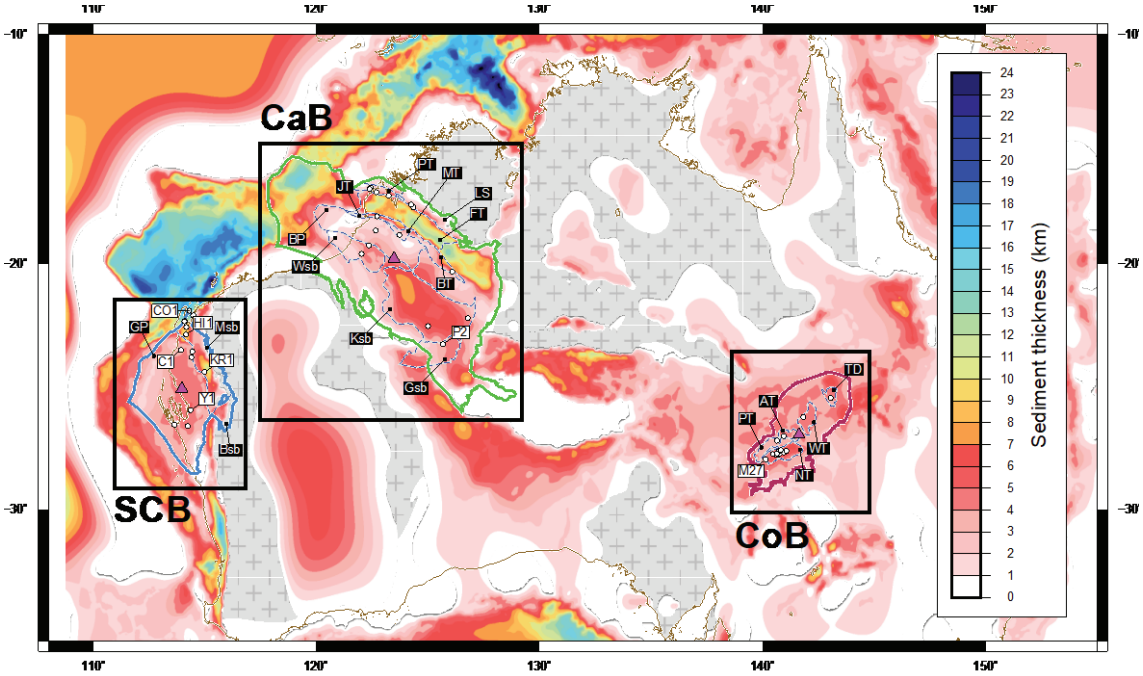

Figure 4.1: Locations of the sedimentary basins and wells considered in this study, and background sediment thickness map (FROGTECH, 2014). Basin abbreviations are: SCB, Southern Carnarvon Basin; CaB, Canning Basin; CoB, Cooper Basin. Basin outlines (CaB; green, SCB; blue and CoB; maroon lines) and basin structural elements (dashed blue lines), coastlines (brown line) are shown. Abbreviations for basin structural elements (black squares labeled in black boxes) are from west to east: SCB: GP, Gascoyne Platform; Msb, Merlinleigh Sub-basin; Bsb, Byro Sub-basin; CaB: BP, Broome Platform; Wsb, Willara Sub-basin; JT, Jurgurra Terrace; PT, Pender Terrace; Ksb, Kidson Sub-basin; MT, Mowla Terrace; FT, Fitzroy Trough; BT, Barbwire Terrace; LS, Lennard Shelf; Gsb, Gunbarrel Sub-basin; CoB: PT, Patchawarra Trough; AT, Arrabury Trough; NT, Nappamerri Trough; WT, Windorah Trough; TD, Thompson Depression. The boreholes used in this study are shown as white circles, and boreholes mentioned in the text are labeled in white boxes with abbreviations from west to east: CO1, Cody-1; C1, Chargoo-1; HI1, Hope Island-1; Y1, Yaringa-1; KR1, Kennedy Range-1; M1, Minjin-1; MO1, Moogana-1; P1, Puratte-1; L1, Lloyd-1; P2, Patience-2; M27, Moomba-27. Magenta triangles are basin central points. Cratons shown as grey and dark grey cross pattern fill.

4.2.2 Canning Basin

The Canning Basin is a long-lived (~500 Myr) sedimentary basin located in north-western Australia (Fig. 4.1). It has experienced multiple phases of extension and compression (Forman and Wales, 1981; Brown et al., 1984; Yeates et al., 1984; Kennard et al., 1994a; Shaw et al., 1994; Parra Garcia et al., 2014). Formed in the Early Ordovician (Kennard et al., 1994a; Romine et al., 1994; Shaw et al., 1994) as a shallow marine basin (Conolly et al., 1984) the earliest deposition was controlled by normal faulting (Conolly et al., 1984; Romine et al., 1994) yet the initial depocentre has the shape of an intracontinental sag basin (Shaw et al., 1994).

The Prices Creek Movement, a period of uplift, folding, tilting and erosion immediately succeeded initial subsidence and has been related to the initial stages of the Alice Springs Orogeny in central Australia (Shaw et al., 1994). Extension during Devonian-Carboniferous times was followed by compression related to the peak phase of the Alice Springs Orogeny (Forman and Wales, 1981; Colwell et al., 1994; Shaw et al., 1994). The compressional event, named the Meda Transpression, produced faulting, fault reactivation, uplift and erosion and resulted in an extensive unconformity at the base of the Permian section (Forman and Wales, 1981; Arne et al., 1989; Kennard et al., 1994a; Shaw et al., 1994; Parra Garcia et al., 2014). The Late Carboniferous-Permian Fitzroy Transpression, an inversion marked by basin-wide folding, faulting, uplift, and erosion (Forman and Wales, 1981; Yeates et al., 1984; Kennard et al., 1994a; Shaw et al., 1994), produced a major unconformity at the base of the Jurassic section (Parra Garcia et al., 2014).

A phase of mild Jurassic-Cretaceous subsidence contemporaneous with dextral transpression, indicated by minor fault inversion, folding and faulting of the Jurassic- Cretaceous levels (Parra Garcia et al., 2014) has been linked to the onset of seafloor spreading in the Argo Abyssal Plain at ~155 Ma (Kennard et al., 1994a).

4.2.3 Southern Carnarvon Basin

The Southern Carnarvon Basin (Gallagher et al., 2013) consists of three Paleozoic sub-basins (Fig. 4.1): the Late Cambrian-Devonian Gascoyne Platform, and the Carboniferous-Permian Merlinleigh and Byro Sub-basins (Mory et al., 2003). First deposition in the Southern Carnarvon Basin was intracontinental and spanned the ?Cambrian-Early Devonian (Iasky et al., 1998; Mory et al., 2003). Growth faults are the only evidence of tectonism during this period (Mory et al., 2003).

Low levels of thermal maturity within the Paleozoic succession on the Gascoyne Platform (Ghori, 1998; Mory et al., 1998) led Mory et al. (2003) to suggest that the area was a positive structural feature during middle Carboniferous-earliest Cretaceous times. In the Merlinleigh Sub-basin, Late Carboniferous-Permian rifting was coeval with extension in the Perth Basin to the south (Iasky et al., 1998). Growth and en-échelon faulting collectively interpreted to represent components of strike-slip movement during west-southwest extension (Iasky et al., 1998).

Following Carboniferous subsidence, no deposition is recorded in the Southern Carnarvon Basin from end Permian-earliest Cretaceous times (~140 Myr) (Iasky et al., 1998; Iasky and Mory, 1999; Iasky et al., 2003; Mory et al., 2003); during which seafloor spreading began in the Meso-Tethys Ocean and Greater India broke away from Australia (Powell et al., 1988). Onshore, these tectonic events are marked by faulting, fault reactivation, and anticlinal folding (Crostella, 1995; Crostella and Iasky, 1997; Mory et al., 2003). The Southern Carnarvon Basin became a passive margin of the Tethys Ocean during continental break-up, indicated by offshore faulting and thick sedimentary sequences (Iasky et al., 1998).

4.3. Methods

4.3.1 Tectonic plate reconstruction

Plate tectonic reconstructions can be used as a boundary condition for time-dependent forward mantle flow models (Ricard et al., 1993; Bunge et al., 1998; Lithgow-Bertelloni and Richards, 1998; McNamara and Zhong, 2005; DiCaprio et al., 2011; Flament, 2019b; Young et al., 2019, Chapter 2). Here we use the first full plate reconstruction that spans continuously from the Neoproterozoic to present-day (Merdith et al., 2021) which is an amalgamation of previous models: Merdith et al. (2017), 1,000-520 Ma; Domeier (2016, 2018), 500-410 Ma; and Young et al. (2019, Chapter 2), 410-0 Ma.

Net rotation is the rotation of the whole lithosphere with respect to the underlying mantle (Torsvik et al., 2010b). It has been shown that global mantle flow models are more consistent with global seismic tomography models if they are set up to reduce net rotation (Rudolph and Zhong, 2014) and mantle flow models forced with global tectonic reconstructions are routinely carried out in a no-net-rotation reference frame (Shephard et al., 2014). Therefore, we removed net rotation from the plate reconstruction. In our global flow models, net rotation between the mantle and the lithosphere arises from lateral viscosity variations due to the composition- and temperature-dependence of viscosity.

Plate tectonic motion results from a coupling of the toroidal and poloidal components of mantle flow and it is the toroidal element that produces net rotation (Ricard et al., 1991). Considering firstly that convection in a laterally homogeneous medium only produces poloidal flow (O'Connell et al., 1991) and secondly, that numerous observations of Earth's net rotation confirm the presence of a toroidal component (Minster et al., 1974; Gordon and Jurdy, 1986; Ricard et al., 1991; Gripp and Gordon, 2002; Cuffaro and Doglioni, 2007; Zheng et al., 2010); then evidently, Earth's internal properties must be laterally heterogeneous. Numerical models of 3D mantle convection including a laterally heterogenous mantle – i.e., lateral viscosity variations – couple the poloidal and toroidal fields and thus, thermally induced density variations indirectly drive toroidal flow (O'Connell et al., 1991; Ricard et al., 1991).

4.3.2 Mantle flow models

4.3.2.1 Model set-up and governing parameters

We modelled global thermochemical convection within Earth's mantle driven by the no-net-rotation plate model for 1,000-0 Ma, solving equations for the conservation of mass, momentum and energy under the extended Boussinesq approximation (Christensen and Yuen, 1985) using a version of the finite element code *CitcomS* (Zhong et al., 2008), modified by Bower et al. (2015) to progressively assimilate tectonic reconstructions with topologically-evolving plate boundaries, from which we derived plate velocities and thermal structure of the lithosphere and shallow slabs in 1 Myr increments. Plate velocities from the reconstructions were used as a surface boundary condition while the base of the mantle is free slip. The structure of the lithosphere and shallow part of slabs (down to ~350 km depth), derived from the plate reconstructions, are imposed as a time-dependent volume condition (see Bower et al., 2015). We considered five cases with different initial ages ranging from 600-1000 Ma in 100 Ma intervals (named M600, M700 etc). The mantle is modelled as a spherical shell and viscosity depends on depth, temperature and composition (Supplementary Fig. 4.1)

The initial temperature condition (Supplementary Fig. 4.2) includes an adiabatic profile between two thermal boundary layers. The basal thermochemical layer is initially uniformly 226 km thick and includes a

113 km thick layer above the CMB that consists of material 4.24% denser than ambient mantle; this density contrast gives a good fit between present-day model temperature and tomography (Flament, 2019b). In the initial condition, slabs are inserted down to 425 km at 45°. During the model run, slabs are read in by the code down to ~350 km depth and merged with the dynamic solution (Bower et al., 2015). The Rayleigh number which determines the vigour of mantle convection is 7.8×10^7 and the dissipation number, which controls shear heating is equal to 1.56. Mantle viscosity varies with temperature and depth. Detailed descriptions of the governing equations solved for mantle convection, the model set up and initial conditions are provided in the Supplementary Section 4.7.1.

4.3.2.2 Computation of dynamic topography

We compute dynamic topography h in 10 to 20 Myr intervals by scaling the total normal stress σ_{rr} using free-slip boundary conditions and ignoring temperature and lateral viscosity variations above 350 km depth following:

$$h = \frac{\sigma_{rr}}{\Delta\rho g_0}$$

(ρ in kg m^{-3}, g in m s^{-2}, σ in kg m^{-1} s^{-2}, therefore h in m) with $\Delta\rho$ the density difference between the mantle and the surface load (air or water). The predicted dynamic topography results from all sources of buoyancy below 350 km. Although preserving lateral viscosity variations above 350 km lowers the long-wavelength amplitude of dynamic topography it also introduces short-wavelength variations (see Figure 5 of Flament, 2019b) that are undesirable for regional studies such as this contribution.

4.3.3 Backstripping procedure and input parameters

The 1-D backstripping procedure used to compute basin tectonic subsidence requires constraints on of the age, thickness, compaction history and paleowater depth of sedimentary strata (Allen and Allen, 2013). In the procedure, sediment accumulation through time is reconstructed from the present-day thickness of each dated stratigraphic unit. The effects of sediment compaction are integrated and paleobathymetry corrections are made to compute a 1-D subsidence history. The effect of sediment loading is removed by de-compacting and removing sedimentary units backwards in time (Steckler and Watts, 1978).

4.3.3.1 Stratigraphic thickness and age

Well data from the Canning (15 wells; Fig. 4.1), Southern Carnarvon (13 wells; Fig. 4.1) and Cooper (14 wells; Fig. 4.1) Basins were used to analyse tectonic subsidence. Wells were selected based on spatial distribution and data availability. Stratigraphic tops and borehole geophysical log data for the Canning and Southern Carnarvon Basins were sourced from the Western Australian Petroleum and Geothermal Information Management System (WAPIMS). Formation tops were reviewed and updated to fit the available WAPIMS biostratigraphic data. Formation ages for the Canning Basin were taken from the Geoscience Australia Canning Basin Biozonation and Stratigraphy Chart (Smith et al., 2013) and formation ages for the Southern Carnarvon Basin are according to Geoscience Australia's Southern Carnarvon Basin Biozonation and Stratigraphy Chart (Nicoll et al., 1998). Formation ages and tops for the Cooper Basin are from Hall et al. (2016). Stratigraphic thickness and age data are provided in Appendix 2.

4.3.3.2 Lithologies

In the Canning and Southern Carnarvon Basins, facies models were generated using wireline log analysis and lithological descriptions from well completion reports. Gamma ray data was used to quantify the shale fraction in each well; limestone and dolostone fractions were determined from sonic and bulk density logs. Facies allocation was verified against lithology descriptions from well reports. For the Cooper Basin the formation lithologies of Hall et al. (2016) are used. Lithological inputs for backstripping are provided in the Appendix 2.

4.3.3.3 Porosity and compaction

The progressive burial of sediment leads to exponential porosity reduction with depth. To find the porosity-depth relationships for lithologies in the Canning and Southern Carnarvon Basins, porosity was calculated using:

$$\emptyset = \frac{\rho_{ma} - \rho_{log}}{\rho_{ma} - \rho_f}$$

with ρ_{ma} the matrix (grain) density, ρ_f the density of the pore fluid (assumed to be fresh water) and ρ_{log} the bulk density as measured by the density tool (Rider and Kennedy, 2011). These data are best fit by the exponential curve:

$$\phi = \phi_0 e^{-z/D}$$

(Athy, 1930), with ϕ_0 the porosity of the sediment at the surface; z, burial depth of the sediment and D the decay constant for the exponential function. For the Cooper Basin, lithology porosity depth relationships are taken from Hall et al. (2016).

4.3.3.4 Paleowater depths

Estimates of paleowater depths in the Canning and Southern Carnarvon Basins are based on deposition environments reported in the WAPIMS biostratigraphic database and Geological Survey of Western Australia reports (Mory and Backhouse, 1997; Haines, 2004; Mory, 2010). Depositional environments were converted to paleowater depth using the zonation of Tipsword et al. (1966). The results suggest Canning and Southern Carnarvon deposition typically occurred in middle shelf environments (20-100 m depth) with some deposition taking place in outer shelf environments (100-200 m depth).

In the Cooper Basin, Deighton and Hill (1998) and Deighton et al. (2003) made estimates of paleowater depth from sedimentological and fossil content, which we used directly in the subsidence models. Fluvial and lacustrine deposition dominated in the Cooper Basin with water depths in the 0-60 m depth range. A Cretaceous marine incursion resulted in Eromanga deposition taking place in middle to outer shelf environments. Detailed paleowater depths are provided in Supplementary Fig. 4.3.

4.3.3.5 Backstripping procedure

Density and porosity of the sediment at depth is calculated following DiCaprio et al. (2009). Porosity of the sediment was determined assuming an exponential decay due to compaction. As in DiCaprio et al. (2009), the average porosity ($\overline{\phi}$) for a sedimentary unit of thickness z_s is given by:

$$\overline{\phi} = D\emptyset_0 \left(\frac{\left(e^{\left(\frac{-z_{bottom}}{D}\right)} - e^{\left(\frac{-z_{top}}{D}\right)} \right)}{z_s} \right).$$

Average density ($\overline{\rho}$) is calculated from:

$$\overline{\rho} = \rho_w \overline{\phi} + \rho_s (1 - \overline{\phi})$$

where ρ_s a given grain density and ρ_w the density of water (assumed to fill the pore space). The complete values of decay length, grain density and ranges of surface porosity are included in Appendix 3 Table A3.1. Sediments are de-compacted and removed back in time using the 1-D backstripping methodology of Steckler and Watts (1978). The main uncertainties in the backstripping workflow are discussed in Section 5.6.

4.3.4 Forward modelling of tectonic subsidence and anomalous vertical motion

Predictions of tectonic subsidence were calculated using a forward model of finite rifting (Jarvis and Mckenzie, 1980) in which rift duration, strain rate and beta factor are derived from fitting the backstripped data. The expression for theoretical subsidence is:

$$S(t) = \left(\frac{t_c(\rho_m - \rho_c)}{(\rho_a - \rho_w)}\right)\left(1 - \frac{1}{\beta}\right) - \left(\frac{\alpha\rho_m}{\rho_a - \rho_w}\right)\left(\int_0^a [T(z,t) - T(z,\infty)\mathrm{d}z]\right).$$

Where, β is the stretching factor; t_c, crustal thickness; ρ_m, mantle density (at 0ºC); ρ_c, crust density (at 0ºC); ρ_a, asthenosphere density (at 1330ºC); ρ_w, water density; α, thermal expansion coefficient; a, lithosphere thickness; $T(z,t)$ the temperature of the lithosphere as a function of depth and time and; $T(z,\infty)$ the equilibrium temperature structure of the lithosphere. We preformed 1D strain rate inversions (White, 1993, 1994) to verify values of β obtained by trial and error (Appendix 3 Figs. A3.5 and A3.10). Values of the controlling parameters used in the forward model calculations are listed in Table 1. For a given continental crust thickness, lithospheric thickness was calculated to be isostatically equilibrated with mid-ocean ridges. We did not carry out a sensitivity analysis since the purpose of these forward models is to obtain a modelled tectonic subsidence history for comparison with the backstripped well data, as opposed to constraining subsidence parameters.

Model parameter	**Symbol**	**Value**	**Units**
Mantle density	0	3350	kg m^{-3}
Water density	w	1030	kg m^{-3}
Density of the continent	c	2780	kg m^{-3}
Thermal expansion coefficient	α	3.28×10^{-5}	K^{-1}
Temperature of the asthenosphere	T_1	1606	K
Thermal diffusivity	κ	8.04×10^{-7}	m^2 s^{-1}

Table 4.1: Values of physical parameters used in forward model of finite pure-shear lithospheric extension. α, T_1 and κ as in Jarvis and Mckenzie (1980).

Anomalous vertical motion was calculated by subtracting the total backstripped well subsidence from the theoretical subsidence model (Xie et al., 2006; Sutherland et al., 2010; Flament et al., 2013a). Positive anomalous vertical motion indicates uplift while negative anomalous vertical motion indicates subsidence. We linearly interpolated dynamic topography to sample it at the ages for which the subsidence history is

constrained. Anomalous vertical motion, dynamic topography and documented tectonic events can be analysed for the wells in each basin to gain insights into the contribution of mantle flow to observed tectonic subsidence (Xie et al., 2006; Sutherland et al., 2010; Flament et al., 2013a; Vibe et al., 2018a, b). We calculated the first derivatives of anomalous motion and dynamic topography to assess synchronicity in their trends. When the first derivatives of dynamic topography and anomalous motion are of the same sign and no tectonism is documented, mantle flow may be considered a plausible contributing mechanism for anomalous motion; although sea level variations and/or undocumented tectonism remain alternative mechanisms.

4.4. Results

4.4.1 Basin subsidence and uplift history: backstripping analysis of borehole data

4.4.1.1 Cooper/ Eromanga Basin

Tectonic subsidence curves from the Cooper/Eromanga Basin (Fig. 4.2) are characterised by three periods of subsidence: Late Carboniferous-Late Triassic (300-240 Ma), Late Triassic-Early Cretaceous (200-100 Ma) and Early-Late Cretaceous (100-90 Ma). Total tectonic subsidence ranges between 1,400-1,800 m and non-rift related subsidence from Late Carboniferous-Early Cretaceous is approximately exponential. Rates of subsidence in the initial phase (Late Carboniferous-Late Triassic) are moderate, varying 10-20 m/Myr between depocenters. The maximum subsidence occurs in the central Nappamerri Trough (Fig. 4.2) with rates decreasing at the southwestern edge of the depocenter. Late Permian (~ 270 Ma) uplift at ~ 10 m/Myr affected the majority of Cooper Basin wells.

Localised Late Triassic deposition (Patchawarra, Windorah and Arrabury Troughs; Fig. 4.2) marks the start of the Eromanga succession. Late Triassic-Early Cretaceous subsidence is generally 400-600 m. Rates of subsidence increased to ~ 40 m/Myr during the Late Cretaceous (~ 110 Ma) (Fig. 4.2) with lower rates in the Nappamerri Trough (~ 40 m/Myr) and largest rates in the Patchawarra Trough (50 m/Myr).

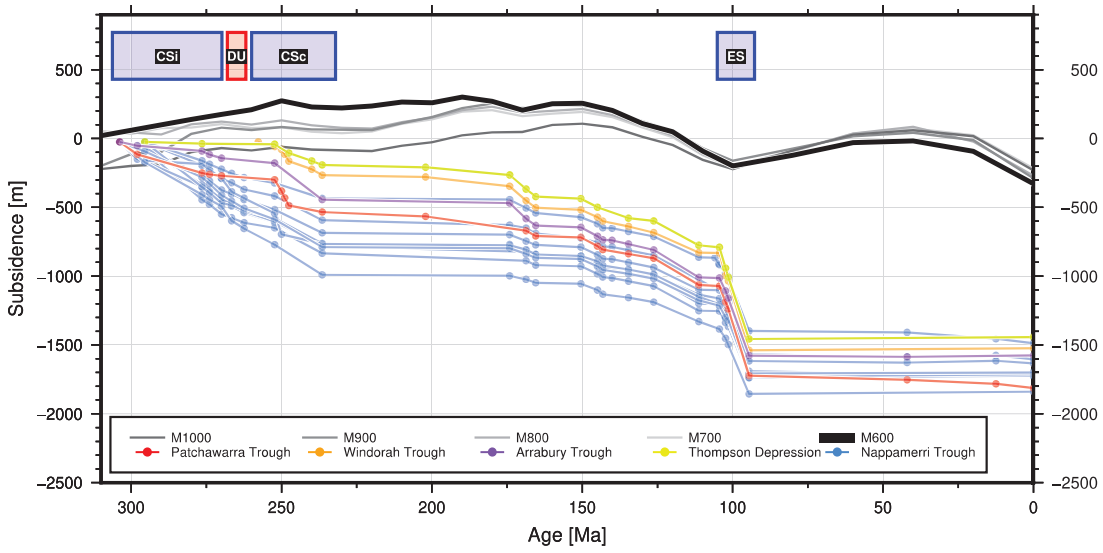

Figure 4.2: Backstripped, air-loaded tectonic subsidence (coloured) for the Cooper Basin, and modelled dynamic topography cases M1000-M600 (grey scale). Tectonic subsidence curves for the analysed wells are grouped and coloured by tectonic region. Episodes of subsidence discussed in the text are highlighted in maroon. Well locations are shown on Figure 1. Red and blue bars mark intervals of major uplift/non-deposition and subsidence, respectively (see text). CSi, Initial Cooper subsidence; DU, Daralingie compressional event; CSc, continued Cooper subsidence and ES, Eromanga Basin subsidence.

4.4.1.2 Canning Basin

Four subsidence phases are identified in the Canning Basin wells (Fig. 4.3); following Shaw et al. (1994): Early Ordovician-Silurian (480-440 Ma) Samphire Marsh extension; Early Devonian-Carboniferous (390-340 Ma) Pillara subsidence ; early Permian-Early Triassic (300-250 Ma) Point Moody extension and Late Jurassic-Early Cretaceous subsidence (160-130 Ma). These phases are separated by uplift-erosional episodes: the Prices Creek Movement (410 Ma); Meda Transpression (330 Ma) and Fitzroy Transpression (200 Ma) (Kennard et al., 1994a; Shaw et al., 1994).

Subsidence rates during Samphire Marsh extension vary between 10-30 m/Myr with greater rates in the Kidson, Willara and Gunbarrel Sub-basins, and on the Mowla Terrace (Fig. 4.3) where subsidence was dominantly controlled by extensional faulting (Romine et al., 1994; Shaw et al., 1994). In the inner regions of the Lennard Shelf and Pender Terrace (Fig. 4.3) the Prices Creek Movement eroded strata deposited during this subsidence phase (Kennard et al., 1994a).

During Pillara extension, growth faults (Shaw et al., 1994) resulted in tectonic subsidence of the Lennard Shelf and Pender and Jurgunna Terraces at up to ~20 m/Myr (Fig. 4.3). Between 3,500-4,000 m of tectonic subsidence is reported for the southern margin of Fitzroy Trough during this period (Kennard et al., 1994a). Other areas of the Canning Basin (Broome Platform, Willara and Kidson Sub-basins) were apparently unaffected by this subsidence (Fig. 4.3).

In the analysed wells, Point Moody (300-250 Ma) extension is marked by rapid subsidence rates between 80-250 m/Myr in the Kidson and Gunbarrel Sub-basins and 50-80 m/Myr on the Lennard and Pender Terraces, and the Willara Sub-basin (Fig. 4.3). Subsidence in the Kidson and Gunbarrel Sub-basins during the early Permian (from 290 Ma) may have been augmented by their proximity to the Central Australian Alice Spring Orogeny and/or crustal responses to continental glaciation. Total tectonic subsidence for Point Moody extension ranges between 200-600 m (Fig. 4.3); it is greatest in wells located adjacent to major fault complexes on the Lennard and Pender Terraces (Shaw et al., 1994).

A mild phase of Late Jurassic-Early Cretaceous subsidence (130-300 m) is apparent on the Pender and Jurgurra Terraces, the Broome Platform, and the Willara and Gunbarrel Sub-basins (Fig. 4.3).

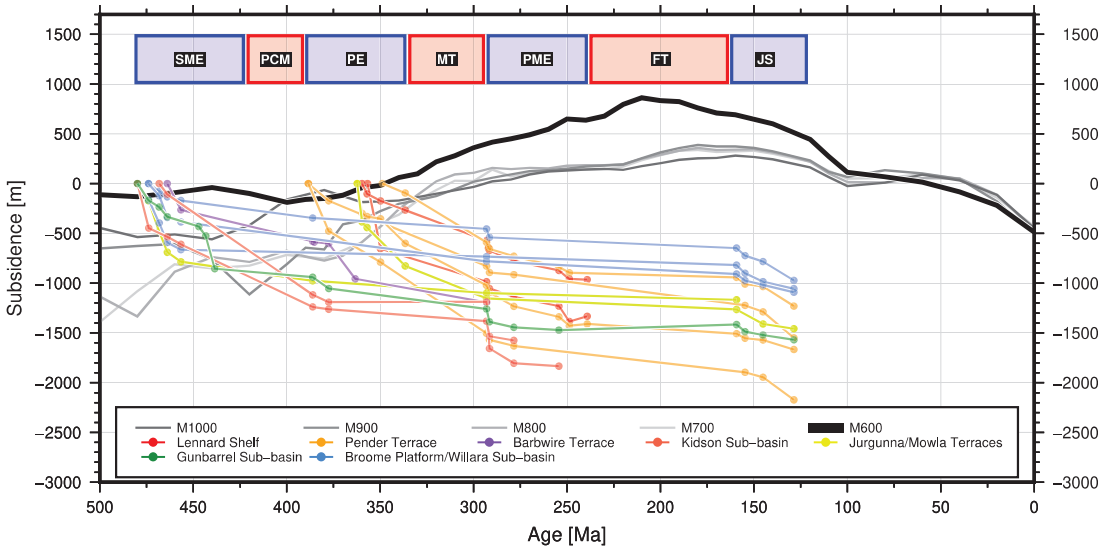

Figure 4.3: Backstripped, water-loaded tectonic subsidence (coloured) for the Canning Basin, and modelled dynamic topography cases M1000-M600 (grey scale). Tectonic subsidence curves for the analysed wells are grouped and colored by tectonic region. Episodes of subsidence discussed in the text highlighted in green. Well locations are shown on Figure 1. Red and blue bars mark intervals of major uplift/non-deposition and subsidence, respectively (see text). SME, Samphire Marsh extension; PCM, Prices Creek Movement; PE, Pillara extension; MT, Meda Transpression; PME, Point Moody extension; FT, Fitzroy Transpression; JS, Jurassic-Cretaceous subsidence.

4.4.1.3 Southern Carnarvon Basin

Three subsidence phases are evident in the Southern Carnarvon subsidence curves: Ordovician-Devonian (440-410 Ma) on the Gascoyne Platform, Carboniferous-Triassic (330-240 Ma) in the Merlinleigh Sub-basin and Early-Late Cretaceous (140-90 Ma) across the basin area (Fig. 4.4). Subsidence in the basin was initiated by extensional events and was followed by periods of erosion/non-deposition.

Gascoyne Platform wells indicate moderate subsidence (~20 m/Myr) during the Ordovician-Devonian (Fig. 4.4); with the exception of a shallow stratigraphic bore (Chargoo-1; Fig. 4.1). Up to 1,000 m of subsidence during this stage was recorded at well Yaringa-1 (Fig. 4.1), adjacent to a major fault (Iasky and Mory, 1999). A long-lived period of non-deposition/erosion occurred on the Gascoyne Platform following this subsidence (Fig. 4.4) and basin modelling constrained by AFTA and vitrinite reflectance data indicate between 1,550 m and 1,800 m of strata was removed before deposition recommenced in Cretaceous times (Ghori, 1999).

The Merlinleigh Sub-basin (Fig. 4.1) underwent Late Carboniferous-Permian rifting that resulted in total tectonic subsidence ranging between 200 m (Hope Island-1; Fig. 4.1) and 1,200 m (Kennedy Range-1; Fig. 4.1). Rapid subsidence (~40 m/Myr; Fig. 4.4) during these times is coeval with the development of en échelon faults (Iasky et al., 1998). Lower Permian uplift of the Merlinleigh Sub-basin is interpreted to represent a period of sedimentary oversupply associated with tectonism (Mory et al., 2003). Ghori (1999) estimated 1,800 m of strata was eroded during this period following initial rifting. As in the Gascoyne Platform, post-rift subsidence is not recorded in the Merlinleigh Sub-basin due to non-deposition/erosion. A final phase of low-moderate Cretaceous subsidence (1-20 m/Myr; Fig. 4.4) occurred during the break-up of Gondwana during which rates of tectonic subsidence range between 250 m inland to 650 m closer to the locus of extension on the northwest margin.

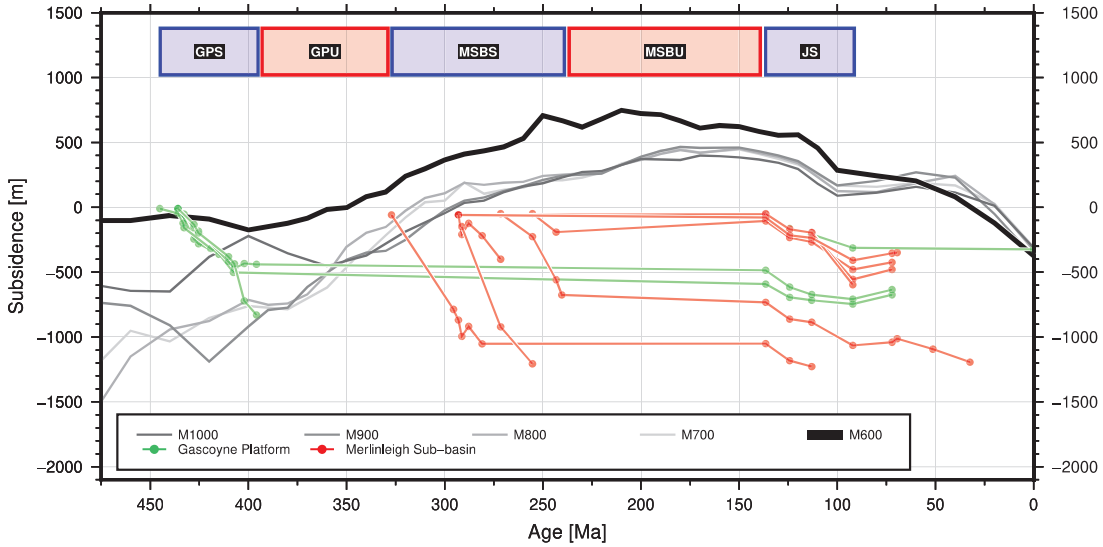

Figure 4.4: Backstripped, water-loaded tectonic subsidence (coloured) for the Southern Carnarvon Basin, and modelled dynamic topography cases M1000-M600 (grey scale). Tectonic subsidence curves for the analysed wells are grouped and coloured by tectonic region. Episodes of subsidence discussed in the text highlighted in blue. Well locations are shown on Fig. 4.1. Red and blue bars mark intervals of major uplift/non-deposition and subsidence, respectively (see text). GPS, Gascoyne Platform subsidence; Gascoyne Platform uplift; MSBS, Merlinleigh Sub-basin subsidence; MSBU, Merlinleigh Sub-basin uplift; JS, Jurassic subsidence.

4.4.2 Dynamic topography

To investigate the influence of mantle flow on the subsidence histories of Australian sedimentary basins, we computed time-dependent dynamic topography from forward models of global mantle flow constrained by a global tectonic reconstruction. The amplitude of dynamic topography for a point central to each basin (Fig. 4.1) was extracted from the model in 20 Myr increments from 600 Ma to present (Fig. 4.5), with a temporal refinement to 10 Myr increments applied between 300-100 Ma. We present results for case M600, which is preferred (see Section 4.3).

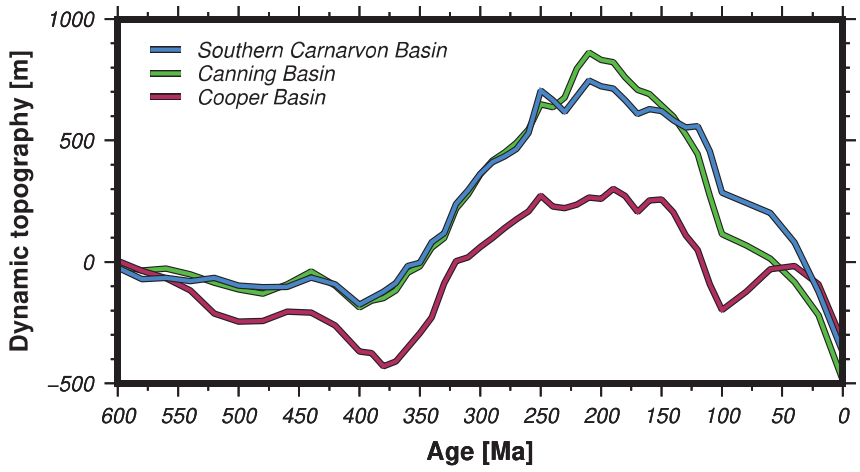

Figure 4.5: Evolution of model case M600 dynamic topography for the basins evaluated in this study. Dynamic topography was extracted at 20 Myr increments from 600 Ma to present, with temporal refinement to 10 Myr increments between 300 Ma and 100 Ma. Southern Carnarvon Basin, blue; Canning Basin, green and Cooper Basin, maroon.

While there is an amplitude difference of ~200 m between the two regions, the dynamic topography histories of the western Australian basins and the Cooper Basin have a similar overall trend (Fig. 4.5). This is expected because of the long-wavelength nature of the dynamic topography predicted by these models (Flament, 2019b). From 600-525 Ma dynamic topography is negative across the basins. During middle Cambrian times (525 Ma) ~200 m of dynamic subsidence associated with subduction along east Australia (Fig. 4.6) occurred in the Cooper Basin. This subsidence did not affect Western Australia, as it was too far away to be influenced by the subduction zone on the eastern margin of Australia (Figs 4.5 and 4.6).

Uplift in all three basins: 790 m in the western Australian basins and 670 m in the Cooper Basin (Fig. 4.5) occurred during Devonian-Permian times and is related to broad mantle upwelling above a deep thermochemical structure in the lower mantle (Fig. 4.7A-B). Dynamic topography peaked at 250 Ma in each basin: 270 m in the Cooper Basin, 650 m in the Canning Basin and 710 m in the Southern Carnarvon Basin (Fig. 4.5). In the western Australian basins, a plume (Figs 4.7 and 4.8) augmented the uplift produced by the whole-mantle upwelling whereas in the Cooper Basin, uplift was the result of dynamic rebound following the sinking of an ancient slab.

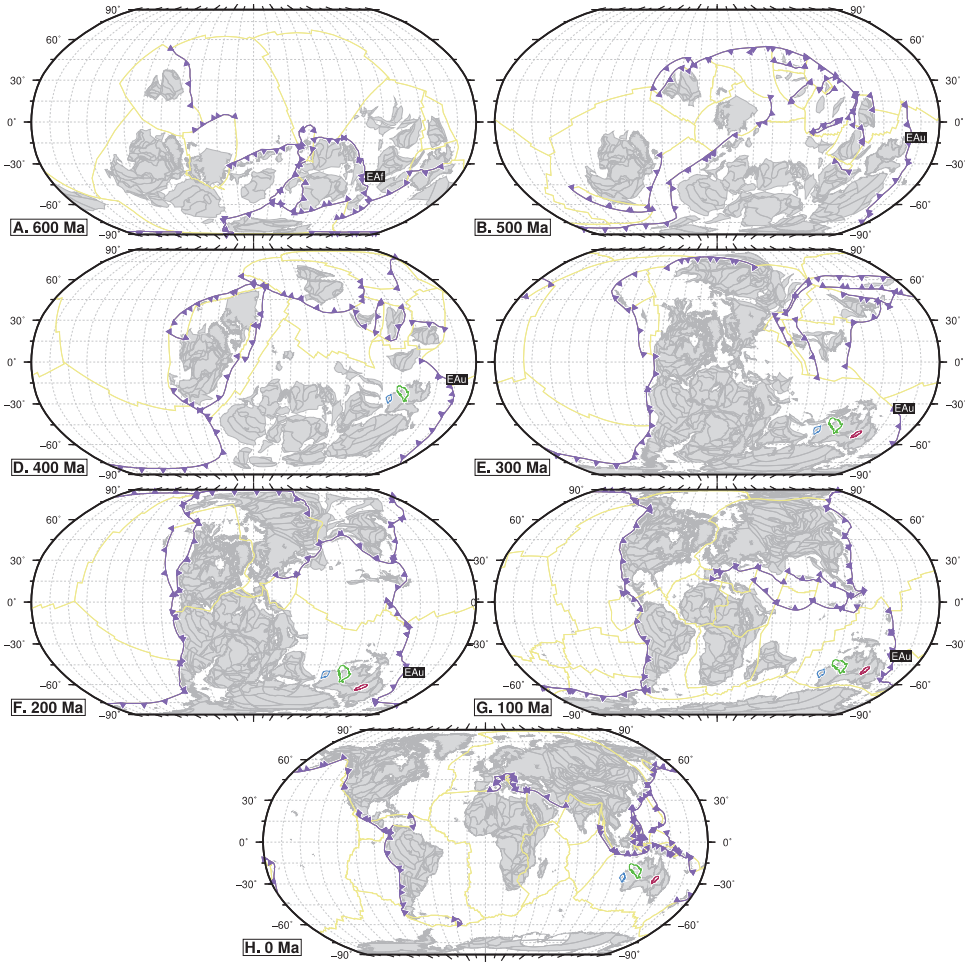

Figure 4.6: Global plate reconstructions in the no-net rotation frame of reference between 600 Ma and Present day in 100 Myr intervals. Purple lines with triangles on the overriding plate indicate subduction zones, and yellow lines denote mid-ocean ridges and transform faults. Reconstructed present-day coastlines (300-0 Ma) and craton outlines (600-400 Ma) are shown as grey polygons. The reconstructed outlines of the Southern Carnarvon, Canning and Cooper basins are shown in blue, green and maroon respectively. Abbreviations are: EAf, East Africa subduction zone; EAu, East Australia subduction zone.

In the Cooper Basin, dynamic uplift at 250 Ma is related to convergence and subduction between East Africa and India (EAf) during the East African Orogeny between 600-550 Ma (Collins and Pisarevsky, 2005; Fig. 4.6) which recycled cold lithosphere beneath Gondwana to ~700 km depth by 550 Ma. From 550-200 the slab proceeded slowly through the transition zone (Fig. 4.7B and D) due to trench retreat on the Gondwana eastern margin at an average rate of ~30 km/Myr; which we suggest is analogous to the Pacific slab under Japan since 40 Myr ago (Seton et al., 2015). From 500-200 Ma Australia drifted south (Fig. 4.6) so that in Permian times the slab was positioned under the Cooper Basin at depths between 500-1000 km (Fig. 4.7B). Contemporaneous subduction initiation along east Australian displaced the EAf slab, pushing it west and deeper into the mantle and away from the Cooper Basin (Fig. 4.7D-F). As the EAf slab sank, the dynamic subsidence it imposed on the surface decreased, resulting in uplift of the Cooper Basin (Figs 4.5 and 4.7F). Gurnis et al. (1998) proposed a similar scenario from regional geodynamic models of Australia from Cretaceous to the present-day; they described a subducted slab associated with Cretaceous Gondwana-Pacific convergence that stalled in the mantle beneath Australia for at least 50 Myr and dynamic uplift occurred when Australia drifted away from the slab. The Cambrian EAf slab lingered near the top of the lower mantle in a similar fashion, although for a longer period of time (250 Myr). By ~150 Ma the EAf slab had sunk to the core mantle boundary (Fig. 4.7); therefore, it cannot be identified in seismic tomography. We note that predicted cold mantle anomalies from younger slabs visually fit high velocity seismic anomalies in P-wave tomography model UU-P07 by Amaru (2007) (Supplementary Fig. 4.4D).

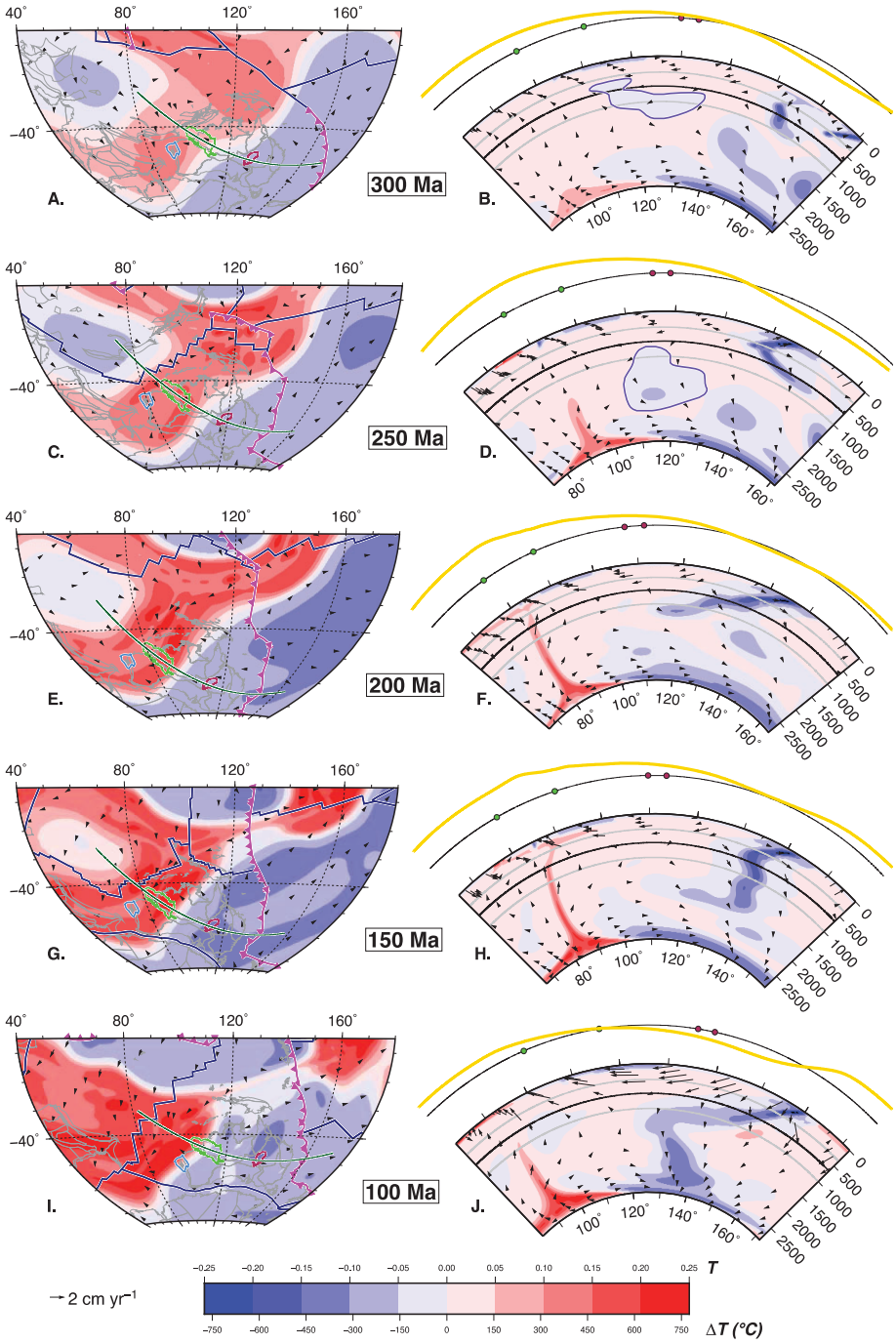

Figure 4.7: Predicted mantle temperature and flow velocity for case M600 at 2,677 km depth (A, C, E, G, I) and along cross-sections (dark green lines) over the Australian plate (B, D, F, H, J) in 50 Myr increments between 300 Ma and 100 Ma. In A, C, E, G and I reconstructed subduction locations are shown as magenta lines with triangles on the overriding plate, reconstructed mid-oceanic ridges and transform faults are shown as dark blue lines, and reconstructed present-day coastlines and craton outlines are shown in grey. Reconstructed positions of the Southern Carnarvon, Canning and Cooper basins are shown in blue, green and maroon respectively. In B, D, F, H and J the black line above each section is the global mean dynamic topography (by definition equal to zero) and the gold line is the 1.25x vertically exaggerated air-loaded dynamic topography along the cross-section. Green and maroon dots mark the intersection between the cross-section and the boundary of the Canning and Cooper basins respectively. Purple contour represents the limit of the Cambrian EAf slab (see Section 4.2). The color scale indicates non-dimensional (numbers above) and dimensional (numbers below) temperatures with respect to the ambient mantle temperature. Graticules at depths of 350 km (grey), 660 km (black) and 1,000 km (grey) are marked on the cross section.

Gondwana breakup began during the Jurassic (180 Ma) with India, Antarctica and Australia drifting east towards the Pacific Ocean (in the mantle reference frame; Fig. 4.6). During the Late Jurassic-Early Cretaceous (150-100 Ma) Australia moved over a dynamic topographic low caused by subduction along eastern Australia

(Fig. 4.7) resulting in 440 m of dynamic subsidence over 50 Myr (Fig. 4.5), which is consistent with the findings of Gurnis et al. (1998).

A long-lived phase of subsidence from 210 Ma is associated with Australia's eastward drift away from the deep mantle upwelling and waning plume. As stated above, from 150 Ma Australia drifted eastward over a slab, which imposed dynamic subsidence in Western Australia (Figs. 4.5 and 4.8).

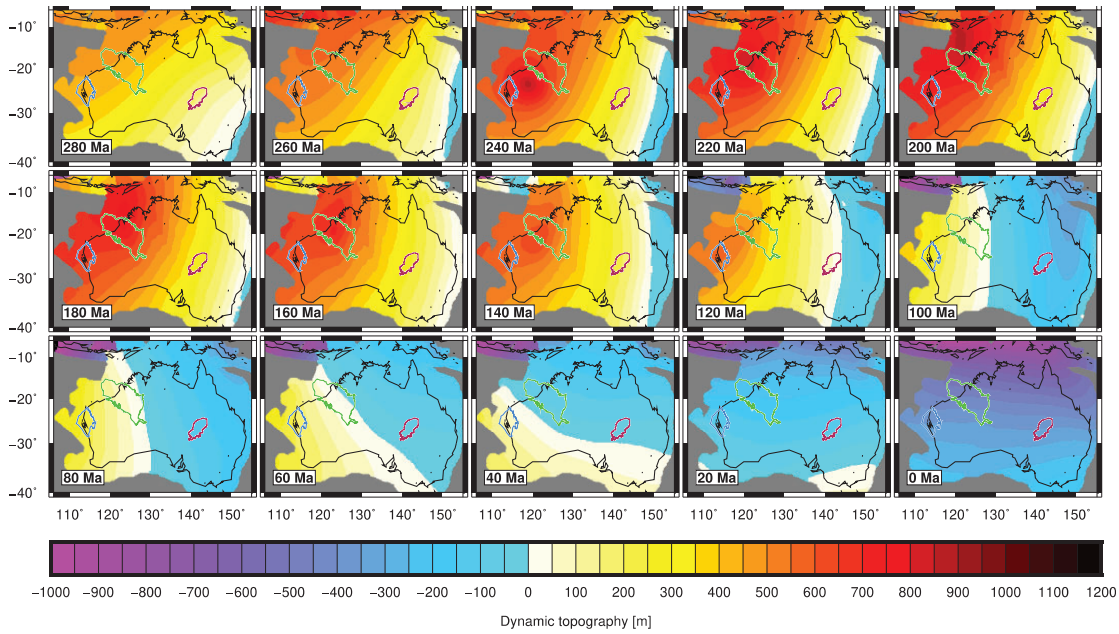

Figure 4.8: Air-loaded dynamic topography for case M600 over Australia in the plate-frame of reference from 300 Ma to the present in 20 Myr steps. Southern Carnarvon, Canning and Cooper basin outlines are shown in blue, green and maroon respectively.

4.4.3 Anomalous vertical motion

Where sufficient strata are preserved, theoretical models of subsidence were fit to the backstripped subsidence curves calculated from well data in order to determine anomalous vertical motion. We present the anomalous vertical motion results for a representative well in each basin (Figs 4.9-4.11; and Appendix 3 Figs. A3.3, A3.4, A3.9 and A3.9).

A forward-modelled tectonic subsidence curve with a stretching factor β = 1.18, a rift duration R_d = 30.5 Ma from 295 Ma and initial continental crustal thickness z_{cc0} = 40 km (Kennett et al., 2011) fits the Cooper Basin Moomba-27 (Fig. 4.1) subsidence curve (Fig. 4.9A). Subsidence is assumed to be air-loaded due to the dominantly terrestrial nature of Cooper Basin strata (Hall et al., 2015). The forward model predicts more subsidence than inferred from the well data from Permian to Late Jurassic times (270-150 Ma). Well subsidence exceeds theoretical subsidence from ~150 Ma, when subsidence of the Eromanga Basin initiated. Anomalous uplift events in the Permian and Late Triassic-Early Jurassic amount to ~150 m (Fig. 4.9B). Interestingly, dynamic uplift occurred during the Permian uplift event (Fig. 4.9). The Triassic uplift is compatible with dynamic topography, although it has been related to a major unconformity associated with northeast-southwest contraction (Kuang, 1985; Apak et al., 1997; Gravestock and Jensen-Schmidt, 1998). During the Cretaceous more than 600 m of anomalous subsidence is observed and the trends in subsidence and dynamic topography are consistent (Fig. 4.9C).

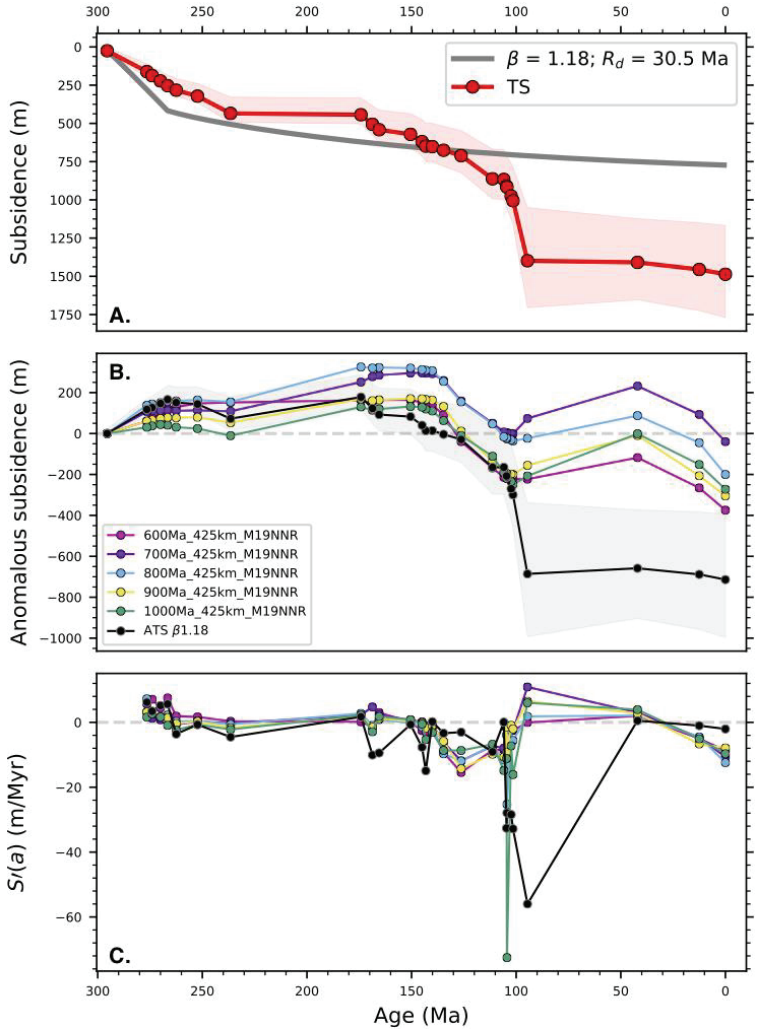

Figure 4.9: Comparison between observed tectonic subsidence, forward modelled tectonic subsidence and predicted dynamic topography for Moomba-27 well from the Cooper Basin (see Fig. 4.1 for location). A: Backstripped, water-loaded tectonic subsidence curve for Moomba-27 (red line and uncertainty envelope) and forward modelled best-fit tectonic subsidence (grey line) for stretching factor β and rift duration R_d. B: Dynamic topography for each case M600-M1000 in the Cooper Basin (coloured lines) and anomalous vertical motion (black line) for well Moomba-27, which is the difference between the backstripped subsidence (red line in A) and the forward modelled subsidence (grey line in A). Positive values represent anomalous uplift and negative values indicate anomalous subsidence. C: First derivatives of dynamic topography for each case M600-M1000 in the Cooper Basin (colour lines) and of anomalous vertical motions (black line). Positive values indicate uplift and negative values indicate subsidence (zero is shown as a grey dashed line).

Well Patience-2 from the Gunbarrel Sub-basin, south-eastern Canning Basin (Fig. 4.1) is fit by a forward-modelled tectonic subsidence with β = 1.2, rifting from 480 Ma with R_d = 41.4 Myr (Fig. 4.10A) and z_{cc0} = 35 km (Heine and Müller, 2008). Subsidence is water loaded as most Canning Basin strata were deposited in a marginal marine to marine environment (Forman and Wales, 1981; Kennard et al., 1994b; Romine et al., 1994). From 480-300 Ma the theoretical and backstripped curves for Patience-2 are generally equivalent (Fig. 4.10A). The theoretical model does not capture the ~300 Ma Point Moody extension and from this time on the tectonic subsidence and theoretical subsidence are out of phase (Fig. 4.10A). Uplift from ~250 Ma and subsidence at 150 Ma are observed in the well data and the modelled dynamic topography (Fig. 4.10 and Section 4.5).

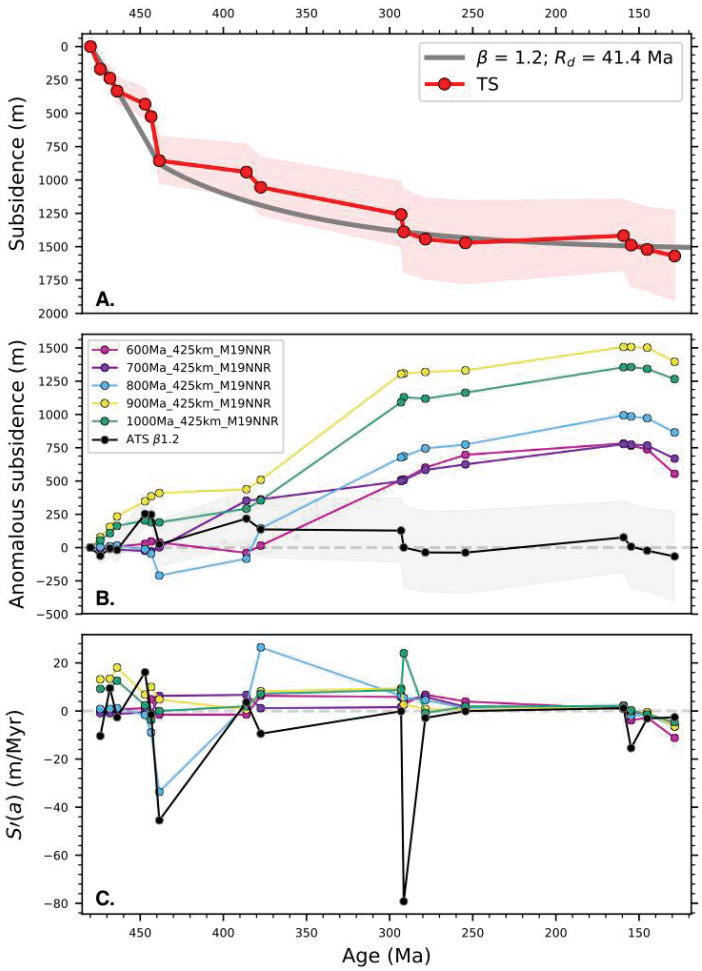

Figure 4.10: Comparison between observed tectonic subsidence, forward modelled tectonic subsidence and predicted dynamic topography for Patience-2 in the Canning Basin (see Fig. 4.1 for well location). A-D as in Fig. 4.9.

Well Cody-1 from the northernmost Merlinleigh Sub-basin, Southern Carnarvon Basin (Fig. 4.1) is fit by a forward-modelled water-loaded tectonic subsidence with a β = 1.13, rifting from 272 Ma with R_d = 31.2 Ma (Fig. 4.11A) and z_{cc0} = 35 km (Kennett et al., 2011). During late Paleozoic-Tertiary times the majority of deposition in the Merlinleigh Sub-basin occurred in marine conditions (Gorter et al., 1994; Iasky et al., 1998), therefore subsidence is water loaded. During rifting (~270-240 Ma) theoretical subsidence is greater than tectonic subsidence (Fig. 4.11A). A period of Triassic-Jurassic non-deposition/erosion is contemporaneous with ~100 m dynamic uplift (Fig. 4.11). A second period of rifting, related to Gondwana break-up, is seen in the well data from ~150 Ma (Fig. 4.11A) and is contemporaneous with model dynamic subsidence (Fig. 4.11C-B).

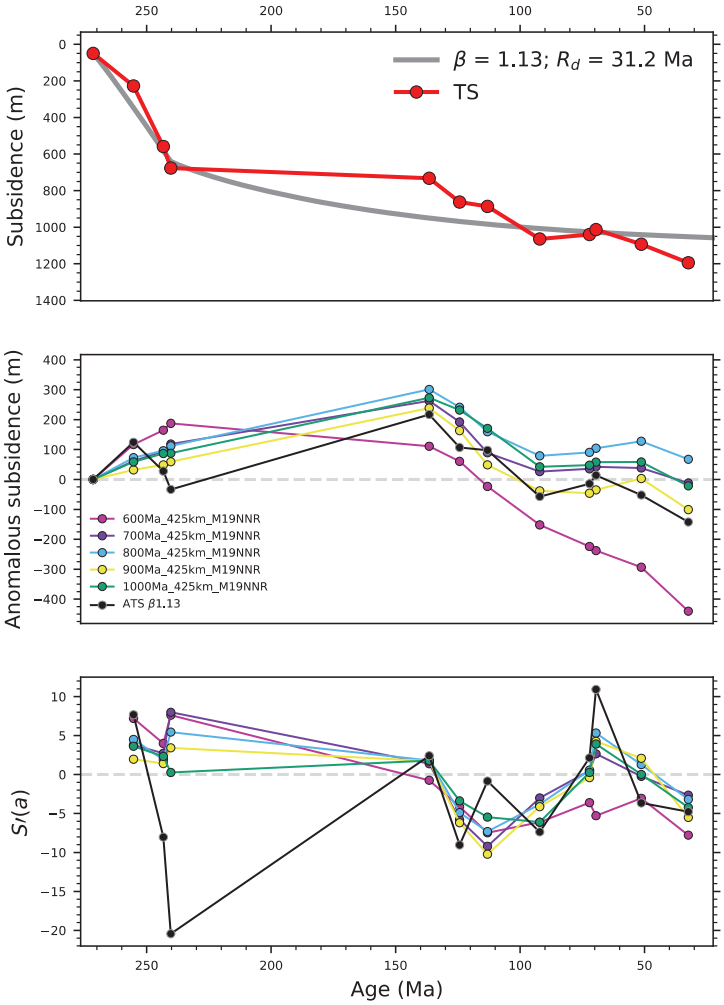

Figure 4.11: Comparison between observed tectonic subsidence, forward modelled tectonic subsidence and predicted dynamic topography for Cody-1 in the Southern Carnarvon Basin (see Fig. 4.1 for well location). A-D as in Fig. 4.9.

The mismatch between the predictions of dynamic topography and the results of the subsidence analysis demonstrate that the complex and long-lived subsidence histories of these intracontinental basins cannot be explained by a simple theoretical subsidence model which only considers lithospheric thinning by initial rifting and thermal subsidence. Subsidence is expected to be affected by other processes including changes in the intraplate stress field, eustatic sea-level change and dynamic topography. The match between dynamic topography and anomalous vertical motion across the Cooper, Canning and Southern Carnarvon Basins (see Appendix 3 Figs A3.13, A3.14 and Table A3.2) is best for model M600 which is used as reference case in the following.

4.5. Discussion

4.5.1 Subsidence due to local lithospheric stretching

The subsidence profiles examined here contain large (> ±200 m) deviations from predicted post-rift thermal subsidence, suggesting that other processes affected their subsidence histories. We attribute accelerated subsidence at ~380 Ma and ~290 Ma in the Canning Basin (Fig. 4.10) to the Pillara and Point Moody extensional events respectively, and accelerated subsidence at ~140 Ma in the Southern Carnarvon Basin

(Fig. 4.11) to extension on the northwest margin. We next consider mantle flow as a mechanism for other phases of anomalous vertical motions.

4.5.2 Influence of mantle flow on the Cooper Basin

Mid-Permian anomalous uplift occurs across all wells in the Cooper Basin and coincides with dynamic uplift (Fig. 4.9 and Appendix 3 Figs. A3.7-A3.9). Two episodes of middle Permian uplift, occurring at approximately 273 Ma and 270 Ma respectively, took place in the in the Cooper Basin and are suggested by stratigraphic, structural, seismic and palynology data (Apak, 1994; Apak et al., 1995; Apak et al., 1997). A denudation rate of ~10 m/Myr, determined from apatite fission track data, has been reported for the nearby Gawler Craton during the Permo-Triassic (Kohn et al., 2002) and is likely to be representative of the Cooper Basin during this time. We suggest mid-Permian uplift may be related to the gradual sinking of the EAf slab into the lower mantle (Fig. 4.7 and Section 4.2).

4.5.3 Permian-Early Jurassic uplift of Western Australia

Triassic-Jurassic strata are absent in the Canning (Kennard et al., 1994b) and Southern Carnarvon Basins (Iasky et al., 1998; Iasky and Mory, 1999; Iasky et al., 2003; Mory et al., 2003). In the Canning Basin, the hiatus is attributed to the Fitzroy Transpression which resulted in substantial uplift, erosion and development of contractional structures (Shaw et al., 1994; Parra Garcia et al., 2014), and in the Southern Carnarvon Basin uplift and erosion of the Late Jurassic successions (Mory et al., 2003) is implied by a cooling episode (Gibson et al., 1998).

Permian-Early Jurassic non-deposition/erosion in the Canning and Southern Carnarvon Basins has been linked to tectonic activity (Shaw et al., 1994; Mory et al., 2003; Parra Garcia et al., 2014). We note that during this time Australia drifted south (Young et al., 2019, Chapter 2) over a whole-mantle upwelling (Fig. 4.7), resulting in dynamic uplift of Western Australia, which would have contributed to the observed early Mesozoic non-deposition/erosion in Western Australia. Similarly, Müller et al. (2016a) attributed part of the mid-late Cenozoic dynamic uplift of north-eastern Australia, documented by Czarnota et al. (2014), to the motion of the plate over the Pacific Superswell.

4.5.4 Early Jurassic-Cretaceous subsidence of Australia

All Cooper Basin wells show rapid Cretaceous subsidence (Fig. 4.2). This subsidence phase is recognised as being non-tectonic as geological evidence for extension in the basin during these times is lacking (Zhou, 1989; Gallagher, 1989). The predicted mantle temperature (Fig. 4.7) shows the subduction of cold, dense material into the mantle along the Australian eastern margin from 260 Ma. Australia's eastward motion over the dynamic topographic low produced by the sinking slab resulted in widespread dynamic subsidence in Cretaceous times (Figs 4.7 and 4.8; Gurnis et al., 1998).

A number of Southern Carnarvon Basin wells (Fig. 4.4) show subsidence at ~130 Ma associated with the break-up of Australia from Greater India (Iasky et al., 1998; Iasky and Mory, 1999; Iasky et al., 2003). Our flow models indicate Late Jurassic dynamic subsidence of Western Australia (Figs 4.3 and 4.5) is synchronous with Jurassic-Cretaceous anomalous tectonic subsidence seen in the Canning and Southern Carnarvon Basin wells (Fig. 4.10-4.11 and Appendix 3 Figs. A3.3 and A3.4). At 150 Ma Australia was drifting east (Young et al.,

2019, Chapter 2), and this motion moved the continent away from the upwelling and towards a downwelling that had developed in response to late Permian (260 Ma) subduction along east Gondwanan (Figs 4.7 and 4.8), which continued throughout the Triassic, resulting in the formation of a prominent slab under Australia by 100 Ma (Fig. 4.7). Australia's motion away from the upwelling and towards the sinking slab caused a dynamic Jurassic-Cretaceous tilting of the plate down to the east (Fig. 4.8), contributing to coeval subsidence in the Canning (Figs 4.3 and 4.10) and Southern Carnarvon (Figs 4.4 and 4.11) Basins, and to the particularly rapid Cretaceous subsidence in the Cooper Basin (Figs 2 and 9); due to its proximity to the downwelling (Fig. 4.7). Given that Late Jurassic dynamic subsidence of Western Australia is contemporaneous with sea floor spreading in the Argo Abyssal Plain one might question its relationship to mantle convection. We note, however, that well Patience-2 is located ~1,200 km from the present-day continent-ocean boundary. It is unclear how distant seafloor spreading (> 1,200 km away) could explain the Late Jurassic subsidence recorded by well Patience-2.

4.5.5 West Australian mantle plume

Case M600 predicts the Triassic arrival of a plume under western Australia (Figs 4.7 and 4.12), which would have produced significant dynamic uplift (Fig. 4.8) consistent with episodes of non-deposition/uplift in the Canning (Fig. 4.3) and Southern Carnarvon (Fig. 4.4) Basins. The locations of mantle plumes predicted by models similar to the ones presented here have been shown to be statistically correlated with the location of large igneous provinces (LIPs) reconstructed to the present day (Hassan et al., 2015). However, the behaviour of model mantle plumes is stochastic, and deep active model upwelling similar to the Hawaiian (Hassan et al., 2016) and the Icelandic (Barnett-Moore et al., 2017) plumes are offset in time and space compared to the associated volcanic products. With this in mind, we note that Bryan and Ferrari (2013) and Rohrman (2015) reported a Late Jurassic (160 Ma) LIP offshore northwest Australia. In case M600 the plume erupts at 260 Ma, which is 100 Myr earlier than, and ~100 km away from the northwest Australian LIP; at 160 Ma the model plume is ~500 km away from the LIP (Fig. 4.12).

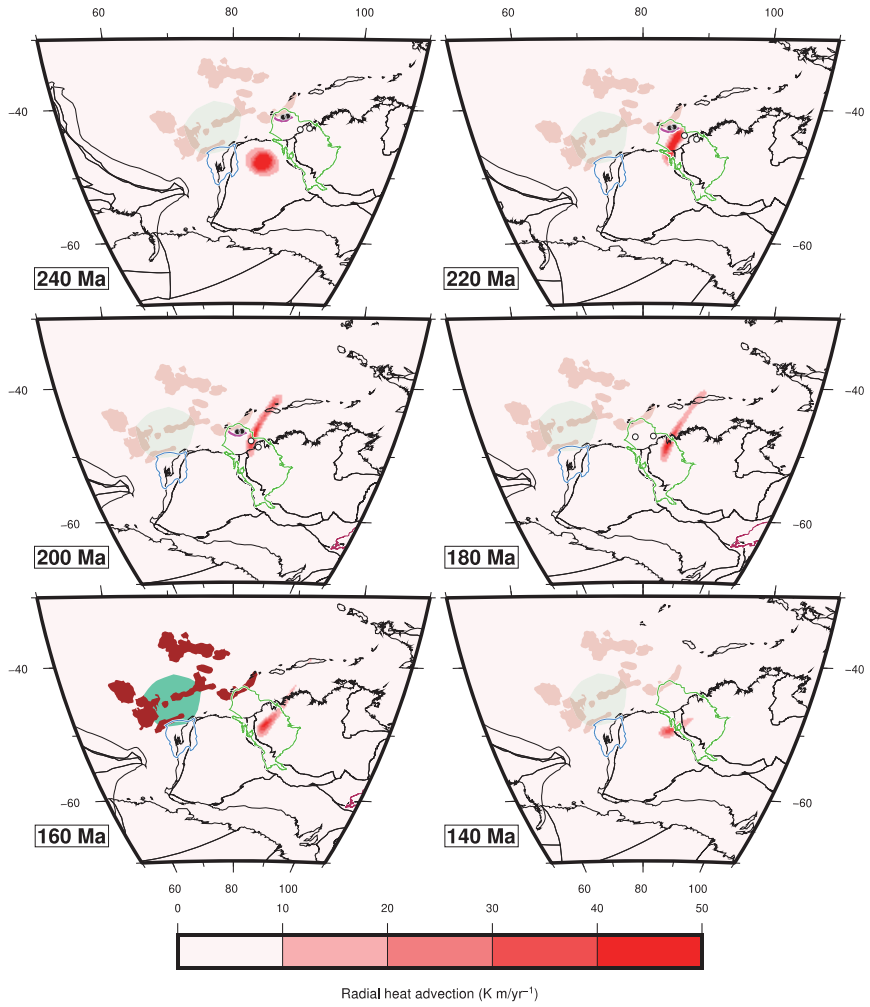

Figure 4.12: M600 plotted as radial heat advection, i.e. the product of mantle temperature and velocity for 240-140 Ma. Reconstructed positions of the Southern Carnarvon (blue), Canning Basin (green) and Cooper Basin (maroon) are shown. Reconstructed present-day coastlines and craton outlines are specified in black. Brown and aquamarine polygons indicate the reconstructed position of northwest Australia LIPs from Bryan and Ferrari (2013) and Rohrman (2015) respectively; these are highlighted at their extrusion age (160 Ma). Landward edge of Rowley Sub-basin volcanic coliforms from Abbott et al. (2019b) is marked by the magenta line. Locations of Canning Basin wells that intersect igneous rocks from Reeckmann and Mebberson (1984) are indicated by white circles and Rowley Sub-basin well intersections in black; the wells are only displayed at times which correspond to the probable age of the intrusions.

Regionally, evidence for Triassic igneous activity is reported at the north-west edge of the Canning Basin (Gleadow and Duddy, 1984; Reeckmann and Mebberson, 1984) and in the Rowley Sub-Basin (MacNeill et al., 2018; Abbott et al., 2019a). On the north-west shelf of Australia, late Permian uplift, faulting and tilting was accompanied by extensive intrusion and extrusion of mafic igneous rocks during the Bedout Movement (Forman and Wales, 1981), which is proposed to be either compressional based on observations of faulting, folding and erosion over the Bedout High (Shaw et al., 1994), or extensional (Forman and Wales, 1981; Reeckmann and Mebberson, 1984; Colwell and Stagg, 1994) and possibly caused by active mantle upwelling (Colwell et al., 1994) based on the extent of volcanism. This latter interpretation is consistent with the results for case M600.

Igneous rocks from Canning Basin wells (Fig. 4.12) yield K/Ar, fission track and stratigraphic ages ranging Permian-Early Jurassic (Forman and Wales, 1981; Gleadow and Duddy, 1984; Reeckmann and Mebberson, 1984; Colwell and Stagg, 1994); no precise dating of these rocks is currently available. Total magnetic intensity data indicate these volcanic rocks cover > 1,250 km^2 (Forman and Wales, 1981). The results

for case M600 and the spatio-temporal extent of igneous rocks on the north-west shelf of Australia suggest an active mantle upwelling could have affected the area between 250-170 Ma (Fig. 4.12).

Recent (2014) 3D seismic acquisition in the Rowley Sub-basin revealed clinoforms dipping 20°-30° landward, interpreted to represent a 10 km thick lava complex that prograded southeast from the Argo/West Burma landmass (MacNeill et al., 2018; Abbott et al., 2019b). Regional stratigraphy suggests the lava flows could be between 250-240 Myr old (MacNeill et al., 2018; Abbott et al., 2019a), and comparable seismic facies from the northwest Rowley Sub-basin may represent younger volcanism (240-210 Ma) (Abbott et al., 2019b). MacNeill et al. (2018) suggest an Early-Middle Triassic mantle plume could have produced the lava complexes; which is consistent with our model, in which a plume occurs within 10 Myr and 650 km of the Rowley Sub-basin lava flows (Fig. 4.12).

4.5.6 Comparison with apatite fission track data

AFTA is an established method to reconstruct the low-temperature thermal evolution of continental crust (Kohn et al., 2002; Flowers et al., 2012; Zhang et al., 2012). Published data from key Australian terranes (Kohn et al., 2002) constrain the long-wavelength patterns of Australian epeirogeny since 300 Ma. The denudation rates generally increased during the Permo-Triassic and decreased from the Jurassic to present-day (Kohn et al., 2002). Our dynamic topography predictions are consistent with this first-order result (Fig. 4.5). In particular, there is a spatio-temporal overlap between the Permo-Triassic dynamic uplift of Western Australia and regional cooling/denudation implied from AFTA, and Cretaceous dynamic subsidence in the Cooper Basin and the inundation/burial of the Gawler Craton (Kohn et al., 2002; Supplementary Fig. 4.5).

4.5.7 Uncertainties

Our study is prone to a number of uncertainties, the first of which is linked to the global plate reconstruction spanning 1,000-0 Ma (Merdith et al., 2021) and relies on paleomagnetic and geological evidence from the continents for times before 180 Ma; for which little to no seafloor is preserved (Müller et al., 2016b). Plate velocities and the location of plate boundaries constitute time-dependent boundary conditions for the geodynamic models, however, due to the lack of data, the majority of oceanic plates and mid-ocean ridges within the plate reconstruction are synthetic and inferred rather than observed. Hence, the velocity of ancient oceanic plates is poorly constrained. Despite these uncertainties, synthetic plate velocities in the Merdith et al. (2021) reconstruction are of the same order of magnitude observed at present-day (~2-20 cm/yr). Continental plate motions are based on a combination of data (e.g., paleomagnetism, episodes of volcanism/metamorphism), diagnostic geoscience (e.g., palynology/paleogeography correlation) and kinematic and geodynamic criteria (e.g., tectonic speed limits, trench kinematics; see Young et al., 2019, Chapter 2). Fortunately, oceanic and continental arcs are generally well preserved, giving some confidence to the reconstruction of past subduction zones (Cao et al., 2017a; Merdith et al., 2019). While uncertainties exist, the Merdith et al. (2021) reconstruction is the first and only full-plate global model available back to 1 Ga and offers a unique opportunity to explore Earth's history in deep geological time.

Uncertainties in the mantle convection model input parameters include the viscosity structure of the mantle, Rayleigh number, dissipation number, initial slab depth and initial thickness of the lower thermal boundary layer. The input parameters of our forward flow models were taken from the preferred model of

Flament (2019b), who investigated the effect of model boundary conditions, set-up and physical assumptions on the predicted present-day dynamic topography and mantle structure constrained by independent data. We investigated the sensitivity of mantle flow and associated dynamic topography to model start time (Bunge et al., 1998; Flament et al., 2017a; Flament, 2019b). The overall trends between the different cases are consistent, although there are temporal and amplitude offsets in dynamic topography (Figs 2, 3 and 4). For example: M600 only integrates the final stages of subduction during Gondwana assembly (Merdith et al., 2017) and thus accumulates less slab material beneath the continent by ~400 Ma, resulting in larger uplift through the late Paleozoic (Figs 4.2, 4.3 and 4.4).

We computed dynamic topography from sources of buoyancy deeper than 350 km. We note that both the lithospheric mantle would elastically filter long-wavelength dynamic topography from deep sources (Golle et al., 2012; Sembroni et al., 2017) and that the uppermost mantle would add short-wavelength dynamic topography of relatively large amplitude (Hoggard et al., 2016; Davies et al., 2019); however, it remains difficult to determine the present-day thermochemical structure of the mantle lithosphere, let alone to model is temporal evolution. Thus, we focus on long-wavelength dynamic topography, which can be modelled back in time. As a consequence, the predicted rate of change of long-wavelength dynamic topography is relatively low and tends to be less than that of tectonic subsidence. For instance, the Cretaceous tectonic subsidence of the Cooper Basin is ~70 m/Myr while the dynamic subsidence is ~10 m/Myr (Fig. 4.9). Short-wavelength dynamic topography might evolve at rates up to ~200 m/Myr (Roberts and White, 2010; Czarnota et al., 2013; Winterbourne et al., 2014) and could reconcile this discrepancy. Nevertheless, the predicted present-day dynamic topography (Fig. 4.8) is consistent with previous studies showing a north-south trending pattern of long-wavelength dynamic topography across Australia (Lithgow-Bertelloni and Richards, 1998; Sandiford, 2007; DiCaprio et al., 2009; Heine et al., 2010; DiCaprio et al., 2011; Czarnota et al., 2014; Flament, 2019b).

The main potential sources of uncertainty in the backstripping analysis are the accuracy of formation age, thickness and compaction inputs as well as paleo-water depth estimates. The use of lithostratigraphy rather than chronostratigraphy results in significant uncertainty and as a result, assigned ages are estimates only. A full sequence stratigraphic analysis of the basins would be required to determine this uncertainty, which is beyond the scope of this work. Additionally, there is uncertainty in comparing stratigraphic to absolute model ages. Here we considered ages to be determined within 1 Myr. Due to the large dispersion of log derived porosity values at a given depth, for each lithology an envelope was built around the best fit function by increasing and decreasing the base case surface porosity by 50% (Appendix 3 Table A3.1 and Supplementary Fig. 4.6) to test the sensitivity of the subsidence models to porosity variability. Paleo-water depths were converted from environments of deposition (Tipsword et al., 1966) resulting in uncertainties up to 100 m. We quantified the uncertainty in backstripped tectonic subsidence due to uncertainties in porosity and paleowater depth (Figs 4.9-4.11 and Appendix 3 Figs A3.2 and A3.7). Subsidence uncertainty ranges 50-730 m in Cooper Basin wells; 0-790 m in Canning Basin wells; and 100-320 m in Southern Carnarvon Basin wells. There is uncertainty introduced by wells that do not penetrate the deeper stratigraphic record of the basin. However, most of the considered wells (14/14 Cooper wells, 11/15 Canning wells and 10/13 Southern Carnarvon) including Patience-2, Cody-1 and Moomba-27 penetrate the deepest 80 % of the section so the uncertainty is relatively small here.

Our subsidence results for the Canning and Cooper Basins are consistent with the analysis of Kennard et al. (1994a) and Hall et al. (2016) respectively. We did not include eustatic sea-level changes in the

backstripping procedure, although deviations between inferred and idealised subsidence can commonly be attributed to changes in eustatic sea-level (Xie and Heller, 2009). The Cooper Basin has been mostly subaerial since Permian times (Isem et al., 2001) thus, the impact of eustatic sea-level on its subsidence history is likely to have been minor. However, for the western Australian basins, which have pre-Permian history dominated by marine deposition, the impact of eustatic sea-level change may be significant. Despite the sensitivity of subsidence modelling to eustatic sea-level changes, we opted not to use available Paleozoic global sea level curves that vary greatly (Vail et al., 1977; Hallam, 1984; Algeo and Seslavinsky, 1995; Haq and Schutter, 2008; Vérard et al., 2015).

4.6. Conclusion

The subsidence histories of intracontinental basins display complex vertical motion histories. Various interacting tectonic mechanism have been invoked to explain these deviations including plume-lithosphere interaction and mantle downwelling. We backstripped well data and produced tectonic subsidence curves for the Canning, Southern Carnarvon and Cooper Basins in order to investigate if mantle flow could have contributed to their complex histories. We analysed episodes of anomalous vertical motion by combining backstripped well subsidence and forward pure shear models, and compared them, in the light of documented tectonic events, to predictions of long-wavelength dynamic topography for the past 600 Myr. Our results suggest that mantle flow could have contributed to the evolution of the Canning, Southern Carnarvon and Cooper Basins, in addition to tectonic processes. In the Cooper Basin, topographic rebound following the sinking of an ancient slab resulted in minor dynamic uplift that may be recorded in the mid-Permian strata of the basin. During Triassic-Jurassic times tectonic uplift, augmented dynamic uplift, resulted in significant erosion in the Canning and Southern Carnarvon Basins. During the Late Jurassic-Cretaceous Gondwana break-up, Australia drifted east away from a mantle upwelling and towards a downwelling produced by Permian subduction. This motion resulted in an episode of dynamic subsidence that is coeval with subsidence in the Canning and Southern Carnarvon Basins. Our models confirm Permian subduction along the east Australian convergent margin produced a downwelling over which the Cooper Basin passed during the Cretaceous, resulting in accelerated subsidence.

4.7. Supplementary material

This section presents details of the geodynamic workflow previewed in the main text, provides the complete results of our subsidence analysis and classification of backstripping uncertainties.

4.7.1. Numerical model of mantle flow and lithospheric deformation

Here we present the equations solved for mantle convection (see also Hassan et al., 2015). Parameters common to all models are presented in Supplementary Table 4.1.

Model parameter	**Symbol**	**Value**	**Units**
Thermal diffusivity	κ_0	1×10^{-6}	$m^2\ s^{-1}$
Rayleigh number	Ra	7.8×10^7	
Dissipation number	Di	1.56	
Reference thermal expansion coefficient	α_0	3×10^{-5}	K^{-1}
Reference density	ρ_0	4000	$kg\ m^{-3}$
Gravity acceleration	g_0	9.81	$m\ s^{-2}$
Temperature change	ΔT	3100	K
Mantle thickness	h_M	2867×10^3	m
Viscosity	η_0	1.1×10^{21}	Pa s
Total internal heating	H	33.5	TW
Surface temperature	T_s	521	K
Specific heat capacity	C_{P_0}	1200	$J\ kg^{-1}\ K^{-1}$

Supplementary Table 4.1: Parameters common to all mantle convection model cases. Subscript "0" indicates reference values.

The conservation of mass is:

$$\nabla \cdot \mathbf{u} = 0$$

where **u** is velocity. The non-dimensional conservation of momentum is:

$$-\nabla P + \nabla \cdot \tau = (CB - \alpha T) g Ra e_r$$

where P, τ, C, B, α, T, Ra, g, and e_r are the dynamic pressure, deviatoric stress tensor, proportion of compositionally-distinct material, the ratio of chemical density anomaly to the maximum thermal density anomaly in the system, coefficient of thermal expansion, temperature, Rayleigh number, acceleration due to gravity, and radial unit vector, respectively. B is defined as:

$$B = \frac{\Delta\rho_{ch}}{\alpha_0 \rho_0 \Delta T}$$

where $\Delta\rho_{ch}$, ρ_0, and ΔT are the chemical density anomaly, density, and the total temperature drop across the mantle, respectively. Quantities subscripted with ''0'' represent dimensional reference values. The Rayleigh number is defined as:

$$Ra = \frac{\alpha_0 \rho_0 g_0 \Delta T h_M^3}{k_0 \eta_0}$$

where h_M, η_0, and κ_0 are the thickness of the whole mantle, viscosity, and thermal diffusivity, respectively. The conservation of energy is:

$$C_p \frac{\partial T}{\partial t} = -c_p \mathbf{u} \cdot \nabla \mathrm{T} + \nabla \cdot \left(c_p k \nabla T\right) - Di(T + T_s)\alpha g u_r + \frac{Di}{Ra}\tau : \dot{\epsilon} + H$$

where C_p, Di, T_s, $\dot{\epsilon}$, and H are the heat capacity at constant pressure, dissipation number, surface temperature, strain rate tensor, and internal heating rate, respectively. The dissipation number, *Di*, is defined as:

$$Di = \frac{\alpha_0 g_0 R_0}{C_{P_0}}.$$

Chemical advection is governed by:

$$\frac{\partial C}{\partial t} + (u \cdot \nabla)C = 0.$$

Composition is advected using tracer particles (McNamara and Zhong, 2004) and the ratio method (Tackley and King, 2003). Since the advection of tracers is computationally expensive (McNamara and Zhong, 2004), we limit the number of tracers in our models to 30 tracers per element initially and further reduce the computational cost of advecting tracers by removing ambient tracers between 410 and 2600 km depths and imposing C=0 in elements that contain no tracers.

4.7.2. Model set up and initial condition

The model consists of $129 \times 129 \times 65 \times 12 \approx 13 \times 10^6$ nodes which give a resolution of $\sim 50 \times 50 \times 15$ km at the surface, $\sim 40 \times 40 \times 100$ km in the mid-mantle and $\sim 28 \times 28 \times 27$ km at the core-mantle boundary (CMB).

As in Hassan et al. (2015) and Flament (2019b), we compute a reference profile for thermal expansion based on the analytical parameterizations of Tosi et al. (2013).

Mantle viscosity varies with temperature and depth following:

$$\eta = \eta(r)\, \eta_0 (1 + \eta_C C) \exp\left\{\frac{\left[E_\eta + Z_\eta (R_0 - r)\right]}{\left[R + \left(T + T_{off}\right)\right]} - \frac{\left[E_\eta + Z_\eta (R_0 - R_c)\right]}{\left[R\left(T_{CBM} + T_{off}\right)\right]}\right\}$$

where $\eta(r)$ is the viscosity for four layers equal to 2×10^{19} Pa s above 160 km depth, 2×10^{18} Pa s between 160-310 km depth, 2×10^{19} Pa s between 310-660 km depth and 2×10^{20} Pa s below 660 km depth (lower mantle). $\eta_0 = 1.1 \times 10^{21}$ Pa s is the reference viscosity, C is the composition field and $\eta_C = 100$ is the compositional viscosity pre-factor for the continental lithosphere. r is the radius; $R_C = 3504$ km which is the radius of the core and; $R_0 = 6371$ km, the Earth's radius. $E_\eta = 258$ kJ mol^{-1} is the activation energy; $Z_\eta = 1.9 \times 10^{-6}$ m^3 mol^{-1}, activation volume; $R = 8.31$ J mol^{-1} K^{-1}, universal gas constant; T, the dimensional temperature; $T_{off} = 452$ K, a temperature offset and $T_{CBM} = 3380$ K, the CMB temperature. The temperature offset is a constant that was adjusted together with the activation energy and activation volume to obtain variations in viscosity by three orders of magnitude over the range of considered temperatures and pressures. Horizontal averages of present- day mantle temperature and viscosity are shown in Supplementary Fig 4.1.

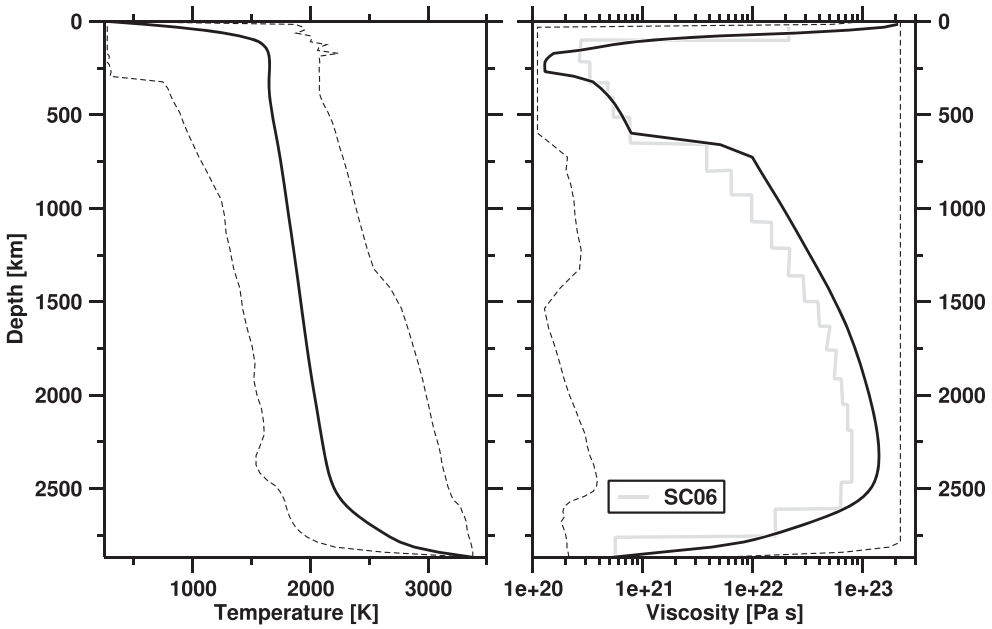

Supplementary Figure 4.1: Horizontally averaged present-day mantle temperature (left) and viscosity (right) for case M600. The solid lines indicate average values, and the dashed lines indicate minimum and maximum values. A published viscosity profile is given for reference; SC06: Steinberger and Calderwood (2006).

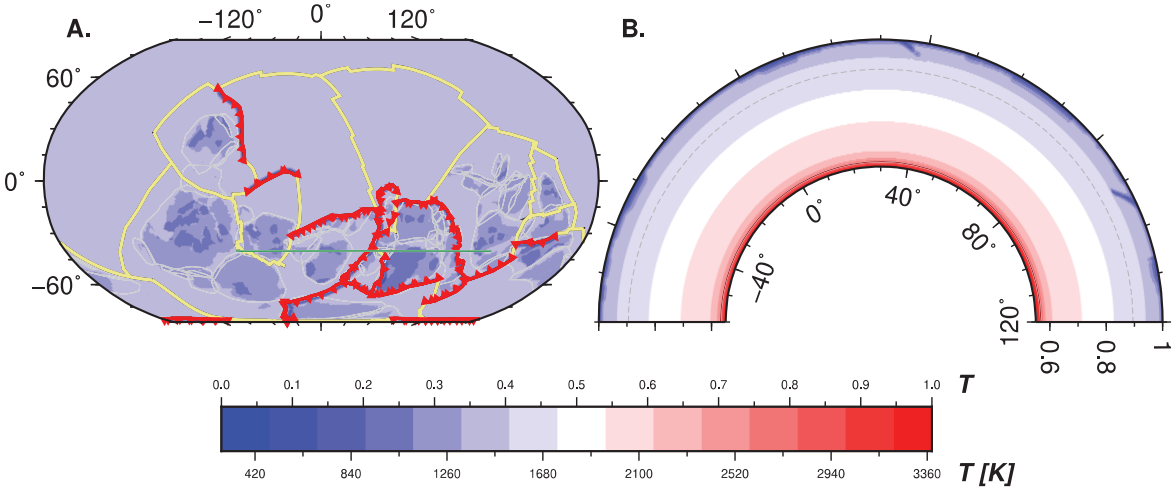

Supplementary Figure 4.2: Initial condition of mantle flow model at 600 Ma for case M600. (A) Mantle temperature at 124 km depth for case M600 at 600 Ma. Reconstructed subduction locations are shown as red lines with triangles on the overriding plate, reconstructed mid-oceanic ridges and transform faults are shown as yellow lines, and reconstructed present-day coastlines and craton outlines are shown in grey. The green line is the location of the cross-section shown in (B). (B) Mantle temperature along the cross-section shown in (A). The apparent dip along the cross-section is different from the dip of slabs in the direction perpendicular to the trench, which is 45º down to 425 km depth. The dashed grey line is the upper–lower-mantle boundary and the brown line outlines the chemically-distinct basal layer. Numbers above the colour palette refer to the non-dimensional temperature, and numbers below the colour palette to the dimensional temperature.

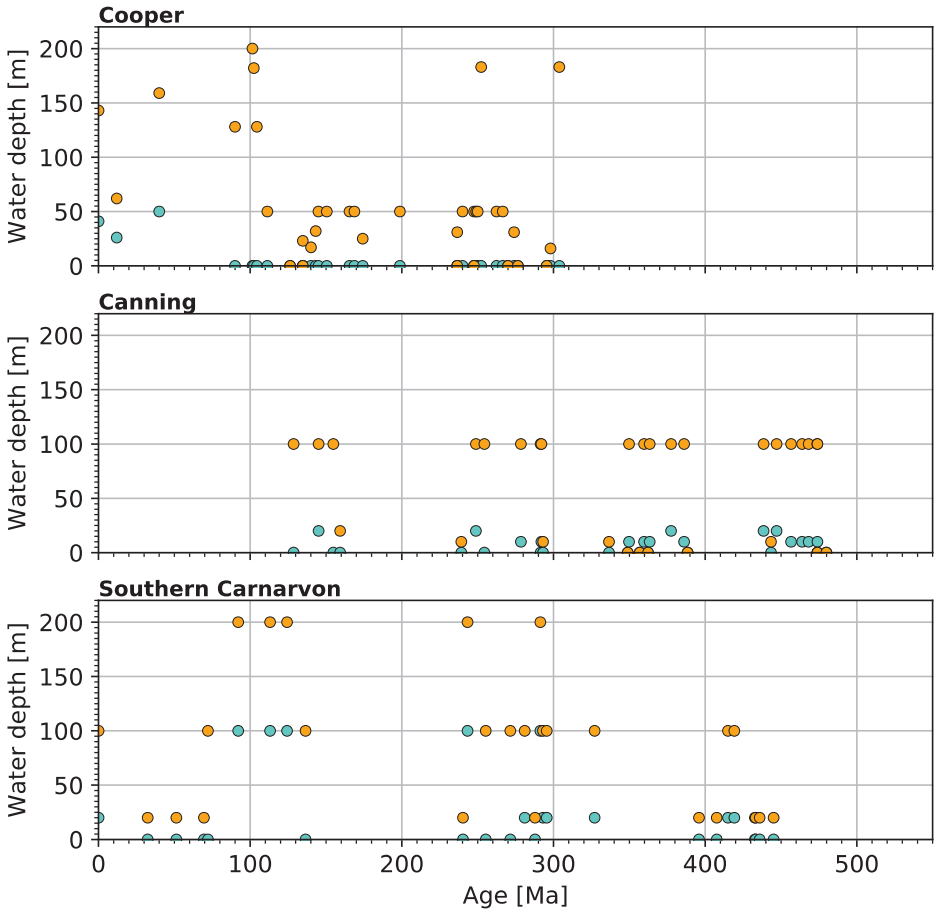

Supplementary Figure 4.3: Paleowater depth model for the Cooper, Canning and Southern Carnarvon basins. Orange dots represent the maximum water depth and cyan the minimum.

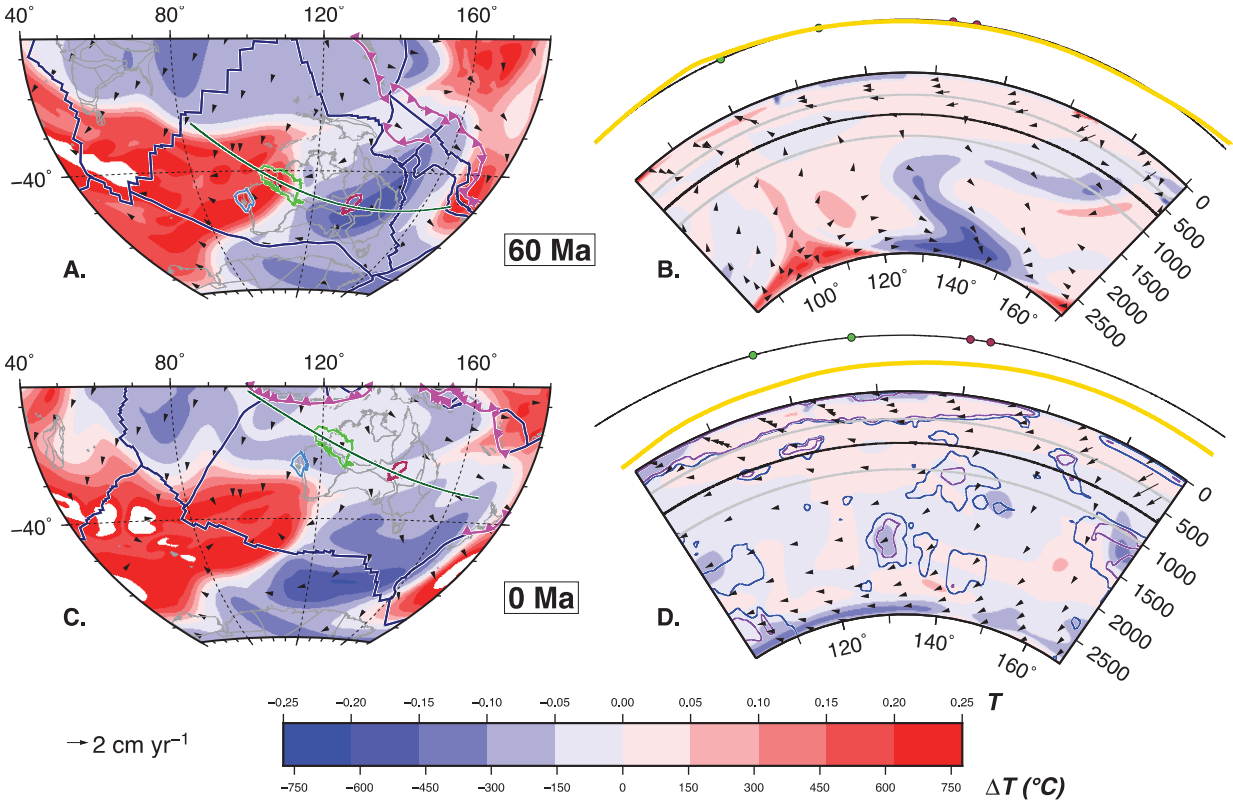

Supplementary Figure 4.4: Predicted mantle temperature and flow velocity for case M600 at 2,677 km depth (A, C) and along cross-sections (dark green lines) over the Australian plate (B, D) in 50 Myr increments between 60 Ma and 0 Ma. In A and C reconstructed subduction locations are shown as magenta lines with triangles on the overriding plate, reconstructed mid-oceanic ridges and transform faults are shown as dark blue lines, and reconstructed present-day coastlines and craton outlines are shown in grey. Reconstructed positions of the Southern Carnarvon, Canning and Cooper basins are shown in blue, green and maroon respectively. In B and D the black line above each section is the global mean dynamic topography (by definition equal to zero) and the gold line is the 1.25x vertically exaggerated air-loaded dynamic topography along the cross-section. Green and maroon dots mark the intersection between the cross-section and the boundary of the Canning and Cooper basins respectively. Purple and blue contours in D represents seismic velocity anomalies 0.3% and 0.1 % faster than average in P-wave model UU-P07 (Amaru, 2007), respectively. The color scale indicates non-dimensional (numbers above) and dimensional (numbers below) temperatures with respect to the ambient mantle temperature. Graticules at depths of 350 km (grey), 660 km (black) and 1,000 km (grey) are marked on the cross section.

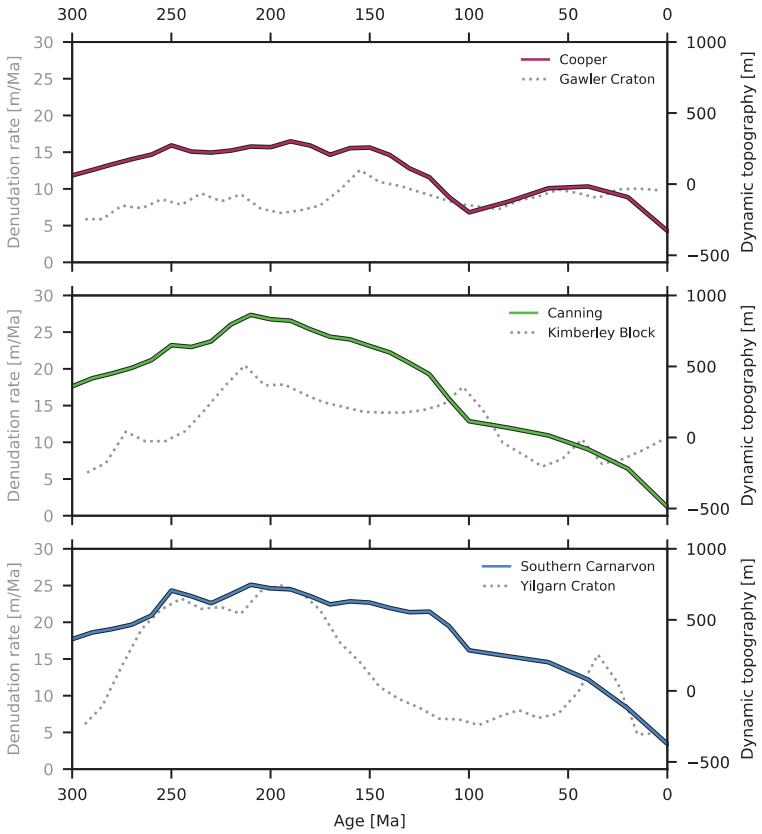

Supplementary Figure 4.5: Long-term denudation chronologies from Kohn et al. (2002) (y-values on the left axis) plotted with time-dependent dynamic topography from model case M600 (y-values on the right axis).

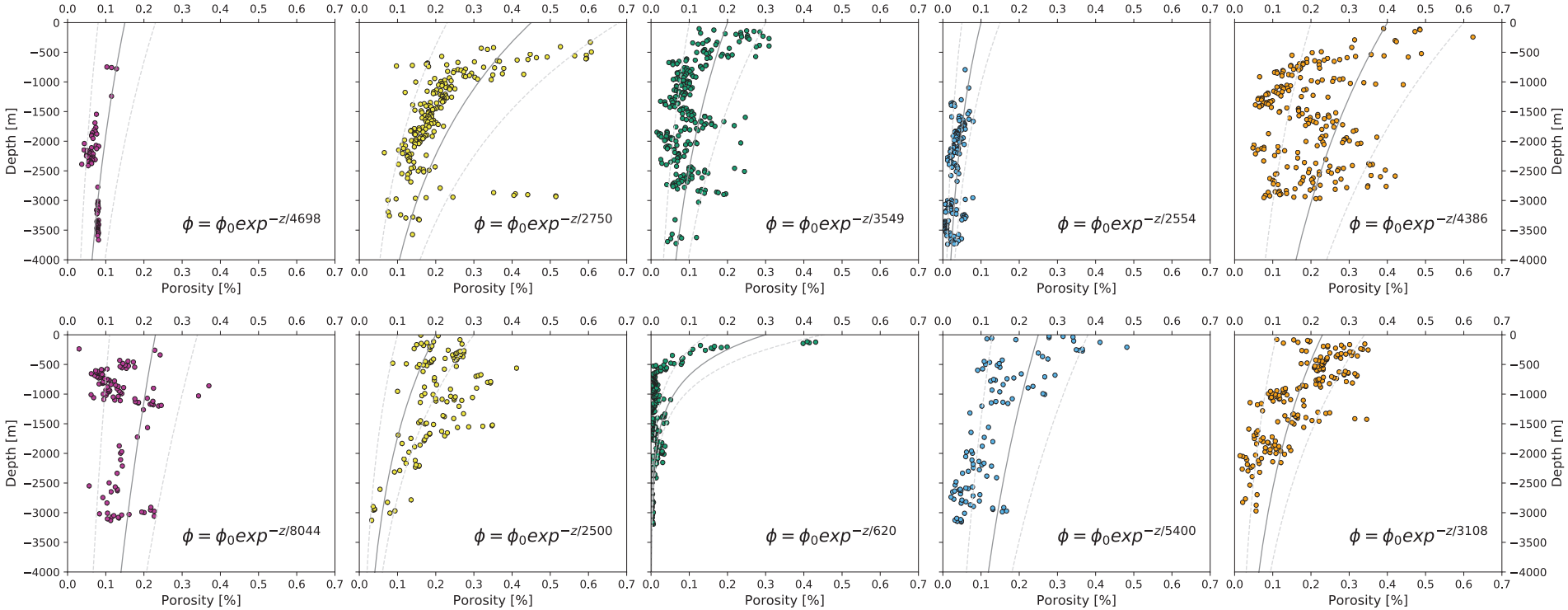

Supplementary Figure 4.6: Porosity models for common lithologies in the Canning Basin (top) and Southern Carnarvon Basin (bottom). Solid grey line is the base case model, dashed lines are min and max models. Pink, dolostone; yellow, sandstone; green, shale; blue, limestone and orange, siltstone log derived porosity values averaged over a 10 m moving window. Best fit exponential function of the log derived porosity is annotated.

Acknowledgments

This research was undertaken with the assistance of resources from the National Computational Infrastructure (NCI), which is supported by the Australian Government. This research has been conducted with the support of the Australian Government Research Training Program Scholarship. NF was supported by Australian Research Council grant DE160101020. ASM was supported through the Deep Energy Community of the Deep Carbon Observatory. We thank Steve Abbott and Karol Czarnota of Geoscience Australia for discussions. We thank Schlumberger Australia for donating the Petrel E&P software platform and the accompanying Geology and Modelling modules used in this study. We thank Fiona Dodd, Arthur Mory and Ameed Ghori from West Australian Department of Mines, Industry Regulation and Safety for providing well data and expertise relevant to Western Australia. Figures were constructed using Generic Mapping Tools (Wessel et al., 2019), GPlates (www.gplates.org) and QGIS. We also thank Nicky White, Mark Hoggard, Lydia DiCaprio, Christian Heine and an anonymous reviewer for their feedback which greatly contributed to the improvement of this manuscript.

Chapter 5. The effect of mantle dynamics on Earth's surface during Phanerozoic times

Abstract

Global eustasy is thought to have fluctuated by hundreds of meters (~400 m) during Phanerozoic times. Since the late 1970's, tracking the temporal evolution of eustatic rise and fall has been achieved using sequence stratigraphy incorporated with lithological and paleontological data. To reconstruct time-dependent Paleozoic eustasy, transgressive and regressive sequences in designated reference districts (Haq and Schutter, 2008) were analysed to represent eustatic change throughout geological time. This approach assumes tectonically quiescent regions are stable, a presupposition that has been shown to be invalid with the advent of dynamic topography i.e., long wavelength vertical displacements of the Earth's surface driven by mantle convection; which precludes attempts to reconstruct sea level from the rock record alone.

To reconstruct the sea-level history of Paleozoic times, sequence stratigraphic studies from the "stable" Australian shield were used to determine eustasy for the latest Cambrian-early Ordovician and early Devonian times. Given the importance of individual *reference districts* in reconstructing Paleozoic eustasy (for Paleozoic times reference districts are used sequentially as opposed to several areas being considered at a given time, as is done to reconstruct sea level for Mesozoic-Cenozoic times) it is worthwhile reviewing their histories with a focus on both the geological and geodynamic components.

In this Chapter, I compare the tectonic history of Australian Paleozoic reference districts with paleogeographic reconstructions, model dynamic topography and long-term eustatic sea level curves and show that the Canning, Amadeus and Georgina Basins (latest Cambrian-early Ordovician reference districts) and the east Australian Tasmanides (early Devonian reference districts) were tectonically and dynamically active during the time intervals of interest for which they have been used as reference districts.

During latest Cambrian-early Ordovician times, a major transgression recorded in the Canning, Amadeus and Georgina Basins is the basis for a sequence stratigraphic eustatic highstand (100-200 m). During these times rifting was occurring in the Canning and Amadeus Basins; in addition, geodynamic models suggest western Australia was dynamically depressed by 750 m. Thus, the recorded transgression is more likely associated with the isostatic and dynamic subsidence of these regions rather than a global eustatic rise.

A long-lived west-dipping subduction zone along the east Australian margin during Devonian times resulted in the dynamic subsidence of this area at a rate of ~8 m/Myr between ~420-400 Ma. In the Waratah Bay and Broken River regions of the Tasmanides, dynamic subsidence was coeval with a regional transgression; represented on sequence stratigraphic sea level curves as a eustatic highstand (200 m). Due to the complex tectonic setting along the east Australian margin during Devonian times it is unclear if this transgression had a eustatic component or if it is more reflective of regional tectonics. The results of my analysis question the reliability of the Australian reference districts for eustatic reconstruction and suggest that tectonic and dynamic topography should be considered when selecting reference districts.

5.1 Introduction

The links among the evolution of dynamic topography, continental flooding and eustasy have been established by combining mantle flow models with paleogeographic data (Gurnis, 1993; Heine et al., 2010; Spasojevic and Gurnis, 2012; Vibe et al., 2018b; Cao et al., 2019). The results of these studies advocate for a dependence between paleogeography and mantle convection and establish an important perspective: that unravelling the interplay between eustasy and dynamic topography is critical for understanding continental uplift, basin subsidence, the evolution of petroleum systems and the waxing and waning of inland seas.

In the preceding chapters time-dependent models of mantle flow were used to compute the evolution of dynamic topography over the past billion years. Models of mantle-induced topography were subsequently incorporated in eustatic calculations and investigations into the subsidence histories of sedimentary basins. Here, as an extension of that work, eustatic and subsidence studies can be integrated with paleogeographic data to explore the effect of mantle flow on Australian continental flooding over the last 500 Myr. The relationship between continental flooding and dynamic topography is of particular interest since sequence stratigraphic studies from reference districts on the relatively "stable" Australian shield have been used for reconstructing the latest Cambrian to early Ordovician (Nicoll et al., 1992; Shergold and Nicoll, 1992) and early Devonian (Talent and Yolkin, 1987; Talent, 1989) intervals of the Paleozoic global eustatic curve (Haq and Schutter, 2008). In addition to the total amplitude and the rate of predicted dynamic uplift and subsidence, fluctuations in the reconstructed sea level can be compared with the regressions and transgressions represented by environmental changes in paleogeographic reconstructions (Totterdell et al., 2001; Cao et al., 2017b). Using the predicted evolutions of dynamic topography and model sea level, the Phanerozoic paleogeography of Australia can be placed in context i.e., regional versus global sea level variations and continental flooding episodes.

5.2 Evolution of Australian paleogeography

Two separate paleogeographic models were utilised in the following analysis: (i) a set of time-dependent global paleogeographic maps spanning 400-10 Ma initially produced by Golonka et al. (2006) that were subsequently updated, refined and digitized by Cao et al. (2017) and (ii) a series of paleogeographic atlases of Australia for the Phanerozoic produced and compiled by the Australian Geological Survey Organisation during the 1980's and 1990's that remained unpublished until 2001 (Totterdell et al., 2001). Note that the regional Totterdell et al. (2001) reconstructions are used for pre-400 Ma times (Figs. 5.2 and 5.4) and the global Golonka et al. (2006)/Cao et al. (2017) reconstructions are used for post-400 Ma times (Figs. 5.5-5.7). The long-wavelength dynamic topography is calculated from sources of buoyancy below 350 km while ignoring lateral viscosity variations above this depth, from mantle flow model C1 presented in Chapter 3 (Fig. 5.1).

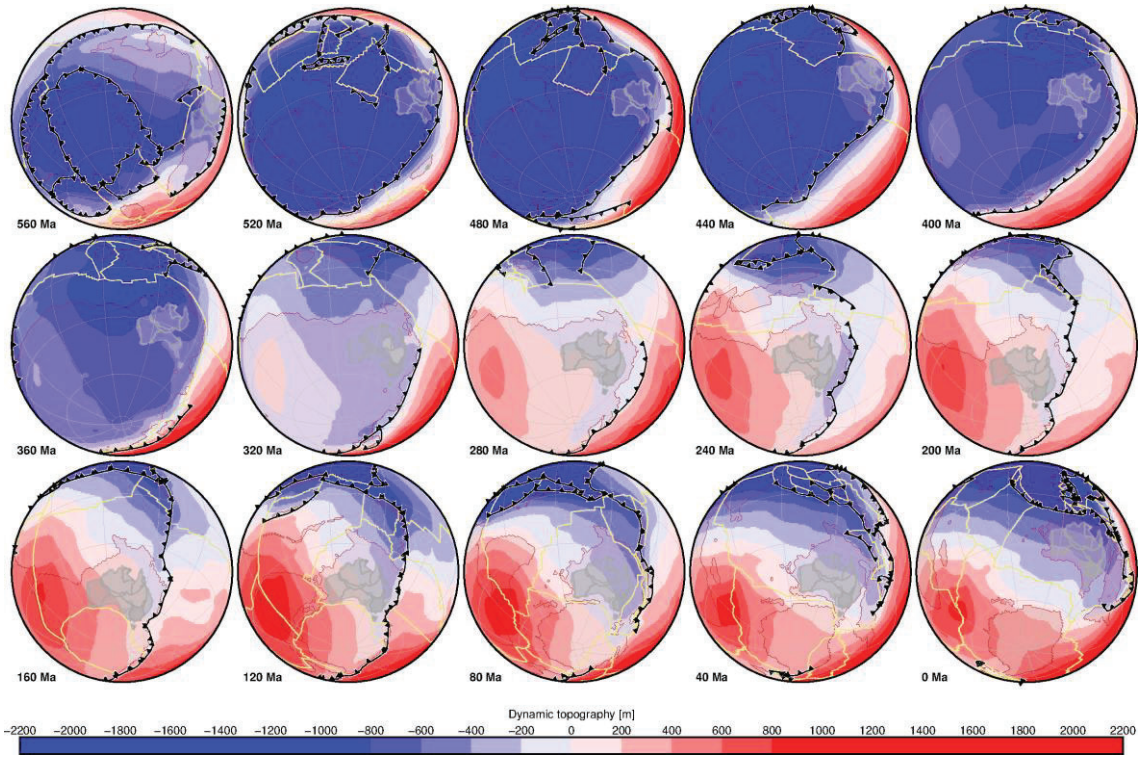

Figure 5.1. Modelled dynamic topography for flow model C1 from 560-0 Ma in 40 Myr increments focused on Australia. Dynamic topography calculated with free-slip boundary conditions from sources of buoyancy deeper than 350 km and ignoring lateral viscosity variations above this depth. Reconstructed subduction locations are shown as black lines with triangles on the overriding plate, reconstructed mid-oceanic ridges and transform faults in khaki, with continent-ocean boundary in brown and Australia in grey.

5.2.1 Ordovician Period

Though the Paleozoic history of eastern Australia is complex, there is a general consensus that throughout much of the Cambrian Period the eastern margin of Australia developed behind a long-lived, west-dipping subduction system (Glen, 2005; Champion et al., 2009; Merdith et al., 2017). While this may be an oversimplification of the tectonic scenario, the depositional history indicates that during Ordovician times, Eastern Australia was the site of deep marine sedimentation while the region including the Adelaide Geosyncline and the Broken Hill area was above sea level (Fig. 5.1). An east-west trending shallow-marine sea – the Larapinta Seaway – covered central Australia, connecting the Canning and Amadeus basins to the open ocean in the east (Fig. 5.2). In the Canning Basin the Samphire Marsh extensional phase was underway (Kennard et al., 1994; Romine et al., 1994; Shaw et al., 1994). At the same time, subsidence rates in the Amadeus Basin notably increased (Shaw et al., 1991); though the cause of this subsidence remains uncertain. Estimates of dynamic topography from C1 suggest that Australia was dynamically depressed by ~750 m during the early Ordovician, due to downwelling developing in response to prolonged subduction along the eastern margin (Fig. 5.1). At ~470 Ma convergence to the north of Australia had ceased (Fig. 5.2) and dynamic rebound lead to uplift (Fig. 5.3).

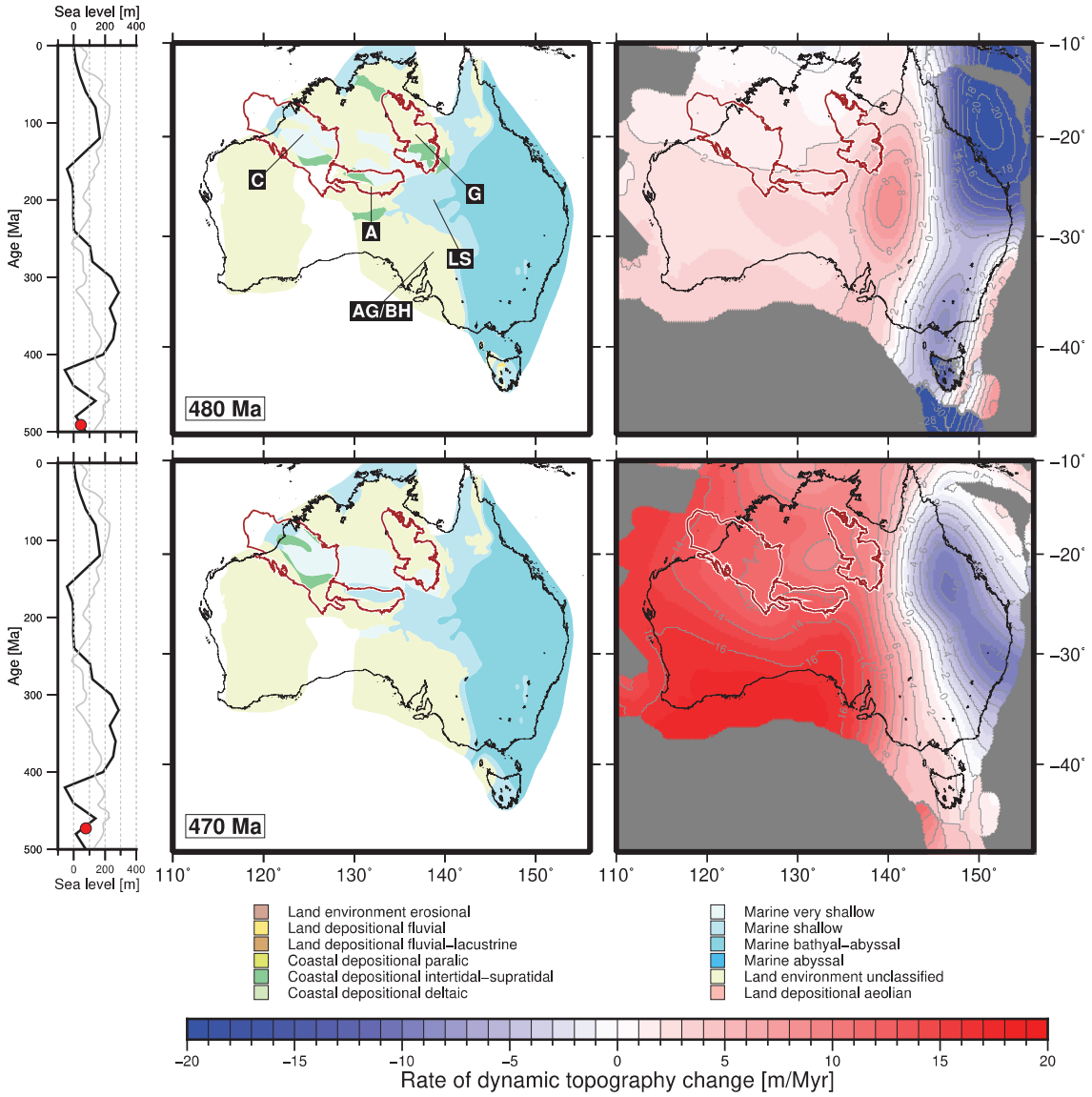

Figure 5.2: Australian paleogeography, rate of dynamic topography change and eustasy for early Ordovician times. Eustatic sea level curves of Haq and Schutter (2008) (grey) and Young et al. (*In revision., Chapter 3*) (black). Red dot marks the calculated sea level from Young et al. (*In revision., Chapter 3*) at the time period represented on maps of: reconstructed paleogeography (Totterdell et al., 2001) (centre) and rate of dynamic topography change (right). Dynamic topography was calculated in the plate frame of reference from mantle flow model C1. Sedimentary basins are outlined in brown and present-day coastlines are in black. Labels, from left to right are: C, the Canning Basin; A, Amadeus Basin; AG/BH, Adelaide Geosyncline-Broken Hill region; LS, Larapinta Seaway; and G, Georgina Basin. The Canning, Amadeus and Georgina basins are the designated Paleozoic reference districts for times between 492 Ma and 473 Ma.

Eustatic studies suggest a global sea level rise during the latest Cambrian-Ordovician (490-470 Ma): Young et al. (*In revision., Chapter 3*) report an increase from 50 m to 80 m and Haq and Schutter (2008) a rise from 160 m to 190 m (Fig. 5.2). The latter is based largely on the interpretation of Nicoll et al. (1992) that early Ordovician sandstones in the Canning Basin represent a major transgressive phase. This interpretation is supported by biostratigraphic data in the eastern Georgina Basin (Shergold and Nicoll, 1992) and is represented in paleogeographic reconstructions of Australia (Fig. 5.2).

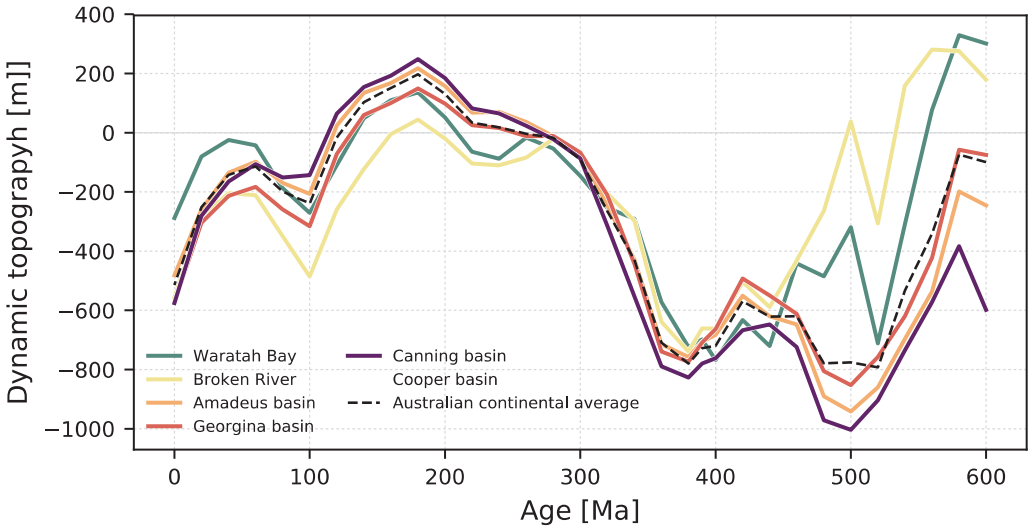

Figure 5.3: Global sea level and the evolution of dynamic topography for the Australian continental platform including the Australian reference districts used in the eustasy study of Haq and Schutter (2008). The amplitude of mean dynamic topography is extracted from the model in 20 Myr increments. For the Broken River and Waratah Bay profiles, dynamic topography at a point central to the region was used (point location shown in Fig. 5.3). For the Australian profile and the Canning, Amadeus and Georgina basin profiles, mean dynamic topography was calculated within a polygon of the basin/coastline outline (Fig. 5.1). The Broken River and Waratah Bay areas are the designated Paleozoic reference districts for times between 415.5 Ma and 399.5 Ma.

Thus, the continental flooding history of Australia and global eustasy appear to be in phase during the early Ordovician (Fig. 5.1). However, indications from basin subsidence and models of dynamic topography suggest that the continent was not entirely stable during these times. Local lithospheric stretching in the Canning and Amadeus occurred while the modelled dynamic topography suggests Western and Central Australia was uplifting at a rate of ~5 m/Myr (Fig. 5.2). Local lithospheric stretching in the Canning Basin (and possibly the Amadeus Basin) would produce isostatic lows prone to inundation as would negative dynamic topography. Consequently, the amplitude of global sea level determined using the sequence stratigraphic approach may overestimate the amplitude of sea level rise during this period due to the effects of local tectonic disturbances and mantle flow.

5.2.2 Devonian Period

Throughout Devonian times most of Australia – excluding the complex eastern margin where marine sedimentation continued – was subaerial (Totterdell et al., 2001; Golonka et al., 2006). In the Canning Basin, the early Devonian-Carboniferous (390-340 Ma) Pillara extension phase (Shaw et al., 1994) was marked by shallow marine deposition (Fig. 5.4). A marine incursion into the region of the south Australian Officer Basin occurred in the early Devonian (Fig. 5.4) but was in regression by 398 Ma and completely absent by 390 Ma (Totterdell et al., 2001). From the earliest Devonian, the results from mantle flow model C1 suggest Australia was dynamically subsided due to long-lived subduction at the eastern margin (Fig. 5.1). However, the development of a mantle upwelling above a basal mantle structure beneath the Tethys margin of Gondwana initiated dynamic uplift in the region that had far-field effects on Australia during the mid-Devonian. From ~380-360 Ma results from model C1 suggest that Australia was undergoing dynamic uplift at a mean rate of 10 m/Myr with higher rates migrating from the west (Fig. 5.4). Published eustatic sea level estimates for the Devonian vary greatly from 40±10 m (Algeo and Seslavinsky, 1995) to 440±140 m (Hallam, 1984). Yet, despite this there is a general consensus

amongst palaeogeographers that during the Devonian, global continental flooding was significant; covering an area of more than 2 × 10^7 km^2 compared to the present day (Ronov, 1994; Walker et al., 2002; Golonka, 2007b; Blakey, 2008; Scotese, 2008).

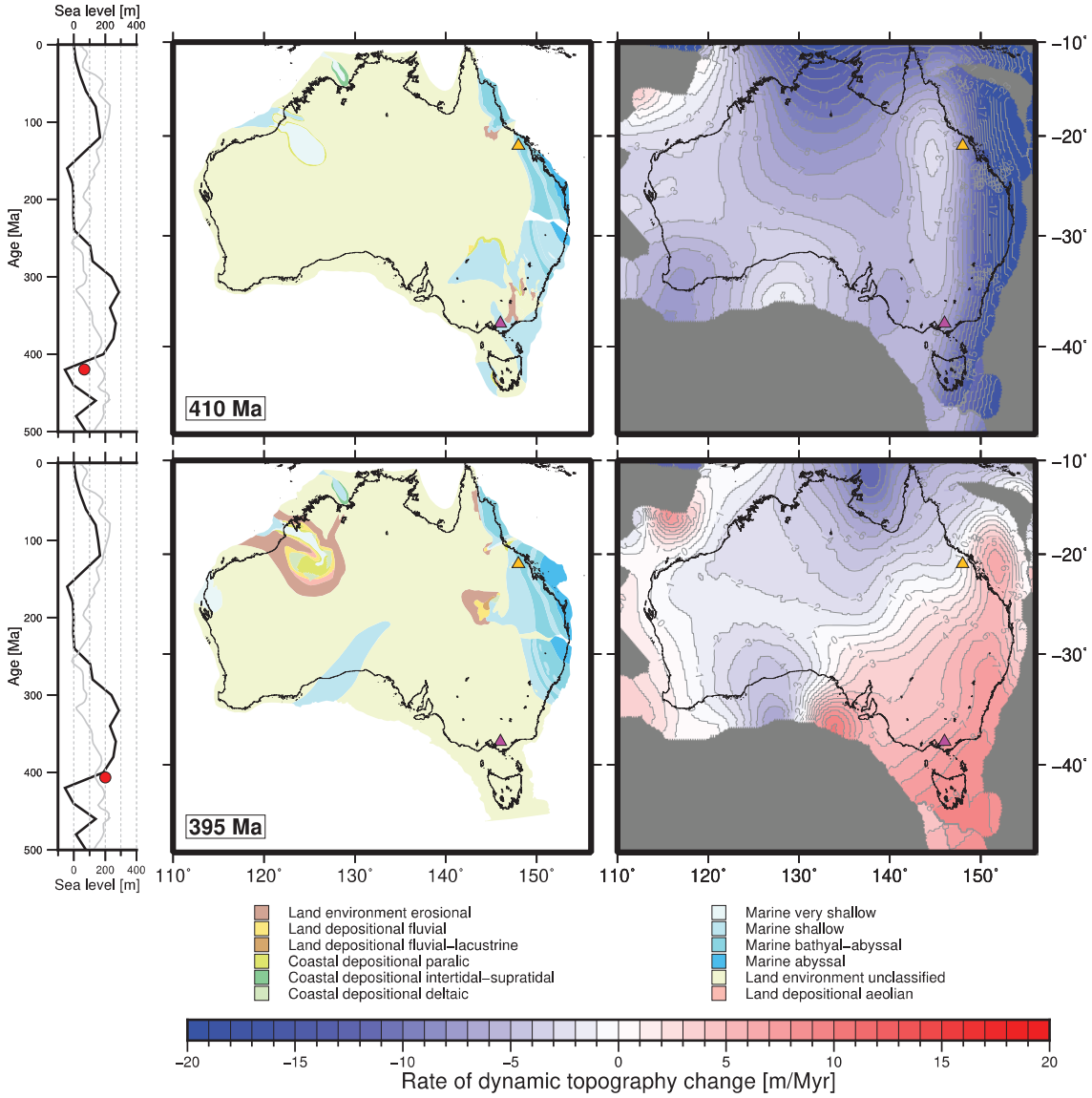

Figure 5.4: Australian paleogeography, rate of dynamic topography change and eustasy for early Devonian times. See Fig. 5.2 caption for general description of figure components. Orange and magenta triangles represent Broken River and Waratah Bay regions respectively.

For the interval between 416-400 Ma, Haq and Schutter (2008) designate the sections at Broken River and Waratah Bay in the east Australian Tasmanides (Fig. 5.3) as the reference districts for Paleozoic sea level. These locations constitute part of the Australian segment of the Terra Australis Orogen, an orogenic system that existed along the western, southern and eastern margins of Gondwana during the Paleozoic (Cawood, 2005). Lying behind the Gondwana-proto-Pacific plate margin, the Tasmanides are a complex example of an accretionary orogen, in which plate boundary migration provoked episodes of contractional deformation interspersed with periods of crustal extension and magmatism (Glen, 2005; Champion et al., 2009; Rosenbaum, 2018).

In the northern Tasmanides (Broken River area), the beginning of Devonian times was marked

by widespread sedimentary basin formation (Henderson et al., 1998; Glen, 2005; Rosenbaum, 2018). Basins were filled by carbonate, turbidites and by the emplacement of granites (Arnold and Fawckner, 1980; Garrad and Bultitude, 1997). Following basin formation, the northern Tasminides appear to have been unaffected by tectonic deformation throughout subsequent Devonian times and sedimentation appears to have continued uninterrupted (Champion et al., 2009). In the southern Tasmanides (Waratah Bay area), arc roll-back had initiated widespread extension and basin formation during the Silurian (Glen, 2004; Spaggiari et al., 2004) resulting in the deposition of deep to shallow marine sediments as well as carbonates (Glen, 2005). By the onset of Devonian times an episode of east-west contractional deformation was affecting the region (VandenBerg, 2000; Glen, 2005; Fergusson, 2017). Contractional deformation, indicated by thrusting, folding and inversion of basin structures continued until ~370 Ma (Glen, 1995; VandenBerg, 2000; Black et al., 2005; Fergusson, 2017).

In summary, throughout the Devonian Australia was mostly subaerial; except for the eastern margin and parts of western Australia. Different geodynamic settings are inferred for western Australia and the northern and southern Tasmanides. There is great uncertainty of global sea level amplitude although there is general consensus it was higher than present day. Global paleogeographic reconstructions indicate that globally, the aerial extent of continental flooding was large.

High sea level elevation (150 m) during the early Devonian interval (~420-400 Ma) of the Haq and Schutter (2008) eustatic curve is based on transgressions recorded in the Broken River and Waratah Bay regions of the east Australian Tasmanides (Talent and Yolkin, 1987; Talent, 1989). Indeed, a significant early Devonian transgressive event is indicated by widespread shallow-bathyal marine deposition up and down the east Australian margin (Totterdell et al., 2001). However, it is unclear if this transgression had a eustatic component or if it is more reflective of widespread sedimentary-tectonic circumstances in eastern Australia. As briefly discussed above; the east Australian margin was a tectonically active place during the early Paleozoic. Therefore, it is possible that these transgressions are local, tectonically based occurrences, amplified by dynamic subsidence (subsiding at a rate of ~8 m/Myr; Fig. 5.2) and not necessarily representative of eustasy.

5.2.3 Carboniferous-Triassic Periods

In Carboniferous-Triassic times the Australian environment was almost exclusively terrestrial (Totterdell et al., 2001; Golonka et al., 2006). Glaciation – which has been attributed to a reorganization of the global ocean currents and the transportation of moisture to the southern continents following the closure of the Rheic ocean (Saltzman, 2003) – proliferated in the latter half of the period (Fig. 5.5). Restricted marine deposition in the Canning Basin during this period is associated with the final stages of Pillara extension (Shaw et al., 1994). As with Devonian times, the published eustatic sea level estimates for the Cretaceous vary significantly; e.g., 50±10 m (Algeo and Seslavinsky, 1995) to 330±70 m (Hallam, 1984). However, there is general agreement amongst the published studies that sea level fell between the Devonian and Carboniferous due to the glaciation (Vail et al., 1977; Hallam, 1984; Haq and Schutter, 2008; Vérard et al., 2015; Guillaume et al., 2016). A global eustatic lowstand in Permian-Triassic times is universally advocated in eustatic reconstructions and is consistent with limited continental inundation as observed in the global record (Ronov, 1994; Walker et al., 2002; Golonka, 2007a, b; Blakey, 2008;

Scotese, 2008). Results from C1 suggest that between 360-300 Ma dynamic topography – produced by the upwelling above the hot basal mantle structure beneath the Tethys margin – resulted in rapid uplift of the Australian plate at a rate of ~10 m/Myr (Fig. 5.5). Uplift rates declined in the Permian (~2 m/Myr). By the onset of Triassic times the Australian plate was elevated by low positive dynamic topography and remained so for the duration of the Mesozoic (Fig. 5.3).

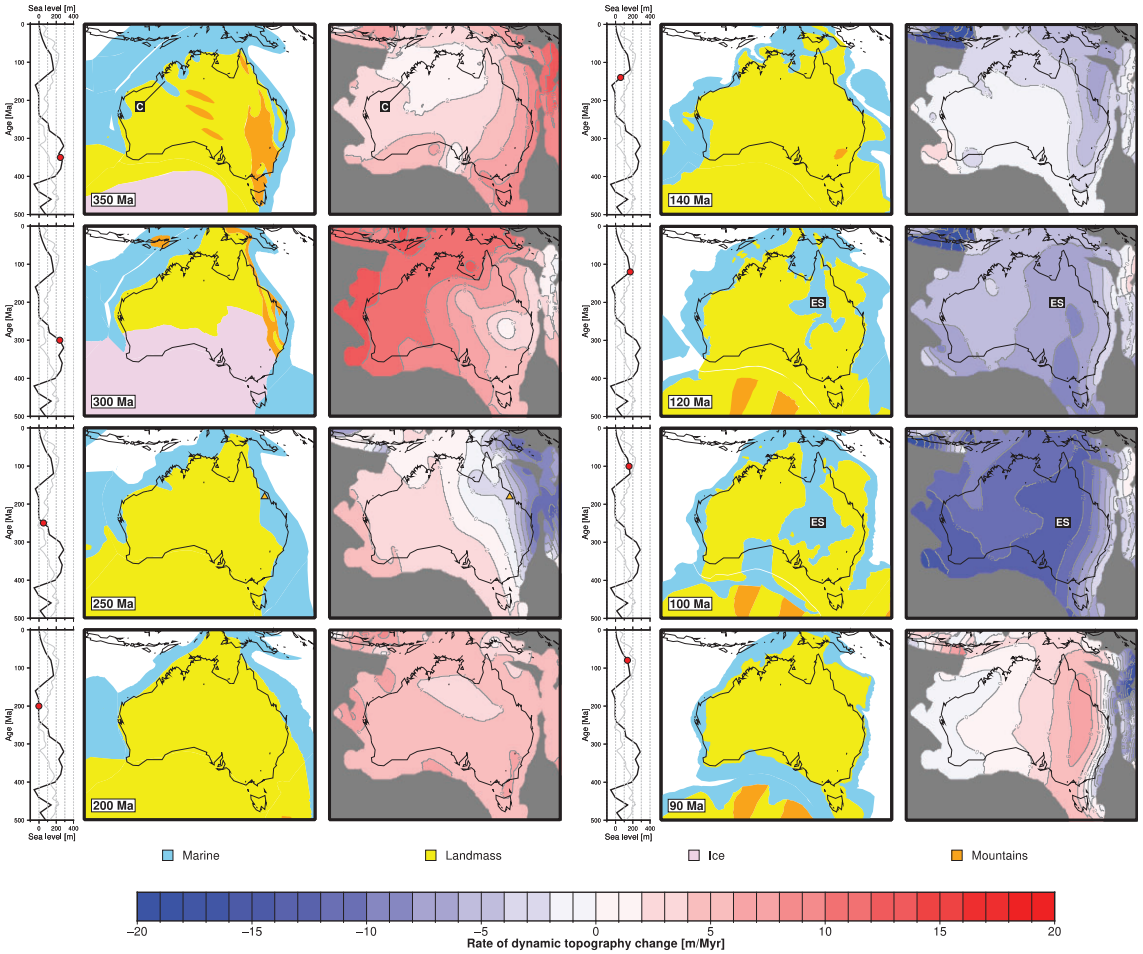

Figure 5.5: Australian paleogeography, rate of dynamic topography change and eustasy for Carboniferous-Triassic (left) and Cretaceous times (right). See Fig. 5.2 caption for general description of figure components. The paleogeographic reconstruction is that of Cao et al. (2017).

In the geological history of Australia, the Carboniferous period is an interesting case study of the complex relationship between sea level, paleogeography and dynamic topography. Between 350-300 Ma, results from C1 suggest that the Australian plate was dynamically depressed (Fig. 5.1); which ought to have resulted in regional transgression. Indeed, high (260±30 m) global sea level during this interval (Young et al., *In revision., Chapter 3*) should make continental inundation even more prevalent. However, the Australian Carboniferous environment was comprehensively terrestrial. What then, explains this disconnection? The answer – according to this analysis – is likely twofold. Firstly, significant volumes of water would be locked up in the aforementioned Carboniferous glaciation, a mechanism of eustatic change not incorporated in the calculations of Young et al. (*In revision., Chapter 3*) and which would result in major sea level fall; indeed, Crowley and Baum (1991) estimated up to 65±15 m. And secondly, although negative, the dynamic topography of the Australian plate rapidly increased during this

interval which can lead to regional regression; this is largely consistent with the paleogeographic record for these times (Fig. 5.5).

At the Permian-Triassic boundary a correlation between the rate of dynamic topography change and paleogeography is manifest in the Broken River region of north-eastern Australia (Fig. 5.5). During this interval, in the Broken River region, mantle flow caused subsidence at a rate of ~2 m/Myr and a marine environment is observed (Fig. 5.5). If, theoretically, decreasing dynamic topography results in regional transgression (Spasojevic and Gurnis, 2012), then synchronicity between the spatiotemporal deposition of marine sediments and dynamic subsidence evokes a dependency among the processes in the Broken River region during the Permo-Triassic. However, marine deposition during these times is associated with foreland loading and accelerated subsidence (Champion et al., 2009; Korsch et al., 2009; Rosenbaum, 2018) and thus precludes the simple correlation between mantle flow and continental flooding. Therefore, notwithstanding evidence for tectonic subsidence, the agreement between observed outcome (paleogeography) and modelled mechanism (dynamic topography) appears to be noteworthy and suggests mantle downwelling contributed to a tectonically-based transgression initially instigated by local lithospheric flexure; despite the global eustatic lowstand and positive dynamic elevation across the majority of the Australian plate (Fig. 5.3).

5.2.4 Cretaceous Period

Paleogeographic data indicate widespread transgression occurred in central Australia creating an epeiric, epicontinental seaway – the Eromanga Sea – during the Cretaceous eustatic highstand (~100 Ma; Fig. 5.5). Notably, the Eromanga Sea regressed in the mid-Cretaceous, resulting in the complete subaerial exposure of Australia despite high global sea level (Fig. 5.3). The discrepancy between Australian paleogeography (universal subaerial exposure) and eustasy (sea level high) is a puzzling phenomenon. Yet, geodynamic studies of mantle convection and dynamic topography have demonstrated how the regression of the Eromanga Sea can be related to the mid-Cretaceous dynamic uplift of Australia (Gurnis et al., 1998).

As described above, throughout the Paleozoic the eastern Australian margin constituted a long-lived, west-dipping convergent margin (Fig. 5.1). Here, the subducted slab produced a downwelling that affected a restricted, narrow north-south trending belt of negative dynamic topography along the eastern Australian margin from the mid-Paleozoic to latest-Cretaceous (Fig. 5.1). Negative dynamic topography was restricted to this corridor due to the dominating influence of the upwelling beneath the southern Meso-Tethys margin (Fig. 5.1). At ~180 Ma Gondwana began to break up resulting in the eastward drift (all motions are described in the hot spot reference frame) of India, Antarctica and Australia away from the locus of the southern Meso-Tethys upwelling. During the Cretaceous, the Cooper Basin passed over the downwelling (which had developed beneath the east Australian margin throughout the Paleozoic) resulting in a phase of accelerated subsidence; in the absence of substantial folding or faulting (Gallagher and Lambeck, 1989; Mavromatidis, 2006; Matthews et al., 2011; Young et al., *2020, Chapter 4*). During this interval (~120-100 Ma) central Australia subsided dynamically at a rate of ~10 m/Myr and the Eromanga Sea formed (Fig. 5.5). Subduction along the east Australian margin continued until ~100 Ma when rifting developed in the Tasman Sea; between Australia and the Lord Howe Rise (Gaina et al.,

1998). Back-arc extension in the Tasman Sea was contemporaneous with the eastward migration of the convergent margin and negative dynamic topography (Fig. 5.1). At the same time, Australia began to drift north. As Australia moved north and the site of strong negative dynamic topography moved east (Czarnota et al., 2014; Müller et al., 2016b; Salles et al., 2017), a broad belt of positive dynamic topography migrated to the west across the continent (Fig. 5.1); the combined effect being the net uplift of the Australian plate at a rate of 5 m/Myr and the regression of the Eromanga Sea (Fig. 5.5). Gurnis et al. (1998) proposed a similar scenario in which Australia moved eastward from 130-90 Ma, over a broad dynamic topographic depression causing the continent to subside and then uplift; the latter phase of vertical motion resulting in the regression of the Eromanga Sea.

5.3 A global perspective

As explored above, in addition to climatic and tectonic forces, changes in the dynamic support of continental platforms can affect regional transgressions and regressions. Of course, the paleogeographic consequences of surface deflections associated with mantle flow are not limited to the Australian plate hence, I will now investigate the relationship between dynamic topography and continental flooding on a global scale.

Maps of dynamic topography and paleogeography (Fig. 5.6) indicate that for the majority of Paleozoic times there is a relationship between positive continental dynamic topography and restricted continental flooding and negative continental dynamic topography and widespread continental flooding. Indeed, the apparent correlation between shallow marine environments and negative dynamic topography is evident from a cursory examination of these maps (Fig. 5.6). In Silurian-Devonian times, negative deflection at continental margins due to subduction – which emplaces slabs beneath the continents and thus focuses mantle downwellings at these locations – caused widespread transgression and marine deposition in Asia, Laurentia, South America and Australia (Fig. 5.6). During the Permo-Triassic, extensive and globally observable regression was coeval with positive continental dynamic topography beneath the Meso-Tethys southern margin (Fig. 5.6). Inundation of the northern Gondwana margin in Triassic times would seem to contradict the relationship between continental flooding and dynamic topography, however, Meso-Tethys rifting at this margin during these times (Metcalfe, 2011) would lead to tectonic subsidence, regional isostatic lows and marine deposition. Another example where the continental flooding-dynamic topography relationship does not hold true is during Jurassic-Cretaceous times, when extensive marine inundation of the African, South American, Antarctic, Indian and Australian continental margins occurred, despite positive dynamic topography (Fig. 5.6). Furthermore, these marine transgressions took place – at least partially – during times of eustatic low (Fig. 5.3). It is during this interval that Gondwana was in the first stages of its break-up (e.g., Jokat et al., 2003) and widespread rifting propagated along the boundaries of the aforementioned plates resulting in abundant passive margins (Bradley, 2008), thermal and tectonic subsidence and hence, shallow marine deposition. Thus, it appears that while dynamic topography influences first order continental flooding patterns on very large scales (~10,000 km), regional tectonics exert a primary control on paleogeography on smaller scales (< 5,000 km).

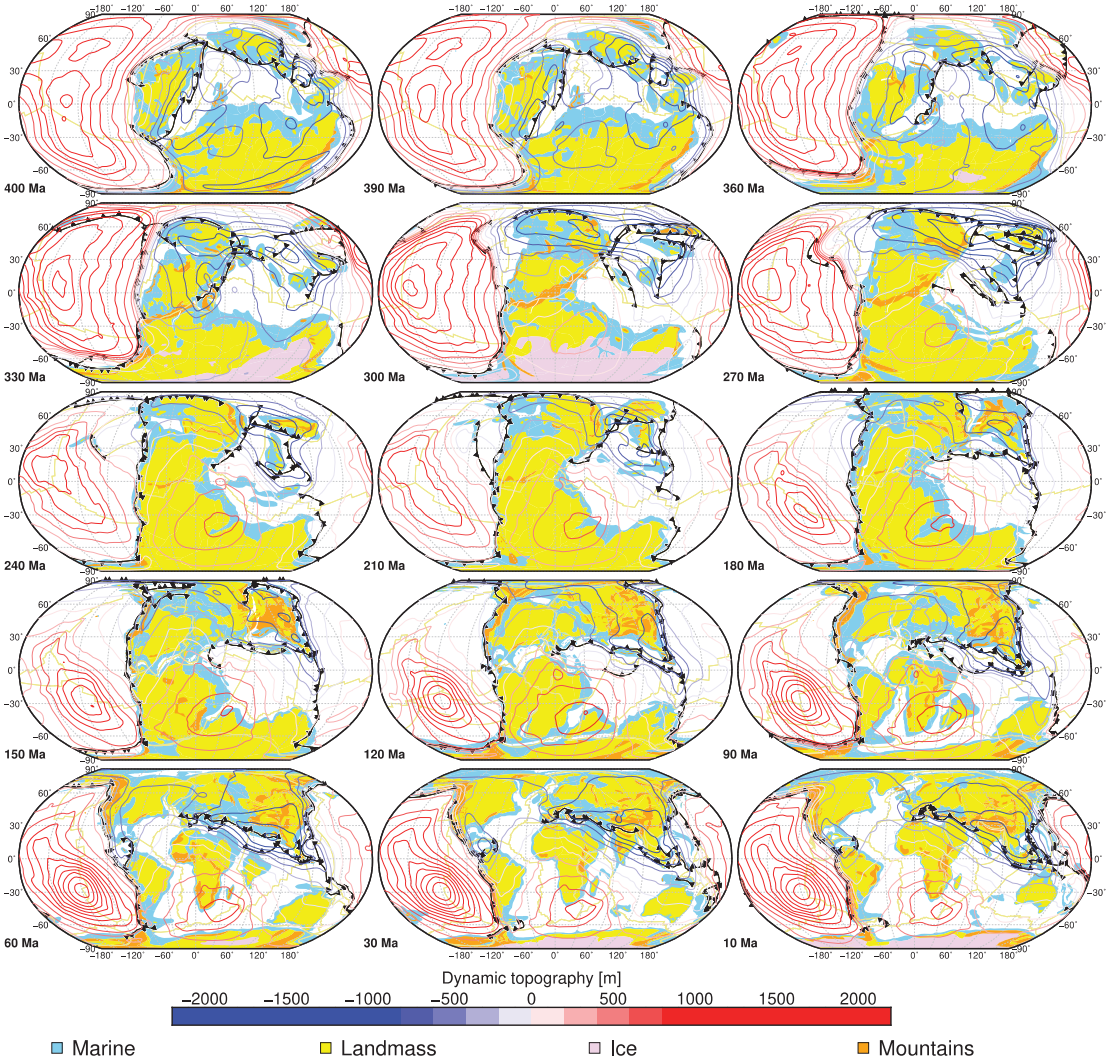

Figure 5.6: Total dynamic topography for mantle flow model C1 and reconstructed paleogeography (Cao et al., 2017b) in the mantle reference frame from 400-10 Ma in ~30 Myr increments. Dynamic topography is contoured in 200 m increments. Reconstructed subduction locations are shown as black lines with triangles on the overriding plate, reconstructed mid-oceanic ridges and transform faults in khaki.

Additional insights into the spatiotemporal evolution of dynamic topography and its effect on paleo-depositional environments can be achieved by examining the rate of dynamic topography change (Fig. 5.7). Maps of paleogeography and rates of dynamic topography change suggest a counter-intuitive interpretation; that is, a correlation between increasing rates of dynamic uplift and continental flooding and increasing rates of dynamic subsidence and marine regression (Fig. 5.7). For example: the results from flow model C1 suggest that widespread mantle supported uplift was occurring at the same time as extensive shallow marine deposition during the Silurian-Carboniferous Periods (see North and South America, northern Africa, Middle East, northern India and eastern Russia; Fig. 5.7) and again during Cenozoic times (see North America and Middle East; Fig. 5.7). Also, between Permian-Cretaceous times limited continental flooding is associated with dynamic subsidence (see North and South America, Africa and Australia; Fig. 5.7).

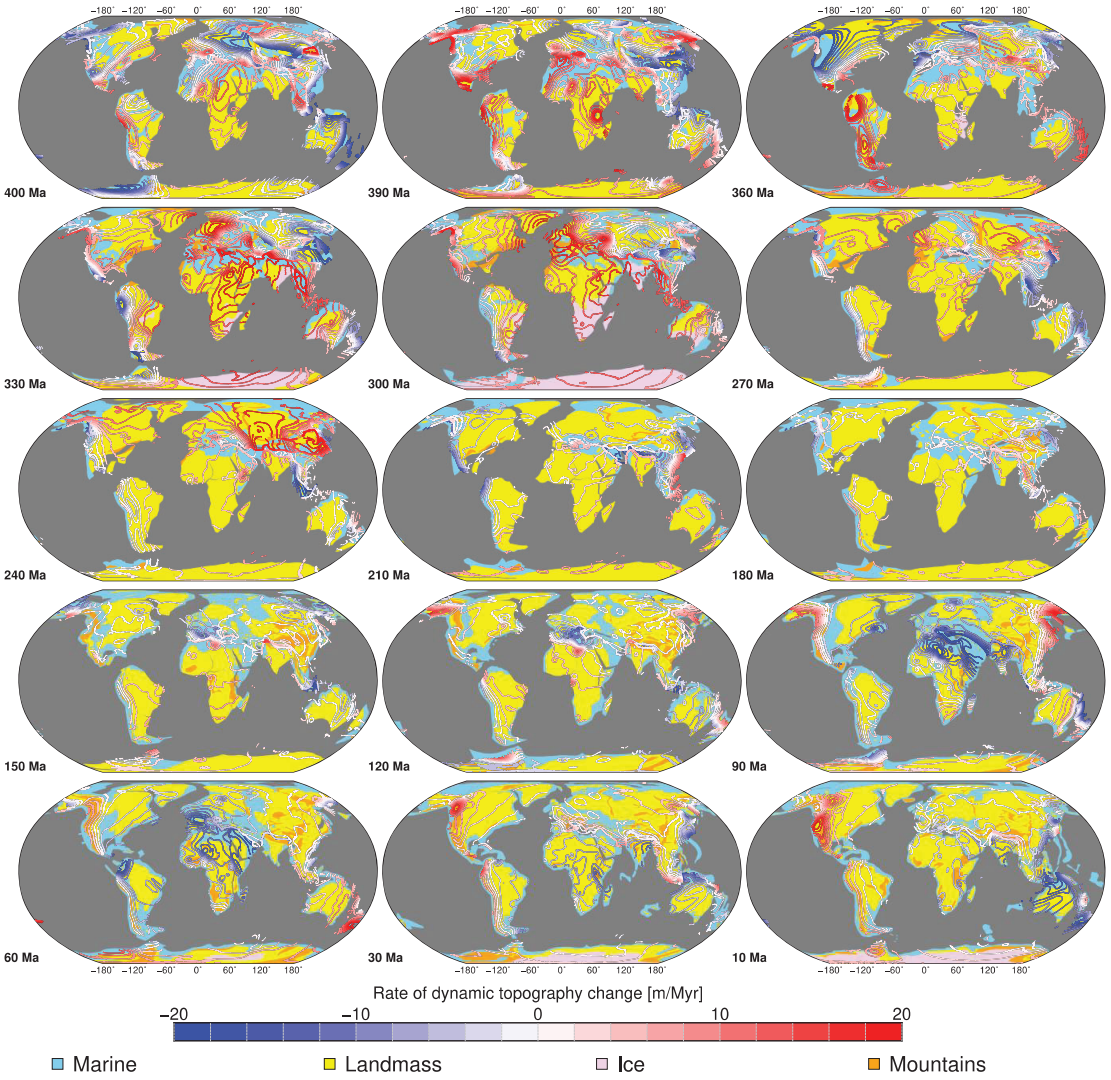

Figure 5.7: Rate of dynamic topography change for mantle flow model C1 and reconstructed paleogeography (Cao et al., 2017b) in the plate reference frame from 400-10 Ma in ~30 Myr increments. Rate of dynamic topography change is contoured in 2 m increments.

To help disentangle the relationship between the evolution of dynamic topography and its effect on depositional environments a more quantitative analysis is explored. This is achieved by analysing both the rates of change and total amplitude of dynamic topography in continental shallow marine and terrestrial environments with frequency histograms (Fig. 5.8). Using the Generic Mapping Tools (Wessel et al., 2019) I converted the Golonka et al. (2006) shallow marine and terrestrial paleogeographies to time-dependent NetCDF rasters of areas ("masks"). I then extracted the dynamic topography rate of change and total dynamic topography (at 1º by 1º spacing) from the paleogeographic masks and plotted grid values as frequency histograms. I also plotted the histogram modes as a timeseries along with the continental flooding record to investigate the spatiotemporal evolution of dynamic topography in different paleo environments.

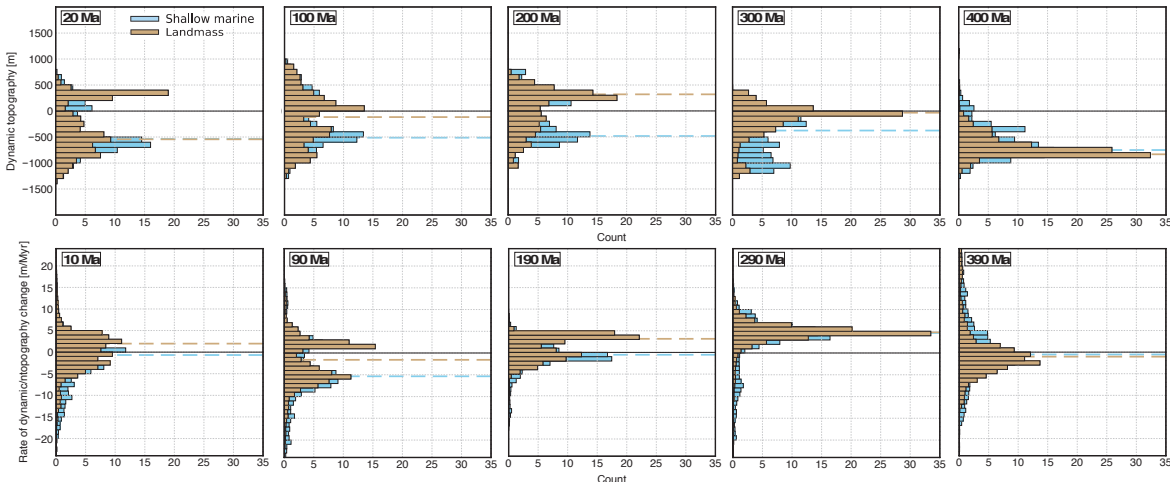

Figure 5.8: Top: time dependent histograms showing amplitudes of dynamic topography from flow model C1 in shallow marine (light blue) and terrestrial (brown) environments (Cao et al., 2017b) binned in 100 m elevations. Dashed line is the histograms LMS (least median of squares). The LMS approximates the mode – i.e., the maximum point on a probability density function. Bottom row: as with top row except histograms show the dynamic topography rate of change binned in 1 m/Myr increments.

Analysis of the time-dependent histograms modes shows that during periods of high negative total dynamic topography, continental flooding is widespread and uplift occurs at higher rates (Fig. 5.9). What is indicated here is that when continents are in a fairly dispersed state (e.g., between 500 and 400 Ma) the continents have overridden the "slab burial grounds" associated with subduction that used to occur along the perimeter of a supercontinent. Thus, there is dynamic subsidence of the continents. As the next supercontinent assembles (Pangea 400-300 Ma) subduction acts to reorganise the mantle structure beneath the converging plates leading to a net-uplift of the continents between supercontinent dispersal and assembly (Fig. 5.9). In contrast a scenario of supercontinent assembly, during supercontinent break-up (e.g., 250-120 Ma), dynamic topography is higher (130-410 m), continental flooding is more limited (~10 M km^2 greater than present-day), and the rate of dynamic change drops to 0±5 m/Myr (Fig. 5.9).

An exception to the observed patterns of dynamic topography and paleogeography is the past ~100 Myr during which global dynamic topography was negative – and dynamic subsidence was occurring – and continental inundation was low (Fig. 5.9). At first glance, this disconnect is counter intuitive. A potential explanation could be that Cenozoic glaciation could have offset the paleogeographic effect of negative dynamic topography. More likely, and indeed more significant however, is the general "aging" of the sea floor which has taken place since the Cretaceous (Pitman, 1978; Kominz, 1984; Müller et al., 2008; Young et al., *In revision., Chapter 3*). Mapping of the sea floor age suggests that in Cretaceous times the average age of the oceanic crust ~ 40 Ma while at present day its ~ 70 Ma (Williams et al., 2021). As the age of the sea floor increases so does its depth (McKenzie, 1967). Hence, oceans with older mean seafloor age are deeper – and more voluminous – than oceans with a younger mean seafloor age. As the mean seafloor age became older and oceanic bathymetry equivalently deeper over the last 100 Myr, a eustatic fall occurred counteracting the paleogeographic effect of decreasing continental dynamic topography i.e., continental flooding.

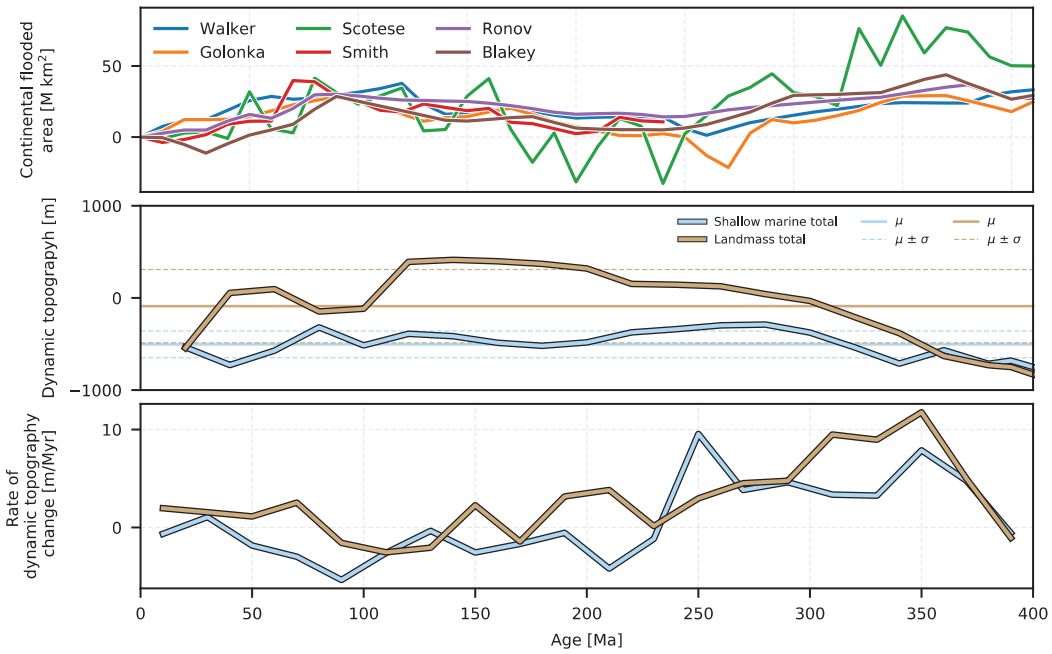

Figure 5.9: Continental flooding history, dynamic topography amplitude and rate of change. Top row: published continental flooded area curves (Ronov, 1994; Walker et al., 2002; Smith et al., 2004) and constructed on the basis of paleogeographic maps; Blakey (Blakey and Wong, 2003; Blakey, 2008), Golonka (Golonka, 2007a, b, 2009a, b, 2012) and Scotese (Scotese, 2010b). Middle row: histogram modes of total dynamic topography from Figure. 8 plotted as a timeseries. Solid borderless lines are the timeseries mean (μ) and dashed lines are time series mean plus/minus one standard deviation (σ). Bottom row: histogram modes of rate of dynamic topography change from Figure. 8 plotted as a timeseries.

5.4 A flooding threshold?

An interesting aspect of the results is that total dynamic topography in shallow marine environments is always negative and 60% of the extracted histogram modes are within one standard deviation (σ = 150 m) of -500 m (Fig. 5.9). On the other hand, total dynamic topography in terrestrial areas is far more variable, ranging -850 m to 400 m with σ = 400 m (Fig. 5.9). A first interpretation of this result is that continental inundation is most likely to occur in areas where dynamic topography is negative. When mantle supported uplift exceeds a threshold (-350±50 m) regression occurs and the geography becomes terrestrial (Fig. 5.9). This hypothesis is best illustrated during the Carboniferous-Jurassic interval. In these times, dynamic topography in terrestrial areas increased (Fig. 5.8). Meanwhile, the area of flooded continental platform decreased yet dynamic topography in shallow marine areas remained steady (Fig. 5.8). If dynamic topography in shallow marine areas preferentially occurs within a range, then, as more and more continental areas pass through the range, they must become subaerial. There are no such dynamic topography limits in terrestrial environments, which may explain the unrestricted increase in dynamic topography recorded in these areas; similar to a moving average sliding window. Indeed, regression of the Eromanga Sea in the Cretaceous would support this hypothesis. At 100 Ma dynamic topography in the Eromanga Sea area was -350 m (Fig. 5.3) and Central Australia was flooded (Fig. 5.5). By 80 Ma dynamic uplift had elevated Central Australia through the "flooding window" to -250 m (Fig. 5.3) and the Eromanga Sea waned (Fig. 5.5). Other cases include the central North American intercontinental Williston, Illinois and Michigan Basins which were flooded and dynamically depressed by more than 350 m from Devonian-Carboniferous times (Fig. 5.6). When Pangea assembled and the central North American interior rose above -350 m these basins became terrestrial.

Similar instances during Devonian-Carboniferous times occur in the North West African intercontinental basins (Fig. 5.6) e.g., Taoudenni, Gourara, Oued Mya and Illizi-Ghadames Basins.

The concept of a flooding threshold has been introduced in studies of the effect of dynamic topography on continental marine inundation (Gurnis, 1993; Müller et al., 2018b). In these analyses, continental inundation predicted by models of dynamic topography is defined by the inequality:

$$hC(t) < S(t) + h_c$$

where hC (m) is continental dynamic topography, t is time, S is eustatic sea level and h_c (m) is a constant that is optimised to match the spatial extent of predicted flooding with selected paleogeographic maps. A direct comparison with the threshold presented herein is not straightforward since the flooding threshold approach (Gurnis, 1993; Müller et al., 2018b) is dependent on: (i) the choice of eustatic curve and paleogeographic reconstruction and (ii) the dynamic topography model. However, I note that the more recent of the aforementioned studies, Müller et al. (2018b) has proposed dynamic topography flooding thresholds across three cases ranging between -325 m and -75 m; -390 m and -140 m; and -295 m and -45 m, which are comparable to the range presented above.

An alternative explanation to the flooding range hypothesis is that the geodynamic models typically produce the most negative dynamic topography at the edges of landmasses near subduction zones (Fig. 5.6) and shallow marine depositional environments are also typically at the edges of landmasses (Fig. 5.6). Therefore, one would expect a correlation between negative dynamic topography and shallow marine deposition.

5.5 Conclusions

Eustatic and subsidence studies integrated with paleogeographic data make for powerful tools with which to investigate the effect of mantle flow on continental flooding and test the usefulness of "stable" continental platforms in reconstructing eustasy from sequence stratigraphic methods. Reference districts on the Australian shield are used for reconstructing the latest Cambrian-early Ordovician and early Devonian intervals of the Haq and Schutter (2008) global eustatic curve. However, in the above analysis I have used models of dynamic topography to confirm that this approach is limited since dynamic topography precludes the existence of stable continental platforms (e.g., Moucha et al., 2008).

In this study I examined the tectonic and dynamic stability of Australian reference districts for reconstructing Paleozoic sea level using sequence stratigraphy. The results of my analysis suggest amplitudes of global seal level determined using the sequence stratigraphic approach may overestimate eustatic change, due to the effects of local tectonic disturbances and mantle flow. Furthermore, my results suggest that sequence stratigraphic models which predict global sea level highs in early Paleozoic times may be inadvertently influenced by the effects of mantle convection; in addition to tectonic events i.e., Ordovician rifting in the Canning and Amadeus basins and subduction along the east Australian margin during Devonian times. I found that although rates of dynamic topography change are relatively low in the Canning, Amadeus and Georgina basins during Ordovician times (~5 m/Myr) and in the Waratah Bay and Broken River regions in the early Devonian (~8 m/Myr) compared to other reference districts – for example, South China in Permian times was subsiding at a rate of ~30 m/Myr (Cao et al., 2019) – these

areas were not tectonically quiescent during the intervals of interest. Thus, their reliability as reference districts for eustatic reconstructions is questionable.

In this analysis I investigated the evolution of Australia's paleogeography throughout Paleozoic times. The results show that during the Carboniferous sea level high, rapid dynamic uplifting of the Australian plate due to mantle upwelling beneath the Tethys margin of Gondwana lead to a regional sea level fall and the complete subaerial exposure of the continent. During the Cretaceous highstand, the northward drift of Australia coupled with back-arc spreading along the Australian eastern margin resulted in dynamic uplift and the regression of the Eromanga Sea. This result is consistent with other studies of the influence of dynamic topography on Cretaceous Australia (Gurnis et al., 1998; Czarnota et al., 2014; Müller et al., 2016b; Salles et al., 2017).

Finally, I compared global maps of dynamic topography with paleogeography and the results indicate a correlation between paleogeography and dynamic topography. I showed that throughout the majority of Paleozoic times positive continental dynamic topography was associated with restricted continental flooding while, negative continental dynamic topography is coeval with widespread continental flooding. The exception to this is during the past 100 Myr times when an increase in the average age of the oceanic crust offset the paleogeographic effect of decreasing continental dynamic topography.

The results I have presented here demonstrate a profound link between mantle dynamics and the evolution of Earth's surface and demonstrate how a gap in the sequence stratigraphic approach to reconstructing eustasy can been filled by integrating tectonic and geodynamic processes (Young et al., *In revision., Chapter 3*).

Chapter 6. Discussion

In this thesis mantle flow models have been used to investigate the effects of the plate-mantle system on the evolution of Earth's surface. Global forward numerical convection models are critical in estimating the long-wavelength evolution of dynamic topography in deep geological time (beyond 400 million years ago) due in large part to their computational efficiency and ability to resolve relatively high spatial (e.g., for global models a horizontal surface resolution of ~50 km) and temporal (1 Myr) resolution. There are two main caveats to these types of forward models: (i) they are dependent on a synthetic initial condition because past mantle structure is a priori unknown, and; (ii) they are kinematically driven by plate motion histories. The former is an unavoidable limitation of forward numerical models; although insights from seismic tomography may provide some control back to ca. 250 Ma and uncertainties regarding suitable initial conditions can be mitigated through exploration of the parameter space (e.g., Flament et al., 2017a). Constraining past plate motion and subduction history represents a separate challenge.

6.1 Limitations and uncertainties in plate tectonic models

A definitive characteristic of geodynamic forward models of mantle flow is the forcing of plate kinematics as a surface boundary condition. Considering the intimate coupling of the plate-mantle system, plate motion history may be regarded as the primary constraint that must be applied to mantle convection models. If the time-dependent impact of dynamic topography on the evolution of Earth's Paleozoic surface is to be investigated, forward mantle flow models constrained by a history of plate motions for these times (540-0 Ma) is a prerequisite. Thus, we reach the primary motivation for the work presented in Chapter 2 i.e., the development and analysis of the Young et al. (2019, Chapter 2) plate model.

Due to its importance in the convection modelling, there are some limitations of and uncertainties in the Young et al. (2019, Chapter 2) plate model that should be mentioned here and could be improved in future work. They concern: constraints on paleolongitude (orthoversion, Large Low Shear Velocity Province (LLSVP) or purely paleomagnetic reference frames), the coverage and reliability of paleomagnetic data, missing and synthetic plates (back-arc basins, micro-blocks and subducted ocean), lithospheric deformation, differing regional interpretations and the use of present-day kinematics to constrain past plate motions. In the following discussion I will elaborate on the uncertainties to which the geodynamic models are most sensitive.

Primary amongst the uncertainties and limitations is the dependence on paleomagnetic data for constraining plate motion for times older than 200 Myr. As we have seen in earlier chapters, a great number of plate tectonic reconstructions have been developed in the past ~60 years. Although each have their own nuances and defining features, a commonality they share is that they are increasingly poorly constrained back in time. Naturally, this is an expected consequence of relying on physical data, as the passing of time inevitably leads to the destruction of the primary rock record. Yet, there is general consensus amongst palaeographers, paleomagnetists and plate tectonic modelers of the configuration and evolution of Earth's tectonic plates since the break-up of Gondwana in Jurassic times (e.g., Lithgow-Bertelloni and Richards, 1998; Stampfli and Borel, 2002; Christopher R. Scotese, 2004; Torsvik et al.,

2008; Golonka, 2009b; Seton et al., 2012). However, for times older than ~200 Ma plate reconstructions become more subjective and less analytical as data becomes scarcer and less reliable. As Mesozoic–Cenozoic marine geophysical evidence (e.g. magnetic anomaly picks, fracture zones, extinct ridges, seamount trails and absolute sea floor ages from deep sea drilling) fades from the geological record, plate modelers turn to observations of paleomagnetism, palaeontology, paleogeography, ophiolite obduction, arc magmatism, tectonic and stratigraphic structures and, high-pressure/ultra-high-pressure metamorphism to reconstruct the spatiotemporal distribution of the Earth's plates. The most important of these for reconstructing the Paleozoic Earth is paleomagnetic data.

Since the early 1950's paleomagnetic data have been used to track the movement of Earth's crustal blocks (e.g., Creer et al., 1954) and vast databases of paleomagnetic information have been built over the decades (see International Association of Geomagnetism and Aeronomy Global Paleomagnetic Database). That said, the spatial and temporal coverage of data is non-uniform and accuracy is often an issue (Van der Voo, 1990). For example, in the Young et al. (2019, Chapter 2) plate model there is a single paleomagnetic pole available from Laurussia and Siberia for 390-340 Ma, and South China has no Carboniferous paleomagnetic data. Thus, motion of these blocks must be interpolated. Furthermore, paleomagnetic data are only useful to resolve the latitudinal component of a crustal block's position and its rotation relative to north. Inherently, these data do not provide information on the longitudinal position since the Earth's time-averaged geomagnetic field is symmetric about its rotation axis hence, paleolongitudes are arbitrary.

As discussed in Chapter 2, attempts have been made to constrain paleolongitude in Paleozoic times by linking surface motions to LLSVPs in the lowermost mantle (Domeier and Torsvik, 2014; Torsvik et al., 2014) and according to the orthoversion model of the supercontinent cycle, as implied by paleomagnetic observations (Mitchell et al., 2012). As shown in Chapter 2, tectonic reconstructions built upon these hypotheses are characterised by large plate speeds (11 cm/yr) and trench speeds (13 cm/yr) in addition to widespread trench advance (70% of trenches) – characteristics that hinder the results of numerical flow models (Alisic et al., 2012; Young et al., 2019, Chapter 2) – and in the case of LLSVP stability, principles that are challenged by geodynamic modelling (e.g. Bunge et al., 1998; Zhang et al., 2010; Zhong and Rudolph, 2015; Flament et al., 2017a; Young et al., 2019, Chapter 2) and statistical analyses of the spatial correlation between LIPs and LLSVP margins (Austermann et al., 2014; Davies et al., 2015).

Beyond 200 Ma only 30% of the Earth's surface is constrained (Domeier and Torsvik, 2019). It is therefore an unavoidable reality that in reconstructing the configuration and plate motion history of the Paleozoic world many unknowns have to be inferred, including plate and plate boundary kinematics. As shown in Chapter 2 and in other studies (Zhang et al., 2010; Bull et al., 2014; Zhong and Rudolph, 2015; Choblet et al., 2016) these assumptions have a profound impact on numerical models that reconstruct the evolution of the long-wavelength lower mantle structure of the Earth. In Chapter 2 as well as the aforementioned studies, models of mantle flow constrained by plate motion suggest that the long-wavelength lower mantle structure is largely established by 250 Ma, because (i) circum-Pangea subduction acts to first organise and then stabilise the lower mantle structure beneath Africa and the Pacific and (ii) the breakup of Pangea does not cause a significant reorganisation of the global subduction

pattern that is fundamental to developing and maintaining this structure. The consensus regarding the establishment of the long-wavelength structure of the lower mantle by 250 Ma is contradicted when geodynamic models are run using plate models that implement large synthetic subduction zones. As shown in Chapter 2, to satisfy LLSVP longitudinal constraints, large (~15,000 km), long-lived (30 Ma) synthetic subduction zones were implemented in the Rheic and Paleotethys Oceans in the Domeier and Torsvik (2014) and Matthews et al. (2016) plate models. When this reconstruction is used as a boundary condition in numerical mantle flow models, the present-day lower mantle structure is not well reproduced (Young et al., 2019, Chapter 2) due to subduction at these synthetic, intra-oceanic plate boundaries, thus highlighting the sensitivity of the geodynamic models to surface constraints. The impact of a shorter and shorter-lived subduction zone is less likely to result in such a significant impact.

6.2 Limitations and uncertainties in numerical forward mantle convection models

The plate tectonic paradigm states the Earth's tectonic plates form an integrated convective system together with the mantle. In this thesis geodynamic models that progressively assimilate plate reconstructions in time-dependent global mantle flow models have been used to investigate how this system gives rise to long-wavelength dynamic topography change at the Earth's surface.

The flow models used in this project are created using the mantle convection code *CitcomS*, the benefits of which were highlighted in Chapter 1. To re-iterate, they include: (i) *CitcomS* has been specifically integrated with tectonic reconstructions so that the thermal structure of the lithosphere, plate velocities and shallow slabs are integrated, thus ensuring asymmetric subduction (Bower et al., 2015); (ii) it is a forward convection code and hence, designed to reconstruct mantle flow in deep geological time; (iii) it is computationally efficient (e.g. each model run is affordable on a modern supercomputer; about 57,600 total CPU hours for a flow model that covers 1,000 Ma); (iv) the parameter space has been extensively explored (Flament et al., 2017a), (v) the convection model is independent from seismic tomography which makes comparison to seismic velocity anomalies possible and (vi) because the model is paleogeographically constrained the results (i.e. predictions) of dynamic topography can be directly compared to the geological record. Nevertheless, there are some caveats worth mentioning.

Firstly, due to numerical limitations in resolving large viscosity variations (LVVs) a comparatively low viscosity contrast must be implemented – we use three orders of magnitude in the presented flow models – which produces large-scale convection. While the LVVs used in this thesis are lower than expected to occur in the Earth (Čadek and Fleitout, 2006) and limit small-scale upper mantle convection as well as the viscosity contrasts between plumes/slabs and their surroundings in addition to the lithosphere-asthenosphere, they can be solved with a resolution that allows us to compute time-dependent mantle flow models suitable for investigations of the global plate mantle-system over long geological timescales (Zhang et al., 2012; Cao et al., 2019). Other numerical codes (e.g., *StagYY*) are able to resolve greater LVVs (Tackley, 2008) though, they are not as well integrated with tectonic reconstructions.

Secondly, as we have seen in Chapter 2, close to the core–mantle boundary two broad regions of anomalies in seismic velocities (LLSVPs) are observed (Garnero et al., 2016). Mantle seismic velocities in these zones are recognised as slower than ambient, but there is debate as to whether thermal anomalies

alone can explain the character of the LLSVPs or if there is a chemical component that distinguishes them from the surrounding mantle (Schuberth et al., 2009; Davies et al., 2012; Bull et al., 2014). *CitcomS* models can be either thermochemical or chemical, though the thermochemical models are easier to reconcile with the present-day long-wavelength mantle structure Earth (McNamara and Zhong, 2005; Zhang et al., 2010; Flament et al., 2017a; Young et al., 2019, Chapter 2). Numerical forward models invoking only thermal convection can be reconciled with tomography models by integrating mineral physics and a tomographic filter (these can account for the effects of uneven geographic data coverage as well as smearing and damping inherent to the tomographic inversion) to the geodynamic model (Bunge and Davies, 2001; Davies and Davies, 2009; Davies et al., 2012). Jointly integrating an equation of mineral physics and tomographic filters to *CitcomS* models is still to be done and is an avenue for future work.

Finally, since the workflow used in this thesis is semi-empirical, it is not entirely self-consistent. Because plate velocities are forced, surface motion is not determined by the system dynamics rather, they are prescribed by the plate tectonic model. Hence, inconsistencies between surface velocities and buoyancy distributions in the convecting mantle can add or remove energy from the system and generate artificial stresses at the surface (Lowman, 2011).

An emerging alternative to forward models of mantle flow is adjoint models. The adjoint method involves finding optimal flow histories relative to the current model state. In order to accomplish this aim, an initial condition is guessed far back in time and the present-day mantle structure is imposed from a seismic tomography model. The optimal initial condition is then found by minimizing a cost function (representative of the difference between predicted present-day model state and observed mantle structure inferred from seismic tomography) by iteratively solving forward and backward convection equations – a computationally intensive task, but one being increasingly enabled by rapid technological advances.

It was mentioned in Chapter 1 that a limitation of backward convection models is that thermal diffusion cannot be simply reversed and therefore, thermal buoyancy cannot be generated back in time. The difficulty arises because when the energy and momentum equations are reversed (to go backward in time) the thermal diffusivity term becomes unstable. To overcome the issues that the process of diffusion causes further back in time, adjoints of the governing equations (i.e., adjoint with respect to the forward equations) have been developed (Bunge et al., 2003; Ismail-Zadeh et al., 2004; Liu and Gurnis, 2008) in which the adjoint diffusion operator involves the opposite sign – a change which stabilises thermal diffusion backward-in-time. Hence, the main advantage of the adjoint method is that it uses a forward solution to converge upon the known tomographic structure.

Use of the adjoint method in geodynamic studies is becoming more established due to its applicability and improving efficiency (Shephard et al., 2010; Colli et al., 2018; Ghelichkhan and Bunge, 2018) and synthetic experiments demonstrate that for an optimal result (no model or data error) adjoint models can restore mantle flow over timescales on the order 100 Myr (Colli et al., 2020). That said, naturally, the validity of adjoint mantle convection models depends on the uncertainty of the inputs i.e., the geodynamic model, history of surface velocities and the model of the present-day mantle seismic structure. Furthermore, adjoint models are still somewhat constrained by hardware (require significant computational costs) and uncertainties (fundamental mantle properties, e.g., viscosity, temperature and

density, must be deduced).

Thus, the adjoint method combines the present-day mantle seismic structure, plate motion histories and mantle convection models to reconstruct past mantle flow and therefore, and therefore has the potential to link observations from a combination of geoscience disciplines (e.g., paleomagnetism, episodes of volcanism/metamorphism, palynology and paleogeographic correlation, seismology, mineral physics, sedimentology) in a dynamically consistent way, opening exciting opportunities for future studies involving geodynamic modelling.

6.3 Limitations and uncertainties in calculation of dynamic topography

Using the normal stresses that arise from the density driven flow in a mantle convection model, dynamic topography can be calculated. Uncertainties and limitations of these calculations were discussed at some length in Chapter 4, but it is worth revisiting quickly here. Long-wavelength dynamic topography in this thesis was calculated from sources of buoyancy deeper than 350 km. In Chapter 3 LVVs above this depth were preserved, while in Chapter 4 and 5 they were not. It was acknowledged in Chapter 4 that by not accounting for the impact of uppermost mantle structure, dynamic topography at long-wavelengths is amplified (Golle et al., 2012; Sembroni et al., 2017) and that the large amplitude, short-wavelength component of dynamic topography is not represented (Hoggard et al., 2016; Davies et al., 2019); however, owing to the difficulties associated with inferring the time-dependent thermochemical structure of the mantle lithosphere, this choice is justified. Thus, the predictive models used herein focus on dynamic topography at long-wavelengths and generated in the deep mantle; although, it should be noted that the uppermost mantle flow also contributes to the signal at the long-wavelength (Colli et al., 2016; Davies et al., 2019). Some of the differences between estimates of long-wavelength dynamic topography calculated with or without including LVVs above 350 km can be illustrated using the results from mantle flow model C1 presented in Chapter 3 (Fig. 6.1).

As was done by Flament (2019b), I plotted the global present-day dynamic topography (calculated with and without including LLVs above 350 km) for case C1 with 1,161 spot constraints from oceanic residual topography from Hoggard et al. (2017) (Fig. 6.1A-B). The standard deviation between dynamic topography calculated with LLVs preserved and the residual topography is 610 m (Fig. 6.1C), 630 m for dynamic topography calculated ignoring LLVs (Fig. 6.1D). The amplitude range of dynamic topography calculated with LLVs preserved is -3,100 m to 800 m (Fig. 6.1C), -1,300 m to 200 m for dynamic topography calculated ignoring LLVs (Fig. 6.1D) and -2,800 m to 2,200 m for the spot constraints of Hoggard et al. (2017). High negative dynamic topography in calculations including LLVs is generated above subduction margins (Fig. 6.1a) while the amplitude of dynamic topography above these features is filtered in the no LLVs calculation (Fig. 6.1B). There is a notable difference between the residual topography and dynamic topography in both instances in the North Atlantic (above the Iceland Plume) and at the western margins of Africa, India and North America (Fig. 6.1A-B). Since there are no spot measurements in continental interiors, this approach is limited by geographical biases. My analysis above is consistent with the findings of Flament (2019b) that the inclusion of LLVs in dynamic topography calculations results in a better correlation with the high-accuracy spot constraints from Hoggard et al. (2017).

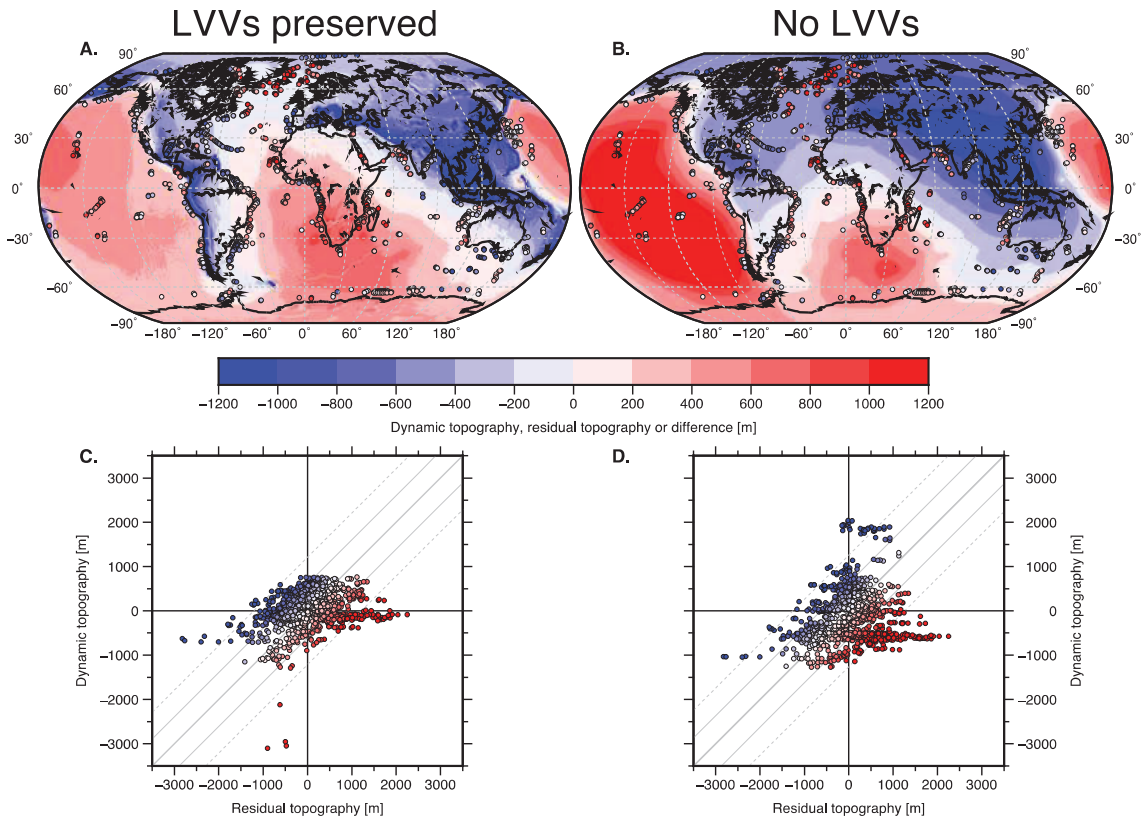

Figure 6.1: Comparison between dynamic topography and spot constraints on residual topography. A: Dynamic topography for case C1 calculated with lateral viscosity variations (LVVs) preserved, and high-accuracy residual topography from Hoggard et al. (2017). B: As with A. except dynamic topography is calculated without considering LVVs. C: Scatter plot of the Hoggard et al. (2017). residual topography and dynamic topography for case C1 calculated with LVVs; sampled at the locations shown in A. The solid grey line is the 1:1 line, the thin grey lines are the 1:1 plus/minus one standard deviation of the linear regression among the variables, and the dashed lines are plus/minus two standard deviations. Symbols are coloured by the difference between residual and dynamic topography. D: Same as C. except dynamic topography is calculated without considering LVVs.

As seen in Figure. 6.1 there are mismatches between calculated dynamic topography and residual topography spot constraints. This is partially due to the exclusion of the uppermost part of the mantle in some of the calculations of dynamic topography. While there is no doubt this region contributes to the total signal (Hoggard et al., 2016; Davies et al., 2019) determining the dynamic topography generated here is difficult as it requires constraints on the thermochemical structure of the mantle lithosphere. In order to circumvent some of the ambiguity associated with calculating time-dependent dynamic topography, one can run backward/adjoint convection models using mantle seismic velocity anomalies to constrain the thermochemical structure of the mantle (Spasojevic et al., 2009). Yet, even for present-day estimates this approach is limited by uncertainties in mineral physics, scaling and geographical biases in data coverage (Perry et al., 2003; Guerri et al., 2016); let alone back in time. Moreover, as mentioned in Chapter 1, backward/adjoint convection models are limited back in time to the past 50-75 Ma since thermal diffusion cannot easily be reversed.

Chapter 7. Conclusions and future work

7.1 Conclusions

Numerical models of mantle convection have been used to investigate the effect of dynamic topography on the evolution of Earth's surface throughout Phanerozoic times in order to improve our understanding of the interactions between Earth's mantle and surface.

The first step of this work was the development of a plate tectonic reconstruction for use as a boundary condition in numerical forward mantle flow models. The new plate model imposes no absolute constraints on Paleozoic paleolongitude, limits Paleozoic plate velocities to the same range observed at present-day (~2–20 cm/yr) and implements alternative (with respect to previous reconstructions) histories for the Paleozoic evolution of North and South China and, the closure of the Rheic Ocean. Using the tectonic reconstruction as boundary conditions for a mantle flow model produced a reconstruction of the lowermost mantle structure that is consistent with the present-day seismic anomalies observed in tomographic models and challenges the proposed fixity of LLSVPs suggesting the African LLSVP margin has moved by as much as 1,450 km since late Permian times (260 Ma). Also, in the plate-mantle scenario presented, South China was proximal to the eastern margin of the African LLSVP during the Permian eruption of the Emeishan Traps and not the western margin of the Pacific LLSVP as previously suggested.

In collaboration with Merdith et al. (2021) the plate model was merged into a continuous, kinematic plate model from 1 Ga to present and was used to develop a new workflow for calculating eustatic change over the entire Phanerozoic Eon. The new method utilises global, time-dependent hypsometry curves to incorporate the main solid Earth mechanisms for sea level change; including, for the first time, time-dependent dynamic topography. Furthermore, the workflow is openly available community development. Using the workflow, Phanerozoic eustatic change was calculated and analysed. The results suggest the main drivers of sea level change over the past 560 Myr include: the changing volume below mid-ocean ridges, 460 m; dynamic topography, 250 m; the deep-water cycle, 230 m; and the volume above trenches, 130 m. Furthermore, the results indicate that changes in ocean basin volume due to changes in the crustal age-area distribution are not balanced by a compensating equal but opposite volume change above subduction zones or by large-scale dynamic vertical motion of the continents.

To investigate the effect of dynamic topography on the continental surface, basin subsidence histories were recovered from backstripped well data in western and central Australia. These locations are located vast distances from active plate boundaries and represent some of the most stable continental platforms in Paleozoic times. Well data were combined with time-dependent models of dynamic topography to test the hypothesis that anomalous basin subsidence may be explained by mantle-flow driven topography. In the presented reconstruction of mantle flow, topographic rebound following the sinking of a Cambrian aged slab resulted in a minor phase of dynamic uplift in the Cooper Basin in the middle Permian. In the Carboniferous – Triassic, a mantle upwelling beneath western Australia caused dynamic uplift which was augmented by a focused active mantle plume during the Permo-Triassic. In the Late Jurassic – Cretaceous, Australia drifted east away from the mantle upwelling resulting in a period of subsidence in western Australia. During the Cretaceous the Cooper Basin moved over a downwelling

produced by long-lived subduction along the east Australian margin, resulting in a period of accelerated subsidence.

Finally, the global plate model, sea level curve and basin subsidence histories were integrated with paleogeographic data to explore the effect of mantle flow on continental flooding over the last 500 Myr and to evaluate the reliability of Australian regional areas as indicator districts for Paleozoic eustasy. Results of this analysis suggest that tectonic activity and dynamic topography affected Ordovician Western and Central Australia and Devonian Eastern Australia, which suggests that these locations may not be suitable as reference districts. This conclusion has implications for the existing reconstruction of Paleozoic sea level change. Furthermore, regression of the Eromanga Sea during the Cretaceous is related to dynamic uplift above a mantle upwelling beneath the Gondwana-Tethys margin coupled with back-arc spreading along the eastern Australian margin. Finally, global maps of dynamic topography and paleogeography suggest a correlation between paleogeography and dynamic topography during the majority of Paleozoic times, wherein positive continental dynamic topography is associated with restricted continental flooding and negative continental dynamic topography is related to widespread continental flooding.

As a whole, the conclusions reached in this thesis support a strong coupling between plate-mantle system, geodynamic processes and surface deformation in deep geological time from a scale of individual basins, to continental platforms, global mantle convection and plate tectonics. This contribution has produced a Paleozoic plate model with a large range of potential applications beyond the immediate outcomes of this project. It has revealed the effect of the solid Earth on global sea level twice as far back in time than has so far been possible and quantifies the effect of mantle flow on long-lived Australian onshore basins, and the continental flooding record thus providing the Australian Earth Science community with a new framework to understand anomalous episodes in the geological record. As a body of work, this thesis also bridges the traditionally distinct fields of sedimentology and mantle convection.

7.2 Future work

As the discussion above has highlighted, a limitation of this thesis is the use of a singular tectonic reconstruction throughout. First and foremost, future work should test how alternative reconstruction scenarios (e.g., orthoversion, LLSVP reference frames) affect the outcomes of the analysis herein. In particular, the workflow presented in Chapter 3 – which is designed to be applied and tested with numerous different plate reconstructions – would be augmented by using alternative plate models.

In Chapter 4 low temperature thermochronology data was used to ground truth models of dynamic topography. Supplementing long wavelength patterns of uplift with comparable apatite fission-track thermochronology data is an important step in linking models with observations. To assist scientists studying the magnitude and spatiotemporal evolution of dynamic topography, an online infrastructure for hosting and maintaining global low temperature thermochronology data could be built and made available to the research community via an opensource platform.

Another key finding in Chapter 4 was the potential relationship between regional igneous rocks reported on the Australian north-west shelf and a mantle plume predicted by flow modelling. While some

dating has been done, a high certainty age of these igneous rocks is still lacking. Furthermore, the source of the rocks remains undetermined. The igneous intrusions in north-west Australian have not received much attention since the 1980's, and there has been little additional drilling in that area. The Geological Survey of Western Australia has cored these intrusions, but geochemistry or modern geochronology has not been done on them, so there is some scope for such a project.

Finally, In Chapter 5 an episodicity in the evolution of dynamic topography was proposed. With advances in plate modelling extending reconstructions back to 1 Ga the opportunity is available to explore the evolution and effects of long-wavelength dynamic topography over more than one supercontinent cycle. Results from geodynamic modelling can be used to examine the influence of dynamic topography on global sedimentation patterns, and biochemical changes within the atmosphere–hydrosphere system; advancing our knowledge of the interactions between mantle dynamics and the Earth's surface over long geological timescales. Furthermore, the analysis in Chapter 5 shows that a regional update is required for the plate motion model along the east Australian Paleozoic margin. Clearly the geological history of this margin is more complex than would be achieved by long-lived west-dipping subduction. Implementing and testing the geodynamic effects of different tectonic scenarios at this margin will be an important next step.

References

Abbott, S., Orlov, C., Bernardel, G., Nicholson, C., Rollet, N., Nguyen, D., and Gunning, M., A Stratigraphic and structural architecture across the central North West Shelf - implications for Triassic petroleum systemsAustralian Petroleum Production & Exploration Association Annual Conference and Exhibition, Brisbane, 2019a, CSIRO *in press*.

Abbott, S., Orlov, C., Bernardel, G., Nicholson, C., Rollet, N., Nguyen, D., and Gunning, M., Palaeogeographic evolution of the Triassic succession, central North West ShelfAustralasian Exploration Geoscience Conference, Perth, 2019b, *in press*.

Adams, M., Stewart, K., Trupe, C., and Willard, R., 1994, Tectonic significance of high-pressure metamorphic rocks and dextral strike-slip faulting in the southern Appalachians. doi:

Alexander, E., Gravestock, D., Cubitt, C., and Chaney, A., 1998, Lithostratigraphy & environments of deposition, *in* Gravestock, D. I., Hibburt, J. E., and Drexel, J. F., eds., *Petroleum geology of South Australia Volume 4: Cooper Basin*, Volume 4: Adelaide, Primary Industries & Resources South Australia, p. 69-117.

Algeo, T., and Wilkinson, B., 1991, Modern and ancient continental hypsometries: Journal of the Geological Society, v. 148, no. 4, p. 643-653. doi: https://doi.org/10.1144/gsjgs.148.4.0643

Algeo, T. J., and Seslavinsky, K. B., 1995, Reconstructing eustatic and epeirogenic trends from Paleozoic continental flooding records, *in* Haq, B. U., ed., *Sequence Stratigraphy and Depositional Response to Eustatic, Tectonic and Climatic Forcing*, Springer, p. 209-246.

Alisic, L., Gurnis, M., Stadler, G., Burstedde, C., and Ghattas, O., 2012, Multi-scale dynamics and rheology of mantle flow with plates: Journal of Geophysical Research: Solid Earth, v. 117, no. B10. doi: https://doi.org/10.1029/2012JB009234

Allen, P. A., and Allen, J. R., 2013, Basin analysis: Principles and application to petroleum play assessment, John Wiley & Sons.

Altherr, R., Henes-Klaiber, U., Hegner, E., Satir, M., and Langer, C., 1999, Plutonism in the Variscan Odenwald (Germany): from subduction to collision: International Journal of Earth Sciences, v. 88, no. 3, p. 422-443. doi:

Amante, C., and Eakins, B. W., 2009, ETOPO1 arc-minute global relief model: procedures, data sources and analysis. doi: https://doi.org/10.1594/PANGAEA.769615

Amaru, M. L., 2007, Global travel time tomography with 3-D reference models. Doctoral thesis: Utrecht University

Apak, S., Stuart, W., and Lemon, N., 1995, Compressional control on sediment and facies distribution SW Nappamerri Syncline and adjacent Murteree High, Cooper Basin: The APPEA Journal, v. 35, no. 1, p. 190-202. doi: 10.1071/AJ94013

Apak, S. N., 1994, Structural development and control on stratigraphy and sedimentation in the Cooper Basin, northeastern South Australia and southwestern Queensland/by Sukru N. Apak

Apak, S. N., Stuart, W. J., Lemon, N. M., and Wood, G., 1997, Structural evolution of the Permian-Triassic Cooper Basin, Australia: relation to hydrocarbon trap styles: AAPG bulletin, v. 81, no. 4, p. 533-555. doi: 10.1306/522B43C5-1727-11D7-8645000102C1865D

Arenas, R., Fernández, R. D., Martínez, S. S., Gerdes, A., Fernandez-Suarez, J., and Albert, R., 2014, Two-stage collision: exploring the birth of Pangea in the Variscan terranes: Gondwana Research, v. 25, no. 2, p. 756-763. doi:

Arne, D., Green, P., Duddy, I., Gleadow, A., Lambert, I., and Lovering, J., 1989, Regional thermal history of the Lennard shelf, Canning Basin, from apatite fission track analysis: Implications for the formation of Pb-Zn ore deposits: Australian Journal of Earth Sciences, v. 36, no. 4, p. 495-513. doi: 10.1080/08120098908729506

Arnold, G., and Fawckner, J., 1980, The Broken River and Hodgkinson Provinces: The geology and geophysics of northeastern Australia, p. 175-189. doi:

Arthaud, F., and Matte, P., 1977, Late Paleozoic strike-slip faulting in southern Europe and northern Africa: Result of a right-lateral shear zone between the Appalachians and the Urals: Geological Society of America Bulletin, v. 88, no. 9, p. 1305-1320. doi:

Athy, L. F., 1930, Density, porosity, and compaction of sedimentary rocks: AAPG Bulletin, v. 14, no. 1, p. 1-24. doi: 10.1306/3D93289E-16B1-11D7-8645000102C1865D

Auer, L., Boschi, L., Becker, T., Nissen-Meyer, T., and Giardini, D., 2014, Savani: A variable resolution whole-mantle model of anisotropic shear velocity variations based on multiple data sets: Journal of Geophysical Research: Solid Earth, v. 119, no. 4, p. 3006-3034. doi:

Augustsson, C., Muenker, C., Bahlburg, H., and Fanning, C. M., 2006, Provenance of late Palaeozoic metasediments of the SW South American Gondwana margin: a combined U–Pb and Hf-isotope study of single detrital zircons: Journal of the Geological Society, v. 163, no. 6, p. 983-995. doi:

Austermann, J., Kaye, B. T., Mitrovica, J. X., and Huybers, P., 2014, A statistical analysis of the correlation between large igneous provinces and lower mantle seismic structure: Geophysical Journal International, v. 197, no. 1, p. 1-9. doi: 10.1093/gji/ggt500

Azor, A., Rubatto, D., Simancas, J., González Lodeiro, F., Martínez Poyatos, D., Martín Parra, L., and Matas, J., 2008, Rheic Ocean ophiolitic remnants in southern Iberia questioned by SHRIMP U-Pb zircon ages on the Beja-Acebuches amphibolites: Tectonics, v. 27, no. 5. doi:

Bahlburg, H., and Hervé, F., 1997, Geodynamic evolution and tectonostratigraphic terranes of northwestern Argentina and northern Chile: Geological Society of America Bulletin, v. 109, no. 7, p. 869-884. doi:

Bahlburg, H., Vervoort, J. D., Du Frane, S. A., Bock, B., Augustsson, C., and Reimann, C., 2009, Timing of crust formation and recycling in accretionary orogens: Insights learned from the western margin of South America: Earth-Science Reviews, v. 97, no. 1, p. 215-241. doi:

Bai, Y., Chen, G., Sun, Q., Sun, Y., Li, Y., Dong, Y., and Sun, D., 1987, Late Paleozoic polar wander path for the Tarim platform and its tectonic significance: Tectonophysics, v. 139, no. 1, p. 145-153. doi: http://dx.doi.org/10.1016/0040-1951(87)90203-4

Barnett-Moore, N., Hassan, R., Flament, N., and Müller, D., 2017, The deep Earth origin of the Iceland plume and its effects on regional surface uplift and subsidence: Solid Earth, v. 8, no. 1, p. 235. doi: 10.5194/se-8-235-2017

Barreiro, J. G., Catalán, J. R. M., Arenas, R., Castiñeiras, P., Abati, J., García, F. D., and Wijbrans, J. R., 2007, Tectonic evolution of the upper allochthon of the Órdenes complex (northwestern Iberian Massif): Structural constraints to a polyorogenic peri-Gondwanan terrane: Geological Society of America Special Papers, v. 423, p. 315-332. doi:

Barrell, J., 1914, The strength of the Earth's crust: The Journal of Geology, v. 22, no. 7, p. 655-683. doi:

Battersby, D., Cooper Basin gas and oil fields, *In* Leslie, R. B., Evans, H. J., and Knight, C. L.(Ed.), Economic Geology of Australia and Papua New Guinea1976, Volume 3, p. 321-368.

Baumgardner, J. R., 1985, Three-dimensional treatment of convective flow in the Earth's mantle: Journal of Statistical Physics, v. 39, no. 5-6, p. 501-511. doi: https://doi.org/10.1007/BF01008348

Benren, Z., Tingchuan, L., Shan, G., Jianping, O., Yinwen, H., and Changlin, G., 1994, Geochemical constraints on the evolution of North China and Yangtze blocks: Journal of Southeast Asian Earth Sciences, v. 9, no. 4, p. 405-416. doi:

Bercovici, D., Ricard, Y., and Richards, M. A., 2000, The relation between mantle dynamics and plate tectonics: A primer: Geophysical Monograph-American Geophysical Union, v. 121, p. 5-46. doi: https://doi.org/10.1029/GM121p0005

Besse, J., and Courtillot, V., 1991, Revised and synthetic apparent polar wander paths of the African, Eurasian, North American and Indian plates, and true polar wander since 200 Ma: Journal of Geophysical Research: Solid Earth, v. 96, no. B3, p. 4029-4050. doi:

Black, L., McClenaghan, M., Korsch, R. J., Everard, J. L., and Foudoulis, C., 2005, Significance of Devonian–Carboniferous igneous activity in Tasmania as derived from U–Pb SHRIMP dating of zircon: Australian Journal of Earth Sciences, v. 52, no. 6, p. 807-829. doi: https://doi.org/10.1080/08120090500304232
Blakey, R., 2011, Global paleogeography, NAU Geology. Northern Arizona University, Flagstaff, USA.
Blakey, R., and Wong, T., Carboniferous–Permian paleogeography of the assembly of Pangaea Proceedings of the XVth International Congress on Carboniferous and Permian Stratigraphy. Utrecht, 2003, Volume 10, p. 16.
Blakey, R. C., 2008, Gondwana paleogeography from assembly to breakup—A 500 my odyssey: Geological Society of America Special Papers, v. 441, p. 1-28. doi: https://doi.org/10.1130/2008.2441(01)
Bond, G. C., and Kominz, M. A., 1991, Disentangling middle Paleozoic sea level and tectonic events in cratonic margins and cratonic basins of North America: Journal of Geophysical Research: Solid Earth, v. 96, no. B4, p. 6619-6639. doi: 10.1029/90JB01432
Boucot, A. J., Xu, C., Scotese, C. R., and Morley, R. J., 2013, Phanerozoic paleoclimate: an atlas of lithologic indicators of climate, Society of Economic Paleontologists and Mineralogists.
Bower, D. J., Gurnis, M., and Flament, N., 2015, Assimilating lithosphere and slab history in 4-D Earth models: Physics of the Earth and Planetary Interiors, v. 238, p. 8-22. doi: https://doi.org/10.1016/j.pepi.2014.10.013
Bower, D. J., Gurnis, M., and Seton, M., 2013, Lower mantle structure from paleogeographically constrained dynamic Earth models: Geochemistry, Geophysics, Geosystems, v. 14, no. 1, p. 44-63. doi:
Bradley, D. C., 2008, Passive margins through earth history: Earth-Science Reviews, v. 91, no. 1-4, p. 1-26. doi: https://doi.org/10.1016/j.earscirev.2008.08.001
Braid, J. A., Murphy, J. B., and Quesada, C., 2010, Structural analysis of an accretionary prism in a continental collisional setting, the Late Paleozoic Pulo do Lobo Zone, Southern Iberia: Gondwana Research, v. 17, no. 2, p. 422-439. doi:
Braid, J. A., Murphy, J. B., Quesada, C., and Mortensen, J., 2011, Tectonic escape of a crustal fragment during the closure of the Rheic Ocean: U–Pb detrital zircon data from the Late Palaeozoic Pulo do Lobo and South Portuguese zones, southern Iberia: Journal of the Geological Society, v. 168, no. 2, p. 383-392. doi:
Braun, J., 2010, The many surface expressions of mantle dynamics: Nature Geoscience, v. 3, no. 12, p. 825-833. doi:
Brown, S., Boserio, I., Jackson, K., and Spence, K., 1984, The geological evolution of the Canning Basin-implications for petroleum exploration, *in* Purcell, P. G., ed., *The Canning Basin WA: Proceedings of Geological Society of Australia/Petroleum Exploration Society of Australia Symposium*: Perth.
Bryan, S. E., and Ernst, R. E., 2008, Revised definition of large igneous provinces (LIPs): Earth-Science Reviews, v. 86, no. 1-4, p. 175-202. doi: https://doi.org/10.1016/j.earscirev.2007.08.008
Bryan, S. E., and Ferrari, L., 2013, Large igneous provinces and silicic large igneous provinces: Progress in our understanding over the last 25 years: GSA Bulletin, v. 125, no. 7-8, p. 1053-1078. doi: 10.1130/B30820.1
Bull, A. L., Domeier, M., and Torsvik, T. H., 2014, The effect of plate motion history on the longevity of deep mantle heterogeneities: Earth and Planetary Science Letters, v. 401, p. 172-182. doi: https://doi.org/10.1016/j.epsl.2014.06.008
Bullard, E., Everett, J. E., and Gilbert Smith, A., 1965, The fit of the continents around the Atlantic: Philosophical Transactions of the Royal Society of London. Series A, Mathematical and Physical Sciences, v. 258, no. 1088, p. 41-51. doi: https://doi.org/10.1098/rsta.1965.0020
Bunge, H.-P., and Davies, J. H., 2001, Tomographic images of a mantle circulation model: Geophysical Research Letters, v. 28, no. 1, p. 77-80. doi: 10.1029/2000gl011804
Bunge, H.-P., Hagelberg, C., and Travis, B., 2003, Mantle circulation models with variational data assimilation: inferring past mantle flow and structure from plate motion histories and seismic tomography: Geophysical Journal International, v. 152, no. 2, p. 280-301. doi: https://doi.org/10.1046/j.1365-246X.2003.01823.x
Bunge, H.-P., Richards, M. A., and Baumgardner, J. R., 1996, Effect of depth-dependent viscosity on the planform of mantle convection: Nature, v. 379, no. 6564, p. 436-438. doi: 10.1038/379436a0
Bunge, H.-P., Richards, M. A., and Baumgardner, J. R., 1997, A sensitivity study of three-dimensional spherical mantle convection at 108 Rayleigh number: Effects of depth-dependent viscosity, heating mode, and an endothermic phase change: Journal of Geophysical Research: Solid Earth, v. 102, no. B6, p. 11991-12007. doi: https://doi.org/10.1029/96JB03806
Bunge, H.-P., Richards, M. A., Lithgow-Bertelloni, C., Baumgardner, J. R., Grand, S. P., and Romanowicz, B. A., 1998, Time scales and heterogeneous structure in geodynamic Earth models: Science, v. 280, no. 5360, p. 91-95. doi: http://10.1126/science.280.5360.91
Burgess, P. M., and Gurnis, M., 1995, Mechanisms for the formation of cratonic stratigraphic sequences: Earth and Planetary Science Letters, v. 136, no. 3-4, p. 647-663. doi:
Burke, K., Steinberger, B., Torsvik, T. H., and Smethurst, M. A., 2008, Plume generation zones at the margins of large low shear velocity provinces on the core–mantle boundary: Earth and Planetary Science Letters, v. 265, no. 1, p. 49-60. doi:
Burke, K., and Torsvik, T. H., 2004, Derivation of large igneous provinces of the past 200 million years from long-term heterogeneities in the deep mantle: Earth and Planetary Science Letters, v. 227, no. 3-4, p. 531-538. doi: https://doi.org/10.1016/j.epsl.2004.09.015
Butler, R. F., 1998, Paleomagnetism: Magnetic domains to geologic terranes: Electronic edition, p. 23. doi:
Butterworth, N., Talsma, A., Müller, R., Seton, M., Bunge, H.-P., Schuberth, B., Shephard, G., and Heine, C., 2014, Geological, tomographic, kinematic and geodynamic constraints on the dynamics of sinking slabs: Journal of Geodynamics, v. 73, p. 1-13. doi:
Büttner, S., Glodny, J., Lucassen, F., Wemmer, K., Erdmann, S., Handler, R., and Franz, G., 2005, Ordovician metamorphism and plutonism in the Sierra de Quilmes metamorphic complex: Implications for the tectonic setting of the northern Sierras Pampeanas (NW Argentina): Lithos, v. 83, no. 1, p. 143-181. doi:
Čadek, O., and Fleitout, L., 2006, Effect of lateral viscosity variations in the core-mantle boundary region on predictions of the long-wavelength geoid: Studia Geophysica et Geodaetica, v. 50, no. 2, p. 217-232. doi: 10.1007/s11200-006-0013-0
Cao, W., Flament, N., Zahirovic, S., Williams, S., and Müller, R. D., 2019, The interplay of dynamic topography and eustasy on continental flooding in the late Paleozoic: Tectonophysics, v. 761, p. 108-121. doi: https://doi.org/10.1016/j.tecto.2019.04.018
Cao, W., Lee, C.-T. A., and Lackey, J. S., 2017a, Episodic nature of continental arc activity since 750 Ma: A global compilation: Earth and Planetary Science Letters, v. 461, p. 85-95. doi: https://doi.org/10.1016/j.epsl.2016.12.044
Cao, W., Zahirovic, S., Flament, N., Williams, S. E., Golonka, J., and Muller, R. D., 2017b, Improving global paleogeography since the late Paleozoic using paleobiology. doi: http://dx.doi.org/10.5194/bg-14-5425-2017
Cao, X., Flament, N., Müller, D., and Li, S., 2018, The dynamic topography of eastern China since the latest Jurassic Period: Tectonics, v. 37, no. 5, p. 1274-1291. doi:
Cardona, A., Cordani, U., Ruiz, J., Valencia, V., Armstrong, R., Chew, D., Nutman, A., and Sanchez, A., 2009, U-Pb zircon geochronology and Nd isotopic signatures of the pre-Mesozoic metamorphic basement of the eastern Peruvian Andes: growth and provenance of a Late Neoproterozoic to Carboniferous accretionary orogen on the northwest margin of Gondwana: The journal of Geology, v. 117, no. 3, p. 285-305. doi:
Carlson, R., Hilde, T., and Uyeda, S., 1983, The driving mechanism of plate tectonics: relation to age of the lithosphere at trenches: Geophysical Research Letters, v. 10, no. 4, p. 297-300. doi: https://doi.org/10.1029/GL010i004p00297

Castro, A., Fernandez, C., De La Rosa, J. D., Moreno-Ventas, I., and Rogers, G., 1996, Significance of MORB-derived amphibolites from the Aracena metamorphic belt, southwest Spain: Journal of Petrology, v. 37, no. 2, p. 235-260. doi:
Catalán, J. R. M., Arenas, R., García, F. D., Cuadra, P. G., Gómez-Barreiro, J., Abati, J., Castiñeiras, P., Fernández-Suárez, J., Martínez, S. S., and Andonaegui, P., 2007, Space and time in the tectonic evolution of the northwestern Iberian Massif: Implications for the Variscan belt: Geological Society of America Memoirs, v. 200, p. 403-423. doi:
Cawood, P. A., 2005, Terra Australis Orogen: Rodinia breakup and development of the Pacific and Iapetus margins of Gondwana during the Neoproterozoic and Paleozoic: Earth-Science Reviews, v. 69, no. 3-4, p. 249-279. doi: https://doi.org/10.1016/j.earscirev.2004.09.001
Cazenave, A., Souriau, A., and Dominh, K., 1989, Global coupling of Earth surface topography with hotspots, geoid and mantle heterogeneities: Nature, v. 340, no. 6228, p. 54-57. doi: 10.1038/340054a0
Champion, D., Kositcin, N., Huston, D., Mathews, E., and Brown, C., 2009, Geodynamic synthesis of the Phanerozoic of eastern Australia and implications for metallogeny: Geoscience Australia Record, v. 18, p. 255. doi:
Charvet, J., Shu, L., Laurent-Charvet, S., Wang, B., Faure, M., Cluzel, D., Chen, Y., and De Jong, K., 2011, Palaeozoic tectonic evolution of the Tianshan belt, NW China: Science China Earth Sciences, v. 54, no. 2, p. 166-184. doi:
Charvet, J., Shu, L. S., and Laurent-Charvet, S., 2007, Paleozoic structural and geodynamic evolution of eastern Tianshan (NW China): welding of the Tarim and Junggar plates: Episodes, v. 30, no. 3, p. 162-186. doi:
Chen, B., Jahn, B., and Tian, W., 2009, Evolution of the Solonker suture zone: constraints from zircon U–Pb ages, Hf isotopic ratios and whole-rock Nd–Sr isotope compositions of subduction-and collision-related magmas and forearc sediments: Journal of Asian Earth Sciences, v. 34, no. 3, p. 245-257. doi:
Chen, B., Jahn, B.-m., Wilde, S., and Xu, B., 2000, Two contrasting paleozoic magmatic belts in northern Inner Mongolia, China: petrogenesis and tectonic implications: Tectonophysics, v. 328, no. 1, p. 157-182. doi: http://dx.doi.org/10.1016/S0040-1951(00)00182-7
Chen, L., Liu, X., Qu, W., and Hu, J., 2014, U–Pb zircon ages and geochemistry of the Wuguan complex in the Qinling orogen, central China: Implications for the late Paleozoic tectonic evolution between the Sino-Korean and Yangtze cratons: Lithos, v. 192, p. 192-207. doi:
Chew, D. M., Schaltegger, U., Košler, J., Whitehouse, M. J., Gutjahr, M., Spikings, R. A., and Miškovic, A., 2007, U-Pb geochronologic evidence for the evolution of the Gondwanan margin of the north-central Andes: Geological Society of America Bulletin, v. 119, no. 5-6, p. 697-711. doi:
Choblet, G., Amit, H., and Husson, L., 2016, Constraining mantle convection models with palaeomagnetic reversals record and numerical dynamos: Geophysical Journal International, v. 207, no. 2, p. 1165-1184. doi: 10.1093/gji/ggw328
Christensen, U. R., and Yuen, D. A., 1985, Layered convection induced by phase transitions: Journal of Geophysical Research: Solid Earth, v. 90, no. B12, p. 10291-10300. doi: https://doi.org/10.1029/JB090iB12p10291
Christopher R. Scotese, 2004, A Continental Drift Flipbook: The Journal of Geology, v. 112, no. 6, p. 729-741. doi: 10.1086/424867
Cocks, L., and Torsvik, T., 2002, Earth geography from 500 to 400 million years ago: a faunal and palaeomagnetic review: Journal of the Geological Society, v. 159, no. 6, p. 631-644. doi:
Cocks, L. R. M., and Torsvik, T. H., 2013, The dynamic evolution of the Palaeozoic geography of eastern Asia: Earth-Science Reviews, v. 117, p. 40-79. doi:
Colli, L., Bunge, H. P., and Oeser, J., 2020, Impact of model inconsistencies on reconstructions of past mantle flow obtained using the adjoint method: Geophysical Journal International, v. 221, no. 1, p. 617-639. doi: 10.1093/gji/ggaa023
Colli, L., Ghelichkhan, S., and Bunge, H. P., 2016, On the ratio of dynamic topography and gravity anomalies in a dynamic Earth: Geophysical Research Letters, v. 43, no. 6, p. 2510-2516. doi:
Colli, L., Ghelichkhan, S., Bunge, H. P., and Oeser, J., 2018, Retrodictions of Mid Paleogene mantle flow and dynamic topography in the Atlantic region from compressible high resolution adjoint mantle convection models: Sensitivity to deep mantle viscosity and tomographic input model: Gondwana Research, v. 53, p. 252-272. doi: https://doi.org/10.1016/j.gr.2017.04.027
Collins, A. S., and Pisarevsky, S. A., 2005, Amalgamating eastern Gondwana: the evolution of the Circum-Indian Orogens: Earth-Science Reviews, v. 71, no. 3-4, p. 229-270. doi: 10.1016/j.earscirev.2005.02.004
Collins, W., 2003, Slab pull, mantle convection, and Pangaean assembly and dispersal: Earth and Planetary Science Letters, v. 205, no. 3, p. 225-237. doi:
Coltice, N., Gérault, M., and Ulvrová, M., 2017, A mantle convection perspective on global tectonics: Earth-science reviews, v. 165, p. 120-150. doi: https://doi.org/10.1016/j.earscirev.2016.11.006
Coltice, N., Larrouturou, G., Debayle, E., and Garnero, E. J., 2018, Interactions of scales of convection in the Earth's mantle: Tectonophysics, v. 746, p. 669-677. doi: https://doi.org/10.1016/j.tecto.2017.06.028
Coltice, N., and Shephard, G. E., 2018, Tectonic predictions with mantle convection models: Geophysical Journal International, v. 213, no. 1, p. 16-29. doi: https://doi.org/10.1093/gji/ggx531
Colwell, J., and Stagg, H., 1994, Structure of the offshore Canning basin: first impressions from a new regional deep-seismic data set, *in* Purcell, P. G., and Purcell, R. R., eds., *The Sedimentary Basins of Western Australia: Proceedings of West Australian Basins Symposium*: Perth, p. 757-768.
Colwell, J. B., Stagg, H. M. J., Symonds, P. A., Wilcox, J. B., and O'Brien, G. W., 1994, Deep reflections on the North West Shelf: changing perceptions of basin formation, *in* Purcell, P. G., and Purcell, R. R., eds., *The Sedimentary Basins of Western Australia: Proceedings of West Australian Basins Symposium*: Perth, p. 63-76.
Conolly, J., Falvey, M., Kingsley, D., Melton, B., and Russell, T., 1984, Geology and petroleum potential of the southern Canning Basin, *in* Purcell, P. G., ed., *The Canning Basin WA: Proceedings of Geological Society of Australia/Petroleum Exploration Society of Australia Symposium*: Perth, p. 137-147.
Conrad, C. P., 2013, The solid Earth's influence on sea level: Bulletin, v. 125, no. 7-8, p. 1027-1052. doi: https://doi.org/10.1130/B30764.1
Conrad, C. P., and Gurnis, M., 2003, Seismic tomography, surface uplift, and the breakup of Gondwanaland: Integrating mantle convection backwards in time: Geochemistry, Geophysics, Geosystems, v. 4, no. 3. doi: https://doi.org/10.1029/2001GC000299
Conrad, C. P., and Husson, L., 2009, Influence of dynamic topography on sea level and its rate of change: Lithosphere, v. 1, no. 2, p. 110-120. doi: https://doi.org/10.1130/L32.1
Creer, K. M., Irving, E., and Runcorn, S. K., 1954, The Direction of the Geomagnetic Field in Remote Epochs in Great Britain: Journal of geomagnetism and geoelectricity, v. 6, no. 4, p. 163-168. doi: http://10.5636/jgg.6.163
Crespo-Blanc, A., and Orozco, M., 1991, The boundary between the Ossa-Morena and Southportuguese Zones (Southern Iberian Massif): Major suture in the European Hercynian Chain: Geologische Rundschau, v. 80, no. 3, p. 691-702. doi:
Crostella, A., 1995, Structural evolution and hydrocarbon potential of the Merlinleigh and Byro Sub-basins, Carnarvon Basin, Western Australia, Geological Survey of Western Australia.
Crostella, A., and Iasky, R. P., 1997, Structural interpretation and hydrocarbon potential of the Giralia area, Carnarvon Basin, Geological Survey of Western Australia.
Crowley, T. J., and Baum, S. K., 1991, Estimating Carboniferous sea-level fluctuations from Gondwanan ice extent: Geology, v. 19, no. 10, p. 975-977. doi: 10.1130/0091-7613(1991)019<0975:Ecslff>2.3.Co;2

Cserepes, L., Rabinowicz, M., and Rosemberg-Borot, C., 1988, Three-dimensional infinite Prandtl number convection in one and two layers with implications for the Earth's gravity field: Journal of Geophysical Research: Solid Earth, v. 93, no. B10, p. 12009-12025. doi: https://doi.org/10.1029/JB093iB10p12009
Cuffaro, M., and Doglioni, C., 2007, Global kinematics in deep versus shallow hotspot reference frames: Special Papers-Geological Society of America, v. 430, p. 359. doi: 10.1130/2007.2430(18)
Czarnota, K., Hoggard, M. J., White, N., and Winterbourne, J., 2013, Spatial and temporal patterns of Cenozoic dynamic topography around Australia: Geochemistry, Geophysics, Geosystems, v. 14, no. 3, p. 634-658. doi: 10.1029/2012GC004392
Czarnota, K., Roberts, G., White, N., and Fishwick, S., 2014, Spatial and temporal patterns of Australian dynamic topography from River Profile Modeling: Journal of Geophysical Research: Solid Earth, v. 119, no. 2, p. 1384-1424. doi: https://doi.org/10.1002/2013JB010436
Dajun, F., Pengyan, W., Zhongyue, S., and Xiaodong, T., 1998, Cenozoic paleomagnetic results and phanerozoic apparent polar wandering path of Tarim Block: Science in China Series D: Earth Sciences, v. 41, p. 105-112. doi:
Dallmeyer, R. D., Franke, W., and Weber, K., 2013, Pre-Permian geology of central and eastern Europe, Springer Science & Business Media.
Dalziel, I. W., 1997, OVERVIEW: Neoproterozoic-Paleozoic geography and tectonics: Review, hypothesis, environmental speculation: Geological Society of America Bulletin, v. 109, no. 1, p. 16-42. doi: https://doi.org/10.1130/0016-7606(1997)109<0016:ONPGAT>2.3.CO;2
Davies, D., Valentine, A., Kramer, S., Rawlinson, N., Hoggard, M., Eakin, C., and Wilson, C., 2019, Earth's multi-scale topographic response to global mantle flow: Nature Geoscience, v. 12, no. 10, p. 845-850. doi: 10.1038/s41561-019-0441-4
Davies, D. R., and Davies, J. H., 2009, Thermally-driven mantle plumes reconcile multiple hot-spot observations: Earth and Planetary Science Letters, v. 278, no. 1, p. 50-54. doi: https://doi.org/10.1016/j.epsl.2008.11.027
Davies, D. R., Davies, J. H., Bollada, P. C., Hassan, O., Morgan, K., and Nithiarasu, P., 2013, A hierarchical mesh refinement technique for global 3-D spherical mantle convection modelling: Geosci. Model Dev., v. 6, no. 4, p. 1095-1107. doi: 10.5194/gmd-6-1095-2013
Davies, D. R., Goes, S., Davies, J. H., Schuberth, B. S. A., Bunge, H. P., and Ritsema, J., 2012, Reconciling dynamic and seismic models of Earth's lower mantle: The dominant role of thermal heterogeneity: Earth and Planetary Science Letters, v. 353-354, p. 253-269. doi: https://doi.org/10.1016/j.epsl.2012.08.016
Davies, D. R., Goes, S., and Sambridge, M., 2015, On the relationship between volcanic hotspot locations, the reconstructed eruption sites of large igneous provinces and deep mantle seismic structure: Earth and Planetary Science Letters, v. 411, p. 121-130. doi: https://doi.org/10.1016/j.epsl.2014.11.052
Deighton, I., Draper, J., Hill, A., and Boreham, C., 2003, A hydrocarbon generation model for the Cooper and Eromanga Basins: The APPEA Journal, v. 43, no. 1, p. 433-451. doi: 10.1071/AJ02023
Deighton, I., and Hill, A., 1998, Thermal and burial history, *in* Gravestock, D. I., Hibburt, J. E., and Drexel, J. F., eds., *Petroleum Geology of South Australia*, Volume 4: Adelaide, Primary Industries & Resources South Australia, p. 143-155.
DiCaprio, L., Gurnis, M., and Müller, R. D., 2009, Long-wavelength tilting of the Australian continent since the Late Cretaceous: Earth and Planetary Science Letters, v. 278, no. 3-4, p. 175-185. doi: 10.1016/j.epsl.2008.11.030
DiCaprio, L., Gurnis, M., Müller, R. D., and Tan, E., 2011, Mantle dynamics of continentwide Cenozoic subsidence and tilting of Australia: Lithosphere, v. 3, no. 5, p. 311-316. doi: 10.1130/L140.1
Domeier, M., 2016, A plate tectonic scenario for the Iapetus and Rheic oceans: Gondwana Research, v. 36, p. 275-295. doi: https://doi.org/10.1016/j.gr.2015.08.003
Domeier, M., 2018, Early Paleozoic tectonics of Asia: towards a full-plate model: Geoscience Frontiers, v. 9, no. 3, p. 789-862. doi: https://doi.org/10.1016/j.gsf.2017.11.012
Domeier, M., and Torsvik, T. H., 2014, Plate tectonics in the late Paleozoic: Geoscience Frontiers, v. 5, no. 3, p. 303-350. doi: https://doi.org/10.1016/j.gsf.2014.01.002
Domeier, M., and Torsvik, T. H., 2019, Full-plate modelling in pre-Jurassic time: Geological Magazine, v. 156, no. 2, p. 261-280. doi: https://doi.org/10.1017/S0016756817001005
Domeier, M., Van der Voo, R., and Torsvik, T. H., 2012, Paleomagnetism and Pangea: the road to reconciliation: Tectonophysics, v. 514, p. 14-43. doi:
Dong, Y., Liu, X., Neubauer, F., Zhang, G., Tao, N., Zhang, Y., Zhang, X., and Li, W., 2013, Timing of Paleozoic amalgamation between the North China and South China Blocks: evidence from detrital zircon U–Pb ages: Tectonophysics, v. 586, p. 173-191. doi:
Dong, Y., and Santosh, M., 2016, Tectonic architecture and multiple orogeny of the Qinling Orogenic Belt, Central China: Gondwana Research, v. 29, no. 1, p. 1-40. doi:
Dong, Y., Zhang, G., Neubauer, F., Liu, X., Genser, J., and Hauzenberger, C., 2011a, Tectonic evolution of the Qinling orogen, China: review and synthesis: Journal of Asian Earth Sciences, v. 41, no. 3, p. 213-237. doi:
Dong, Y., Zhang, G., Hauzenberger, C., Neubauer, F., Yang, Z., and Liu, X., 2011b, Palaeozoic tectonics and evolutionary history of the Qinling orogen: evidence from geochemistry and geochronology of ophiolite and related volcanic rocks: Lithos, v. 122, no. 1, p. 39-56. doi:
Dong, Y., Zhang, G., Lai, S., Zhou, D., and Zhu, B., 1999, An ophiolitic tectonic melange first discovered in Huashan area, south margin of Qinling Orogenic Belt, and its tectonic implications: Science in China Series D: Earth Sciences, v. 42, no. 3, p. 292-302. doi: 10.1007/bf02878966
Doucet, L. S., Li, Z.-X., Ernst, R. E., Kirscher, U., El Dien, H. G., and Mitchell, R. N., 2020, Coupled supercontinent–mantle plume events evidenced by oceanic plume record: Geology, v. 48, no. 2, p. 159-163. doi: https://doi.org/10.1130/G46754.1
Dutkiewicz, A., Müller, R., Wang, X., O'callaghan, S., Cannon, J., and Wright, N., 2017, Predicting sediment thickness on vanished ocean crust since 200 Ma: Geochemistry, Geophysics, Geosystems, v. 18, no. 12, p. 4586-4603. doi: https://doi.org/10.1002/2017GC007258
Dziewonski, A. M., and Anderson, D. L., 1981, Preliminary reference Earth model: Physics of the earth and planetary interiors, v. 25, no. 4, p. 297-356. doi:
Eakins, B., and Sharman, G., 2012, Hypsographic curve of Earth's surface from ETOPO1: NOAA National Geophysical Data Center, Boulder, CO. doi:
Eden, C., and Andrews, J., Middle to upper Devonian melanges in SW Spain and their relationship to the Meneage formation in south CornwallProc. Ussher Soc1990, Volume 7, p. 217-222.
Eden, C. P., 1991, Tectonostratigraphic analysis of the northern extent of the oceanic exotic terrane, Northwestern Huelva Province, Spain: University of Southampton
Enkin, R. J., Yang, Z., Chen, Y., and Courtillot, V., 1992, Paleomagnetic constraints on the geodynamic history of the major blocks of China from the Permian to the present: Journal of Geophysical Research: Solid Earth, v. 97, no. B10, p. 13953-13989. doi:
Evans, D. A., 2003, True polar wander and supercontinents: Tectonophysics, v. 362, no. 1, p. 303-320. doi:
Fang, D. J., Jin, G. H., Jiang, L. P., Wang, P. Y., and Wang, Z. L., 1996, Paleozoic paleomagnetic results and the tectonic significance of Tarim palte: Chinese Journal of Geophysics, v. 4. doi:

Fatka, O., and Mergl, M., 2009, The 'microcontinent'Perunica: status and story 15 years after conception: Geological Society, London, Special Publications, v. 325, no. 1, p. 65-101. doi:
Fergusson, C. L., 2017, Mid to late Paleozoic shortening pulses in the Lachlan Orogen, southeastern Australia: a review: Australian Journal of Earth Sciences, v. 64, no. 1, p. 1-39. doi: https://doi.org/10.1080/08120099.2017.1273257
Fernández-Suárez, J., Gutiérrez-Alonso, G., Pastor-Galán, D., Hofmann, M., Murphy, J., and Linnemann, U., 2014, The Ediacaran–Early Cambrian detrital zircon record of NW Iberia: Possible sources and paleogeographic constraints: International Journal of Earth Sciences, v. 103, no. 5, p. 1335-1357. doi:
Feroni, A. C., Ellero, A., Malusà, M. G., Musumeci, G., Ottria, G., Polino, R., and Leoni, L., 2010, Transpressional tectonics and nappe stacking along the Southern Variscan Front of Morocco: International journal of earth sciences, v. 99, no. 5, p. 1111-1122. doi:
Fischer, A., Berggren, W., and Van Couvering, J., 1984, The two Phanerozoic supercycles, *Catastrophes and Earth history: The new uniformitarianism*, Princeton University Press Princeton, NJ, p. 129-150.
Flament, N., 2019a, The deep roots of Earth's surface: Nature Geoscience, v. 12, no. 10, p. 787-788. doi:
Flament, N., 2019b, Present-day dynamic topography and lower-mantle structure from palaeogeographically constrained mantle flow models: Geophysical Journal International, v. 216, no. 3, p. 2158-2182. doi: https://doi.org/10.1093/gji/ggy526
Flament, N., Coltice, N., and Rey, P. F., 2008, A case for late-Archaean continental emergence from thermal evolution models and hypsometry: Earth and Planetary Science Letters, v. 275, no. 3-4, p. 326-336. doi: https://doi.org/10.1016/j.epsl.2008.08.029
Flament, N., Gurnis, M., and Müller, R. D., 2013a, A review of observations and models of dynamic topography: Lithosphere, v. 5, no. 2, p. 189-210. doi: 10.1130/L245.1
Flament, N., Coltice, N., and Rey, P. F., 2013b, The evolution of the 87Sr/86Sr of marine carbonates does not constrain continental growth: Precambrian Research, v. 229, p. 177-188. doi: https://doi.org/10.1016/j.precamres.2011.10.009
Flament, N., Gurnis, M., Williams, S., Seton, M., Skogseid, J., Heine, C., and Müller, R. D., 2014, Topographic asymmetry of the South Atlantic from global models of mantle flow and lithospheric stretching: Earth and Planetary Science Letters, v. 387, p. 107-119. doi: https://doi.org/10.1016/j.epsl.2013.11.017
Flament, N., Williams, S., Müller, R., Gurnis, M., and Bower, D., 2017a, Origin and evolution of the deep thermochemical structure beneath Eurasia: Nature Communications, v. 8, p. 14164. doi: 10.1038/ncomms14164
Flament, N., Williams, S., Müller, R. D., Gurnis, M., and Bower, D. J., 2017b, Correspondence: Reply to 'Numerical modelling of the PERM anomaly and the Emeishan large igneous province': Nature communications, v. 8, no. 1, p. 822. doi:
Flowers, R. M., Ault, A. K., Kelley, S. A., Zhang, N., and Zhong, S., 2012, Epeirogeny or eustasy? Paleozoic–Mesozoic vertical motion of the North American continental interior from thermochronometry and implications for mantle dynamics: Earth and Planetary Science Letters, v. 317, p. 436-445. doi: 10.1016/j.epsl.2011.11.015
Floyd, P., 1982, Chemical variation in Hercynian basalts relative to plate tectonics: Journal of the Geological Society, v. 139, no. 4, p. 505-520. doi:
Floyd, P., 1995, Igneous activity, *Pre-Permian Geology of Central and Eastern Europe*, Springer, p. 59-81.
Fluteau, F., Besse, J., Broutin, J., and Berthelin, M., 2001, Extension of Cathaysian flora during the Permian: Climatic and paleogeographic constraints: Earth and Planetary Science Letters, v. 193, no. 3-4, p. 603-616. doi:
Fonseca, P., and Ribeiro, A., 1993, Tectonics of the Beja-Acebuches Ophiolite: a major suture in the Iberian Variscan Foldbelt: Geologische Rundschau, v. 82, no. 3, p. 440-447. doi:
Forman, D. J., and Wales, D. W., 1981, Geological evolution of the Canning Basin, Western Australia, Canberra, Australian Government Publishing Service.
Forsyth, D., and Uyeda, S., 1975, On the relative importance of the driving forces of plate motion: Geophysical Journal International, v. 43, no. 1, p. 163-200. doi: https://doi.org/10.1111/j.1365-246X.1975.tb00631.x
Fortey, R., Pankhurst, R. J., and Herve, F., 1992, Devonian trilobites at buill, Chile (42 S): Andean Geology, v. 19, no. 2, p. 133-143. doi:
Franke, W., 2000, The mid-European segment of the Variscides: tectonostratigraphic units, terrane boundaries and plate tectonic evolution: Geological Society of London Special Publications, v. 179, p. 35-61. doi:
French, S., and Romanowicz, B., 2014, Whole-mantle radially anisotropic shear velocity structure from spectral-element waveform tomography: Geophysical Journal International, v. 199, no. 3, p. 1303-1327. doi:
Fritzell, E. H., Bull, A. L., and Shephard, G. E., 2016, Closure of the Mongol–Okhotsk Ocean: Insights from seismic tomography and numerical modelling: Earth and Planetary Science Letters, v. 445, p. 1-12. doi: http://dx.doi.org/10.1016/j.epsl.2016.03.042
FROGTECH, 2014, Bioregional Assessment Source Dataset, Viewed 12 December 2019, http://data.bioregionalassessments.gov.au/dataset/26e0fbd9-d8d0-4212-be52-ca317e27b3bd.
Gaina, C., Müller, D. R., Royer, J. Y., Stock, J., Hardebeck, J., and Symonds, P., 1998, The tectonic history of the Tasman Sea: a puzzle with 13 pieces: Journal of Geophysical Research: Solid Earth, v. 103, no. B6, p. 12413-12433. doi: https://doi.org/10.1029/98JB00386
Gallagher, K., and Lambeck, K., 1989, Subsidence, sedimentation and sea-level changes in the Eromanga Basin, Australia: Basin Research, v. 2, no. 2, p. 115-131. doi: 10.1111/j.1365-2117.1989.tb00030.x
Gallagher, R., Commonwealth of, A., Zhang, W., Totterdell, J. M., Raymond, O. L., and Stewart, A. J., 2013, Australian Geological Provinces, 2013.01 edition, Geoscience Australia.
Gao, J., and Klemd, R., 2003, Formation of HP–LT rocks and their tectonic implications in the western Tianshan Orogen, NW China: geochemical and age constraints: Lithos, v. 66, no. 1, p. 1-22. doi:
Gao, J., Klemd, R., Qian, Q., Zhang, X., Li, J., Jiang, T., and Yang, Y., 2011, The collision between the Yili and Tarim blocks of the Southwestern Altaids: Geochemical and age constraints of a leucogranite dike crosscutting the HP–LT metamorphic belt in the Chinese Tianshan Orogen: Tectonophysics, v. 499, no. 1, p. 118-131. doi: http://dx.doi.org/10.1016/j.tecto.2011.01.001
Garnero, E. J., McNamara, A. K., and Shim, S.-H., 2016, Continent-sized anomalous zones with low seismic velocity at the base of Earth's mantle: Nature Geoscience, v. 9, no. 7, p. 481-489. doi: 10.1038/ngeo2733
Garrad, P., and Bultitude, R. J., 1997, Geology, mining history and mineralisation of the Hodgkinson and Kennedy provinces, Cairns region, North Queensland, Department of Mines and Energy.
Ge, R., Zhu, W., Wu, H., Zheng, B., Zhu, X., and He, J., 2012, The Paleozoic northern margin of the Tarim craton: Passive or active?: Lithos, v. 142, p. 1-15. doi:
Ghelichkhan, S., and Bunge, H. P., 2018, The adjoint equations for thermochemical compressible mantle convection: derivation and verification by twin experiments: Proceedings of the Royal Society A: Mathematical, Physical and Engineering Sciences, v. 474, no. 2220, p. 20180329. doi: 10.1098/rspa.2018.0329
Ghori, K., 1998, Petroleum generating potential and thermal history of the Palaeozoic, Carnarvon Basin, Western Australia, *in* Purcell, P. G., and Purcell, R. R., eds., *The Sedimentary Basins of Western Australia 2: Proceedings of West Australian Basins Symposium*: Perth, p. 553-569.
Ghori, K., 1999, Silurian-Devonian petroleum source-rock potential and thermal history, Carnarvon Basin, Western Australia, Geological Survey of Western Australia, v. 72.

Gibson, H., Marshallsea, S., and Watson, P., 1998, Thermal history reconstruction in Carnarvon Basin wells Barrabiddy 1A, Yaringa East 1, Coburn 1 and an outcrop sample using apatite fission-track analysis and vitrinite reflectance: A report prepared for the Petroleum Exploration Initiatives Group of the Geological Survey of Western Australia, Geotrack International Pty Ltd (GEOTRACK), Report, v. 670. doi:
Gilder, S., and Courtillot, V., 1997, Timing of the North-South China collision from new middle to late Mesozoic paleomagnetic data from the North China Block: Journal of Geophysical Research: Solid Earth, v. 102, no. B8, p. 17713-17727. doi:
Gilder, S., Zhao, X., Coe, R., Meng, Z., Courtillot, V., and Besse, J., 1996, Paleomagnetism and tectonics of the southern Tarim basin, northwestern China: Journal of Geophysical Research: Solid Earth, v. 101, no. B10, p. 22015-22031. doi:
Gleadow, A., and Duddy, I., 1984, Fission track dating and thermal history analysis of apatites from wells in the north-west Canning Basin, *in* Purcell, P. G., ed., *The Canning Basin WA: Proceedings of Geological Society of Australia/Petroleum Exploration Society of Australia Symposium*: Perth, p. 377-389.
Glen, R., 1995, Thrusts and thrust-associated mineralization in the Lachlan Orogen: Economic Geology, v. 90, no. 6, p. 1402-1429. doi: https://doi.org/10.2113/gsecongeo.90.6.1402
Glen, R., Plate tectonics of the Lachlan Orogen: a framework for understanding its metallogenesis. Geological Society of Australia Abstracts. 2004, Volume 74, Geological Society of Australia; 1999, p. 33-36.
Glen, R., 2005, The Tasmanides of eastern Australia: Special Publication-Geological Society of London, v. 246, p. 23. doi: https://doi.org/10.1144/GSL.SP.2005.246.01.02
Golle, O., Dumoulin, C., Choblet, G., and Cadek, O., 2012, Topography and geoid induced by a convecting mantle beneath an elastic lithosphere: Geophysical Journal International, v. 189, no. 1, p. 55-72. doi: 10.1111/j.1365-246X.2012.05364.x
Golonka, J., 2007a, Late Triassic and Early Jurassic palaeogeography of the world: Palaeogeography, Palaeoclimatology, Palaeoecology, v. 244, no. 1-4, p. 297-307. doi: https://doi.org/10.1016/j.palaeo.2006.06.041
Golonka, J., 2007b, Phanerozoic paleoenvironment and paleolithofacies maps: late Palezoic: Geologia/Akademia Górniczo-Hutnicza im. Stanisława Staszica w Krakowie, v. 33, no. 2, p. 145-209. doi: http://10.13140/2.1.3481.4403
Golonka, J., 2009a, Phanerozoic paleoenvironment and paleolithofacies maps: Early Paleozoic: Geologia/Akademia Górniczo-Hutnicza im. Stanisława Staszica w Krakowie, v. 35, p. 589-654. doi:
Golonka, J., 2009b, Phanerozoic paleoenvironment and paleolithofacies maps: Cenozoic: Geologia/Akademia Górniczo-Hutnicza im. Stanisława Staszica w Krakowie, v. 35, p. 507-587. doi:
Golonka, J., 2012, Paleozoic paleoenvironment and paleolithofacies maps of Gondwana, AGH University of Science and Technology Press.
Golonka, J., Krobicki, M., Pajak, J., Nguyen, V. G., and Zuchiewicz, W., 2006, Global plate tectonics and paleogeography of Southeast Asia: Faculty of Geology, Geophysics and Environmental Protection, AGH University of Science and Technology, Arkadia, Krakow, Poland. doi:
Golonka, J., Ross, M., and Scotese, C., 1994, Phanerozoic paleogeographic and paleoclimatic modeling maps. doi:
Gordon, R. G., and Jurdy, D. M., 1986, Cenozoic global plate motions: Journal of Geophysical Research: Solid Earth, v. 91, no. B12, p. 12389-12406. doi: 10.1029/JB091iB12p12389
Gorter, J. D., Nicoll, R. S., and Foster, C. B., 1994, Lower Palaeozoic facies in the Carnarvon Basin, Western Australia: stratigraphy and hydrocarbon prospectivity, *in* Purcell, P. G., and Purcell, R. R., eds., *The Sedimentary Basins Of WA: Proceedings of West Australian Basins Symposium*: Perth, p. 373-396.
Gracht, W. A. J. M. v. W. v. d., Willis, B., Chamberlin, R. T., Joly, J., Molengraaff, G. A. F., Gregory, J. W., Wegener, A., Schuchert, C., Longwell, C. R., Taylor, F. B., Bowie, W., White, D., Singewald, J. T., Jr., and Berry, E. W., 1928, Theory of Continental Drift: A Symposium on the Origin and Movement of Land Masses Both Inter-Continental and Intra-Continental, as Proposed by Alfred Wegener, American Association of Petroleum Geologists.
Gravestock, D., and Jensen-Schmidt, B., 1998, Structural setting, *in* Gravestock, D. I., Hibburt, J. E., and Drexel, J. F., eds., *Petroleum geology of South Australia Volume 4: Cooper Basin*, Volume 4: Adelaide, Primary Industries & Resources South Australia, p. 47-67.
Gregori, D. A., Saini-Eidukat, B., Benedini, L., Strazzere, L., Barros, M., and Kostadinoff, J., 2016, The Gondwana Orogeny in northern North Patagonian Massif: Evidences from the Caita Có granite, La Seña and Pangaré mylonites, Argentina: Geoscience Frontiers, v. 7, no. 4, p. 621-638. doi: http://dx.doi.org/10.1016/j.gsf.2015.06.002
Gripp, A. E., and Gordon, R. G., 2002, Young tracks of hotspots and current plate velocities: Geophysical Journal International, v. 150, no. 2, p. 321-361. doi: 10.1046/j.1365-246X.2002.01627.x
Guerri, M., Cammarano, F., and Tackley, P. J., 2016, Modelling Earth's surface topography: Decomposition of the static and dynamic components: Physics of the Earth and Planetary Interiors, v. 261, p. 172-186. doi: https://doi.org/10.1016/j.pepi.2016.10.009
Guillaume, B., Pochat, S., Monteux, J., Husson, L., and Choblet, G., 2016, Can eustatic charts go beyond first order? Insights from the Permian–Triassic: Lithosphere, v. 8, no. 5, p. 505-518. doi: https://doi.org/10.1130/L523.1
Guowei, Z., Zaiping, Y., Yong, S., Shunyou, C., Taohong, L., Feng, X., and Chengli, Z., 1989, The major suture zone of the Qinling orogenic belt: Journal of Southeast Asian Earth Sciences, v. 3, no. 1-4, p. 63-76. doi:
Gurnis, M., 1990a, Ridge spreading, subduction, and sea level fluctuations: Science, v. 250, no. 4983, p. 970-972. doi: https://doi.org/10.1126/science.250.4983.970
Gurnis, M., 1990b, Bounds on global dynamic topography from Phanerozoic flooding of continental platforms: Nature, v. 344, no. 6268, p. 754-756. doi: https://doi.org/10.1038/344754a0
Gurnis, M., 1993, Phanerozoic marine inundation of continents driven by dynamic topography above subducting slabs: Nature, v. 364, no. 6438, p. 589-593. doi: https://doi.org/10.1038/364589a0
Gurnis, M., Müller, R. D., and Moresi, L., 1998, Cretaceous vertical motion of Australia and the AustralianAntarctic discordance: Science, v. 279, no. 5356, p. 1499-1504. doi: 10.1126/science.279.5356.1499
Gurnis, M., and Torsvik, T. H., 1994, Rapid drift of large continents during the late Precambrian and Paleozoic: Paleomagnetic constraints and dynamic models: Geology, v. 22, no. 11, p. 1023-1026. doi:
Gurnis, M., Turner, M., Zahirovic, S., DiCaprio, L., Spasojevic, S., Müller, R. D., Boyden, J., Seton, M., Manea, V. C., and Bower, D. J., 2012, Plate tectonic reconstructions with continuously closing plates: Computers & Geosciences, v. 38, no. 1, p. 35-42. doi: https://doi.org/10.1016/j.cageo.2011.04.014
Gurnis, M., Yang, T., Cannon, J., Turner, M., Williams, S., Flament, N., and Müller, R. D., 2018, Global tectonic reconstructions with continuously deforming and evolving rigid plates: Computers & geosciences, v. 116, p. 32-41. doi: https://doi.org/10.1016/j.cageo.2018.04.007
Hager, B., 1980, Eustatic sea level and spreading rate are not simply related: Eos Trans. AGU, v. 61, p. 374. doi:
Hager, B. H., Clayton, R. W., Richards, M. A., Comer, R. P., and Dziewonski, A. M., 1985, Lower mantle heterogeneity, dynamic topography and the geoid: Nature, v. 313, no. 6003, p. 541-545. doi: https://doi.org/10.1038/313541a0
Hager, B. H., Richards, M. A., apos, Nions, R. K., Clayton, R., and Parsons, B., 1989, Long-wavelength variations in Earth's geoid: physical models and dynamical implications: Philosophical Transactions of the Royal Society of London. Series A, Mathematical and Physical Sciences, v. 328, no. 1599, p. 309-327. doi: 10.1098/rsta.1989.0038

Haines, P., 2004, Depositional facies and regional correlations of the Ordovician Goldwyer and Nita Formations, Canning Basin, Western Australia, with implications for petroleum exploration.
Hall, L., Hill, A., Troup, A., Korsch, R., Radke, B., Nicoll, R., Palu, T., Wang, L., and Stacey, A., 2015, Cooper Basin architecture and lithofacies: regional hydrocarbon prospectivity of the Cooper Basin, Part 1: Geoscience Australia Record 2015, v. 31. doi: 10.11636/Record.2015.031
Hall, L., Palu, T., Murray, A., Edwards, D., Hill, A., and Troup, A., 2016, Cooper Basin Petroleum Systems Analysis: Regional Hydrocarbon Prospectivity of the Cooper Basin, Part 3: Geoscience Australia Record 2016, v. 2016. doi: 10.11636/Record.2016.029
Hallam, A., 1974, Changing patterns of provinciality and diversity of fossil animals in relation to plate tectonics: Journal of Biogeography, p. 213-225. doi:
Hallam, A., 1984, Pre-Quaternary Sea-Level Changes: Annual Review of Earth and Planetary Sciences, v. 12, no. 1, p. 205-243. doi: https://doi.org/10.1146/annurev.ea.12.050184.001225
Hallam, A., 1989, The case for sea-level change as a dominant causal factor in mass extinction of marine invertebrates: Philosophical Transactions of the Royal Society of London. B, Biological Sciences, v. 325, no. 1228, p. 437-455. doi: https://doi.org/10.1098/rstb.1989.0098
Hamdani, Y., Mareschal, J.-C., and Arkani-Hamed, J., 1994, Phase change and thermal subsidence of the Williston basin: Geophysical Journal International, v. 116, no. 3, p. 585-597. doi: 10.1111/j.1365-246X.1994.tb03282.x
Han, A., Yang, Z., Tong, Y., and Jing, X., 2015, New paleomagnetic results from Late Ordovician rocks of the Yangtze Block, South China, and their paleogeographic implications: Journal of Geophysical Research: Solid Earth, v. 120, no. 7, p. 4759-4772. doi:
Han, B.-F., He, G.-Q., Wang, X.-C., and Guo, Z.-J., 2011, Late Carboniferous collision between the Tarim and Kazakhstan–Yili terranes in the western segment of the South Tian Shan Orogen, Central Asia, and implications for the Northern Xinjiang, western China: Earth-Science Reviews, v. 109, no. 3, p. 74-93. doi: http://dx.doi.org/10.1016/j.earscirev.2011.09.001
Han, Y., Zhao, G., Sun, M., Eizenhöfer, P. R., Hou, W., Zhang, X., Liu, D., Wang, B., and Zhang, G., 2015, Paleozoic accretionary orogenesis in the Paleo-Asian Ocean: Insights from detrital zircons from Silurian to Carboniferous strata at the northwestern margin of the Tarim Craton: Tectonics, v. 34, no. 2, p. 334-351. doi:
Hanning, W., Rixiang, Z., Lixin, B., Bin, G., and Jianjun, L., 1998, Revised apparent polar wander path of the Yangtze Block and its tectonic implications: Science in China Series D: Earth Sciences, v. 41, no. 2, p. 78-90. doi:
Haq, B. U., 2014, Cretaceous eustasy revisited: Global and Planetary change, v. 113, p. 44-58. doi: https://doi.org/10.1016/j.gloplacha.2013.12.007
Haq, B. U., Hardenbol, J. A. N., and Vail, P. R., 1987, Chronology of Fluctuating Sea Levels Since the Triassic: Science, v. 235, no. 4793, p. 1156. doi: 10.1126/science.235.4793.1156
Haq, B. U., and Schutter, S. R., 2008, A Chronology of Paleozoic Sea-Level Changes: Science, v. 322, no. 5898, p. 64-68. doi: http://10.1126/science.1161648
Harrison, C., 1999, Constraints on ocean volume change since the Archean: Geophysical Research Letters, v. 26, no. 13, p. 1913-1916. doi: https://doi.org/10.1029/1999GL900425
Harrison, C., Miskell, K., Brass, G., Saltzman, E., and Sloan, J., 1983, Continental hypsography: Tectonics, v. 2, no. 4, p. 357-377. doi: https://doi.org/10.1029/TC002i004p00357
Hartley, A. J., and Otava, J., 2001, Sediment provenance and dispersal in a deep marine foreland basin: the Lower Carboniferous Culm Basin, Czech Republic: Journal of the Geological Society, v. 158, no. 1, p. 137-150. doi:
Hassan, R., Flament, N., Gurnis, M., Bower, D. J., and Müller, D., 2015, Provenance of plumes in global convection models: Geochemistry, Geophysics, Geosystems, v. 16, no. 5, p. 1465-1489. doi: 10.1002/2015GC005751
Hassan, R., Müller, R. D., Gurnis, M., Williams, S. E., and Flament, N., 2016, A rapid burst in hotspot motion through the interaction of tectonics and deep mantle flow: Nature, v. 533, no. 7602, p. 239. doi: 10.1038/nature17422
Havlíček, V., Vaněk, J., and Fatka, O., 1994, Perunica microcontinent in the Ordovician (its position within the Mediterranean Province, series division, benthic and pelagic associations): Sborník geologických věd, Geologie, v. 46, p. 23-56. doi:
Hawkesworth, C., Cawood, P., Kemp, T., Storey, C., and Dhuime, B., 2009, Geochemistry: A matter of preservation: Science, v. 323, p. 49-50. doi:
Hays, J. D., and Pitman, W. C., 1973, Lithospheric plate motion, sea level changes and climatic and ecological consequences: Nature, v. 246, no. 5427, p. 18-22. doi: https://doi.org/10.1038/246018a0
He, B., Jiao, C., Xu, Z., Cai, Z., Zhang, J., Liu, S., Li, H., Chen, W., and Yu, Z., 2016, The paleotectonic and paleogeography reconstructions of the Tarim Basin and its adjacent areas (NW China) during the late Early and Middle Paleozoic: Gondwana Research, v. 30, p. 191-206. doi:
Heine, C., and Müller, R., 2008, The Intracontinental basins (ICONS) atlas-applications in eastern Australia, *in* Blevin, J., Bradshaw, B., and Uruski, C., eds., *Eastern Australasian Basins Symposium III*: Sydney, Petroleum Exploration Society of Australia, Special Publication, p. 275–290.
Heine, C., Müller, R. D., Steinberger, B., and DiCaprio, L., 2010, Integrating deep Earth dynamics in paleogeographic reconstructions of Australia: Tectonophysics, v. 483, no. 1-2, p. 135-150. doi: http://10.1016/j.tecto.2009.08.028
Heine, C., Müller, R. D., Steinberger, B., and Torsvik, T. H., 2008, Subsidence in intracontinental basins due to dynamic topography: Physics of the Earth and Planetary Interiors, v. 171, no. 1-4, p. 252-264. doi: 10.1016/j.pepi.2008.05.008
Hellinger, S., 1981, The uncertainties of finite rotations in plate tectonics: Journal of Geophysical Research: Solid Earth, v. 86, no. B10, p. 9312-9318. doi:
Henderson, R., Davis, B., and Fanning, C., 1998, Stratigraphy, age relationships and tectonic setting of rift-phase infill in the Drummond Basin, central Queensland: Australian Journal of Earth Sciences, v. 45, no. 4, p. 579-595. doi: https://doi.org/10.1080/08120099808728414
Hernlund, J. W., and Houser, C., 2008, On the statistical distribution of seismic velocities in Earth's deep mantle: Earth and Planetary Science Letters, v. 265, no. 3, p. 423-437. doi:
Hess, H., 1962, History of Ocean Basins: Geological Society of America Bulletin: Petrologic Studies: A Volume to Honour AF Buddington, p. 559-620. doi:
Hibbard, J., and Waldron, J. W., 2009, Truncation and translation of Appalachian promontories: Mid-Paleozoic strike-slip tectonics and basin initiation: Geology, v. 37, no. 6, p. 487-490. doi:
Hibbard, J. P., Stoddard, E. F., Secor, D. T., and Dennis, A. J., 2002, The Carolina Zone: overview of Neoproterozoic to Early Paleozoic peri-Gondwanan terranes along the eastern flank of the southern Appalachians: Earth-Science Reviews, v. 57, no. 3-4, p. 299-339. doi:
Hirth, G., and Kohlstedt, D., 2004, Rheology of the Upper Mantle and the Mantle Wedge: A View from the Experimentalists, *Inside the Subduction Factory*, p. 83-105.
Hoggard, M. J., White, N., and Al-Attar, D., 2016, Global dynamic topography observations reveal limited influence of large-scale mantle flow: Nature Geoscience, v. 9, no. 6, p. 456. doi: 10.1038/ngeo2709
Hoggard, M. J., Winterbourne, J., Czarnota, K., and White, N., 2017, Oceanic residual depth measurements, the plate cooling model, and global dynamic topography: Journal of Geophysical Research: Solid Earth, v. 122, no. 3, p. 2328-2372. doi:

Höink, T., and Lenardic, A., 2010, Long wavelength convection, Poiseuille–Couette flow in the low-viscosity asthenosphere and the strength of plate margins: Geophysical Journal International, v. 180, no. 1, p. 23-33. doi: 10.1111/j.1365-246X.2009.04404.x
Holmes, A., 1931, XVIII. Radioactivity and earth movements: Transactions of the Geological Society of Glasgow, v. 18, no. 3, p. 559-606. doi:
Holmes, A., 1951, The sequence of Precambrian orogenic belts in south and central Africa: Proceed. 18th Internat. Geol. Congr. London 1948, v. 14, p. 254-269. doi:
Hopper, E., Fischer, K. M., Wagner, L. S., and Hawman, R. B., 2017, Reconstructing the end of the Appalachian orogeny: Geology, v. 45, no. 1, p. 15-18. doi:
Hosseini, K., Matthews, K. J., Sigloch, K., Shephard, G. E., Domeier, M., and Tsekhmistrenko, M., 2018, SubMachine: Web-based tools for exploring seismic tomography and other models of Earth's deep interior: Geochemistry, Geophysics, Geosystems, v. 19, no. 5, p. 1464-1483. doi:
Houseman, G., 1988, The dependence of convection planform on mode of heating: Nature, v. 332, no. 6162, p. 346-349. doi: https://doi.org/10.1038/332346a0
Huang, K., and Opdyke, N. D., 1991, Paleomagnetism of Jurassic rocks from southwestern Sichuan and the timing of the closure of the Qinling Suture: Tectonophysics, v. 200, no. 1, p. 299-316. doi: http://dx.doi.org/10.1016/0040-1951(91)90021-J
Huang, K., Opdyke, N. D., and Zhu, R., 2000, Further paleomagnetic results from the Silurian of the Yangtze Block and their implications: Earth and Planetary Science Letters, v. 175, no. 3, p. 191-202. doi:
Husson, L., and Conrad, C. P., 2006, Tectonic velocities, dynamic topography, and relative sea level: Geophysical Research Letters, v. 33, no. 18. doi: https://doi.org/10.1029/2006GL026834
Iasky, R., D'ercole, C., Ghori, K., Mory, A., and Lockwood, A., 2003, Structure and petroleum prospectivity of the Gascoyne Platform, Western Australia: Geological Survey of Western Australia, Report, v. 87, p. 1-56. doi:
Iasky, R. P., Mory, A., Ghori, K., and Shevchenko, S., 1998, Structure and petroleum potential of the southern Merlinleigh Sub-basin, Carnarvon Basin, Western Australia, Geological Survey of Western Australia Perth.
Iasky, R. P., and Mory, A. J., 1999, Geology and petroleum potential of the Gascoyne platform southern Carnarvon basin Western Australia, Geological Survey of Western Australia Perth, v. 69.
Isacks, B., Oliver, J., and Sykes, L. R., 1968, Seismology and the new global tectonics: Journal of Geophysical Research, v. 73, no. 18, p. 5855-5899. doi:
Isem, A. R., Brakel, A. T., Olissoff, S., Strusz, D. L., Langford, R. P., Truswell, E. M., Yeung, M., Cook, P. J., Bradshaw, M. T., Wilford, G. E., Yeates, A. N., and Totterdell, J. M., 2001, Palaeogeographic Atlas of Australia (a set of ten volumes), Commonwealth of Australia (Geoscience Australia).
Ismail-Zadeh, A., Schubert, G., Tsepelev, I., and Korotkii, A., 2004, Inverse problem of thermal convection: numerical approach and application to mantle plume restoration: Physics of the Earth and Planetary Interiors, v. 145, no. 1, p. 99-114. doi: https://doi.org/10.1016/j.pepi.2004.03.006
Jarvis, G. T., and Mckenzie, D. P., 1980, Sedimentary basin formation with finite extension rates: Earth and Planetary Science Letters, v. 48, no. 1, p. 42-52. doi: 10.1016/0012-821X(80)90168-5
Jaupart, C., Labrosse, S., and Mareschal, J., 2007, 7.06—Temperatures, heat and energy in the mantle of the earth: Treatise on geophysics, v. 7, p. 223-270. doi:
Jiang, C., 1992, Opening-closing evolution of the Kunlun Mountains: Opening Closing Tectonics of Kunlun Shan, p. 205-217. doi:
Johansson, L., Zahirovic, S., and Müller, R. D., 2018, The Interplay Between the Eruption and Weathering of Large Igneous Provinces and the Deep-Time Carbon Cycle: Geophysical Research Letters, v. 45, no. 11, p. 5380-5389. doi: https://doi.org/10.1029/2017GL076691
Jokat, W., Boebel, T., König, M., and Meyer, U., 2003, Timing and geometry of early Gondwana breakup: Journal of Geophysical Research: Solid Earth, v. 108, no. B9. doi: https://doi.org/10.1029/2002JB001802
Kaminski, E., and Jaupart, C., 2000, Lithosphere structure beneath the Phanerozoic intracratonic basins of North America: Earth and Planetary Science Letters, v. 178, no. 1-2, p. 139-149. doi: 10.1016/S0012-821X(00)00067-4
Karlsen, K. S., Conrad, C. P., and Magni, V., 2019, Deep Water Cycling and Sea Level Change Since the Breakup of Pangea: Geochemistry, Geophysics, Geosystems. doi: https://doi.org/10.1029/2019GC008232
Karlsen, K. S., Domeier, M., Gaina, C., and Conrad, C. P., 2020, A tracer-based algorithm for automatic generation of seafloor age grids from plate tectonic reconstructions: Computers & Geosciences, v. 140, p. 104508. doi: https://doi.org/10.1016/j.cageo.2020.104508
Kennard, J. M., Jackson, M. J., Romine, R. R., and Southgate, P. N., 1994a, Canning Basin Project Stage II-Geohistory Modelling, Australian Geological Survey Organisation.
Kennard, J. M., Jackson, M. J., Romine, K. K., Shaw, R. D., Southgate, P. N., Purcell, P. G., and Purcell, R. R., 1994b, Depositional sequences and associated petroleum systems of the Canning Basin, WA, *in* Purcell, P. G., and Purcell, R. R., eds., *The Sedimentary Basins of Western Australia: Proceedings of West Australian Basins Symposium*: Perth, p. 657-676.
Kennard, J. M., Southgate, P. N., Jackson, M. J., O'Brien, P. E., Christie-Blick, N., Holmes, A. E., and " Rick" Sarg, J., 1992, New sequence perspective on the Devonian reef complex and the Frasnian-Famennian boundary, Canning Basin, Australia: Geology, v. 20, no. 12, p. 1135-1138. doi:
Kennett, B., Salmon, M., Saygin, E., and Group, A. W., 2011, AusMoho: the variation of Moho depth in Australia: Geophysical Journal International, v. 187, no. 2, p. 946-958. doi: 10.1111/j.1365-246X.2011.05194.x
Kircher, A., 1668, Systema ideale quo exprimitur, aquarum per canales hydragogos subterraneos ex mari et in montium hydrophylacia protrusio, aquarumq[ue] subterrestrium per pyragogos canales concoctus: Apud Joannem Janssonium & Elizeum Weyerstraten, Hand-drawn, color, Not drawn to scale. *Norman B. Leventhal Map & Education Center*. https://collections.leventhalmap.org/search/commonwealth:n8710p88b (accessed June 16, 2020)
Kirschner, J. P., Kominz, M. A., and Mwakanyamale, K. E., 2010, Quantifying extension of passive margins: Implications for sea level change: Tectonics, v. 29, no. 4. doi: https://doi.org/10.1029/2009TC002557
Kirschvink, J. L., Ripperdan, R. L., and Evans, D. A., 1997, Evidence for a large-scale reorganization of Early Cambrian continental masses by inertial interchange true polar wander: Science, v. 277, no. 5325, p. 541-545. doi:
Klemd, R., Bröcker, M., Hacker, B. R., Gao, J., Gans, P., and Wemmer, K., 2005, New Age Constraints on the Metamorphic Evolution of the High-Pressure/Low-Temperature Belt in the Western Tianshan Mountains, NW China: The Journal of Geology, v. 113, no. 2, p. 157-168. doi: 10.1086/427666
Kohn, B., Gleadow, A., Brown, R., Gallagher, K., O'sullivan, P., and Foster, D., 2002, Shaping the Australian crust over the last 300 million years: insights from fission track thermotectonic imaging and denudation studies of key terranes: Australian Journal of Earth Sciences, v. 49, no. 4, p. 697-717. doi: https://doi.org/10.1046/j.1440-0952.2002.00942.x
Kominz, M. A., 1984, Oceanic Ridge Volumes and Sea-Level Change - An Error Analysis., *in* Schlee, J. S., ed., *Interregional Unconformities and Hydrocarbon Accumulation.*, Volume 36, American Association of Petroleum Geologists, p. 109-127.
Kominz, M. A., and Bond, G. C., 1991, Unusually large subsidence and sea-level events during middle Paleozoic time: New evidence supporting mantle convection models, for supercontinent assembly: Geology, v. 19, no. 1, p. 56-60. doi: 10.1130/0091-7613(1991)019<0056:ULSASL>2.3.CO;2

Kominz, M. A., Browning, J., Miller, K., Sugarman, P., Mizintseva, S., and Scotese, C., 2008, Late Cretaceous to Miocene sea-level estimates from the New Jersey and Delaware coastal plain coreholes: An error analysis: Basin Research, v. 20, no. 2, p. 211-226. doi: https://doi.org/10.1111/j.1365-2117.2008.00354.x
Korenaga, J., 2017, On the extent of mantle hydration caused by plate bending: Earth and Planetary Science Letters, v. 457, p. 1-9. doi: https://doi.org/10.1016/j.epsl.2016.10.011
Korsch, R., Totterdell, J., Fomin, T., and Nicoll, M., 2009, Contractional structures and deformational events in the Bowen, Gunnedah and Surat Basins, eastern Australia: Australian Journal of Earth Sciences, v. 56, no. 3, p. 477-499. doi: https://doi.org/10.1080/08120090802698745
Kramer, S. C., Wilson, C. R., and Davies, D. R., 2012, An implicit free surface algorithm for geodynamical simulations: Physics of the Earth and Planetary Interiors, v. 194-195, p. 25-37. doi: https://doi.org/10.1016/j.pepi.2012.01.001
Kröner, A., Zhang, G., and Sun, Y., 1993, Granulites in the Tongbai area, Qinling belt, China: geochemistry, petrology, single zircon geochronology, and implications for the tectonic evolution of eastern Asia: Tectonics, v. 12, no. 1, p. 245-255. doi:
Kroner, U., Hahn, T., Romer, R. L., and Linnemann, U., 2007, The Variscan orogeny in the Saxo-Thuringian zone—heterogenous overprint of Cadomian/Paleozoic peri-Gondwana crust: Geological Society of America Special Papers, v. 423, p. 153-172. doi:
Kroner, U., Mansy, J., Mazur, S., Aleksandrowski, P., Hann, H., Huckriede, H., Lacquement, F., Lamarche, J., Ledru, P., and Pharaoh, T., 2008, Variscan tectonics: The Geology of Central Europe, v. 1, p. 599-664. doi:
Kroner, U., and Romer, R., 2013, Two plates—many subduction zones: the Variscan orogeny reconsidered: Gondwana Research, v. 24, no. 1, p. 298-329. doi:
Krs, M., 1968, Rheological aspects of palaeomagnetism: XIII Internat. Geolog. Congr, v. 5, p. 87-96. doi:
Krs, M., Pruner, P., and Man, O., 2001, Tectonic and paleogeographic interpretation of the paleomagnetism of Variscan and pre-Variscan formations of the Bohemian Massif, with special reference to the Barrandian terrane: Tectonophysics, v. 332, no. 1, p. 93-114. doi:
Kuang, K., 1985, History and style of Cooper-Eromanga Basin structures: Exploration Geophysics, v. 16, no. 3, p. 245-248. doi: 10.1071/EG985245
Kustowski, B., Ekström, G., and Dziewoński, A., 2008, Anisotropic shear-wave velocity structure of the Earth's mantle: A global model: Journal of Geophysical Research: Solid Earth, v. 113, no. B6. doi:
Lai, S., Zhang, G., Dong, Y., Pei, X., and Chen, L., 2004, Geochemistry and regional distribution of ophiolites and associated volcanics in Mianlue suture, Qinling-Dabie Mountains: SCIENCE IN CHINA SERIES D EARTH SCIENCES-ENGLISH EDITION-, v. 47, no. 4, p. 289-299. doi:
Langenstrassen, F., 1983, Neritic sedimentation of the Lower and Middle Devonian in the Rheinische Schiefergebirge east of the River Rhine, *Intracontinental fold belts*, Springer, p. 43-76.
Langford, R., Wilford, G., Truswell, E., and Isern, A., 1995, Palaeogeographic atlas of Australia: Canberra, Australian Geological Survey Organisation, scale, v. 1, p. 10,000,000. doi:
Laurent-Charvet, S., Charvet, J., Monié, P., and Shu, L., 2003, Late Paleozoic strike-slip shear zones in eastern Central Asia (NW China): New structural and geochronological data: Tectonics, v. 22, no. 2. doi:
Laurent-Charvet, S., Charvet, J., Shu, L., Ma, R., and Lu, H., 2002, Palaeozoic late collisional strike-slip deformations in Tianshan and Altay, Eastern Xinjiang, NW China: Terra Nova, v. 14, no. 4, p. 249-256. doi:
Leeder, M., 1982, Upper Palaeozoic basins of the British Isles—Caledonide inheritance versus Hercynian plate margin processes: Journal of the Geological Society, v. 139, no. 4, p. 479-491. doi:
Lehmann, J., Schulmann, K., Lexa, O., Corsini, M., Kröner, A., Štípská, P., Tomurhuu, D., and Otgonbator, D., 2010, Structural constraints on the evolution of the Central Asian Orogenic Belt in SW Mongolia: American Journal of Science, v. 310, no. 7, p. 575-628. doi:
Lekic, V., Cottaar, S., Dziewonski, A., and Romanowicz, B., 2012, Cluster analysis of global lower mantle tomography: A new class of structure and implications for chemical heterogeneity: Earth and Planetary Science Letters, v. 357, p. 68-77. doi:
Lerch, M., Xue, F., Kröner, A., Zhang, G., and Tod, W., 1995, A middle Silurian-Early Devonian magmatic arc in the Qinling Mountains of central China: The Journal of Geology, v. 103, no. 4, p. 437-449. doi:
Lewandowski, M., 2003, ASSEMBLY OF PANGEA: COMBINED PALEOMAGNETIC AND PALEOCLIMATIC APPROACH, *Advances in Geophysics*, Volume Volume 46, Elsevier, p. 199-236.
Li, S., Hou, Z., Yang, Y., Sun, W., Zhang, G., and Li, Q., 2004, Timing and geochemical characters of the Sanchazi magmatic arc in Mianlue tectonic zone, South Qinling: SCIENCE IN CHINA SERIES D EARTH SCIENCES-ENGLISH EDITION-, v. 47, no. 4, p. 317-328. doi:
Li, S., Sun, W., Zhang, G., Chen, J., and Yang, Y., 1996, Chronology and geochemistry of metavolcanic rocks from Heigouxia Valley in the Mian-Lue tectonic zone, South Qinling——Evidence for a Paleozoic oceanic basin and its close time: Science in China Series D-Earth Sciences, v. 39, no. 3, p. 300-310. doi:
Li, Y., McWillams, M., Sharps, R., Cox, A., Li, Y., Li, Q., Gao, Z., Zhang, Z., and Zhai, Y., 1990, A Devonian paleomagnetic pole from red beds of the Tarim Block, China: Journal of Geophysical Research: Solid Earth, v. 95, no. B12, p. 19185-19198. doi:
Li, Y., Sun, L., Yang, H., Zhang, G., Zeng, C., Feng, X., Wen, L., Zhang, Q., and Jia, T., 2014, New discovery of late Silurian-Carboniferous extensional structure in Tarim Basin and its geological significance: Chin. J. Geol, v. 49, no. 1, p. 30-48. doi:
Li, Y., Yang, J., Dilek, Y., Zhang, J., Pei, X., Chen, S., Xu, X., and Li, J., 2015, Crustal architecture of the Shangdan suture zone in the early Paleozoic Qinling orogenic belt, China: record of subduction initiation and backarc basin development: Gondwana Research, v. 27, no. 2, p. 733-744. doi:
Li, Z.-X., Bogdanova, S., Collins, A., Davidson, A., De Waele, B., Ernst, R., Fitzsimons, I., Fuck, R., Gladkochub, D., and Jacobs, J., 2008, Assembly, configuration, and break-up history of Rodinia: a synthesis: Precambrian research, v. 160, no. 1-2, p. 179-210. doi: https://doi.org/10.1016/j.precamres.2007.04.021
Li, Z.-X., and Zhong, S., 2009, Supercontinent–superplume coupling, true polar wander and plume mobility: plate dominance in whole-mantle tectonics: Physics of the Earth and Planetary interiors, v. 176, no. 3-4, p. 143-156. doi: https://doi.org/10.1016/j.pepi.2009.05.004
Liao, X.-y., Wang, Y.-w., Liu, L., Wang, C., and Santosh, M., 2017, Detrital zircon U-Pb and Hf isotopic data from the Liuling Group in the South Qinling belt: Provenance and tectonic implications: Journal of Asian Earth Sciences, v. 134, p. 244-261. doi: http://doi.org/10.1016/j.jseaes.2016.11.020
Lin, J.-L., and Fuller, M., 1990, Palaeomagnetism, North China and South China collision, and the Tan-lu fault: Philosophical Transactions of the Royal Society of London A: Mathematical, Physical and Engineering Sciences, v. 331, no. 1620, p. 589-598. doi:
Linnemann, U., McNaughton, N. J., Romer, R. L., Gehmlich, M., Drost, K., and Tonk, C., 2004, West African provenance for Saxo-Thuringia (Bohemian Massif): did Armorica ever leave pre-Pangean Gondwana?–U/Pb-SHRIMP zircon evidence and the Nd-isotopic record: International Journal of Earth Sciences, v. 93, no. 5, p. 683-705. doi:
Lithgow-Bertelloni, C., and Gurnis, M., 1997, Cenozoic subsidence and uplift of continents from time-varying dynamic topography: Geology, v. 25, no. 8, p. 735-738. doi:
Lithgow-Bertelloni, C., and Silver, P. G., 1998, Dynamic topography, plate driving forces and the African superswell: Nature, v. 395, no. 6699, p. 269-272. doi: https://doi.org/10.1038/26212

Lithgow-Bertelloni, C., and Richards, M. A., 1998, The dynamics of Cenozoic and Mesozoic plate motions: Reviews of Geophysics, v. 36, no. 1, p. 27-78. doi: https://doi.org/10.1029/97RG02282
Liu, L., and Gurnis, M., 2008, Simultaneous inversion of mantle properties and initial conditions using an adjoint of mantle convection: Journal of Geophysical Research: Solid Earth, v. 113, no. B8. doi: https://doi.org/10.1029/2008JB005594
Liu, L., Spasojević, S., and Gurnis, M., 2008, Reconstructing Farallon plate subduction beneath North America back to the Late Cretaceous: Science, v. 322, no. 5903, p. 934-938. doi: http://10.1126/science.1162921
Liu, S., Nummedal, D., and Liu, L., 2011, Migration of dynamic subsidence across the Late Cretaceous United States Western Interior Basin in response to Farallon plate subduction: Geology, v. 39, no. 6, p. 555-558. doi:
Liu, Y., Genser, J., Neubauer, F., Jin, W., Ge, X., Handler, R., and Takasu, A., 2005, 40 Ar/39 Ar mineral ages from basement rocks in the eastern Kunlun Mountains, NW China, and their tectonic implications: Tectonophysics, v. 398, no. 3, p. 199-224. doi:
Lowman, J. P., 2011, Mantle convection models featuring plate tectonic behavior: An overview of methods and progress: Tectonophysics, v. 510, no. 1, p. 1-16. doi: https://doi.org/10.1016/j.tecto.2011.04.015
Lucassen, F., Becchio, R., Wilke, H., Franz, G., Thirlwall, M., Viramonte, J., and Wemmer, K., 2000, Proterozoic–Paleozoic development of the basement of the Central Andes (18–26 S)—a mobile belt of the South American craton: Journal of South American Earth Sciences, v. 13, no. 8, p. 697-715. doi:
Lynner, C., and Long, M. D., 2014, Lowermost mantle anisotropy and deformation along the boundary of the African LLSVP: Geophysical Research Letters, v. 41, no. 10, p. 3447-3454. doi:
Ma, C., She, Z., Xu, P., and Wang, L., 2005, Silurian A-type granitoids in the southern margin of the Tongbai-Dabieshan: Evidence from SHRIMP zircon geochronology and geochemistry: Science in China Series D: Earth Sciences, v. 48, no. 8, p. 1134-1145. doi: 10.1360/03yd0487
Ma, X., McElhinny, M. W., Embleton, B. J., and Zhang, Z., 1993, Permo-Triassic palaeomagnetism in the Emei mountain region, southwest China: Geophysical Journal International, v. 114, no. 2, p. 293-303. doi:
Machetel, P., Rabinowicz, M., and Bernardet, P., 1986, Three-dimensional convection in spherical shells: Geophysical & Astrophysical Fluid Dynamics, v. 37, no. 1-2, p. 57-84. doi: https://doi.org/10.1080/03091928608210091
MacNeill, M., Marshall, N., and McNamara, C., 2018, New Insights into a major Early-Middle Triassic Rift Episode in the NW Shelf of Australia: ASEG Extended Abstracts, v. 2018, no. 1, p. 1-5. doi: 10.1071/ASEG2018abM3_3B
Marcano, M. C., Van der Voo, R., and Mac Niocaill, C., 1999, True polar wander during the Permo^ Triassic: Journal of Geodynamics, v. 28, no. 2, p. 75-95. doi:
Mattauer, M., Matte, P., Malavieille, J., Tapponnier, P., Maluski, H., Qin, X. Z., Lun, L. Y., and Qin, T. Y., 1985, Tectonics of the Qinling belt: build-up and evolution of eastern Asia: Nature, v. 317, no. 6037, p. 496-500. doi:
Matte, P., Tapponnier, P., Arnaud, N., Bourjot, L., Avouac, J., Vidal, P., Qing, L., Yusheng, P., and Yi, W., 1996, Tectonics of Western Tibet, between the Tarim and the Indus: Earth and Planetary Science Letters, v. 142, no. 3-4, p. 311-330. doi:
Mattern, F., Schneider, W., Li, Y., and Li, X., 1996, A traverse through the western Kunlun (Xinjiang, China): tentative geodynamic implications for the Paleozoic and Mesozoic: Geologische Rundschau, v. 85, no. 4, p. 705-722. doi: 10.1007/bf02440106
Matthews, K. J., Hale, A. J., Gurnis, M., Müller, R. D., and DiCaprio, L., 2011, Dynamic subsidence of Eastern Australia during the Cretaceous: Gondwana Research, v. 19, no. 2, p. 372-383. doi: https://doi.org/10.1016/j.gr.2010.06.006
Matthews, K. J., Maloney, K. T., Zahirovic, S., Williams, S. E., Seton, M., and Mueller, R. D., 2016, Global plate boundary evolution and kinematics since the late Paleozoic: Global and Planetary Change, v. 146, p. 226-250. doi: https://doi.org/10.1016/j.gloplacha.2016.10.002
Mavromatidis, A., 2006, Burial/exhumation histories for the Cooper-Eromanga Basins and implications for hydrocarbon exploration, Eastern Australia: Basin Research, v. 18, no. 3, p. 351-373. doi: 10.1111/j.1365-2117.2006.00294.x
McElhinny, M. W., Embleton, B. J. J., Ma, X. H., and Zhang, Z. K., 1981, Fragmentation of Asia in the Permian: Nature, v. 293, no. 5829, p. 212-216. doi:
McKenzie, D. P., 1967, Some remarks on heat flow and gravity anomalies: Journal of Geophysical Research, v. 72, no. 24, p. 6261-6273. doi: https://doi.org/10.1029/JZ072i024p06261
McKenzie, D. P., 1969, Speculations on the consequences and causes of plate motions: Geophysical Journal International, v. 18, no. 1, p. 1-32. doi:
McKerrow, W., and Cocks, L., 1976, Progressive faunal migration across the Iapetus Ocean: Nature, v. 263, no. 5575, p. 304-306. doi: https://doi.org/10.1038/263304a0
McKerrow, W., Mac Niocaill, C., Ahlberg, P. E., Clayton, G., Cleal, C., and Eagar, R., 2000, The late Palaeozoic relations between Gondwana and Laurussia: Geological Society, London, Special Publications, v. 179, no. 1, p. 9-20. doi:
McNamara, A. K., and Zhong, S., 2004, Thermochemical structures within a spherical mantle: Superplumes or piles?: Journal of Geophysical Research: Solid Earth, v. 109, no. B7. doi: 10.1029/2003jb002847
McNamara, A. K., and Zhong, S., 2005, Thermochemical structures beneath Africa and the Pacific Ocean: Nature, v. 437, no. 7062, p. 1136-1139. doi: https://doi.org/10.1038/nature04066
Meere, P. A., and Mulchrone, K. F., 2006, Timing of deformation within Old Red Sandstone lithologies from the Dingle Peninsula, SW Ireland: Journal of the Geological Society, v. 163, no. 3, p. 461-469. doi:
Meert, J. G., 1999, A paleomagnetic analysis of Cambrian true polar wander: Earth and Planetary Science Letters, v. 168, no. 1, p. 131-144. doi:
Meert, J. G., and Torsvik, T. H., 2003, The making and unmaking of a supercontinent: Rodinia revisited: Tectonophysics, v. 375, no. 1-4, p. 261-288. doi: https://doi.org/10.1016/S0040-1951(03)00342-1
Mégnin, C., and Romanowicz, B., 2000, The three-dimensional shear velocity structure of the mantle from the inversion of body, surface and higher-mode waveforms: Geophysical Journal International, v. 143, no. 3, p. 709-728. doi:
Meng, Q.-R., and Zhang, G.-W., 1999, Timing of collision of the North and South China blocks: controversy and reconciliation: Geology, v. 27, no. 2, p. 123-126. doi:
Meng, Q.-R., and Zhang, G.-W., 2000, Geologic framework and tectonic evolution of the Qinling orogen, central China: Tectonophysics, v. 323, no. 3, p. 183-196. doi:
Merdith, A. S., Collins, A. S., Williams, S. E., Pisarevsky, S., Foden, J. D., Archibald, D. B., Blades, M. L., Alessio, B. L., Armistead, S., Plavsa, D., Clark, C., and Müller, R. D., 2017, A full-plate global reconstruction of the Neoproterozoic: Gondwana Research. doi: http://dx.doi.org/10.1016/j.gr.2017.04.001
Merdith, A. S., Williams, S. E., Brune, S., Collins, A. S., and Müller, R. D., 2019, Rift and plate boundary evolution across two supercontinent cycles: Global and planetary change, v. 173, p. 1-14. doi: https://doi.org/10.1016/j.gloplacha.2018.11.006
Merdith, A. S., Williams, S. E., Collins, A. S., Tetley, M. G., Mulder, J. A., Blades, M. L., Young, A., Armistead, S. E., Cannon, J., Zahirovic, S., and Müller, R. D., 2021, Extending full-plate tectonic models into deep time: Linking the neoproterozoic and the phanerozoic: Earth-Science Reviews, p. 103477. doi: https://doi.org/10.1016/j.earscirev.2020.103477

Metcalfe, I., 2011, Tectonic framework and Phanerozoic evolution of Sundaland: Gondwana Research, v. 19, no. 1, p. 3-21. doi: https://doi.org/10.1016/j.gr.2010.02.016
Middleton, M., 1980, A model of intracratonic basin formation, entailing deep crustal metamorphism: Geophysical Journal International, v. 62, no. 1, p. 1-14. doi: 10.1111/j.1365-246X.1980.tb04839.x
Miller, B. V., Samson, S. D., and D'LEMOS, R. S., 2001, U–Pb geochronological constraints on the timing of plutonism, volcanism, and sedimentation, Jersey, Channel Islands, UK: Journal of the Geological Society, v. 158, no. 2, p. 243-251. doi:
Miller, K. G., Kominz, M. A., Browning, J. V., Wright, J. D., Mountain, G. S., Katz, M. E., Sugarman, P. J., Cramer, B. S., Christie-Blick, N., and Pekar, S. F., 2005, The Phanerozoic record of global sea-level change: science, v. 310, no. 5752, p. 1293-1298. doi: https://doi.org/10.1126/science.1116412
Minster, J., Jordan, T., Molnar, P., and Haines, E., 1974, Numerical modelling of instantaneous plate tectonics: Geophysical Journal International, v. 36, no. 3, p. 541-576. doi: 10.1111/j.1365-246X.1973.tb02435.x
Mišković, A., Spikings, R. A., Chew, D. M., Košler, J., Ulianov, A., and Schaltegger, U., 2009, Tectonomagmatic evolution of Western Amazonia: Geochemical characterization and zircon U-Pb geochronologic constraints from the Peruvian Eastern Cordilleran granitoids: Geological Society of America Bulletin, v. 121, no. 9-10, p. 1298-1324. doi:
Mitchell, R. N., Kilian, T. M., and Evans, D. A. D., 2012, Supercontinent cycles and the calculation of absolute palaeolongitude in deep time: Nature, v. 482, no. 7384, p. 208-211. doi: 10.1038/nature10800
Mitrovica, J., Beaumont, C., and Jarvis, G., 1989, Tilting of continental interiors by the dynamical effects of subduction: Tectonics, v. 8, no. 5, p. 1079-1094. doi: 10.1029/TC008i005p01079
Molnar, P., England, P. C., and Jones, C. H., 2015, Mantle dynamics, isostasy, and the support of high terrain: Journal of Geophysical Research: Solid Earth, v. 120, no. 3, p. 1932-1957. doi: 10.1002/2014jb011724
Moore, D., and Weiss, N., 1973, Two-dimensional Rayleigh-Bénard convection: Journal of Fluid Mechanics, v. 58, no. 2, p. 289-312. doi: https://doi.org/10.1017/S0022112073002600
Moresi, L., and Gurnis, M., 1996, Constraints on the lateral strength of slabs from three-dimensional dynamic flow models: Earth and Planetary Science Letters, v. 138, no. 1-4, p. 15-28. doi: https://doi.org/10.1016/0012-821X(95)00221-W
Moresi, L. N., and Solomatov, V., 1995, Numerical investigation of 2D convection with extremely large viscosity variations: Physics of Fluids, v. 7, no. 9, p. 2154-2162. doi: https://doi.org/10.1063/1.868465
Morgan, W. J., 1968, Rises, trenches, great faults, and crustal blocks: Journal of Geophysical Research, v. 73, no. 6, p. 1959-1982. doi:
Mory, A., 2010, A review of mid-Carboniferous to Triassic stratigraphy, Canning Basin, Western Australia.
Mory, A., and Backhouse, J., 1997, Permian stratigraphy and palynology of the Carnarvon Basin, Western Australia.
Mory, A. J., Iasky, R. P., and Ghori, K., 2003, A summary of the geological evolution and petroleum potential of the Southern Carnarvon Basin, Western Australia, Geological Survey of Western Australia.
Mory, A. J., Nicoll, R. S., and Gorter, J. D., 1998, Lower Palaeozoic correlations and thermal maturity, Carnarvon Basin, WA, *in* Purcell, P. G., and Purcell, R. R., eds., *The Sedimentary Basins of Western Australia 2: Proceedings of West Australian Basins Symposium*: Perth, p. 599-611.
Moucha, R., Forte, A. M., Mitrovica, J. X., Rowley, D. B., Quéré, S., Simmons, N. A., and Grand, S. P., 2008, Dynamic topography and long-term sea-level variations: There is no such thing as a stable continental platform: Earth and Planetary Science Letters, v. 271, no. 1-4, p. 101-108. doi: https://doi.org/10.1016/j.epsl.2008.03.056
Moussavi Harami, S. R., 1996, Burial history of the Cooper Basin region in South Australia: PESA Journal, v. 24. doi: 10.1111/j.1365-2117.2006.00294.x
Müller, R. D., Seton, M., Zahirovic, S., Williams, S. E., Matthews, K. J., Wright, N. M., Shephard, G. E., Maloney, K., Barnett-Moore, N., and Hosseinpour, M., 2016a, Ocean basin evolution and global-scale plate reorganization events since Pangea breakup: Annual Review of Earth and Planetary Sciences, v. 44, no. 1, p. 107-138. doi:
Müller, R. D., Flament, N., Matthews, K. J., Williams, S. E., and Gurnis, M., 2016b, Formation of Australian continental margin highlands driven by plate–mantle interaction: Earth and Planetary Science Letters, v. 441, p. 60-70. doi: https://doi.org/10.1016/j.epsl.2016.02.025
Müller, R. D., Cannon, J., Qin, X., Watson, R. J., Gurnis, M., Williams, S., Pfaffelmoser, T., Seton, M., Russell, S. H., and Zahirovic, S., 2018a, GPlates: building a virtual Earth through deep time: Geochemistry, Geophysics, Geosystems, v. 19, no. 7, p. 2243-2261. doi: https://doi.org/10.1029/2018GC007584
Müller, R. D., Hassan, R., Gurnis, M., Flament, N., and Williams, S. E., 2018b, Dynamic topography of passive continental margins and their hinterlands since the Cretaceous: Gondwana Research, v. 53, p. 225-251. doi: https://doi.org/10.1016/j.gr.2017.04.028
Müller, R. D., Lim, V. S., and Isern, A. R., 2000, Late Tertiary tectonic subsidence on the northeast Australian passive margin: response to dynamic topography?: Marine Geology, v. 162, no. 2-4, p. 337-352. doi:
Müller, R. D., Royer, J.-Y., and Lawver, L. A., 1993, Revised plate motions relative to the hotspots from combined Atlantic and Indian Ocean hotspot tracks: Geology, v. 21, no. 3, p. 275-278. doi:
Müller, R. D., Sdrolias, M., Gaina, C., Steinberger, B., and Heine, C., 2008, Long-term sea-level fluctuations driven by ocean basin dynamics: science, v. 319, no. 5868, p. 1357-1362. doi: https://doi.org/10.1126/science.1151540
Murphy, J. B., Gutierrez-Alonso, G., Nance, R. D., Fernandez-Suarez, J., Keppie, J. D., Quesada, C., Strachan, R. A., and Dostal, J., 2006, Origin of the Rheic Ocean: Rifting along a Neoproterozoic suture?: Geology, v. 34, no. 5, p. 325-328. doi:
Murphy, J. B., Keppie, J. D., Nance, R. D., and Dostal, J., 2010, Comparative evolution of the Iapetus and Rheic Oceans: A North America perspective: Gondwana Research, v. 17, no. 2–3, p. 482-499. doi: http://dx.doi.org/10.1016/j.gr.2009.08.009
Murphy, J. B., van Staal, C. R., and Keppie, J. D., 1999, Middle to late Paleozoic Acadian orogeny in the northern Appalachians: A Laramide-style plume-modified orogeny?: Geology, v. 27, no. 7, p. 653-656. doi:
Murphy, J. B., Waldron, J. W., Kontak, D. J., Pe-Piper, G., and Piper, D. J., 2011, Minas Fault Zone: Late Paleozoic history of an intra-continental orogenic transform fault in the Canadian Appalachians: Journal of Structural Geology, v. 33, no. 3, p. 312-328. doi:
Naimark, B. M., and Ismail-Zadeh, A. T., 1995, Numerical models of a subsidence mechanism in intracratonic basins: Application to North American basins: Geophysical Journal International, v. 123, no. 1, p. 149-160. doi: 10.1111/j.1365-246X.1995.tb06667.x
Nance, R. D., Gutiérrez-Alonso, G., Keppie, J. D., Linnemann, U., Murphy, J. B., Quesada, C., Strachan, R. A., and Woodcock, N. H., 2010, Evolution of the Rheic Ocean: Gondwana Research, v. 17, no. 2–3, p. 194-222. doi: http://dx.doi.org/10.1016/j.gr.2009.08.001
Nance, R. D., and Linnemann, U., 2008, The Rheic Ocean: origin, evolution, and significance: GSA Today, v. 18, no. 12, p. 4-12. doi:
Natarov, S. I., and Conrad, C. P., 2012, The role of Poiseuille flow in creating depth-variation of asthenospheric shear: Geophysical Journal International, v. 190, no. 3, p. 1297-1310. doi: 10.1111/j.1365-246X.2012.05562.x
Nicoll, R., Laurie, J., Shergold, J., and Nielsen, A. T., 1992, Preliminary correlation of latest Cambrian to Early Ordovician sea-level events in Australia and Scandinavia, *Global Perspectives on Ordovician Geology*, AA Balkema, p. 381-394.
Nicoll, R., Mory, A., Backhouse, J., Shafik, S., and Glenn, K., 1998, Southern Carnarvon Basin Biozonation and Stratigraphy.
O'Connell, R. J., Gable, C. W., and Hager, B. H., 1991, Toroidal-Poloidal Partitioning of Lithospheric Plate Motions, *in* Sabadini, R., Lambeck, K., and Boschi, E., eds., *Glacial Isostasy, Sea-Level and Mantle Rheology*: Dordrecht, Springer Netherlands, p. 535-551.

Oncken, O., 1988, Aspects of the reconstruction of the stress history of a fold and thrust belt (Rhenish Massif, Federal Republic of Germany): Tectonophysics, v. 152, no. 1-2, p. 19-40. doi:
Opdyke, N. D., Huang, K., Xu, G., Zhang, W., and Kent, D. V., 1987, Paleomagnetic results from the Silurian of the Yangtze paraplatform: Tectonophysics, v. 139, no. 1, p. 123-132. doi:
Pankhurst, R. J., Rapela, C. W., De Luchi, M. L., Rapalini, A., Fanning, C., and Galindo, C., 2014, The Gondwana connections of northern Patagonia: Journal of the Geological Society, v. 171, no. 3, p. 313-328. doi:
Pankhurst, R. J., Rapela, C. W., Loske, W., Márquez, M., and Fanning, C., 2003, Chronological study of the pre-Permian basement rocks of southern Patagonia: Journal of South American Earth Sciences, v. 16, no. 1, p. 27-44. doi:
Paris, F., 1993, Evolution paléogéographique de l'Europe au Paléozoïque inférieur: le test des Chitinozoaires: Comptes rendus de l'Académie des sciences. Série 2, Mécanique, Physique, Chimie, Sciences de l'univers, Sciences de la Terre, v. 316, no. 2, p. 273-280. doi:
Parra Garcia, M., Sanchez, G., Dentith, M., and George, A., 2014, Regional Structural and Stratigraphic Study of the Canning Basin, Western Australia, Perth, Department of Mines and Petroleum Government of Western Australia.
Parsons, B., 1982, Causes and consequences of the relation between area and age of the ocean floor: Journal of Geophysical Research: Solid Earth, v. 87, no. B1, p. 289-302. doi: https://doi.org/10.1029/JB087iB01p00289
Parsons, B., and Daly, S., 1983, The relationship between surface topography, gravity anomalies, and temperature structure of convection: Journal of Geophysical Research: Solid Earth, v. 88, no. B2, p. 1129-1144. doi: 10.1029/JB088iB02p01129
Parsons, B., and Sclater, J. G., 1977, An analysis of the variation of ocean floor bathymetry and heat flow with age: Journal of geophysical research, v. 82, no. 5, p. 803-827. doi: https://doi.org/10.1029/JB082i005p00803
Pastor-Galán, D., Gutiérrez-Alonso, G., Fernández-Suárez, J., Murphy, J. B., and Nieto, F., 2013, Tectonic evolution of NW Iberia during the Paleozoic inferred from the geochemical record of detrital rocks in the Cantabrian Zone: Lithos, v. 182, p. 211-228. doi:
Patočka, F., Pruner, P., and Štorch, P., 2003, Palaeomagnetism and geochemistry of early Palaeozoic rocks of the Barrandian (Teplá-Barrandian Unit, Bohemian Massif): palaeotectonic implications: Physics and Chemistry of the Earth, Parts A/B/C, v. 28, no. 16, p. 735-749. doi:
Pavlis, N. K., Holmes, S. A., Kenyon, S. C., and Factor, J. K., 2012, The development and evaluation of the Earth Gravitational Model 2008 (EGM2008): Journal of geophysical research: solid earth, v. 117, no. B4. doi:
Pekeris, C. L., 1935, Thermal convection in the interior of the Earth: Geophysical Journal International, v. 3, p. 343-367. doi:
Perry, H. K. C., Forte, A. M., and Eaton, D. W. S., 2003, Upper-mantle thermochemical structure below North America from seismic–geodynamic flow models: Geophysical Journal International, v. 154, no. 2, p. 279-299. doi: 10.1046/j.1365-246X.2003.01961.x
Peslier, A. H., Schönbächler, M., Busemann, H., and Karato, S.-I., 2017, Water in the Earth's interior: Distribution and origin: Space Science Reviews, v. 212, no. 1-2, p. 743-810. doi: https://doi.org/10.1007/s11214-017-0387-z
Petersen, K. D., Nielsen, S., Clausen, O., Stephenson, R., and Gerya, T., 2010, Small-scale mantle convection produces stratigraphic sequences in sedimentary basins: Science, v. 329, no. 5993, p. 827-830. doi:
Pin, C., Fonseca, P. E., Paquette, J.-L., Castro, P., and Matte, P., 2008, The ca. 350 Ma Beja Igneous Complex: A record of transcurrent slab break-off in the Southern Iberia Variscan Belt?: Tectonophysics, v. 461, no. 1, p. 356-377. doi:
Pin, C., and Rodríguez, J., 2009, Comment on "Rheic Ocean ophiolitic remnants in southern Iberia questioned by SHRIMP U-Pb zircon ages on the Beja-Acebuches amphibolites" by A. Azor et al: Tectonics, v. 28, no. 5. doi:
Pitman, W. C., 1978, Relationship between eustacy and stratigraphic sequences of passive margins: Geological Society of America Bulletin, v. 89, no. 9, p. 1389-1403. doi: https://doi.org/10.1130/0016-7606(1978)89<1389:RBEASS>2.0.CO;2
Powell, C. M., Roots, S., and Veevers, J., 1988, Pre-breakup continental extension in East Gondwanaland and the early opening of the eastern Indian Ocean: Tectonophysics, v. 155, no. 1-4, p. 261-283. doi: 10.1016/0040-1951(88)90269-7
Pysklywec, R. N., and Mitrovica, J. X., 1999, The role of subduction-induced subsidence in the evolution of the Karoo Basin: The Journal of geology, v. 107, no. 2, p. 155-164. doi: 10.1086/314338
Qin, J., Lai, S., and Li, Y., 2008, Slab breakoff model for the Triassic post-collisional adakitic granitoids in the Qinling Orogen, Central China: Zircon U-Pb ages, geochemistry, and Sr-Nd-Pb isotopic constraints: International Geology Review, v. 50, no. 12, p. 1080-1104. doi:
Qingren, M., Feng, X., and Guowei, Z., 1994, Conglomerate Sedimentation and its Tectonic Implication, Heihe Area Within Shangdan Zone of the Qinling [J]: Acta Sedimentologica Sinica, v. 3. doi:
Quesada, C., 1997, A reappraisal of the structure of the Spanish segment of the Iberian Pyrite Belt: Mineralium Deposita, v. 33, no. 1-2, p. 31-44. doi:
Ramos, V. A., 2008, Patagonia: A paleozoic continent adrift?: Journal of South American Earth Sciences, v. 26, no. 3, p. 235-251. doi:
Rapalini, A. E., 2005, The accretionary history of southern South America from the latest Proterozoic to the Late Palaeozoic: some palaeomagnetic constraints: Geological Society, London, Special Publications, v. 246, no. 1, p. 305-328. doi:
Rapalini, A. E., de Luchi, M. G. L., Dopico, C. M., Klinger, F. G. L., Giménez, M. E., and Martínez, P., 2010, Did Patagonia collide with Gondwana in the Late Paleozoic? Some insights from a multidisciplinary study of magmatic units of the North Patagonian Massif: Geologica Acta, v. 8, no. 4, p. 349-371. doi:
Ratschbacher, L., Hacker, B. R., Calvert, A., Webb, L. E., Grimmer, J. C., McWilliams, M. O., Ireland, T., Dong, S., and Hu, J., 2003, Tectonics of the Qinling (Central China): tectonostratigraphy, geochronology, and deformation history: Tectonophysics, v. 366, no. 1–2, p. 1-53. doi: http://doi.org/10.1016/S0040-1951(03)00053-2
Reeckmann, S., and Mebberson, A., 1984, Igneous intrusions in the north-west Canning Basin and their impact on oil exploration, *in* Purcell, P. G., ed., *The Canning Basin WA: Proceedings of Geological Society of Australia/Petroleum Exploration Society of Australia Symposium*: Perth, p. 389-401.
Ricard, Y., Doglioni, C., and Sabadini, R., 1991, Differential rotation between lithosphere and mantle: A consequence of lateral mantle viscosity variations: Journal of Geophysical Research: Solid Earth, v. 96, no. B5, p. 8407-8415. doi: https://doi.org/10.1029/91JB00204
Ricard, Y., Richards, M., Lithgow-Bertelloni, C., and Le Stunff, Y., 1993, A geodynamic model of mantle density heterogeneity: Journal of Geophysical Research: Solid Earth, v. 98, no. B12, p. 21895-21909. doi: 10.1029/93JB02216
Ricard, Y., and Vigny, C., 1989, Mantle dynamics with induced plate tectonics: Journal of Geophysical Research: Solid Earth, v. 94, no. B12, p. 17543-17559. doi: https://doi.org/10.1029/JB094iB12p17543
Richards, F., Hoggard, M., Cowton, L., and White, N., 2018, Reassessing the thermal structure of oceanic lithosphere with revised global inventories of basement depths and heat flow measurements: Journal of Geophysical Research: Solid Earth, v. 123, no. 10, p. 9136-9161. doi: https://doi.org/10.1029/2018JB015998
Richards, M. A., and Hager, B. H., 1984, Geoid anomalies in a dynamic Earth: Journal of Geophysical Research: Solid Earth, v. 89, no. B7, p. 5987-6002. doi: https://doi.org/10.1029/JB089iB07p05987
Richardson, R. M., 1992, Ridge forces, absolute plate motions, and the intraplate stress field: Journal of Geophysical Research: Solid Earth, v. 97, no. B8, p. 11739-11748. doi: https://doi.org/10.1029/91JB00475
Richter, F. M., 1973, Dynamical models for sea floor spreading: Reviews of Geophysics, v. 11, no. 2, p. 223-287. doi: https://doi.org/10.1029/RG011i002p00223

Rider, M. H., and Kennedy, M., 2011, The geological interpretation of well logs (Third edition), Scotland, Rider-French.
Ritsema, J., Deuss, a. A., Van Heijst, H., and Woodhouse, J., 2011, S40RTS: a degree-40 shear-velocity model for the mantle from new Rayleigh wave dispersion, teleseismic traveltime and normal-mode splitting function measurements: Geophysical Journal International, v. 184, no. 3, p. 1223-1236. doi:
Robardet, M., 2003, The Armorica 'microplate': fact or fiction? Critical review of the concept and contradictory palaeobiogeographical data: Palaeogeography, Palaeoclimatology, Palaeoecology, v. 195, no. 1, p. 125-148. doi:
Robardet, M., and Doré, F., 1988, The Late Ordovician diamictic formations from southwestern Europe: north-Gondwana glaciomarine deposits: Palaeogeography, Palaeoclimatology, Palaeoecology, v. 66, no. 1-2, p. 19-31. doi:
Roberts, G. G., and White, N., 2010, Estimating uplift rate histories from river profiles using African examples: Journal of Geophysical Research: Solid Earth, v. 115, no. B2. doi: 10.1029/2009JB006692
Rohrman, M., 2015, Delineating the Exmouth mantle plume (NW Australia) from denudation and magmatic addition estimates: Lithosphere, v. 7, no. 5, p. 589-600. doi: 10.1130/L445.1
Romine, K., Southgate, P., Kennard, J., and Jackson, M., 1994, The Ordovician to Silurian phase of the Canning Basin, WA: structure and sequence evolution, *in* Purcell, P. G., and Purcell, R. R., eds., *The Sedimentary Basins of Western Australia: Proceedings of West Australian Basins Symposium*: Perth, p. 677-696.
Ronov, A. B., 1994, Phanerozoic transgressions and regressions on the continents; a quantitative approach based on areas flooded by the sea and areas of marine and continental deposition: American Journal of Science, v. 294, no. 7, p. 777-801. doi: http://10.2475/ajs.294.7.777
Rosenbaum, G., 2018, The Tasmanides: Phanerozoic tectonic evolution of eastern Australia: Annual Review of Earth and Planetary Sciences, v. 46, p. 291-325. doi: https://doi.org/10.1146/annurev-earth-082517-010146
Ross, M., and Scotese, C., 2000, PaleoGIS/Arcview 3.5, PALEOMAP Project: Arlington, TX: University of Texas at Arlington. doi:
Rowley, D. B., 2002, Rate of plate creation and destruction: 180 Ma to present: Geological Society of America Bulletin, v. 114, no. 8, p. 927-933. doi: https://doi.org/10.1130/0016-7606(2002)114<0927:ROPCAD>2.0.CO;2
Rowley, D. B., 2017, Earth's constant mean elevation: implication for long-term sea level controlled by oceanic lithosphere dynamics in a Pitman world: The Journal of Geology, v. 125, no. 2, p. 141-153. doi: https://doi.org/10.1086/690197
Rubey, M., Brune, S., Heine, C. J., Davies, R. D., Williams, S. E., and Muller, R. D., 2017, Global patterns in Earth's dynamic topography since the Jurassic: the role of subducted slabs. doi: http://dx.doi.org/10.5194/se-8-899-2017
Rudolph, M. L., and Zhong, S., 2014, History and dynamics of net rotation of the mantle and lithosphere: Geochemistry, Geophysics, Geosystems, v. 15, no. 9, p. 3645-3657. doi: https://doi.org/10.1002/2014GC005457
Runcorn, S. K., 1955, Paleomagnetic comparisons between Europe and North America: Proc Geol Assoc Canada, v. 8, p. 77-85. doi:
Rüpke, L. H., Morgan, J. P., Hort, M., and Connolly, J. A., 2004, Serpentine and the subduction zone water cycle: Earth and Planetary Science Letters, v. 223, no. 1-2, p. 17-34. doi: https://doi.org/10.1016/j.epsl.2004.04.018
Russell, M., and Gurnis, M., 1994, The planform of epeirogeny: vertical motions of Australia during the Cretaceous: Basin Research, v. 6, no. 2-3, p. 63-76. doi: 10.1111/j.1365-2117.1994.tb00076.x
Safonova, I., Kotlyarov, A., Krivonogov, S., and Xiao, W., 2017, Intra-oceanic arcs of the Paleo-Asian Ocean: Gondwana Research, v. 50, p. 167-194. doi: https://doi.org/10.1016/j.gr.2017.04.005
Salamon, M., and Königshof, P., 2010, Middle Devonian olistostromes in the Rheno-Hercynian zone (Rheinisches Schiefergebirge)—an indication of back arc rifting on the southern shelf of Laurussia: Gondwana Research, v. 17, no. 2, p. 281-291. doi:
Salles, T., Flament, N., and Müller, D., 2017, Influence of mantle flow on the drainage of eastern A ustralia since the J urassic P eriod: Geochemistry, Geophysics, Geosystems, v. 18, no. 1, p. 280-305. doi: https://doi.org/10.1002/2016GC006617
Saltzman, M. R., 2003, Late Paleozoic ice age: Oceanic gateway or p CO2?: Geology, v. 31, no. 2, p. 151-154. doi: https://doi.org/10.1130/0091-7613(2003)031%3C0151:LPIAOG%3E2.0.CO;2
Samson, S. D., D'Lemos, R. S., Miller, B. V., and Hamilton, M. A., 2005, Neoproterozoic palaeogeography of the Cadomia and Avalon terranes: constraints from detrital zircon U–Pb ages: Journal of the Geological Society, v. 162, no. 1, p. 65-71. doi:
Sandiford, M., 2007, The tilting continent: a new constraint on the dynamic topographic field from Australia: Earth and Planetary Science Letters, v. 261, no. 1-2, p. 152-163. doi: 10.1016/j.epsl.2007.06.023
Schellart, W., Stegman, D., and Freeman, J., 2008, Global trench migration velocities and slab migration induced upper mantle volume fluxes: Constraints to find an Earth reference frame based on minimizing viscous dissipation: Earth-Science Reviews, v. 88, no. 1, p. 118-144. doi:
Schubert, G., and Sandwell, D., 1989, submarine plateaus: Earth and Planetary Science Letters, v. 92, p. 234-246. doi: https://doi.org/10.1016/0012-821X(89)90049-6
Schuberth, B. S. A., Bunge, H.-P., and Ritsema, J., 2009, Tomographic filtering of high-resolution mantle circulation models: Can seismic heterogeneity be explained by temperature alone?: Geochemistry, Geophysics, Geosystems, v. 10, no. 5. doi: 10.1029/2009gc002401
Scotese, C., 2008, The PALEOMAP Project PaleoAtlas for ArcGIS, version 1: Volume, v. 2, p. 16-31. doi:
Scotese, C., 2010a, Point tracker. PALEOMAP Project, University of Texas Arlington.
Scotese, C. R., 1991, Jurassic and Cretaceous plate tectonic reconstructions: Palaeogeography, Palaeoclimatology, Palaeoecology, v. 87, no. 1-4, p. 493-501. doi: https://doi.org/10.1016/0031-0182(91)90145-H
Scotese, C. R., 2004, A continental drift flipbook: The Journal of Geology, v. 112, no. 6, p. 729-741. doi:
Scotese, C. R., 2010b, Plate tectonic maps and Continental drift animations by C. R. Scotese, PALEOMAP Project. www.scotese.com
Scotese, C. R., Bambach, R. K., Barton, C., Van der Voo, R., and Ziegler, A. M., 1979, Paleozoic base maps: The Journal of Geology, v. 87, no. 3, p. 217-277. doi: https://doi.org/10.1086/628416
Scotese, C. R., and Golonka, J., 1997, Paleogeographic atlas, PALEOMAP Project, University of Texas at Arlington Arlington.
Sembroni, A., Kiraly, A., Faccenna, C., Funiciello, F., Becker, T. W., Globig, J., and Fernandez, M., 2017, Impact of the lithosphere on dynamic topography: Insights from analogue modeling: Geophysical Research Letters, v. 44, no. 6, p. 2693-2702. doi: 10.1002/2017GL072668
Şengör, A., 1985, Geology: east Asian tectonic collage: Nature, v. 318, no. 6041, p. 16-17. doi:
Servais, T., and Sintubin, M., 2009, Avalonia, Armorica, Perunica: terranes, microcontinents, microplates or palaeobiogeographical provinces?: Geological Society, London, Special Publications, v. 325, no. 1, p. 103-115. doi:
Seton, M., Flament, N., Whittaker, J., Müller, R. D., Gurnis, M., and Bower, D. J., 2015, Ridge subduction sparked reorganization of the Pacific plate-mantle system 60–50 million years ago: Geophysical Research Letters, v. 42, no. 6, p. 1732-1740. doi: 10.1002/2015GL063057
Seton, M., Müller, R., Zahirovic, S., Gaina, C., Torsvik, T., Shephard, G., Talsma, A., Gurnis, M., Turner, M., and Maus, S., 2012, Global continental and ocean basin reconstructions since 200 Ma: Earth-Science Reviews, v. 113, no. 3-4, p. 212-270. doi: https://doi.org/10.1016/j.earscirev.2012.03.002

Sharps, R., McWilliams, M., Yianping, L., Cox, A., Zhengkun, Z., Yongjian, Z., Zhenjia, G., Yongan, L., and Qiang, L., 1989, Lower Permian paleomagnetism of the Tarim block, northwestern China: Earth and Planetary Science Letters, v. 92, no. 3, p. 275-291. doi: http://dx.doi.org/10.1016/0012-821X(89)90052-6
Shaw, R., Etheridge, M., and Lambeck, K., 1991, Development of the Late Proterozoic to Mid-Paleozoic, intracratonic Amadeus Basin in central Australia: A key to understanding tectonic forces in plate interiors: Tectonics, v. 10, no. 4, p. 688-721. doi: https://doi.org/10.1029/90TC02417
Shaw, R. D., Sexton, M. J., and Zeilinger, I., 1994, The tectonic framework of the Canning Basin, WA, including 1: 2 million structural elements map of the Canning Basin, Australian Geological Survey Organisation.
Shephard, G., Flament, N., Williams, S., Seton, M., Gurnis, M., and Müller, R., 2014, Circum-Arctic mantle structure and long-wavelength topography since the Jurassic: Journal of Geophysical Research: Solid Earth, v. 119, no. 10, p. 7889-7908. doi: 10.1002/2014JB011078
Shephard, G., Müller, R., Liu, L., and Gurnis, M., 2010, Miocene drainage reversal of the Amazon River driven by plate–mantle interaction: Nature Geoscience, v. 3, no. 12, p. 870-875. doi:
Shergold, J., and Nicoll, R., 1992, Revised Cambrian-Ordovician boundary biostratigraphy, Black Mountain, western Queensland: Webby, BD and Laurie, JR, p. 81-92. doi:
Simmons, N. A., Forte, A. M., Boschi, L., and Grand, S. P., 2010, GyPSuM: A joint tomographic model of mantle density and seismic wave speeds: Journal of Geophysical Research: Solid Earth, v. 115, no. B12. doi:
Singharajwarapan, S., and Berry, R., 2000, Tectonic implications of the Nan Suture Zone and its relationship to the Sukhothai Fold Belt, Northern Thailand: Journal of Asian Earth Sciences, v. 18, no. 6, p. 663-673. doi: http://dx.doi.org/10.1016/S1367-9120(00)00017-1
Sloss, L., 1963, Sequences in the cratonic interior of North America: Geological Society of America Bulletin, v. 74, no. 2, p. 93-114. doi:
Smith, A. G., Smith, D. G., and Funnell, B. M., 2004, Atlas of Mesozoic and Cenozoic coastlines, Cambridge University Press.
Smith, T., Edwards, D., Kelman, A. P., Laurie, J., le Poidevin, S., Nicoll, R., Mory, A., Haines, P., and Hocking, R., 2013, Canning Basin Biozonation and Stratigraphy.
Snedden, J., and Liu, C., 2010, A compilation of Phanerozoic sea-level change, coastal onlaps and recommended sequence designations: Search and discovery article, v. 40594, p. 3. doi:
Sone, M., and Metcalfe, I., 2008, Parallel Tethyan sutures in mainland Southeast Asia: New insights for Palaeo-Tethys closure and implications for the Indosinian orogeny: Comptes Rendus Geoscience, v. 340, no. 2–3, p. 166-179. doi: http://dx.doi.org/10.1016/j.crte.2007.09.008
Soper, N., and Woodcock, N., 2003, The lost Lower Old Red Sandstone of England and Wales: a record of post-Iapetan flexure or Early Devonian transtension?: Geological Magazine, v. 140, no. 06, p. 627-647. doi:
Spaggiari, C. V., Gray, D. R., and Foster, D. A., 2004, Ophiolite accretion in the Lachlan Orogen, southeastern Australia: Journal of Structural Geology, v. 26, no. 1, p. 87-112. doi: https://doi.org/10.1016/S0191-8141(03)00084-1
Spasojevic, S., and Gurnis, M., 2012, Sea level and vertical motion of continents from dynamic earth models since the Late Cretaceous: AAPG bulletin, v. 96, no. 11, p. 2037-2064. doi: https://doi.org/10.1306/03261211121
Spasojevic, S., Liu, L., and Gurnis, M., 2009, Adjoint models of mantle convection with seismic, plate motion, and stratigraphic constraints: North America since the Late Cretaceous: Geochemistry, Geophysics, Geosystems, v. 10, no. 5. doi: 10.1029/2008gc002345
Stampfli, G. M., and Borel, G., 2002, A plate tectonic model for the Paleozoic and Mesozoic constrained by dynamic plate boundaries and restored synthetic oceanic isochrons: Earth and Planetary Science Letters, v. 196, no. 1, p. 17-33. doi:
Stampfli, G. M., von Raumer, J. F., and Borel, G. D., 2002, Paleozoic evolution of pre-Variscan terranes: from Gondwana to the Variscan collision: Special Papers-Geological Society of America, p. 263-280. doi:
Steckler, M., and Watts, A., 1978, Subsidence of the Atlantic-type continental margin off New York: Earth and planetary science letters, v. 41, no. 1, p. 1-13. doi: 10.1016/0012-821X(78)90036-5
Steinberger, B., 2007, Effects of latent heat release at phase boundaries on flow in the Earth's mantle, phase boundary topography and dynamic topography at the Earth's surface: Physics of the Earth and Planetary Interiors, v. 164, no. 1-2, p. 2-20. doi: https://doi.org/10.1016/j.pepi.2007.04.021
Steinberger, B., and Becker, T. W., 2018, A comparison of lithospheric thickness models: Tectonophysics, v. 746, p. 325-338. doi: https://doi.org/10.1016/j.tecto.2016.08.001
Steinberger, B., and Calderwood, A. R., 2006, Models of large-scale viscous flow in the Earth's mantle with constraints from mineral physics and surface observations: Geophysical Journal International, v. 167, no. 3, p. 1461-1481. doi: 10.1111/j.1365-246X.2006.03131.x
Steinberger, B., and O'Connell, R. J., 1998, Advection of plumes in mantle flow: implications for hotspot motion, mantle viscosity and plume distribution: Geophysical Journal International, v. 132, no. 2, p. 412-434. doi: 10.1046/j.1365-246x.1998.00447.x
Steinberger, B., and Torsvik, T., 2010, Toward an explanation for the present and past locations of the poles: Geochemistry, Geophysics, Geosystems, v. 11, no. 6. doi:
Steinberger, B., and Torsvik, T. H., 2008, Absolute plate motions and true polar wander in the absence of hotspot tracks: Nature, v. 452, no. 7187, p. 620-623. doi:
Stern, R. J., 2004, Subduction initiation: spontaneous and induced: Earth and Planetary Science Letters, v. 226, no. 3, p. 275-292. doi: https://doi.org/10.1016/j.epsl.2004.08.007
Stotz, I. L., Iaffaldano, G., and Davies, D. R., 2018, Pressure-Driven Poiseuille Flow: A Major Component of the Torque-Balance Governing Pacific Plate Motion: Geophysical Research Letters, v. 45, no. 1, p. 117-125. doi: https://doi.org/10.1002/2017GL075697
Straume, E., Gaina, C., Medvedev, S., Hochmuth, K., Gohl, K., Whittaker, J. M., Abdul Fattah, R., Doornenbal, J., and Hopper, J. R., 2019, GlobSed: Updated total sediment thickness in the world's oceans: Geochemistry, Geophysics, Geosystems, v. 20, no. 4, p. 1756-1772. doi: https://doi.org/10.1029/2018GC008115
Su, W., Gao, J., Klemd, R., Li, J.-L., Zhang, X., Li, X.-H., Chen, N.-S., and Zhang, L., 2010, U–Pb zircon geochronology of Tianshan eclogites in NW China: implication for the collision between the Yili and Tarim blocks of the southwestern Altaids: European Journal of Mineralogy, v. 22, no. 4, p. 473-478. doi:
Sun, W., Li, S., Chen, Y., and Li, Y., 2002, Timing of synorogenic granitoids in the South Qinling, central China: Constraints on the evolution of the Qinling-Dabie orogenic belt: The Journal of geology, v. 110, no. 4, p. 457-468. doi:
Sun, W., Li, S., Sun, Y., Zhang, G., and Zhang, Z., 1996, Chronology and geochemistry of a lava pillow in the Erlangping Group at Xixia in the northern Qinling Mountains: Geol. Rev, v. 42, p. 144-153. doi:
Sun, Z., Li, H., Pei, J., Pan, J., Zhang, L., Li, C., Si, J., and Liu, D., Late Carboniferous paleomagnetism of the Southwestern Tarim block and its implications for the paleogeography of central Asia, AGU Fall Meeting Abstracts. 2014, Volume 1, p. 3629.
Sutherland, R., Spasojevic, S., and Gurnis, M., 2010, Mantle upwelling after Gondwana subduction death explains anomalous topography and subsidence histories of eastern New Zealand and West Antarctica: Geology, v. 38, no. 2, p. 155-158. doi: 10.1130/G30613.1
Sutton, J., 1963, Long-term cycles in the evolution of the continents: Nature, v. 198, no. 4882, p. 731-735. doi:
Tackley, P. J., 1998, Self-consistent generation of tectonic plates in three-dimensional mantle convection: Earth and Planetary Science Letters, v. 157, no. 1-2, p. 9-22. doi:

Tackley, P. J., 2000, Self-consistent generation of tectonic plates in time-dependent, three-dimensional mantle convection simulations: Geochemistry, Geophysics, Geosystems, v. 1, no. 8. doi: 10.1029/2000gc000036
Tackley, P. J., 2008, Modelling compressible mantle convection with large viscosity contrasts in a three-dimensional spherical shell using the yin-yang grid: Physics of the Earth and Planetary Interiors, v. 171, no. 1-4, p. 7-18. doi: https://doi.org/10.1016/j.pepi.2008.08.005
Tackley, P. J., and King, S. D., 2003, Testing the tracer ratio method for modeling active compositional fields in mantle convection simulations: Geochemistry, Geophysics, Geosystems, v. 4, no. 4. doi: 10.1029/2001GC000214
Tackley, P. J., Stevenson, D. J., Glatzmaier, G. A., and Schubert, G., 1993, Effects of an endothermic phase transition at 670 km depth in a spherical model of convection in the Earth's mantle: Nature, v. 361, no. 6414, p. 699-704. doi: https://doi.org/10.1038/361699a0
Tait, J., 1999, New Early Devonian paleomagnetic data from NW France: paleogeography and implications for the Armorican microplate hypothesis: Journal of Geophysical Research: Solid Earth, v. 104, no. B2, p. 2831-2839. doi:
Tait, J., Bachtadse, V., and Dinarès-Turell, J., 2000, Paleomagnetism of Siluro-Devonian sequences, NE Spain: Journal of Geophysical Research, v. 105, no. 23, p. 595-603. doi:
Tait, J., Bachtadse, V., and Soffel, H., 1994, Silurian paleogeography of Armorica: new paleomagnetic data from central Bohemia: Journal of Geophysical Research: Solid Earth, v. 99, no. B2, p. 2897-2907. doi:
Talent, J., 1989, Transgression-regression pattern for the Silurian and Devonian of Australia: Pathways in Geology, Essays in Honour of Edwin Sherbon Hills. Melbourne: Blackwells, v. 201, p. 219. doi:
Talent, J., and Yolkin, E., 1987, Transgression-regression patterns for the Devonian of Australia and southern West Siberia: Courier Forschungsinstitut Senckenberg, v. 92, p. 235-249. doi:
Tan, E., Choi, E., Thoutireddy, P., Gurnis, M., and Aivazis, M., 2006, GeoFramework: Coupling multiple models of mantle convection within a computational framework: Geochemistry, Geophysics, Geosystems, v. 7, no. 6. doi: https://doi.org/10.1029/2005GC001155
Tan, E., Gurnis, M., Armendariz, L., Strand, L., and Kientz, S., 2010, CitcomS user manual: Comput. Infrastruct. for Geodyn., Univ. of Calif., Davis.(Available at http://www. geodynamics. org/cig/software/citcoms). doi:
Tan, E., Leng, W., Zhong, S., and Gurnis, M., 2011, On the location of plumes and lateral movement of thermochemical structures with high bulk modulus in the 3-D compressible mantle: Geochemistry, Geophysics, Geosystems, v. 12, no. 7. doi:
Tipsword, H., Setzer, F., and Smith Jr, F. L., 1966, Interpretation of depositional environment in Gulf Coast petroleum exploration from paleoecology and related stratigraphy. doi:
Torsvik, T. H., Burke, K., Steinberger, B., Webb, S. J., and Ashwal, L. D., 2010a, Diamonds sampled by plumes from the core–mantle boundary: Nature, v. 466, no. 7304, p. 352-355. doi: https://doi.org/10.1038/nature09216
Torsvik, T. H., Steinberger, B., Gurnis, M., and Gaina, C., 2010b, Plate tectonics and net lithosphere rotation over the past 150 My: Earth and Planetary Science Letters, v. 291, no. 1-4, p. 106-112. doi: 10.1016/j.epsl.2009.12.055
Torsvik, T. H., and Cocks, L. R. M., 2004, Earth geography from 400 to 250 Ma: a palaeomagnetic, faunal and facies review: Journal of the Geological Society, v. 161, no. 4, p. 555-572. doi:
Torsvik, T. H., Müller, R. D., Van der Voo, R., Steinberger, B., and Gaina, C., 2008, Global plate motion frames: Toward a unified model: Reviews of Geophysics, v. 46, no. 3. doi: 10.1029/2007rg000227
Torsvik, T. H., and Van der Voo, R., 2002, Refining Gondwana and Pangea palaeogeography: estimates of Phanerozoic non-dipole (octupole) fields: Geophysical Journal International, v. 151, no. 3, p. 771-794. doi:
Torsvik, T. H., van der Voo, R., Doubrovine, P. V., Burke, K., Steinberger, B., Ashwal, L. D., Trønnes, R. G., Webb, S. J., and Bull, A. L., 2014, Deep mantle structure as a reference frame for movements in and on the Earth: Proceedings of the National Academy of Sciences, v. 111, no. 24, p. 8735. doi: http://10.1073/pnas.1318135111
Tosi, N., Yuen, D. A., de Koker, N., and Wentzcovitch, R. M., 2013, Mantle dynamics with pressure-and temperature-dependent thermal expansivity and conductivity: Physics of the Earth and Planetary Interiors, v. 217, p. 48-58. doi: 10.1016/j.pepi.2013.02.004
Totterdell, J. M., Cook, P. J., Bradshaw, M. T., Wilford, G. E., Yeates, A. N., Yeung, M., Truswell, E. M., Brakel, A. T., Isem, A. R., Olissoff, S., Strusz, D. L., and Langford, R. P., 2001, Palaeogeographic Atlas of Australia (a set of ten volumes).
Turcotte, D. L., and Schubert, G., 2002, Geodynamics, Cambridge university press.
Umbgrove, J. H. F., 1940, Periodicity in terrestrial processes: American Journal of Science, v. 238, no. 8, p. 573-576. doi:
Vail, P., Mitchum Jr, R., and Thompson III, S., 1977, Seismic stratigraphy and global changes of sea level: Part 4. Global cycles of relative changes of sea level.: Section 2. Application of seismic reflection configuration to stratigraphic interpretation. doi: https://doi.org/10.1306/M26490C6
Valentine, J., and Moores, E., 1970, Plate-tectonic regulation of faunal diversity and sea level: a model: Nature, v. 228, no. 5272, p. 657-659. doi:
Van der Meer, D., van Saparoea, A. v. d. B., Van Hinsbergen, D., Van de Weg, R., Godderis, Y., Le Hir, G., and Donnadieu, Y., 2017, Reconstructing first-order changes in sea level during the Phanerozoic and Neoproterozoic using strontium isotopes: Gondwana Research, v. 44, p. 22-34. doi: https://doi.org/10.1016/j.gr.2016.11.002
Van der Voo, R., 1967, The rotation of Spain: palaeomagnetic evidence from the Spanish Meseta: Palaeogeography, Palaeoclimatology, Palaeoecology, v. 3, p. 393-416. doi:
Van der Voo, R., 1990, The reliability of paleomagnetic data: Tectonophysics, v. 184, no. 1, p. 1-9. doi: https://doi.org/10.1016/0040-1951(90)90116-P
Van der Voo, R., 1994, True polar wander during the middle Paleozoic?: Earth and Planetary Science Letters, v. 122, no. 1-2, p. 239-243. doi:
Van der Voo, R., 2004, Paleomagnetism, oroclines, and growth of the continental crust: GSa Today, v. 14, no. 12, p. 4-9. doi:
Van der Voo, R., van Hinsbergen, D. J., Domeier, M., Spakman, W., and Torsvik, T. H., 2015, Latest Jurassic–earliest Cretaceous closure of the Mongol-Okhotsk Ocean: A paleomagnetic and seismological-tomographic analysis: Geological Society of America Special Papers, v. 513, p. 589-606. doi:
Van Hinte, J., 1978, Geohistory analysis--application of micropaleontology in exploration geology: AAPG Bulletin, v. 62, no. 2, p. 201-222. doi:
van Staal, C. R., Barr, S. M., and Murphy, J. B., 2012, Provenance and tectonic evolution of Ganderia: Constraints on the evolution of the Iapetus and Rheic oceans: Geology, v. 40, no. 11, p. 987-990. doi:
VandenBerg, A., 2000, The Tasman Fold Belt system in Victoria: geology and mineralisation of Proterozoic to Carboniferous rocks, Geological Survey of Victoria.
Veevers, J. J., 2004, Gondwanaland from 650–500 Ma assembly through 320 Ma merger in Pangea to 185–100 Ma breakup: supercontinental tectonics via stratigraphy and radiometric dating: Earth-Science Reviews, v. 68, no. 1–2, p. 1-132. doi: http://dx.doi.org/10.1016/j.earscirev.2004.05.002
Vérard, C., 2019, Plate tectonic modelling: review and perspectives: Geological Magazine, v. 156, no. 2, p. 208-241. doi: 10.1017/S0016756817001030
Vérard, C., Hochard, C., Baumgartner, P. O., Stampfli, G. M., and Liu, M., 2015, 3D palaeogeographic reconstructions of the Phanerozoic versus sea-level and Sr-ratio variations: Journal of Palaeogeography, v. 4, no. 1, p. 64-84. doi: https://doi.org/10.3724/SP.J.1261.2015.00068

Vibe, Y., Bunge, H.-P., and Clark, S. R., 2018a, Anomalous subsidence history of the West Siberian Basin as an indicator for episodes of mantle induced dynamic topography: Gondwana Research, v. 53, p. 99-109. doi: 10.1016/j.gr.2017.03.011
Vibe, Y., Friedrich, A. M., Bunge, H. P., and Clark, S. R., 2018b, Correlations of oceanic spreading rates and hiatus surface area in the North Atlantic realm: Lithosphere, v. 10, no. 5, p. 677-684. doi: 10.1130/L736.1
Vine, F. J., and Matthews, D. H., 1963, Magnetic anomalies over oceanic ridges: Nature, v. 199, no. 4897, p. 947-949. doi:
Von Gosen, W., 2003, Thrust tectonics in the North Patagonian Massif (Argentina): implications for a Patagonia plate: Tectonics, v. 22, no. 1. doi:
von Raumer, J. F., and Stampfli, G. M., 2008, The birth of the Rheic Ocean—Early Palaeozoic subsidence patterns and subsequent tectonic plate scenarios: Tectonophysics, v. 461, no. 1-4, p. 9-20. doi:
Waldron, J. W., Barr, S. M., Park, A. F., White, C. E., and Hibbard, J., 2015, Late Paleozoic strike-slip faults in Maritime Canada and their role in the reconfiguration of the northern Appalachian orogen: Tectonics, v. 34, no. 8, p. 1661-1684. doi:
Walker, L. J., Wilkinson, B. H., and Ivany, L. C., 2002, Continental Drift and Phanerozoic Carbonate Accumulation in Shallow-Shelf and Deep-Marine Settings: The Journal of Geology, v. 110, no. 1, p. 75-87. doi: http://10.1086/324318
Wang, B., Faure, M., Shu, L., de Jong, K., Charvet, J., Cluzel, D., Jahn, B.-m., Chen, Y., and Ruffet, G., 2010, Structural and geochronological study of high-pressure metamorphic rocks in the Kekesu section (Northwestern China): implications for the late Paleozoic tectonics of the southern Tianshan: The Journal of Geology, v. 118, no. 1, p. 59-77. doi:
Wang, B., Shu, L., Faure, M., Jahn, B.-m., Cluzel, D., Charvet, J., Chung, S.-L., and Meffre, S., 2011, Paleozoic tectonics of the southern Chinese Tianshan: insights from structural, chronological and geochemical studies of the Heiyingshan ophiolitic mélange (NW China): Tectonophysics, v. 497, no. 1, p. 85-104. doi:
Wang, H., Wu, Y.-B., Gao, S., Qin, Z.-W., Hu, Z.-C., Zheng, J.-P., and Yang, S.-H., 2016, Continental growth through accreted oceanic arc: Zircon Hf–O isotope evidence for granitoids from the Qinling orogen: Geochimica et Cosmochimica Acta, v. 182, p. 109-130. doi:
Wanvming, D., 1995, Geological Features of Ophiolite and Tectonic Significance in the Karakorum-West Kunlun Mts: ACTA PETROLOGICA SINICA, p. S1. doi:
Wegener, A., 1912, Die Entstehung der Kontinente: Geologische Rundschau, v. 3, no. 4, p. 276-292. doi: 10.1007/BF02202896
Weil, A. B., Gutiérrez-Alonso, G., Johnston, S., and Pastor-Galán, D., 2013, Kinematic constraints on buckling a lithospheric-scale orocline along the northern margin of Gondwana: A geologic synthesis: Tectonophysics, v. 582, p. 25-49. doi:
Wessel, P., Luis, J., Uieda, L., Scharroo, R., Wobbe, F., Smith, W., and Tian, D., 2019, The generic mapping tools version 6: Geochemistry, Geophysics, Geosystems. doi: 10.1029/2019GC008515
Wessel, P., Smith, W. H., Scharroo, R., Luis, J., and Wobbe, F., 2013, Generic mapping tools: improved version released: Eos, Transactions American Geophysical Union, v. 94, no. 45, p. 409-410. doi:
Wheeler, P., and White, N., 2002, Measuring dynamic topography: An analysis of Southeast Asia: Tectonics, v. 21, no. 5, p. 4-1-4-26. doi:
White, N., 1993, Recovery of strain rate variation from inversion of subsidence data: Nature, v. 366, no. 6454, p. 449. doi: 10.1038/366449a0
White, N., 1994, An inverse method for determining lithospheric strain rate variation on geological timescales: Earth and Planetary Science Letters, v. 122, no. 3-4, p. 351-371. doi: 10.1016/0012-821X(94)90008-6
Whittaker, J., Afonso, J., Masterton, S., Müller, R., Wessel, P., Williams, S., and Seton, M., 2015, Long-term interaction between mid-ocean ridges and mantle plumes: Nature Geoscience, v. 8, no. 6, p. 479-483. doi: https://doi.org/10.1038/ngeo2437
Williams, S., Flament, N., Dietmar Müller, R., and Butterworth, N., 2015, Absolute plate motions since 130 Ma constrained by subduction zone kinematics: Earth and Planetary Science Letters, v. 418, p. 66-77. doi: https://doi.org/10.1016/j.epsl.2015.02.026
Williams, S., Wright, N. M., Cannon, J., Flament, N., and Müller, R. D., 2020, Reconstructing seafloor age distributions in lost ocean basins: Geoscience Frontiers. doi: https://doi.org/10.1016/j.gsf.2020.06.004
Williams, S., Wright, N. M., Cannon, J., Flament, N., and Müller, R. D., 2021, Reconstructing seafloor age distributions in lost ocean basins: Geoscience Frontiers, v. 12, no. 2, p. 769-780. doi: https://doi.org/10.1016/j.gsf.2020.06.004
Willner, A. P., Thomson, S. N., Kröner, A., Wartho, J.-a., Wijbrans, J. R., and Herve, F., 2005, Time markers for the evolution and exhumation history of a Late Palaeozoic paired metamorphic belt in North–Central Chile (34–35 30′ S): Journal of Petrology, v. 46, no. 9, p. 1835-1858. doi:
Wilson, J. T., 1965, A new class of faults and their bearing on continental drift: Nature, v. 207, no. 4995, p. 343-347. doi:
Wilson, J. T., 1966, Did the Atlantic close and then re-open?: Nature, v. 211, no. 5050, p. 676-681. doi:
Winterbourne, J., White, N., and Crosby, A., 2014, Accurate measurements of residual topography from the oceanic realm: Tectonics, v. 33, no. 6, p. 982-1015. doi: 10.1002/2013TC003372
Woodcock, N., Soper, N., and Strachan, R., 2007, A Rheic cause for the Acadian deformation in Europe: Journal of the Geological Society, v. 164, no. 5, p. 1023-1036. doi:
Worsley, T., Nance, R., and Moody, J., 1982, Plate tectonic episodicity: a deterministic model for periodic “Pangeas”: Eos, Transactions of the American Geophysical Union, v. 65, no. 45, p. 1104. doi:
Worsley, T. R., Nance, D., and Moody, J. B., 1984, Global tectonics and eustasy for the past 2 billion years: Marine Geology, v. 58, no. 3-4, p. 373-400. doi: https://doi.org/10.1016/0025-3227(84)90209-3
Wright, N., Seton, M., Williams, S. E., and Dietmar Müller, R., Global sea level fluctuations and uncertainties through a Wilson cycle based on ocean basin volume reconstructions. EGU General Assembly Conference Abstracts. 2017, Volume 19, p. 6977.
Wu, L., Murphy, J. B., Quesada, C., Li, Z.-X., Waldron, J. W. F., Williams, S., Pisarevsky, S., and Collins, W. J., 2020, The amalgamation of Pangea: Paleomagnetic and geological observations revisited: GSA Bulletin. doi: 10.1130/B35633.1
Wu, Y.-B., and Zheng, Y.-F., 2013, Tectonic evolution of a composite collision orogen: an overview on the Qinling–Tongbai–Hong'an–Dabie–Sulu orogenic belt in central China: Gondwana Research, v. 23, no. 4, p. 1402-1428. doi:
Xiao, W., Han, F., Windley, B. F., Yuan, C., Zhou, H., and Li, J., 2003, Multiple accretionary orogenesis and episodic growth of continents: Insights from the Western Kunlun Range, central Asia: International Geology Review, v. 45, no. 4, p. 303-328. doi:
Xie, X., and Heller, P. L., 2009, Plate tectonics and basin subsidence history: Geological Society of America Bulletin, v. 121, no. 1-2, p. 55-64. doi: 10.1130/B26398.1
Xie, X., Müller, R. D., Li, S., Gong, Z., and Steinberger, B., 2006, Origin of anomalous subsidence along the Northern South China Sea margin and its relationship to dynamic topography: Marine and Petroleum Geology, v. 23, no. 7, p. 745-765. doi: 10.1016/j.marpetgeo.2006.03.004
Xu, J.-f., Wang, Q., and Yu, X.-y., 2000, Geochemistry of high-Mg andesites and adakitic andesite from the Sanchazi block of the Mian-Lue ophiolitic melange in the Qinling Mountains, central China: Evidence of partial melting of the subducted Paleo-Tethyan crust: Geochemical Journal, v. 34, no. 5, p. 359-377. doi:
Xu, J.-f., Zhang, B.-r., and Han, Y.-w., 2008, Geochemistry of the Mian-Lue ophiolites in the Qinling Mountains, central China: Constraints on the evolution of the Qinling orogenic belt and collision of the North and South China Cratons: Journal of Asian Earth Sciences, v. 32, no. 5–6, p. 336-347. doi: http://dx.doi.org/10.1016/j.jseaes.2007.11.004
Xue, F., Lerch, M., Kröner, A., and Reischmann, T., 1996, Tectonic evolution of the East Qinling Mountains, China, in the Palaeozoic: a review and new tectonic model: Tectonophysics, v. 253, no. 3-4, p. 271-284. doi:

Yan, Q., Chen, J., Wang, Z., Yan, Z., Wang, T., Li, Q., Zhang, Z., and Jiang, C., 2007, Tectonic setting and SHRIMP age of volcanic rocks in the Xieyuguan and Caotangou Group: Implications for the North Qinling orogenic belt: Acta Geol. Sinica, v. 81, p. 488-500. doi:
Yan, Q., Chen, J., Wang, Z., Yan, Z., Wang, T., Li, Q., Zhang, Z., and Jiang, C., 2008, Zircon U-Pb and geochemical analyses for leucocratic intrusive rocks in pillow lavas in the Danfeng Group, north Qinling Mountains, China: Science in China Series D: Earth Sciences, v. 51, no. 2, p. 249-262. doi:
Yan, Z., Fu, C., Wang, Z., Yan, Q., Chen, L., and Chen, J., 2016, Late Paleozoic subduction–accretion along the southern margin of the North Qinling terrane, central China: evidence from zircon U-Pb dating and geochemistry of the Wuguan Complex: Gondwana Research, v. 30, p. 97-111. doi:
Yan, Z., Wang, Z., Yan, Q., Wang, T., and Guo, X., 2012, Geochemical constraints on the provenance and depositional setting of the Devonian Liuling Group, East Qinling Mountains, Central China: implications for the tectonic evolution of the Qinling Orogenic Belt: Journal of Sedimentary Research, v. 82, no. 1, p. 9-20. doi:
Yang, J.-S., Robinson, P., Jiang, C.-F., and Xu, Z.-Q., 1996, Ophiolites of the Kunlun Mountains, China and their tectonic implications: Tectonophysics, v. 258, no. 1, p. 215-231. doi:
Yang, W.-S., and Baumgardner, J. R., 2000, A matrix-dependent transfer multigrid method for strongly variable viscosity infinite Prandtl number thermal convection: Geophysical & Astrophysical Fluid Dynamics, v. 92, no. 3-4, p. 151-195. doi: 10.1080/03091920008203715
Yeates, A., Gibson, D., Towner, R., and Crowe, R., 1984, Regional geology of the onshore Canning Basin, WA, *in* Purcell, P. G., ed., *The Canning Basin WA: Proceedings of Geological Society of Australia/Petroleum Exploration Society of Australia Symposium*: Perth, p. 23-57.
Yin, A., and Harrison, T. M., 2000, Geologic evolution of the Himalayan-Tibetan orogen: Annual Review of Earth and Planetary Sciences, v. 28, no. 1, p. 211-280. doi:
Yin, A., and Nie, S., 1993, An indentation model for the North and South China collision and the development of the Tan-Lu and Honam fault systems, eastern Asia: Tectonics, v. 12, no. 4, p. 801-813. doi:
Young, A., Flament, N., Hall, L., and Merdith, A., 2020, The influence of mantle flow on intracontinental basins: Three examples from Australia: Basin Research, v. n/a, no. n/a. doi: https://doi.org/10.1111/bre.12520
Young, A., Flament, N., Maloney, K., Williams, S., Matthews, K., Zahirovic, S., and Müller, R. D., 2019, Global kinematics of tectonic plates and subduction zones since the late Paleozoic Era: Geoscience Frontiers, v. 10, no. 3, p. 989-1013. doi: https://doi.org/10.1016/j.gsf.2018.05.011
Young, A., Flament, N., Williams, S., Merdith, A., and Müller, R. D., *In revision.*, Long-term Phanerozoic sea level change from solid Earth processes: Earth and Planetary Science Letters. doi:
Youngun, Y., and Hsü, K., 1994, Origin of the Kunlun Mountains by arc-arc and arc-continent collisions: Island Arc, v. 3, no. 2, p. 75-89. doi:
Yuan, C., 1999, Magmatism and tectonic evolution of the West Kunlun Mountains: HKU Theses Online (HKUTO). doi:
Yunpeng, D., Dingwu, Z., Guowei, Z., and Bingquan, Z., 1999, Geochemistry of the Caledonian basic volcanic rocks at the south margin of the Qinling orogenic belt, and its tectonic implications: Chinese Journal of Geochemistry, v. 18, no. 3, p. 193-200. doi:
Zahirovic, S., Müller, R. D., Seton, M., and Flament, N., 2015, Tectonic speed limits from plate kinematic reconstructions: Earth and Planetary Science Letters, v. 418, p. 40-52. doi: https://doi.org/10.1016/j.epsl.2015.02.037
Zaiping, Y., and Qingren, M., 1995, Late Paleozoic sedimentary and tectonic evolution of the Shangdan suture zone, eastern Qinling, China: Journal of Southeast Asian Earth Sciences, v. 11, no. 3, p. 237-242. doi:
Zeh, A., and Gerdes, A., 2010, Baltica-and Gondwana-derived sediments in the Mid-German Crystalline Rise (Central Europe): implications for the closure of the Rheic ocean: Gondwana Research, v. 17, no. 2, p. 254-263. doi:
Zeh, A., and Will, T. M., 2010, The mid-German crystalline zone: Pre-Mesozoic Geology of Saxo-Thuringia–from the Cadomian Active Margin to the Variscan Orogen. Schweizerbart, Stuttgart, p. 195-220. doi:
Zhang, G., Meng, Q., and Lai, S., 1995, Tectonics and structure of Qinling orogenic belt: Science in China (Scienctia Sinica) Series B, v. 11, no. 38, p. 1379-1394. doi:
Zhang, N., Zhong, S., and Flowers, R. M., 2012, Predicting and testing continental vertical motion histories since the Paleozoic: Earth and Planetary Science Letters, v. 317, p. 426-435. doi: https://doi.org/10.1016/j.epsl.2011.10.041
Zhang, N., Zhong, S., Leng, W., and Li, Z. X., 2010, A model for the evolution of the Earth's mantle structure since the Early Paleozoic: Journal of Geophysical Research: Solid Earth, v. 115, no. B6. doi: https://doi.org/10.1029/2009JB006896
Zhao, P., Chen, Y., Zhan, S., Xu, B., and Faure, M., 2014, The Apparent Polar Wander Path of the Tarim block (NW China) since the Neoproterozoic and its implications for a long-term Tarim–Australia connection: Precambrian Research, v. 242, p. 39-57. doi:
Zhao, Z., Zhang, Z., Santosh, M., Huang, H., Cheng, Z., and Ye, J., 2015, Early Paleozoic magmatic record from the northern margin of the Tarim Craton: Further insights on the evolution of the Central Asian Orogenic Belt: Gondwana Research, v. 28, no. 1, p. 328-347. doi:
Zheng, L., Gordon, R., Argus, D., DeMets, C., and Kreemer, C., Current plate motion relative to the hotspots and to the mantleAGU Fall Meeting Abstracts2010.
Zhenyu, Y., Xinghua, M., Baochun, H., Zhiming, S., and Yaoxiu, Z., 1998, Apparent polar wander path and tectonic movement of the North China Block in Phanerozoic: Science in China Series D: Earth Sciences, v. 41, no. 2, p. 51-65. doi:
Zhihong, W., 2004, Tectonic evolution of the western Kunlun orogenic belt, western China: Journal of Asian Earth Sciences, v. 24, no. 2, p. 153-161. doi: https://doi.org/10.1016/j.jseaes.2003.10.007
Zhong, S., and Davies, G. F., 1999, Effects of plate and slab viscosities on the geoid: Earth and Planetary Science Letters, v. 170, no. 4, p. 487-496. doi: https://doi.org/10.1016/S0012-821X(99)00124-7
Zhong, S., Gurnis, M., and Hulbert, G., 1993, Accurate determination of surface normal stress in viscous flow from a consistent boundary flux method: Physics of the Earth and Planetary Interiors, v. 78, no. 1, p. 1-8. doi: https://doi.org/10.1016/0031-9201(93)90078-N
Zhong, S., McNamara, A., Tan, E., Moresi, L., and Gurnis, M., 2008, A benchmark study on mantle convection in a 3-D spherical shell using CitcomS: Geochemistry, Geophysics, Geosystems, v. 9, no. 10. doi: https://doi.org/10.1029/2008GC002048
Zhong, S., and Rudolph, M. L., 2015, On the temporal evolution of long-wavelength mantle structure of the E arth since the early P aleozoic: Geochemistry, Geophysics, Geosystems, v. 16, no. 5, p. 1599-1615. doi: https://doi.org/10.1002/2015GC005782
Zhong, S., Zuber, M. T., Moresi, L., and Gurnis, M., 2000, Role of temperature-dependent viscosity and surface plates in spherical shell models of mantle convection: Journal of Geophysical Research: Solid Earth, v. 105, no. B5, p. 11063-11082. doi: https://doi.org/10.1029/2000JB900003
Zhou, S., Subsidence history of the Eromanga Basin, Australia, *In* O'Neil, B. J.(Ed.), The Cooper and Eromanga Basins, Australia, Proceedings of Petroleum Exploration Society of Australia, Society of Petroleum Engineers, Australian Society of Exploration Geophysicists (SA Branches), Adelaide, 1989, PESA, p. 329-335.
Zhou, S., 1993, A 3-D Backstripping Method and Its Application to the Eromanga Basin In Central and Eastern Australia: Geophysical Journal International, v. 112, no. 2, p. 225-243. doi:

Appendix 1. Volumes of submarine LIPs

OLIP	Area[m^2]	Height[m]	Max_depth[m]	Min_depth[m]	Volume[m^3]
Africa	2.56E+11	2093	-5313	-3220	5.36E+14
Agrentine Rise	4.34E+11	284	-5568	-5284	1.23E+14
Agulhas Plateau	1.17E+11	1551	-5425	-3874	1.81E+14
Alpha Ridge	2.85E+11	2902	-6102	-3200	8.28E+14
Antarctic LIP	1.38E+11	1469	-7997	-6528	2.02E+14
Broken Ridge	4.48E+11	500	-4647	-4147	2.24E+14
Canning Basin	1.60E+11	2028	-6405	-4377	3.25E+14
Caribbean	9.03E+11	0	-5003	-5003	0
Central Kerguelen	4.27E+11	-3	-1291	-1294	-1.28E+12
Chagon LIP	1.55E+11	752	-5104	-4352	1.17E+14
Chagon Laccadive Central	4.52E+11	1570	-5039	-3469	7.10E+14
Chagon Laccadive North	2.59E+11	2154	-5039	-2885	5.57E+14
Chagon Laccadive South	1.40E+11	1928	-5107	-3180	2.70E+14
Cocos Ridge	1.13E+11	872	-3946	-3074	9.84E+13
Conrad Rise	3.15E+11	164	-4812	-4648	5.17E+13
Coral Sea LIP	1.29E+11	287	-5023	-4736	3.70E+13
del Cano Rise	1.03E+11	898	-4627	-3730	9.25E+13
Eauripik Rise	1.07E+11	1480	-4161	-2681	1.58E+14
Elan Bank	1.40E+11	333	-5096	-4763	4.68E+13
Hess	1.18E+11	1476	-5518	-4042	1.75E+14
Hikurangi	2.98E+11	1732	-6231	-4499	5.17E+14
Hikurangi pt2	1.05E+11	28	-4467	-4439	2.94E+12
Iceland	3.56E+11	1338	-1428	-90	4.76E+14
Kerguelen Plateau	1.40E+11	333	-5096	-4763	4.68E+13
madagascar	4.45E+11	1617	-5029	-3412	7.20E+14
Manihiki	7.83E+11	789	-5727	-4938	6.18E+14
Mariana Basin	3.42E+11	-427	-5964	-6391	-1.46E+14
Mendelev Ridge	1.14E+11	1280	-4646	-3366	1.46E+14
Mozambique Ridge	2.10E+11	2502	-6524	-4022	5.25E+14
Nauru Basin	5.11E+11	-602	-4835	-5437	-3.08E+14
Nazca Ridge	2.28E+11	366	-4470	-4104	8.36E+13
Newfoundland Ridge	1.30E+11	227	-6244	-6017	2.95E+13
Ninetyeast Ridge	1.11E+11	2211	-4382	-2171	2.44E+14
North Atlantic Igneous Province pt1	3.07E+11	-893	-3777	-4670	-2.74E+14
North Atlantic Igneous Province pt2	1.29E+11	-1817	-4038	-5855	-2.35E+14
North Kerguelen	4.06E+11	940	-5172	-4232	3.81E+14
Ontong	1.88E+12	346	-4581	-4235	6.50E+14
Pacific SeaMounts pt1	1.44E+11	154	-5280	-5126	2.22E+13
PacificSeaMounts pt2	1.67E+11	1360	-5513	-4153	2.27E+14
PacificSeaMounts pt3	2.54E+11	1701	-5880	-4179	4.32E+14
Pigafetta Basin	2.22E+11	-255	-5922	-6177	-5.66E+13
South Atlantic margin - Africa	1.54E+11	-4676	-6050	-10726	-7.22E+14
South Atlantic margin - South America	6.52E+11	-2831	-7779	-10610	-1.85E+15
Shatsky	3.60E+11	847	-6214	-5367	3.05E+14
Sierra Leone Rise	1.59E+11	1454	-6227	-4773	2.31E+14
Southern Kerguelen	4.35E+11	1509	-6075	-4566	6.56E+14
Tutamounts seamounts	3.33E+11	1652	-4690	-3038	5.49E+14

West Pacific LIP	2.16E+11	2648	-6261	-3613	5.73E+14

Appendix 2. Stratigraphic thickness, age data and lithological inputs for backstripping

Cooper Basin wells

Well identifier	Formation	Geological age (Ma)	Top depth (MD)	Base depth (MD)	Water depth min (m)	Water depth max (m)	Sandstone %	Siltstone %	Shale %	Conglomerate %	Coal %	Limestone %
Beanbush_1	Basement	303.8	3700	3700	0	50	1	0	0	0	0	0
Beanbush_1	Merrimelia Formation	298	3542	3700	0	50	0.8	0.05	0.05	0.1	0	0
Beanbush_1	Patchawarra Formation	276.5	3297	3542	0	50	0.8	0.05	0.05	0.1	0	0
Beanbush_1	Murteree Shale	274	3277	3297	0	50	0.35	0.3	0.3	0	0.05	0
Beanbush_1	Epsilon Formation	270	3259	3277	0	50	0.33	0.33	0.33	0	0	0.01
Beanbush_1	Toolachee Formation	252.3	3202	3259	0	50	0.05	0.25	0.65	0	0	0.05
Beanbush_1	Callamurra Member	250	3030	3202	0	50	0.05	0.05	0.85	0.05	0	0
Beanbush_1	Paning Member	249	2925	3030	0	50	0.24	0.24	0.5	0	0	0.02
Beanbush_1	Wimma Sandstone	247.6	2811	2925	0	50	0.45	0.45	0.1	0	0	0
Beanbush_1	Nappamerri Group	236.5	2712	2811	0	50	0.4	0.4	0.1	0.05	0.05	0
Beanbush_1	Cuddapan Formation	202.1	2645	2712	0	50	0.34	0.33	0.33	0	0	0
Beanbush_1	Hutton Formation	168.7	2414	2645	0	50	0.5	0.25	0.25	0	0	0
Beanbush_1	Birkhead Formation	165.5	2322	2414	0	50	0.8	0.1	0	0.1	0	0
Beanbush_1	Adori Sandstone	150.5	2301	2322	0	50	0.375	0.375	0.2	0	0.05	0
Beanbush_1	Westbourne Formation	145	2149	2301	0	50	0.98	0.01	0.01	0	0	0
Beanbush_1	Namur Sandstone	143.2	2088	2149	0	50	0.73	0.26	0.01	0	0	0
Beanbush_1	Murta Formation	134.7	2024	2088	0	50	0.3	0.3	0.3	0	0.1	0
Beanbush_1	Cadna-owie Formation	126.3	1947	2024	0	50	0.81	0.19	0	0	0	0
Beanbush_1	Bulldog Shale	111.3	1494	1947	0	50	0.55	0.44	0.01	0	0	0
Beanbush_1	Toolebuc Formation	104.4	1473	1494	0	50	0.15	0.8	0.05	0	0	0
Beanbush_1	Allaru Mudstone	102.4	1274	1473	0	50	0.25	0.05	0	0	0.7	0
Beanbush_1	Mackunda Formation	101.5	1156	1274	0	50	0.57	0.34	0.06	0	0.03	0
Beanbush_1	Winton Formation	94.6	243	1156	0	200	0	0.95	0.05	0	0	0
Beanbush_1	Eyre Formation	42	165	243	60	130	0.23	0.43	0.19	0	0.15	0
Beanbush_1	Namba Formation	12.5	46	165	30	120	0.25	0.66	0.09	0	0	0
Beanbush_1	Recent	0	5	46	30	140	0	0	1	0	0	0

Boston_1	Basement	303.8	3756	3756	0	50	1	0	0	0	0	0
Boston_1	Tirrawarra Sandstone	295.5	3697	3756	0	50	0.6	0	0.2	0.1	0.1	0
Boston_1	Patchawarra Formation	276.5	3199	3697	0	50	0.3	0.3	0.3	0	0.1	0
Boston_1	Murteree Shale	274	3122	3199	0	50	0.1	0.45	0.45	0	0	0
Boston_1	Epsilon Formation	270	2982	3122	0	50	0.5	0.2	0.2	0	0.1	0
Boston_1	Roseneath Shale	266.6	2914	2982	0	50	0.2	0.4	0.4	0	0	0
Boston_1	Daralingie Formation	262.5	2804	2914	0	50	0.3	0.3	0.3	0	0.1	0
Boston_1	Toolachee Formation	252.3	2645	2804	0	50	0.3	0.3	0.3	0	0.1	0
Boston_1	Nappamerri Group	236.5	2219	2645	0	50	0.01	0.24	0.75	0	0	0
Boston_1	Poolowanna Formation	174.2	2199	2219	0	50	0.2375	0.2375	0.2375	0.2375	0.05	0
Boston_1	Hutton Formation	168.7	2100	2199	0	50	0.98	0.01	0.01	0	0	0
Boston_1	Birkhead Formation	165.5	2026	2100	0	50	0.375	0.375	0.2	0	0.05	0
Boston_1	Adori Sandstone	150.5	2002	2026	0	50	0.8	0.1	0	0.1	0	0
Boston_1	Westbourne Formation	145	1851	2002	0	50	0.5	0.25	0.25	0	0	0
Boston_1	Namur Sandstone	143.2	1782	1851	0	50	0.34	0.33	0.33	0	0	0
Boston_1	Murta Formation	134.7	1724	1782	0	50	0.4	0.4	0.1	0.05	0.05	0
Boston_1	Cadna-owie Formation	126.3	1636	1724	0	50	0.45	0.45	0.1	0	0	0
Boston_1	Bulldog Shale	111.3	1237	1636	0	50	0.24	0.24	0.5	0	0	0.02
Boston_1	Toolebuc Formation	104.4	1132	1237	0	50	0.05	0.05	0.85	0.05	0	0
Boston_1	Allaru Mudstone	102.4	888	1132	0	50	0.05	0.25	0.65	0	0	0.05
Boston_1	Mackunda Formation	101.5	838	888	0	50	0.33	0.33	0.33	0	0	0.01
Boston_1	Winton Formation	94.6	9	838	0	200	0.28	0.6	0	0	0.02	0
Boston_1	Recent	0	8	9	30	140	1	0	0.1	0	0	0
Bulyeroo_1	Basement	295.5	3484	3484	0	50	1	0	0	0	0	0
Bulyeroo_1	Patchawarra Formation	276.5	3167	3484	0	50	0.16	0.17	0.66	0	0.01	0
Bulyeroo_1	Murteree Shale	274	3097	3167	0	50	0.1	0.45	0.45	0	0	0
Bulyeroo_1	Epsilon Formation	270	2975	3097	0	50	0.2	0.25	0.53	0	0.02	0
Bulyeroo_1	Roseneath Shale	266.6	2915	2975	0	50	0.2	0.4	0.4	0	0	0
Bulyeroo_1	Daralingie Formation	262.5	2814	2915	0	50	0.12	0.42	0.45	0	0.01	0
Bulyeroo_1	Toolachee Formation	252.3	2719	2814	0	50	0.3	0.3	0.3	0	0.1	0
Bulyeroo_1	Nappamerri Group	236.5	2322	2719	0	50	0.07	0.3	0.63	0	0	0
Bulyeroo_1	Poolowanna Formation	174.2	2239	2322	0	50	0.2375	0.2375	0.2375	0.2375	0.05	0

Bulyeroo_1	Hutton Formation	168.7	2182	2239	0	50	0.98	0.01	0.01	0	0	0
Bulyeroo_1	Birkhead Formation	165.5	2096	2182	0	50	0.375	0.375	0.2	0	0.05	0
Bulyeroo_1	Adori Sandstone	150.5	2009	2096	0	50	0.8	0.1	0	0.1	0	0
Bulyeroo_1	Westbourne Formation	145	1928	2009	0	50	0.5	0.25	0.25	0	0	0
Bulyeroo_1	Namur Sandstone	143.2	1866	1928	0	50	0.34	0.33	0.33	0	0	0
Bulyeroo_1	McKinlay Member	140.1	1856	1866	0	50	0	0	1	0	0	0
Bulyeroo_1	Murta Formation	134.7	1801	1856	0	50	0.4	0.4	0.1	0.05	0.05	0
Bulyeroo_1	Cadna-owie Formation	126.3	1712	1801	0	50	0.45	0.45	0.1	0	0	0
Bulyeroo_1	Allaru Mudstone	102.4	1042	1712	0	50	0.3	0.3	0.4	0	0	0
Bulyeroo_1	Mackunda Formation	101.5	946	1042	0	50	0.33	0.33	0.33	0	0	0.01
Bulyeroo_1	Winton Formation	94.6	152	946	0	200	0.28	0.6	0.1	0	0.02	0
Bulyeroo_1	Eyre Formation	42	85	152	60	130	0.8	0.05	0.05	0.1	0	0
Bulyeroo_1	Namba Formation	12.5	55	85	30	120	0.8	0.05	0.05	0.1	0	0
Bulyeroo_1	Recent	0	3	55	30	140	1	0	0	0	0	0
Burley_2	Basement	303.8	3662	3662	0	50	1	0	0	0	0	0
Burley_2	Merrimelia Formation	298	3613	3662	0	50	0.25	0.25	0.25	0.25	0	0
Burley_2	Basement	295.5	3590	3613	0	50	0.6	0	0.2	0.1	0.1	0
Burley_2	Patchawarra Formation	276.5	3196	3590	0	50	0.16	0.17	0.66	0	0.01	0
Burley_2	Murteree Shale	274	3118	3196	0	50	0.1	0.45	0.45	0	0	0
Burley_2	Epsilon Formation	270	2978	3118	0	50	0.2	0.25	0.53	0	0.02	0
Burley_2	Roseneath Shale	266.6	2919	2978	0	50	0.2	0.4	0.4	0	0	0
Burley_2	Daralingie Formation	262.5	2830	2919	0	50	0.12	0.42	0.45	0	0.01	0
Burley_2	Toolachee Formation	252.3	2673	2830	0	50	0.5	0.21	0.19	0	0.1	0
Burley_2	Nappamerri Group	236.5	2281	2673	0	50	0.07	0.3	0.63	0	0	0
Burley_2	Poolowanna Formation	174.2	2249	2281	0	50	0.2375	0.2375	0.2375	0.2375	0.05	0
Burley_2	Hutton Formation	168.7	2118	2249	0	50	0.98	0.01	0.01	0	0	0
Burley_2	Birkhead Formation	165.5	2053	2118	0	50	0.375	0.375	0.2	0	0.05	0
Burley_2	Adori Sandstone	150.5	2011	2053	0	50	0.8	0.1	0	0.1	0	0
Burley_2	Westbourne Formation	145	1875	2011	0	50	0.5	0.25	0.25	0	0	0
Burley_2	Namur Sandstone	143.2	1805	1875	0	50	0.34	0.33	0.33	0	0	0
Burley_2	McKinlay Member	140.1	1797	1805	0	50	0	0	1	0	0	0
Burley_2	Murta Formation	134.7	1740	1797	0	50	0.4	0.4	0.1	0.05	0.05	0

Burley_2	Cadna-owie Formation	126.3	1650	1740	0	50	0.45	0.45	0.1	0	0	0
Burley_2	Bulldog Shale	111.3	1256	1650	0	50	0.24	0.24	0.5	0	0	0.02
Burley_2	Toolebuc Formation	104.4	1251	1256	0	50	0.075	0.075	0.8	0.05	0	0
Burley_2	Allaru Mudstone	102.4	976	1251	0	50	0	0.35	0.6	0	0	0.05
Burley_2	Mackunda Formation	101.5	884	976	0	50	0.33	0.33	0.33	0	0	0.01
Burley_2	Winton Formation	94.6	109	884	0	200	0.28	0.6	0.1	0	0.02	0
Burley_2	Eyre Formation	42	58	109	60	130	0.8	0.05	0.05	0.1	0	0
Burley_2	Namba Formation	12.5	38	58	30	120	0.8	0.05	0.05	0.1	0	0
Burley_2	Recent	0	7	38	30	140	1	0	0	0	0	0
Dashwood_1	Basement	295.5	3904	3904	0	50	1	0	0	0	0	0
Dashwood_1	Patchawarra Formation	276.5	3299	3904	0	50	0.3	0.3	0.3	0	0.1	0
Dashwood_1	Murteree Shale	274	3212	3299	0	50	0.1	0.45	0.45	0	0	0
Dashwood_1	Epsilon Formation	270	3064	3212	0	50	0.5	0.2	0.2	0	0.1	0
Dashwood_1	Roseneath Shale	266.6	3028	3064	0	50	0.2	0.4	0.4	0	0	0
Dashwood_1	Daralingie Formation	262.5	2952	3028	0	50	0.3	0.3	0.3	0	0.1	0
Dashwood_1	Toolachee Formation	252.3	2827	2952	0	50	0.3	0.3	0.3	0	0.1	0
Dashwood_1	Nappamerri Group	236.5	2381	2827	0	50	0.01	0.24	0.75	0	0	0
Dashwood_1	Poolowanna Formation	174.2	2361	2381	0	50	0.2375	0.2375	0.2375	0.2375	0.05	0
Dashwood_1	Hutton Formation	168.7	2239	2361	0	50	0.98	0.01	0.01	0	0	0
Dashwood_1	Birkhead Formation	165.5	2168	2239	0	50	0.375	0.375	0.2	0	0.05	0
Dashwood_1	Adori Sandstone	150.5	2134	2168	0	50	0.8	0.1	0	0.1	0	0
Dashwood_1	Westbourne Formation	145	1997	2134	0	50	0.5	0.25	0.25	0	0	0
Dashwood_1	Namur Sandstone	143.2	1935	1997	0	50	0.34	0.33	0.33	0	0	0
Dashwood_1	Murta Formation	134.7	1876	1935	0	50	0.4	0.4	0.1	0.05	0.05	0
Dashwood_1	Cadna-owie Formation	126.3	1789	1876	0	50	0.45	0.45	0.1	0	0	0
Dashwood_1	Bulldog Shale	111.3	1425	1789	0	50	0.24	0.24	0.5	0	0	0.02
Dashwood_1	Toolebuc Formation	104.4	1351	1425	0	50	0.05	0.05	0.85	0.05	0	0
Dashwood_1	Allaru Mudstone	102.4	1118	1351	0	50	0.05	0.25	0.65	0	0	0.05
Dashwood_1	Mackunda Formation	101.5	985	1118	0	50	0.33	0.33	0.33	0	0	0.01
Dashwood_1	Winton Formation	94.6	8	985	0	200	0.5	0.3	0.1	0.08	0.02	0
Dashwood_1	Recent	0	7	8	30	140	1	0	0	0	0	0
Encounter_1	Basement	303.8	4005	4005	0	50	1	0	0	0	0	0

Encounter_1	Basement	295.5	3772	4005	0	50	0.6	0	0.2	0.1	0.1	0
Encounter_1	Patchawarra Formation	276.5	3568	3617	0	50	0.56	0.38	0.04	0	0.02	0
Encounter_1	Murteree Shale	274	3492	3568	0	50	0.1	0.45	0.45	0	0	0
Encounter_1	Epsilon Formation	270	3369	3492	0	50	0.27	0.3	0.42	0	0.01	0
Encounter_1	Roseneath Shale	266.6	3175	3369	0	50	0.2	0.4	0.4	0	0	0
Encounter_1	Daralingie Formation	262.5	3072	3175	0	50	0.05	0.24	0.67	0	0.04	0
Encounter_1	Toolachee Formation	252.3	2842	3072	0	50	0.3	0.3	0.3	0	0.1	0
Encounter_1	Callamurra Member	250	2494	2842	0	50	0.1	0.45	0.45	0	0	0
Encounter_1	Nappamerri Group	236.5	2318	2494	0	50	0.01	0.24	0.75	0	0	0
Encounter_1	Poolowanna Formation	174.2	2294	2318	0	50	0.2375	0.2375	0.2375	0.2375	0.05	0
Encounter_1	Hutton Formation	168.7	2205	2294	0	50	0.98	0.01	0.01	0	0	0
Encounter_1	Birkhead Formation	165.5	2120	2205	0	50	0.375	0.375	0.2	0	0.05	0
Encounter_1	Adori Sandstone	150.5	2088	2120	0	50	0.8	0.1	0	0.1	0	0
Encounter_1	Westbourne Formation	145	1988	2088	0	50	0.5	0.25	0.25	0	0	0
Encounter_1	Namur Sandstone	143.2	1915	1988	0	50	0.34	0.33	0.33	0	0	0
Encounter_1	Murta Formation	134.7	1841	1915	0	50	0.4	0.4	0.1	0.05	0.05	0
Encounter_1	Cadna-owie Formation	126.3	1749	1841	0	50	0.45	0.45	0.1	0	0	0
Encounter_1	Bulldog Shale	111.3	1340	1749	0	50	0.24	0.24	0.5	0	0	0.02
Encounter_1	Toolebuc Formation	104.4	1204	1340	0	50	0.05	0.05	0.85	0.05	0	0
Encounter_1	Allaru Mudstone	102.4	1034	1204	0	50	0.05	0.3	0.6	0	0	0.05
Encounter_1	Mackunda Formation	101.5	833	1034	0	50	0.33	0.33	0.33	0	0	0.01
Encounter_1	Winton Formation	94.6	8	833	0	200	0.45	0.35	0.1	0.08	0.02	0
Encounter_1	Recent	0	8	8	30	140	1	0	0	0	0	0
Halifax_1	Basement	303.8	4501	4501	0	50	1	0	0	0	0	0
Halifax_1	Tirrawarra Sandstone	295.5	4236	4501	0	50	0.6	0	0.2	0.1	0.1	0
Halifax_1	Patchawarra Formation	276.5	3774	4236	0	50	0.3	0.3	0.3	0	0.1	0
Halifax_1	Murteree Shale	274	3696	3774	0	50	0.1	0.45	0.45	0	0	0
Halifax_1	Epsilon Formation	270	3557	3662	0	50	0.5	0.2	0.2	0	0.1	0
Halifax_1	Roseneath Shale	266.6	3319	3557	0	50	0.2	0.4	0.4	0	0	0
Halifax_1	Daralingie Formation	262.5	3191	3319	0	50	0.3	0.3	0.3	0	0.1	0
Halifax_1	Toolachee Formation	252.3	2912	3191	0	50	0.3	0.3	0.3	0	0.1	0
Halifax_1	Nappamerri Group	236.5	2314	2912	0	50	0.01	0.24	0.75	0	0	0

Halifax_1	Poolowanna Formation	174.2	2290	2314	0	50	0.2375	0.2375	0.2375	0.2375	0.05	0
Halifax_1	Hutton Formation	168.7	2202	2290	0	50	0.98	0.01	0.01	0	0	0
Halifax_1	Birkhead Formation	165.5	2131	2202	0	50	0.375	0.375	0.2	0	0.05	0
Halifax_1	Adori Sandstone	150.5	2111	2131	0	50	0.8	0.1	0	0.1	0	0
Halifax_1	Westbourne Formation	145	1973	2111	0	50	0.5	0.25	0.25	0	0	0
Halifax_1	Namur Sandstone	143.2	1888	1973	0	50	0.34	0.33	0.33	0	0	0
Halifax_1	Murta Formation	134.7	1816	1888	0	50	0.4	0.4	0.1	0.05	0.05	0
Halifax_1	Cadna-owie Formation	126.3	1722	1816	0	50	0.45	0.45	0.1	0	0	0
Halifax_1	Bulldog Shale	111.3	1329	1722	0	50	0.24	0.24	0.5	0	0	0.02
Halifax_1	Toolebuc Formation	104.4	1182	1329	0	50	0.05	0.05	0.85	0.05	0	0
Halifax_1	Allaru Mudstone	102.4	985	1182	0	50	0.05	0.3	0.6	0	0	0.05
Halifax_1	Mackunda Formation	101.5	848	985	0	50	0.33	0.33	0.33	0	0	0.01
Halifax_1	Winton Formation	94.6	8	848	0	200	0.45	0.35	0.1	0.08	0.02	0
Halifax_1	Recent	0	8	8	30	140	1	0	0	0	0	0
Holdfast_1	Basement	303.8	3892	3892	0	50	1	0	0	0	0	0
Holdfast_1	Tirrawarra Sandstone	295.5	3777	3892	0	50	0.6	0	0.2	0.1	0.1	0
Holdfast_1	Patchawarra Formation	276.5	3430	3777	0	50	0.56	0.38	0.04	0	0.02	0
Holdfast_1	Murteree Shale	274	3341	3430	0	50	0.1	0.45	0.45	0	0	0
Holdfast_1	Epsilon Formation	270	3172	3341	0	50	0.27	0.3	0.42	0	0.01	0
Holdfast_1	Roseneath Shale	266.6	3083	3172	0	50	0.2	0.4	0.4	0	0	0
Holdfast_1	Daralingie Formation	262.5	2969	3083	0	50	0.05	0.24	0.67	0	0.04	0
Holdfast_1	Toolachee Formation	252.3	2796	2969	0	50	0.3	0.3	0.3	0	0.1	0
Holdfast_1	Nappamerri Group	236.5	2296	2796	0	50	0.01	0.24	0.75	0	0	0
Holdfast_1	Poolowanna Formation	174.2	2272	2296	0	50	0.2375	0.2375	0.2375	0.2375	0.05	0
Holdfast_1	Hutton Formation	168.7	2155	2272	0	50	0.98	0.01	0.01	0	0	0
Holdfast_1	Birkhead Formation	165.5	2081	2155	0	50	0.375	0.375	0.2	0	0.05	0
Holdfast_1	Adori Sandstone	150.5	2058	2081	0	50	0.8	0.1	0	0.1	0	0
Holdfast_1	Westbourne Formation	145	1919	2058	0	50	0.5	0.25	0.25	0	0	0
Holdfast_1	Namur Sandstone	143.2	1852	1919	0	50	0.34	0.33	0.33	0	0	0
Holdfast_1	Murta Formation	134.7	1777	1852	0	50	0.4	0.4	0.1	0.05	0.05	0
Holdfast_1	Cadna-owie Formation	126.3	1686	1777	0	50	0.45	0.45	0.1	0	0	0
Holdfast_1	Bulldog Shale	111.3	1285	1686	0	50	0.24	0.24	0.5	0	0	0.02

Holdfast_1	Toolebuc Formation	104.4	1187	1285	0	50	0.05	0.05	0.85	0.05	0	0
Holdfast_1	Allaru Mudstone	102.4	959	1187	0	50	0.05	0.3	0.6	0	0	0.05
Holdfast_1	Mackunda Formation	101.5	903	959	0	50	0.33	0.33	0.33	0	0	0.01
Holdfast_1	Winton Formation	94.6	31	903	0	200	0.45	0.35	0.1	0.08	0.02	0
Holdfast_1	Recent	0	7	31	30	140	1	0	0	0	0	0
Kirby_1	Basement	303.8	3866	3866	0	50	1	0	0	0	0	0
Kirby_1	Merrimelia Formation	298	3808	3866	0	50	0.25	0.25	0.25	0.25	0	0
Kirby_1	Basement	295.5	3770	3808	0	50	0.6	0	0.2	0.1	0.1	0
Kirby_1	Patchawarra Formation	276.5	3089	3770	0	50	0.56	0.38	0.04	0	0.02	0
Kirby_1	Murteree Shale	274	3019	3089	0	50	0.1	0.45	0.45	0	0	0
Kirby_1	Epsilon Formation	270	2869	3019	0	50	0.27	0.3	0.42	0	0.01	0
Kirby_1	Roseneath Shale	266.6	2813	2869	0	50	0.2	0.4	0.4	0	0	0
Kirby_1	Daralingie Formation	262.5	2732	2813	0	50	0.05	0.24	0.67	0	0.04	0
Kirby_1	Toolachee Formation	252.3	2653	2732	0	50	0.35	0.25	0.31	0	0.09	0
Kirby_1	Nappamerri Group	236.5	2209	2653	0	50	0.09	0.26	0.65	0	0	0
Kirby_1	Hutton Formation	168.7	2054	2209	0	50	0.98	0.01	0.01	0	0	0
Kirby_1	Birkhead Formation	165.5	1977	2054	0	50	0.375	0.375	0.2	0	0.05	0
Kirby_1	Adori Sandstone	150.5	1954	1977	0	50	0.8	0.1	0	0.1	0	0
Kirby_1	Westbourne Formation	145	1812	1954	0	50	0.5	0.25	0.25	0	0	0
Kirby_1	Namur Sandstone	143.2	1756	1812	0	50	0.34	0.33	0.33	0	0	0
Kirby_1	McKinlay Member	140.1	1739	1756	0	50	0	0	1	0	0	0
Kirby_1	Murta Formation	134.7	1681	1740	0	50	0.4	0.4	0.1	0.05	0.05	0
Kirby_1	Cadna-owie Formation	126.3	1587	1681	0	50	0.45	0.45	0.1	0	0	0
Kirby_1	Bulldog Shale	111.3	1134	1587	0	50	0.24	0.24	0.5	0	0	0.02
Kirby_1	Toolebuc Formation	104.4	1127	1134	0	50	0.05	0.05	0.85	0.05	0	0
Kirby_1	Allaru Mudstone	102.4	913	1128	0	50	0.05	0.3	0.6	0	0	0.05
Kirby_1	Mackunda Formation	101.5	832	913	0	50	0.33	0.33	0.33	0	0	0.01
Kirby_1	Winton Formation	94.6	6	832	0	200	0.45	0.35	0.1	0.08	0.02	0
Kirby_1	Recent	0	6	6	30	140	1	0	0	0	0	0
Marengo_1	Basement	257.8	2977	2977	0	50	0	0	0	0	0	0
Marengo_1	Toolachee Formation	252.3	2924	2977	0	50	0.32	0.26	0.36	0	0.06	0
Marengo_1	Callamurra Member	250	2887	2924	0	50	0.1	0.45	0.45	0	0	0

Marengo_1	Paning Member	249	2828	2887	0	50	0.4	0.3	0.3	0	0	0
Marengo_1	Wimma Sandstone	247.6	2742	2828	0	50	0.5	0.25	0.25	0	0	0
Marengo_1	Doonmulla Member	240	2639	2742	0	50	0.6	0.2	0.2	0	0	0
Marengo_1	Nappamerri Group	236.5	2563	2639	0	50	0.2	0.7	0	0	0.1	0
Marengo_1	Cuddapan Formation	202.1	2543	2563	0	50	0.34	0.62	0.04	0	0	0
Marengo_1	Poolowanna Formation	174.2	2420	2543	0	50	0.3	0.3	0.3	0.05	0.05	0
Marengo_1	Hutton Formation	168.7	2216	2420	0	50	0.98	0.01	0.01	0	0	0
Marengo_1	Birkhead Formation	165.5	2119	2216	0	50	0.375	0.375	0.2	0	0.05	0
Marengo_1	Adori Sandstone	150.5	2087	2119	0	50	0.8	0.1	0	0.1	0	0
Marengo_1	Westbourne Formation	145	1984	2087	0	50	0.5	0.25	0.25	0	0	0
Marengo_1	Namur Sandstone	143.2	1929	1984	0	50	0.34	0.33	0.33	0	0	0
Marengo_1	Murta Formation	134.7	1853	1929	0	50	0.4	0.25	0.25	0	0.1	0
Marengo_1	Cadna-owie Formation	126.3	1764	1853	0	50	0.45	0.45	0.1	0	0	0
Marengo_1	Bulldog Shale	111.3	1464	1764	0	50	0.24	0.24	0.5	0	0	0.02
Marengo_1	Toolebuc Formation	104.4	1457	1464	0	50	0.05	0.05	0.85	0.05	0	0
Marengo_1	Allaru Mudstone	102.4	1097	1457	0	50	0.05	0.3	0.6	0	0	0.05
Marengo_1	Mackunda Formation	101.5	1003	1097	0	50	0.33	0.33	0.33	0	0	0.01
Marengo_1	Winton Formation	94.6	6	1003	0	200	0.32	0.32	0.32	0	0.04	0
Marengo_1	Recent	0	6	6	30	140	1	0	0	0	0	0
McLeod_1	Basement	303.8	3806	3806	0	50	1	0	0	0	0	0
McLeod_1	Merrimelia Formation	298	3585	3806	0	50	0.64	0.32	0.04	0	0	0
McLeod_1	Basement	295.5	3558	3585	0	50	0.88	0.12	0	0	0	0
McLeod_1	Patchawarra Formation	276.5	3204	3558	0	50	0.25	0.29	0.41	0	0.05	0
McLeod_1	Murteree Shale	274	3130	3204	0	50	0	0.99	0.01	0	0	0
McLeod_1	Epsilon Formation	270	2974	3130	0	50	0.1	0.24	0.64	0	0.02	0
McLeod_1	Roseneath Shale	266.6	2909	2974	0	50	0	1	0	0	0	0
McLeod_1	Daralingie Formation	262.5	2807	2909	0	50	0.11	0.31	0.57	0	0.01	0
McLeod_1	Toolachee Formation	252.3	2647	2807	0	50	0.26	0.22	0.4	0	0.12	0
McLeod_1	Nappamerri Group	236.5	2224	2647	0	50	0.01	0.24	0.75	0	0	0
McLeod_1	Hutton Formation	168.7	2098	2224	0	50	0.98	0.01	0.01	0	0	0
McLeod_1	Birkhead Formation	165.5	2010	2098	0	50	0.375	0.375	0.2	0	0.05	0
McLeod_1	Adori Sandstone	150.5	1966	2010	0	50	0.8	0.1	0	0.1	0	0

McLeod_1	Westbourne Formation	145	1847	1966	0	50	0.5	0.25	0.25	0	0	0
McLeod_1	Namur Sandstone	143.2	1786	1847	0	50	0.34	0.33	0.33	0	0	0
McLeod_1	McKinlay Member	140.1	1780	1786	0	50	0	0	1	0	0	0
McLeod_1	Murta Formation	134.7	1722	1780	0	50	0.4	0.4	0.1	0.05	0.05	0
McLeod_1	Cadna-owie Formation	126.3	1631	1722	0	50	0.45	0.45	0.1	0	0	0
McLeod_1	Bulldog Shale	111.3	1139	1631	0	50	0.24	0.24	0.5	0	0	0.02
McLeod_1	Toolebuc Formation	104.4	1130	1139	0	50	0.05	0.05	0.85	0.05	0	0
McLeod_1	Allaru Mudstone	102.4	950	1130	0	50	0.05	0.3	0.6	0	0	0.05
McLeod_1	Mackunda Formation	101.5	857	950	0	50	0.33	0.33	0.33	0	0	0.01
McLeod_1	Winton Formation	94.6	40	857	0	200	0.28	0.6	0.1	0	0.02	0
McLeod_1	Recent	0	6	40	103	140	1	0	0	0	0	0
Moomba_27	Basement	295.5	2978	2978	0	50	1	0	0	0	0	0
Moomba_27	Patchawarra Formation	276.5	2752	2978	0	50	0.18	0.4	0.32	0	0.1	0
Moomba_27	Murteree Shale	274	2706	2752	0	50	0.1	0.45	0.45	0	0	0
Moomba_27	Epsilon Formation	270	2643	2706	0	50	0.08	0.28	0.55	0	0.09	0
Moomba_27	Roseneath Shale	266.6	2588	2643	0	50	0.2	0.4	0.4	0	0	0
Moomba_27	Daralingie Formation	262.5	2534	2588	0	50	0.36	0.56	0.04	0	0.04	0
Moomba_27	Toolachee Formation	252.3	2465	2534	0	50	0.48	0.31	0.06	0	0.15	0
Moomba_27	Nappamerri Group	236.5	2255	2465	0	50	0.05	0.75	0.2	0	0	0
Moomba_27	Poolowanna Formation	174.2	2239	2255	0	50	0.2375	0.2375	0.2375	0.2375	0.05	0
Moomba_27	Hutton Formation	168.7	2107	2239	0	50	0.98	0.01	0.01	0	0	0
Moomba_27	Birkhead Formation	165.5	2038	2107	0	50	0.375	0.375	0.2	0	0.05	0
Moomba_27	Adori Sandstone	150.5	1975	2038	0	50	0.8	0.1	0	0.1	0	0
Moomba_27	Westbourne Formation	145	1878	1975	0	50	0.5	0.25	0.25	0	0	0
Moomba_27	Namur Sandstone	143.2	1819	1878	0	50	0.34	0.33	0.33	0	0	0
Moomba_27	McKinlay Member	140.1	1813	1819	0	50	0	0	1	0	0	0
Moomba_27	Murta Formation	134.7	1765	1813	0	50	0.4	0.4	0.1	0.05	0.05	0
Moomba_27	Cadna-owie Formation	126.3	1692	1765	0	50	0.45	0.45	0.1	0	0	0
Moomba_27	Bulldog Shale	111.3	1370	1692	0	50	0.1	0.1	0.8	0	0	0
Moomba_27	Coorikiana Sandstone	105.9	1358	1370	0	50	0.9	0.05	0	0.05	0	0
Moomba_27	Oodnadatta Sandstone	104.6	1239	1358	0	50	1	0	0	0	0	0
Moomba_27	Toolebuc Formation	104.4	1227	1239	0	50	0.05	0.05	0.85	0.05	0	0

Moomba_27	Allaru Mudstone	102.4	1097	1227	0	50	0.05	0.3	0.6	0	0	0.05
Moomba_27	Mackunda Formation	101.5	1026	1097	0	50	0.33	0.33	0.33	0	0	0.01
Moomba_27	Winton Formation	94.6	271	1026	0	200	0.45	0.35	0.1	0.08	0.02	0
Moomba_27	Eyre Formation	42	230	271	60	130	0.8	0.05	0.05	0.1	0	0
Moomba_27	Namba Formation	12.5	59	230	30	120	0.8	0.05	0.05	0.1	0	0
Moomba_27	Recent	0	3	59	30	140	1	0	0	0	0	0
Moothandella_1	Basement	295.5	2675	2675	0	50	0	0	0	0	0	0
Moothandella_1	Patchawarra Formation	276.5	2656	2675	0	50	0.87	0.13	0	0	0	0
Moothandella_1	Toolachee Formation	252.3	2648	2656	0	50	0	0.05	0.35	0	0.6	0
Moothandella_1	Wimma Sandstone	247.6	2547	2648	0	50	0.5	0.25	0.25	0	0	0
Moothandella_1	Doonmulla Member	240	2450	2547	0	50	0.6	0.2	0.2	0	0	0
Moothandella_1	Nappamerri Group	236.5	2404	2450	0	50	0.3	0.6	0	0	0.1	0
Moothandella_1	Cuddapan Formation	202.1	2376	2404	0	50	0.3	0.3	0.4	0	0	0
Moothandella_1	Poolowanna Formation	174.2	2281	2376	0	50	0.3	0.3	0.3	0.05	0.05	0
Moothandella_1	Hutton Formation	168.7	2091	2281	0	50	0.98	0.01	0.01	0	0	0
Moothandella_1	Birkhead Formation	165.5	1994	2091	0	50	0.375	0.375	0.2	0	0.05	0
Moothandella_1	Adori Sandstone	150.5	1969	1994	0	50	0.8	0.1	0	0.1	0	0
Moothandella_1	Westbourne Formation	145	1852	1969	0	50	0.5	0.25	0.25	0	0	0
Moothandella_1	Murta Formation	134.7	1709	1852	0	50	0.4	0.25	0.25	0	0.1	0
Moothandella_1	Cadna-owie Formation	126.3	1670	1709	0	50	0.45	0.45	0.1	0	0	0
Moothandella_1	Bulldog Shale	111.3	1326	1670	0	50	0.24	0.24	0.5	0	0	0.02
Moothandella_1	Toolebuc Formation	104.4	1298	1326	0	50	0.05	0.05	0.85	0.05	0	0
Moothandella_1	Allaru Mudstone	102.4	978	1298	0	50	0.05	0.3	0.6	0	0	0.05
Moothandella_1	Mackunda Formation	101.5	828	978	0	50	0.33	0.33	0.33	0	0	0.01
Moothandella_1	Winton Formation	94.6	6	828	0	200	0.26	0.32	0.32	0	0.08	0.02
Moothandella_1	Recent	0	6	6	30	140	1	0	0	0	0	0
Paning_1	Basement	303.8	3141	3141	0	50	0	0	0	0	0	0
Paning_1	Merrimelia Formation	298	3037	3081	0	50	0.25	0.25	0.25	0.25	0	0
Paning_1	Patchawarra Formation	276.5	2979	3037	0	50	0.26	0.28	0.09	0	0.37	0
Paning_1	Murteree Shale	274	2963	3007	0	50	0.1	0.45	0.45	0	0	0
Paning_1	Epsilon Formation	270	2903	2947	0	50	0.77	0.12	0	0	0.11	0
Paning_1	Toolachee Formation	252.3	2852	2903	0	50	0.24	0.12	0	0	0.64	0

Paning_1	Nappamerri Group	236.5	2372	2852	0	50	0.4	0.45	0.15	0	0	0
Paning_1	Poolowanna Formation	174.2	2321	2372	0	50	0.3	0.3	0.3	0.05	0.05	0
Paning_1	Hutton Formation	168.7	2089	2321	0	50	0.98	0.01	0.01	0	0	0
Paning_1	Birkhead Formation	165.5	1992	2089	0	50	0.375	0.375	0.2	0	0.05	0
Paning_1	Adori Sandstone	150.5	1964	1992	0	50	0.8	0.1	0	0.1	0	0
Paning_1	Westbourne Formation	145	1834	1964	0	50	0.5	0.25	0.25	0	0	0
Paning_1	Namur Sandstone	143.2	1783	1834	0	50	0.34	0.33	0.33	0	0	0
Paning_1	McKinlay Member	140.1	1772	1783	0	50	0	0	1	0	0	0
Paning_1	Murta Formation	134.7	1720	1772	0	50	0.4	0.4	0.1	0.05	0.05	0
Paning_1	Cadna-owie Formation	126.3	1629	1720	0	50	0.45	0.45	0.1	0	0	0
Paning_1	Bulldog Shale	111.3	1204	1629	0	50	0.24	0.24	0.5	0	0	0.02
Paning_1	Toolebuc Formation	104.4	1193	1204	0	50	0.05	0.05	0.85	0.05	0	0
Paning_1	Allaru Mudstone	102.4	983	1193	0	50	0.05	0.3	0.6	0	0	0.05
Paning_1	Mackunda Formation	101.5	853	983	0	50	0.33	0.33	0.33	0	0	0.01
Paning_1	Winton Formation	94.6	47	853	0	200	0.32	0.32	0.32	0	0.04	0
Paning_1	Eyre Formation	42	5	47	60	130	0.8	0.05	0.05	0.1	0	0
Paning_1	Recent	0	5	5	30	140	1	0	0	0	0	0

Canning Basin wells

Well identifier	Formation	Geological age (Ma)	Top depth (MD)	Base depth (MD)	Water depth min (m)	Water depth max (m)	Sand %	Shale %	Siltstone %	Limestone %	Dolostone %
Aquila_1	Basement?	479.9	1740	1740	0	0	1.00				
Aquila_1	Nambeet Fm	474	1554	1740	10	100	0.09	0.40	0.51	0.00	0.00
Aquila_1	Willara Fm	468.2	1169	1554	10	100	0.52	0.20	0.28	0.00	0.00
Aquila_1	Goldwyer Fm	463.9	800	1169	10	100	0.14	0.31	0.56	0.00	0.00
Aquila_1	Nita Fm	456.6	672	800	10	100	0.76	0.00	0.02	0.01	0.21
Aquila_1	Grant Gp	293.1	467	672	0	10	0.21	0.00	0.79	0.00	0.00
Aquila_1	Wallal Sandstone	159.3	340	467	0	20	1.00	0.00	0.00	0.00	0.00
Aquila_1	Alexander Fm	154.8	273	340	0	100	1.00	0.00	0.00	0.00	0.00
Aquila_1	Jarlemai Siltstone	145.1	153	273	20	100	1.00	0.00	0.00	0.00	0.00
Aquila_1	Broome Sandstone	128.6	15	153	0	100	1.00	0.00	0.00	0.00	0.00
Blackstone_1	Yellow Drum Fm	356.8	2967	2967	0	0	1.00				
Blackstone_1	Laurel Fm	349.8	1486	2967	10	100	0.09	0.40	0.15	0.27	0.08
Blackstone_1	Grant Gp	293.1	799	1486	0	10	0.69	0.08	0.22	0.01	0.00
Blackstone_1	Poole Sandstone	291.5	751	799	0	100	0.25	0.36	0.39	0.00	0.00
Blackstone_1	Noonkanbah Fm	278.5	511	751	10	100	0.00	0.70	0.30	0.00	0.00
Blackstone_1	Liveringa Gp	254.4	319	511	0	100	0.20	0.09	0.71	0.00	0.00
Blackstone_1	Blina Shale	248.8	9	319	20	100	0.01	0.17	0.83	0.00	0.00
Blackstone_1	Erskine Sandstone	239.2	5	9	0	10	0.00	0.00	1.00	0.00	0.00
Cow_Bore_1	Base Gumhole	362.3	2925	2925	0	0	1.00				
Cow_Bore_1	Gumhole Fm	359.7	2084	2925	10	100	0.03	0.54	0.09	0.13	0.22
Cow_Bore_1	Yellow Drum Fm	357	1999	2084	20	100	0.04	0.00	0.92	0.04	0.00
Cow_Bore_1	Anderson Fm	336.6	1106	1999	0	10	0.12	0.12	0.59	0.16	0.01
Cow_Bore_1	Grant Gp	293.1	517	1106	0	10	0.78	0.02	0.20	0.01	0.00
Cow_Bore_1	Wallal Sandstone	159.3	320	517	0	20	0.82	0.00	0.18	0.00	0.00
Cow_Bore_1	Jarlemai Siltstone	145.1	115	320	20	100	0.26	0.08	0.66	0.00	0.00
Cow_Bore_1	Broome Sandstone	128.6	12	115	0	100	1.00	0.00	0.00	0.00	0.00
Great_Sandy_1	Base Willara	474	1725	1725	0	0	1.00				
Great_Sandy_1	Willara Fm	468.2	1673	1725	10	100	0.00	0.66	0.00	0.33	0.00
Great_Sandy_1	Goldwyer Fm	463.9	1536	1673	10	100	0.00	0.91	0.00	0.09	0.00

Great_Sandy_1	Nita Fm	456.6	1433	1536	10	100	0.00	0.09	0.04	0.65	0.23
Great_Sandy_1	Tandalgoo Fm	386.1	1098	1433	10	100	0.02	0.49	0.46	0.03	0.00
Great_Sandy_1	Grant Gp	293.1	805	1098	0	10	0.10	0.39	0.50	0.00	0.00
Great_Sandy_1	Poole Sandstone	291.5	702	805	0	100	0.00	0.88	0.12	0.00	0.00
Great_Sandy_1	Wallal Sandstone	159.3	475	702	0	20	0.49	0.02	0.50	0.00	0.00
Great_Sandy_1	Alexander Fm	154.8	403	475	0	100	0.01	0.37	0.63	0.00	0.00
Great_Sandy_1	Jarlemai Siltstone	145.1	321	403	20	100	0.00	0.00	0.99	0.00	0.00
Great_Sandy_1	Broome Sandstone	128.6	10	321	0	100	0.82	0.00	0.17	0.00	0.00
Kambara_1	Dominic Shale	388.4	3147	3147	0	0	1.00				
Kambara_1	Mellinjerie Limestone	377.5	2099	3147	20	100	0.03	0.01	0.02	0.86	0.01
Kambara_1	Laurel Fm	349.8	1568	2099	10	100	0.02	0.19	0.42	0.18	0.00
Kambara_1	Grant Gp	293.1	854	1568	0	10	0.00	0.12	0.12	0.01	0.00
Kambara_1	Poole Sandstone	291.5	809	854	0	100	0.01	0.66	0.20	0.02	0.00
Kambara_1	Noonkanbah Fm	278.5	654	809	10	100	0.01	0.95	0.05	0.00	0.00
Kambara_1	Alexander Fm	154.8	452	654	0	100	0.00	0.00	0.00	0.00	0.00
Kambara_1	Jarlemai Siltstone	145.1	397	452	20	100	1.00	0.00	0.00	0.00	0.00
Kambara_1	Broome Sandstone	128.6	47	397	0	100	1.00	0.00	0.00	0.00	0.00
Kidson_1	Willara Fm	468.2	4413	4413	0	0	1.00				
Kidson_1	Goldwyer Fm	463.9	4279	4413	10	100	0.00	1.00	0.00	0.00	0.00
Kidson_1	Tandalgoo Fm	386.1	1837	4279	10	100	0.34	0.10	0.17	0.00	0.39
Kidson_1	Mellinjerie Limestone	377.5	1572	1837	20	100	0.00	0.00	0.28	0.72	0.00
Kidson_1	Grant Gp	293.1	1477	1572	0	10	0.95	0.00	0.05	0.00	0.00
Kidson_1	Poole Sandstone	291.5	600	1477	0	100	0.77	0.00	0.23	0.00	0.00
Kidson_1	Noonkanbah Fm	278.5	289	600	10	100	0.80	0.00	0.20	0.00	0.00
Kidson_1	Liveringa Gp	254.4	212	289	0	100	0.96	0.00	0.04	0.00	0.00
Lloyd_1	Gumhole Fm	359.7	2005	2005	0	0	1.00				
Lloyd_1	Yellow Drum Fm	357	1877	2005	20	100	0.00	0.00	0.00	1.00	0.00
Lloyd_1	Laurel Fm	349.8	1686	1877	10	100	0.03	0.31	0.08	0.59	0.00
Lloyd_1	Anderson Fm	336.6	1433	1686	0	10	0.19	0.39	0.43	0.00	0.00
Lloyd_1	Grant Gp	293.1	927	1433	0	10	0.76	0.12	0.12	0.00	0.00
Lloyd_1	Nura Nura Mbr	292	874	927	10	100	0.51	0.27	0.22	0.00	0.00
Lloyd_1	Poole Sandstone	291.5	824	874	0	100	0.27	0.26	0.46	0.00	0.00

Lloyd_1	Noonkanbah Fm	278.5	533	824	10	100	0.00	0.87	0.13	0.00	0.00
Lloyd_1	Liveringa Gp	254.4	355	533	0	100	0.00	0.00	1.00	0.00	0.00
Lloyd_1	Blina Shale	248.8	97	355	20	100	0.00	1.00	0.00	0.00	0.00
Lloyd_1	Erskine Sandstone	239.2	5	97	0	10	1.00	0.00	0.00	0.00	0.00
Minjin_1	Dominic Shale	388.4	1849	1849	0	0	1.00				
Minjin_1	Mellinjerie Limestone	377.5	1540	1849	20	100	0.03	0.00	0.00	0.50	0.46
Minjin_1	Grant Gp	293.1	827	1540	0	10	0.12	0.07	0.20	0.00	0.00
Minjin_1	Poole Sandstone	291.5	790	827	0	100	0.01	0.67	0.16	0.06	0.00
Minjin_1	Noonkanbah Fm	278.5	746	790	10	100	0.01	0.88	0.08	0.01	0.00
Minjin_1	Alexander Fm	154.8	518	746	0	100	0.00	0.00	0.00	0.00	0.00
Minjin_1	Jarlemai Siltstone	145.1	442	518	20	100	1.00	0.00	0.00	0.00	0.00
Minjin_1	Broome Sandstone	128.6	53	442	0	100	1.00	0.00	0.00	0.00	0.00
Moogana_1	Base Anderson	348.9	2204	2204	0	0	1.00				
Moogana_1	Anderson Fm	336.6	1993	2204	0	10	0.01	0.41	0.17	0.16	0.24
Moogana_1	Grant Gp	293.1	1167	1993	0	10	0.73	0.06	0.20	0.01	0.00
Moogana_1	Nura Nura Mbr	292	1159	1167	10	100	0.10	0.25	0.21	0.44	0.00
Moogana_1	Poole Sandstone	291.5	1118	1159	0	100	0.18	0.50	0.32	0.00	0.00
Moogana_1	Noonkanbah Fm	278.5	920	1118	10	100	0.02	0.78	0.20	0.00	0.00
Moogana_1	Liveringa Gp	254.4	713	920	0	100	0.91	0.00	0.00	0.00	0.09
Moogana_1	Blina Shale	248.8	636	713	20	100	1.00	0.00	0.00	0.00	0.00
Moogana_1	Wallal Sandstone	159.3	462	636	0	20	1.00	0.00	0.00	0.00	0.00
Moogana_1	Alexander Fm	154.8	412	462	0	100	1.00	0.00	0.00	0.00	0.00
Moogana_1	Jarlemai Siltstone	145.1	388	412	20	100	1.00	0.00	0.00	0.00	0.00
Moogana_1	Broome Sandstone	128.6	5	388	0	100	0.99	0.00	0.01	0.00	0.00
Patience_2	Basement?	479.9	3474	3474	0	0	1.00				
Patience_2	Nambeet Fm	474	3281	3474	10	100	0.91	0.00	0.09	0.00	0.00
Patience_2	Willara Fm	468.2	3158	3281	10	100	0.87	0.03	0.10	0.00	0.00
Patience_2	Goldwyer Fm	463.9	2923	3158	10	100	0.02	0.74	0.24	0.00	0.00
Patience_2	Nibil Fm	447.1	2739	2923	20	100	0.32	0.26	0.41	0.00	0.00
Patience_2	Mallowa Salt	443.4	2425	2739	0	10	0.00	0.00	0.00	0.00	0.00
Patience_2	Sahara Fm	438.5	1805	2425	20	100	0.16	0.30	0.54	0.00	0.00
Patience_2	Tandalgoo Fm	386.1	1633	1805	10	100	0.99	0.00	0.01	0.00	0.00

Patience_2	Mellinjerie Limestone	377.5	1349	1633	20	100	0.04	0.47	0.50	0.00	0.00
Patience_2	Grant Gp	293.1	779	1349	0	10	0.37	0.22	0.41	0.00	0.00
Patience_2	Poole Sandstone	291.5	592	779	0	100	0.42	0.20	0.38	0.00	0.00
Patience_2	Noonkanbah Fm	278.5	406	592	10	100	0.12	0.85	0.03	0.00	0.00
Patience_2	Liveringa Gp	254.4	289	406	0	100	0.03	0.78	0.19	0.00	0.00
Patience_2	Wallal Sandstone	159.3	259	234	0	20	1.00	0.00	0.00	0.00	0.00
Patience_2	Alexander Fm	154.8	234	289	0	100	0.92	0.00	0.08	0.00	0.00
Patience_2	Jarlemai Siltstone	145.1	210	259	20	100	0.00	0.00	1.00	0.00	0.00
Patience_2	Broome Sandstone	128.6	100	210	0	100	0.92	0.07	0.02	0.00	0.00
Percival_1	Goldwyer Fm	463.9	2444	2444	0	0	1.00				
Percival_1	Nita Fm	456.6	2013	2444	10	100	0.19	0.61	0.16	0.02	0.02
Percival_1	Tandalgoo Fm	386.1	1430	2013	10	100	0.65	0.29	0.06	0.00	0.00
Percival_1	Dominic Shale	385.3	1412	1430	10	100	0.30	0.39	0.31	0.00	0.00
Percival_1	Mellinjerie Limestone	377.5	1377	1412	20	100	0.00	0.00	0.00	0.00	0.98
Percival_1	Nullara Limestone	363.4	487	1377	10	100	0.48	0.00	0.00	0.00	0.52
Percival_1	Grant Gp	293.1	5	487	0	10	0.99	0.00	0.00	0.00	0.00
Pictor_1	Basement?	479.9	2138	2138	0	0	1.00				
Pictor_1	Nambeet Fm	474	1932	2138	10	100	0.02	0.32	0.65	0.01	0.00
Pictor_1	Willara Fm	468.2	1415	1932	10	100	0.49	0.13	0.37	0.00	0.00
Pictor_1	Goldwyer Fm	463.9	1041	1415	10	100	0.29	0.10	0.61	0.00	0.00
Pictor_1	Nita Fm	456.6	879	1041	10	100	0.71	0.03	0.26	0.00	0.00
Pictor_1	Tandalgoo Fm	386.1	517	879	10	100	0.19	0.06	0.75	0.00	0.00
Pictor_1	Grant Gp	293.1	108	517	0	10	0.38	0.03	0.27	0.00	0.32
Pictor_1	Wallal Sandstone	159.3	0	108	0	20	1.00	0.00	0.00	0.00	0.00
Puratte_1	Base Gumhole	362.3	3742	3742	0	0	1.00				
Puratte_1	Gumhole Fm	359.7	3073	3742	10	100	0.08	0.00	0.08	0.64	0.19
Puratte_1	Yellow Drum Fm	357	2989	3073	20	100	0.02	0.00	0.01	0.78	0.19
Puratte_1	Laurel Fm	349.8	2938	2989	10	100	0.78	0.00	0.00	0.22	0.00
Puratte_1	Anderson Fm	336.6	2360	2938	0	10	0.25	0.26	0.48	0.00	0.00
Puratte_1	Grant Gp	293.1	1504	2360	0	10	0.61	0.14	0.24	0.00	0.00
Puratte_1	Nura Nura Mbr	292	1496	1504	10	100	0.10	0.30	0.13	0.47	0.00
Puratte_1	Poole Sandstone	291.5	1435	1496	0	100	0.21	0.30	0.48	0.00	0.00

Puratte_1	Noonkanbah Fm	278.5	1016	1435	10	100	0.01	0.67	0.31	0.00	0.00
Puratte_1	Liveringa Gp	254.4	784	1016	0	100	0.23	0.07	0.70	0.00	0.00
Puratte_1	Blina Shale	248.8	549	784	20	100	0.00	0.57	0.43	0.00	0.00
Puratte_1	Erskine Sandstone	239.2	425	549	0	10	0.21	0.78	0.02	0.00	0.00
Puratte_1	Wallal Sandstone	159.3	251	425	0	20	0.77	0.00	0.23	0.00	0.00
Puratte_1	Alexander Fm	154.8	222	251	0	100	0.00	0.99	0.01	0.00	0.00
Puratte_1	Jarlemai Siltstone	145.1	195	222	20	100	0.25	0.75	0.00	0.00	0.00
Puratte_1	Broome Sandstone	128.6	0	195	0	100	1.00	0.00	0.00	0.00	0.00
Wilson_Cliffs_1	Basement?	479.9	3722	3722	0	0	1.00				
Wilson_Cliffs_1	Wilson Cliff Sandstone	473.9	2848	3722	0	100	0.18	0.54	0.21	0.03	0.03
Wilson_Cliffs_1	Goldwyer Fm	463.9	2661	2848	10	100	0.01	0.50	0.49	0.00	0.00
Wilson_Cliffs_1	Nita Fm	456.6	2493	2661	10	100	0.05	0.42	0.50	0.01	0.02
Wilson_Cliffs_1	Tandalgoo Fm	386.1	1094	2493	10	100	0.57	0.01	0.17	0.00	0.24
Wilson_Cliffs_1	Mellinjerie Limestone	377.5	968	1094	20	100	0.00	0.00	0.00	1.00	0.00
Wilson_Cliffs_1	Grant Gp	293.1	579	968	0	10	0.44	0.18	0.38	0.00	0.00
Wilson_Cliffs_1	Poole Sandstone	291.5	373	579	0	100	1.00	0.00	0.00	0.00	0.00
Wilson_Cliffs_1	Noonkanbah Fm	278.5	182	373	10	100	0.00	1.00	0.00	0.00	0.00
Woods_Hills_1	Base Willara	474	1951	1951	0	0	1.00				
Woods_Hills_1	Willara Fm	468.2	1832	1951	10	100	0.03	0.27	0.60	0.07	0.01
Woods_Hills_1	Goldwyer Fm	463.9	1419	1832	10	100	0.01	0.47	0.53	0.00	0.00
Woods_Hills_1	Nita Fm	456.6	1319	1419	10	100	0.30	0.07	0.16	0.43	0.04
Woods_Hills_1	Grant Gp	293.1	448	1319	0	10	0.21	0.39	0.40	0.00	0.00
Woods_Hills_1	Wallal Sandstone	159.3	255	448	0	20	1.00	0.00	0.00	0.00	0.00
Woods_Hills_1	Alexander Fm	154.8	213	255	0	100	1.00	0.00	0.00	0.00	0.00
Woods_Hills_1	Jarlemai Siltstone	145.1	157	213	20	100	1.00	0.00	0.00	0.00	0.00
Woods_Hills_1	Broome Sandstone	128.6	15	157	0	100	0.80	0.00	0.20	0.00	0.00

Southern Carnarvon wells

Well	Formation	Geological age (Ma)	Top Depth (MD)	Base Depth (MD)	Water depth min (m)	Water depth max (m)	Sandstone %	Siltstone %	Shale %	Limestone %	Dolostone %
Burna_1	Callytharra Fm	293	575	575	20	100	0	0.3	0.7	0	0
Burna_1	Cordalia Fm (base Wooramel)	291.3	478	575	100	200	0	0.3	0.7	0	0
Burna_1	Moogooloo Sandstone (upper Wooramel Gp)	287.8	395	478	0	20	0.6	0.3	0.1	0	0
Burna_1	Billidee Fm	281	330	395	20	100	0.6	0.4	0	0	0
Burna_1	Byro Gp	271.5	24	330	0	100	0.2	0.8	0	0	0
Chargoo_1	Callytharra Fm	293	383	383	20	100	0.1	0	0.2	0	0.7
Chargoo_1	Birdrong Sandstone	136.5	366	383	0	100	0.3	0	0	0	0.7
Chargoo_1	Muderong Shale	124.3	360	366	100	200	0	0.9	0	0	0
Chargoo_1	Windalia Radiolarite	113.1	299	360	100	200	0.9	0.1	0	0	0
Chargoo_1	Gearle Siltstone	92.1	142	299	100	200	0.2	0.8	0	0	0
Chargoo_1	Quaternary	0	1	142	20	100	1	0	0	0	0
Coburn_1	Tumblagooda Sandstone	445.1	975	975	0	20	0.2	0.5	0.2	0	0
Coburn_1	Marron Mbr (Ajana Fm)	432.8	912	975	0	20	0.1	0.2	0.7	0	0
Coburn_1	Ajana Fm	435.9	849	912	0	20	0.2	0.2	0.3	0.1	0.2
Coburn_1	Yaringa Fm	433.3	745	849	0	20	0.4	0.1	0.1	0.1	0.2
Coburn_1	Coburn Fm	419.2	579	745	20	100	0.3	0.1	0	0.1	0.4
Coburn_1	Faure Fm	415	507	579	20	100	0.1	0.6	0.2	0	0.1
Coburn_1	Kopke Sandstone	407.6	242	507	0	20	0.9	0	0	0	0
Coburn_1	Birdrong Sandstone	136.5	167	242	0	100	1	0	0	0	0
Coburn_1	Muderong Shale	124.3	164	167	100	200	0	0	1	0	0
Coburn_1	Windalia Radiolarite	113.1	127	164	100	200	1	0	0	0	0
Coburn_1	Gearle Siltstone	92.1	79	127	100	200	0	1	0	0	0
Coburn_1	Toolonga Calcilutite	72.1	22	79	0	100	0	0	0	1	0
Cody_1	Byro Gp	271.5	3088	3088	0	100	0	0	0	0.6	0.4
Cody_1	Kennedy Gp	255.3	2758	3088	0	100	0.1	0.1	0.2	0.2	0.4
Cody_1	Locker Shale	243.3	2233	2758	100	200	0	0.1	0.7	0.2	0.1
Cody_1	Mungaroo Fm	240.3	1678	2233	0	20	0.2	0.4	0.4	0	0
Cody_1	Birdrong Sandstone	136.5	1642	1678	0	100	0.9	0.1	0	0	0

Cody_1	Muderong Shale	124.3	1571	1642	100	200	0	0.2	0.8	0	0
Cody_1	Windalia Radiolarite	113.1	1516	1571	100	200	0.9	0.1	0	0	0
Cody_1	Gearle Siltstone	92.1	1184	1516	100	200	0.1	0.8	0	0	0
Cody_1	Toolonga Calcilutite	72.1	1027	1184	0	100	0	1	0	0	0
Cody_1	Korojon Calcarenite	69.5	1000	1027	0	20	0	1	0	0	0
Cody_1	Cardabia Calcarenite	51.3	818	1000	0	20	0	0.3	0	0.7	0
Cody_1	Giralia Calcarenite	32.4	580	818	0	20	0	0	0	0.9	0.1
Hope_Island_1	Kennedy Gp	255.3	986	986	0	100	0.2	0.2	0.5	0	0.1
Hope_Island_1	Locker Shale	243.3	911	986	100	200	0	0	0.9	0	0.1
Hope_Island_1	Birdrong Sandstone	136.5	890	911	0	100	0.8	0	0	0.1	0.1
Hope_Island_1	Muderong Shale	124.3	838	890	100	200	0	0.1	0.9	0	0
Hope_Island_1	Windalia Radiolarite	113.1	786	838	100	200	0.5	0.5	0	0	0
Hope_Island_1	Gearle Siltstone	92.1	428	786	100	200	0	0.9	0.1	0	0
Hope_Island_1	Toolonga Calcilutite	72.1	352	428	0	100	0.3	0.4	0.2	0.1	0
Kennedy_Range_1	Cordalia Fm (base Wooramel)	291.3	2101	2101	100	200	0	0.1	0.3	0.2	0.4
Kennedy_Range_1	Byro Gp	271.5	519	2101	0	100	0.1	0.6	0.2	0	0
Kennedy_Range_1	Kennedy Gp	255.3	0	519	0	100	0.5	0.5	0	0	0
Remarkable_Hill_1	Quail Fm	327.1	2356	2356	20	100	0	0.2	0.6	0.1	0
Remarkable_Hill_1	Lyons Gp	295.5	888	2356	20	100	0	0.5	0.5	0	0
Remarkable_Hill_1	Callytharra Fm	293	695	888	20	100	0	0.2	0.8	0	0
Remarkable_Hill_1	Cordalia Fm (base Wooramel)	291.3	602	695	100	200	0	0.1	0.9	0	0
Remarkable_Hill_1	Moogooloo Sandstone (upper Wooramel Gp)	287.8	458	602	0	20	0	0.9	0.1	0	0
Remarkable_Hill_1	Billidee Fm	281	273	458	20	100	0	1	0	0	0
Remarkable_Hill_1	Birdrong Sandstone	136.5	256	273	0	100	0.8	0.2	0	0	0
Remarkable_Hill_1	Muderong Shale	124.3	183	256	100	200	0	0	1	0	0
Remarkable_Hill_1	Windalia Radiolarite	113.1	79	183	100	200	0	1	0	0	0
Roberts_Hill_1	Callytharra Fm	293	1171	1171	20	100	0	0	0.9	0.1	0
Roberts_Hill_1	Birdrong Sandstone	136.5	1166	1171	0	100	0.7	0.1	0	0.2	0
Roberts_Hill_1	Muderong Shale	124.3	1143	1166	100	200	0	0	1	0	0
Roberts_Hill_1	Windalia Radiolarite	113.1	1099	1143	100	200	0.6	0.3	0.1	0	0
Roberts_Hill_1	Gearle Siltstone	92.1	505	1099	100	200	0.1	0.9	0	0	0
Roberts_Hill_1	Toolonga Calcilutite	72.1	462	505	0	100	0	0	0.3	0.7	0

Rough_Range_11	Birdrong Sandstone	136.5	1113	1113	0	100	0.2	0	0	0.5	0.3
Rough_Range_11	Muderong Shale	124.3	1077	1113	100	200	0	0.1	0.9	0	0
Rough_Range_11	Windalia Radiolarite	113.1	1037	1077	100	200	0.9	0.1	0	0	0
Rough_Range_11	Gearle Siltstone	92.1	445	1037	100	200	0.1	0.8	0	0	0
Tamala_1	Tumblagooda Sandstone	435.9	1118	1118	0	20	0	0	0	0	1
Tamala_1	Marron Mbr (Ajana Fm)	432.8	1038	1118	0	20	0	0	0	0	1
Tamala_1	Ajana Fm	427.7	867	1038	0	20	0	0	0	0	0.9
Tamala_1	Yaringa Fm	425.4	813	867	0	20	0.1	0	0	0.1	0.9
Tamala_1	Coburn Fm	410.2	510	813	20	100	0	0	0	0	0.9
Tamala_1	Faure Fm	407.1	425	510	20	100	0.5	0	0	0.2	0.3
Tamala_1	Kopke Sandstone	402.1	406	425	0	20	0.6	0.1	0	0.3	0
Tamala_1	Sweeney Mia Fm	395.9	398	406	0	20	0.8	0	0	0.2	0
Tamala_1	Birdrong Sandstone	136.5	390	398	0	100	1	0	0	0	0
Tamala_1	Muderong Shale	124.3	348	390	100	200	1	0	0	0	0
Tamala_1	Windalia Radiolarite	113.1	263	348	100	200	1	0	0	0	0
Tamala_1	Gearle Siltstone	92.1	206	263	100	200	0	1	0	0	0
Tamala_1	Toolonga Calcilutite	72.1	162	206	0	100	0	1	0	0	0
Wandagee_1	Tumblagooda Sandstone	435.9	944	944	0	20	0.9	0.1	0	0	0
Wandagee_1	Marron Mbr (Ajana Fm)	432.8	811	944	0	20	0	0.3	0.7	0	0
Wandagee_1	Ajana Fm	427.7	587	811	0	20	0.6	0.3	0	0	0
Wandagee_1	Yaringa Fm	425.4	525	587	0	20	0.4	0.1	0.1	0.1	0.3
Wandagee_1	Coburn Fm	410.2	399	525	20	100	0.4	0.1	0	0.3	0.3
West_Giralia_1	Callytharra Fm	293	712	712	20	100	0	0	0.6	0.3	0.1
West_Giralia_1	Birdrong Sandstone	136.5	665	712	0	100	0.6	0.1	0	0.3	0.1
West_Giralia_1	Muderong Shale	124.3	596	665	100	200	0	0	1	0	0
West_Giralia_1	Windalia Radiolarite	113.1	563	596	100	200	0	0.9	0.1	0	0
West_Giralia_1	Gearle Siltstone	92.1	278	563	100	200	0	0.9	0.1	0	0
West_Giralia_1	Toolonga Calcilutite	72.1	193	278	0	100	0	0	0	1	0
West_Giralia_1	Korojon Calcarenite	69.5	141	193	0	20	1	0	0	0	0
Yaringa_1	Tumblagooda Sandstone	435.9	1526	1526	0	20	0.6	0.2	0.1	0	0
Yaringa_1	Ajana Fm	427.7	1300	1526	0	20	0.3	0.2	0.1	0.3	0.2
Yaringa_1	Yaringa Fm	425.4	1195	1300	0	20	0.6	0	0	0.2	0.2

Yaringa_1	Coburn Fm	410.2	947	1195	20	100	0.1	0	0	0.3	0.6
Yaringa_1	Faure Fm	407.1	855	947	20	100	0.5	0	0	0.4	0.1
Yaringa_1	Kopke Sandstone	402.1	326	855	0	20	1	0	0	0	0
Yaringa_1	Sweeney Mia Fm	395.9	146	326	0	20	0.9	0	0	0.1	0

Appendix 3. Chapter 4 supporting infomation

Basin	Lithology	Porosity base case	Porosity min	Porosity max	Density (kg/m^3)	Decay length (m)
Canning	Dolostone	0.15	0.08	0.23	2756	4698
	Limestone	0.1	0.05	0.15	2660	2554
	Salt	0.2	0.2	0.2	2160	750
	Sandstone	0.45	0.23	0.68	2373	2750
	Shale	0.2	0.1	0.3	2351	3549
	Siltstone	0.4	0.2	0.6	2299	4386
Cooper	Coal	0.4	0.2	0.6	1600	1721
	Conglomerate	0.4	0.2	0.6	2700	4328
	Limestone	0.35	0.175	0.525	2710	1542
	Sandstone	0.4	0.2	0.6	2650	3059
	Shale	0.6	0.3	0.9	2720	1489
	Siltstone	0.5	0.25	0.75	2650	2492
Southern Carnarvon	Dolostone	0.23	0.11	0.34	2630	8044
	Limestone	0.25	0.13	0.38	2580	5400
	Sandstone	0.2	0.1	0.3	2340	2500
	Shale	0.3	0.15	0.45	2520	620
	Siltstone	0.23	0.11	0.34	2330	3108

Table A3.1: Common lithologic properties for calculating sediment porosity decay with depth.

	M600	M700	M800	M900	M1000
Canning Basin Euclidean distance	1896	1584	2145	2949	2739
Cooper Basin Euclidean distance	940	1577	1504	1011	1004
Southern Carnarvon Basin (Cody-1 only) Euclidean distance	580	299	442	187	326
Mean	**1138**	**1154**	**1364**	**1382**	**1356**
Canning Basin first derivative Euclidean distance	80	82	87	88	100
Cooper Basin first derivative Euclidean distance	94	101	91	98	86
Southern Carnarvon Basin (Cody-1 only) first derivative Euclidean distance	38	35	32	31	27
Mean	**71**	**73**	**70**	**72**	**71**

Table A3.2: Euclidean distance summary.

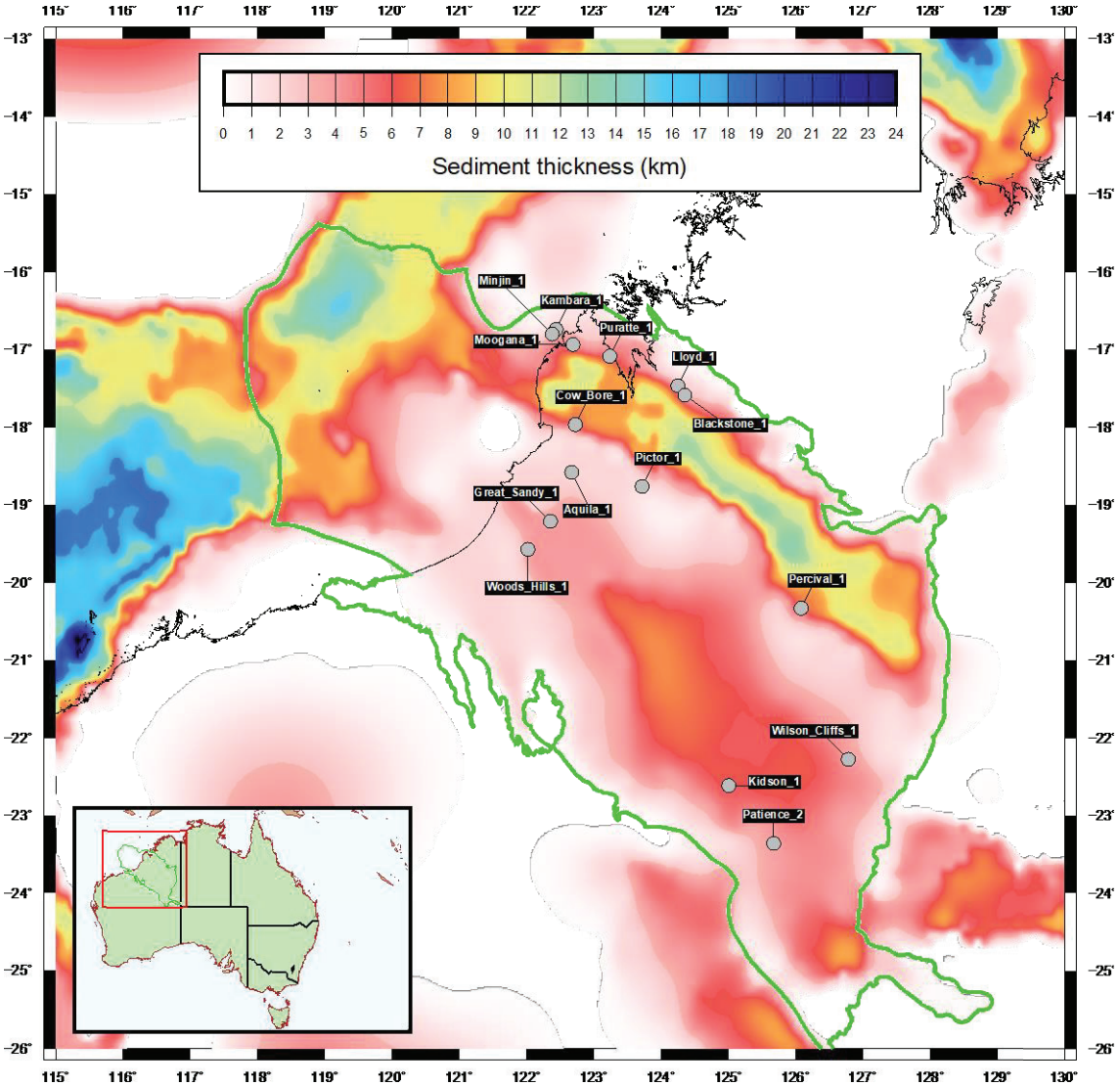

Supplementary Figure A3.1: Location map for Canning Basin wells.

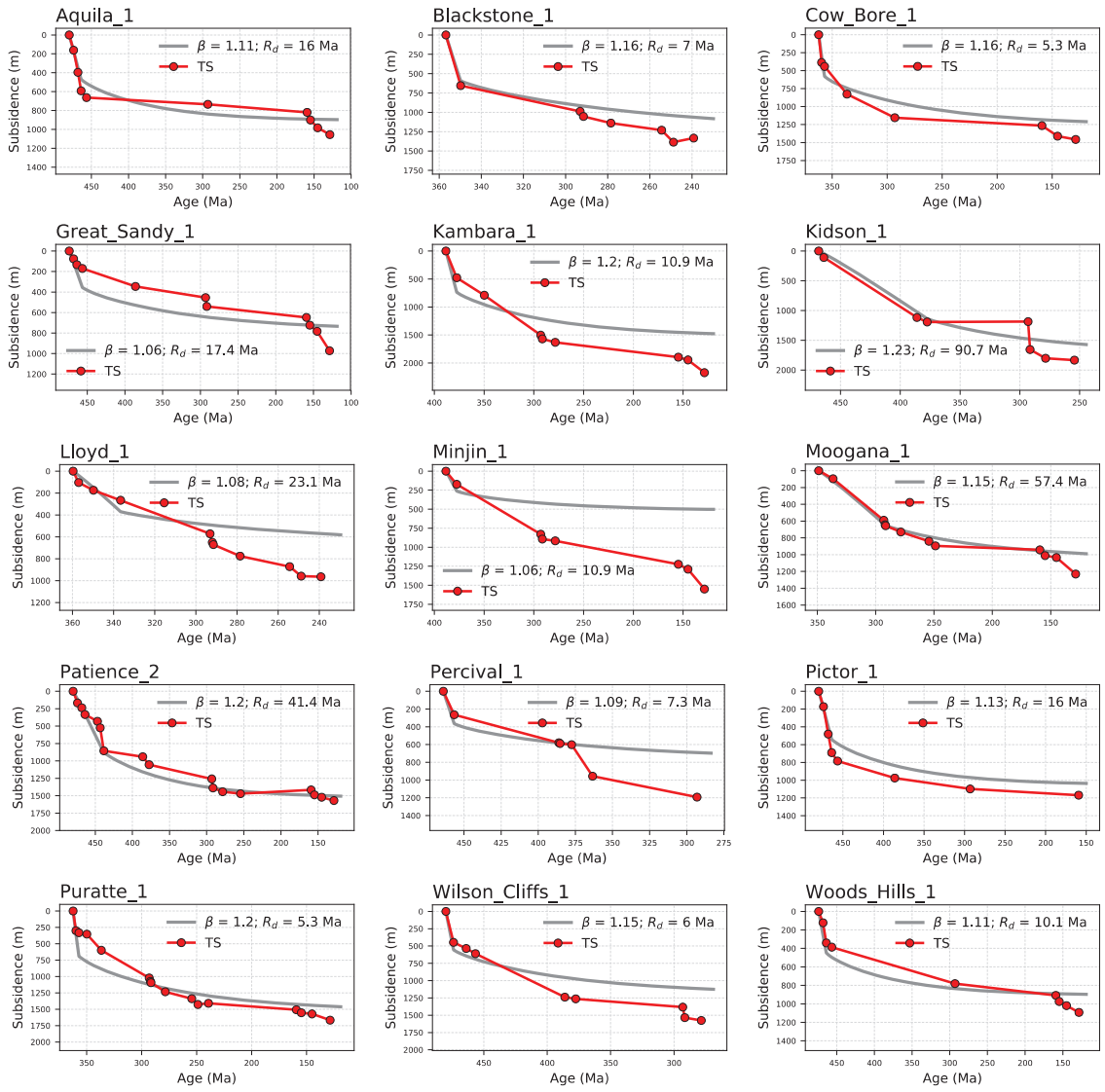

Supplementary Figure A3.2: Backstripped, water-loaded tectonic subsidence curve for wells in the Canning Basin (red line and uncertainty envelope) and forward modelled best-fit tectonic subsidence (grey line) for stretching factor β and rift duration R_d.

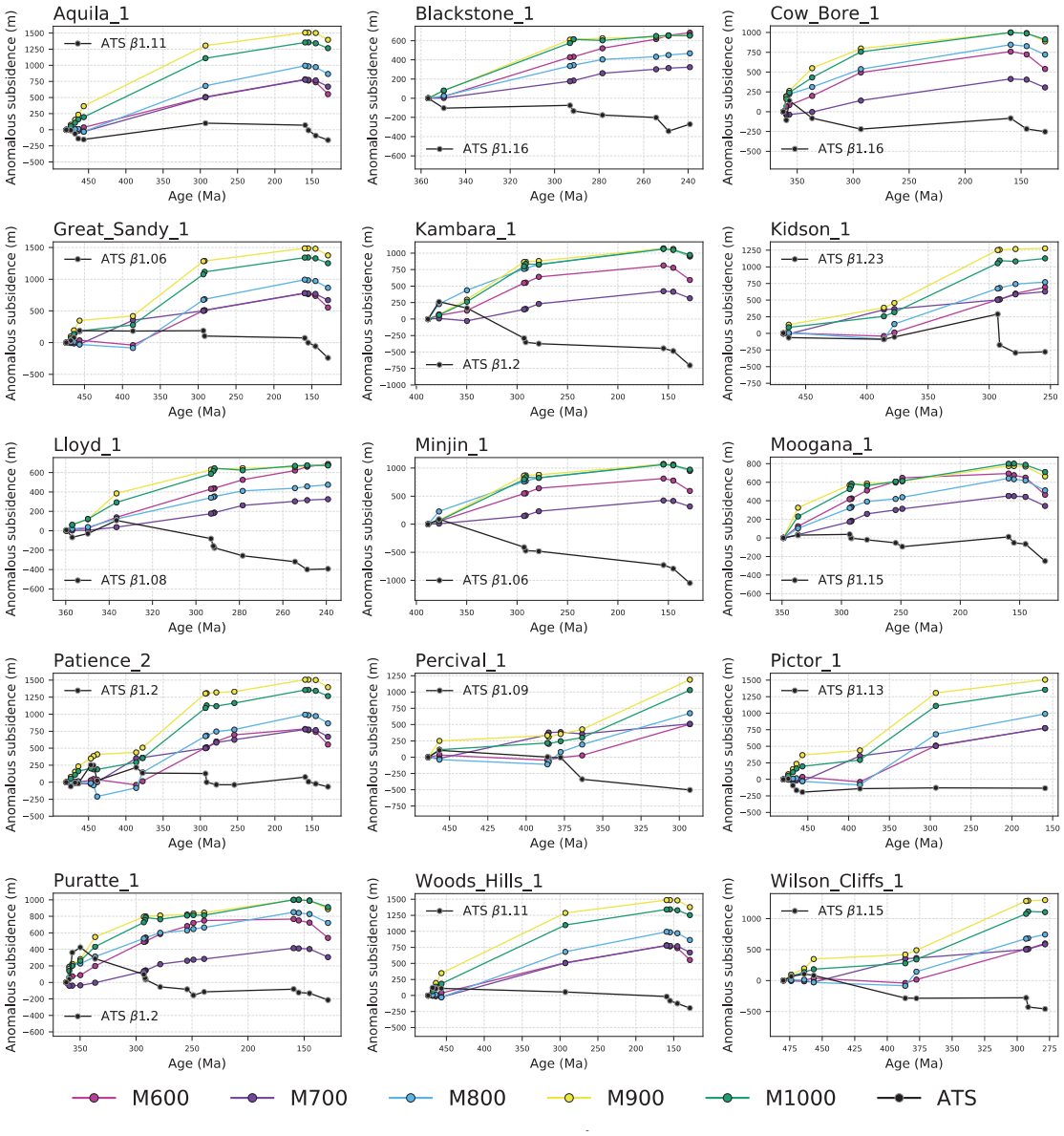

Supplementary Figure A3.3: Dynamic topography for flow models M600–M1000 and anomalous vertical motion (black line) for wells in the Canning Basin. Anomalous vertical motion is the difference between the backstripped tectonic subsidence and the forward modelled subsidence. Positive values represent anomalous uplift and negative values indicate anomalous subsidence.

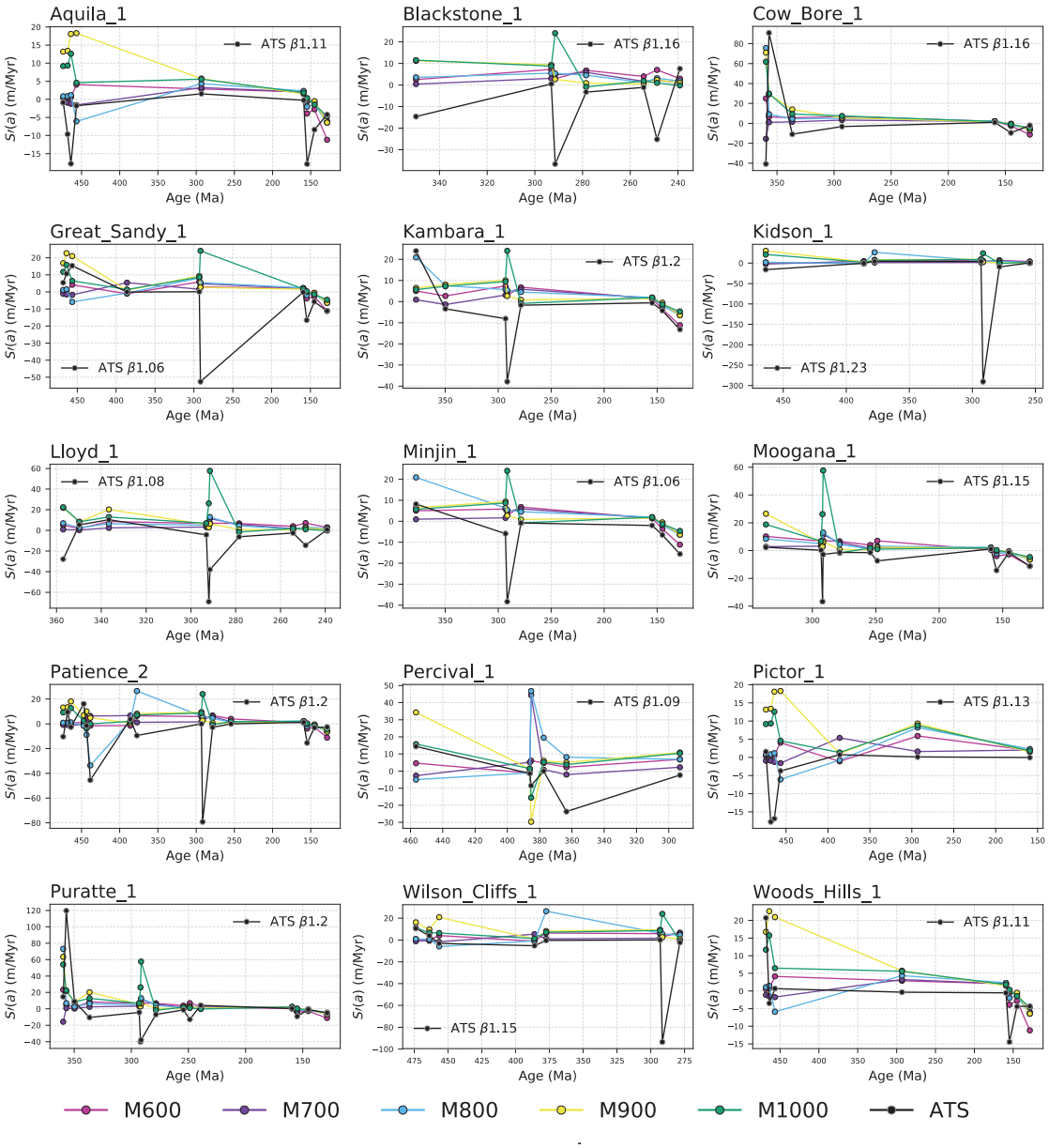

Supplementary Figure A3.4: First derivatives of dynamic topography for each case M600–M1000 in the Canning Basin (coloured lines) and of anomalous vertical motions (black line). Positive values indicate uplift and negative values indicate subsidence.

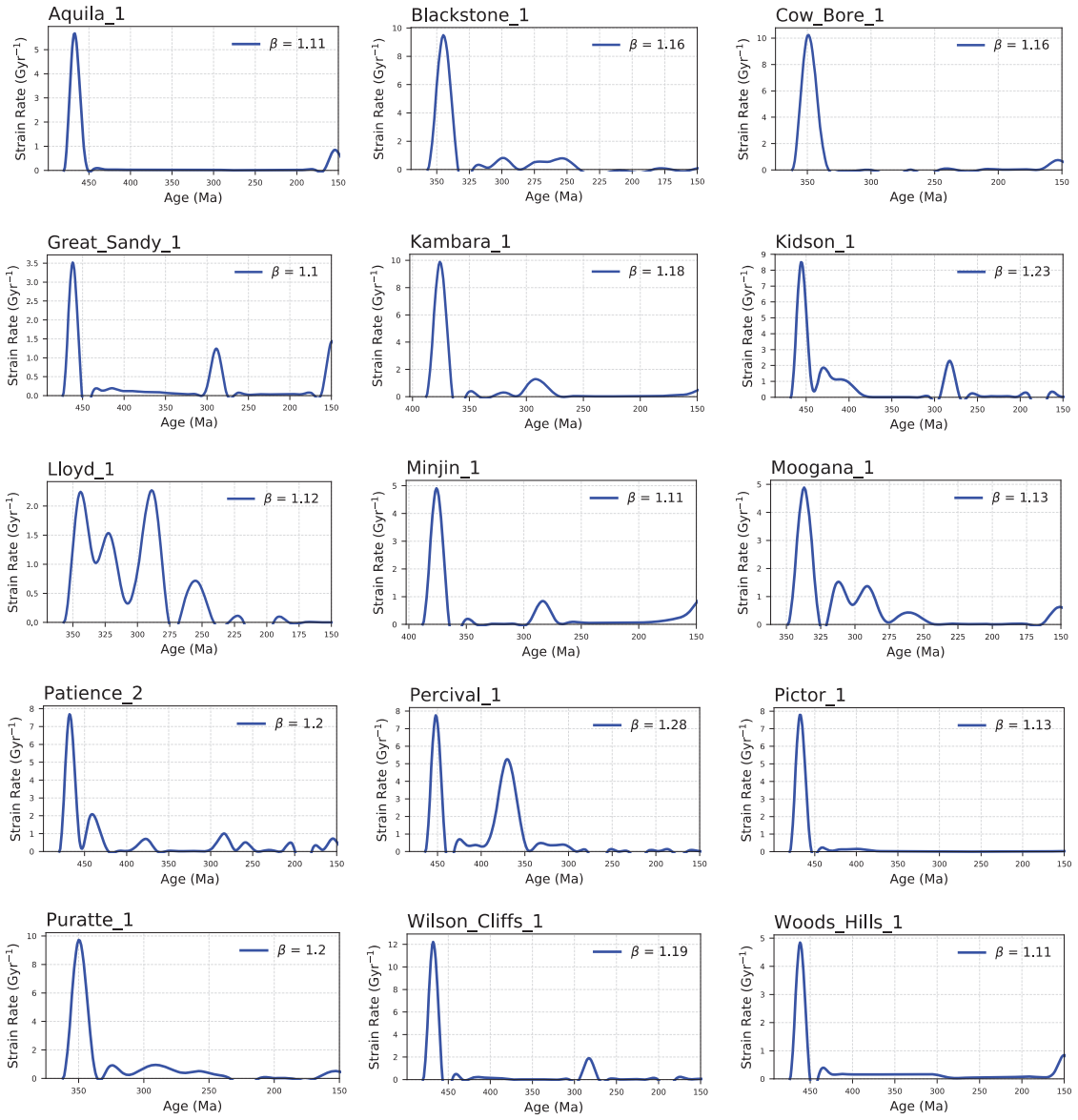

Supplementary Figure A3.5: Strain rate inversion results for wells in the Canning Basin. Note: we do not show anything younger than 150 Ma since there is limited/no data for these times.

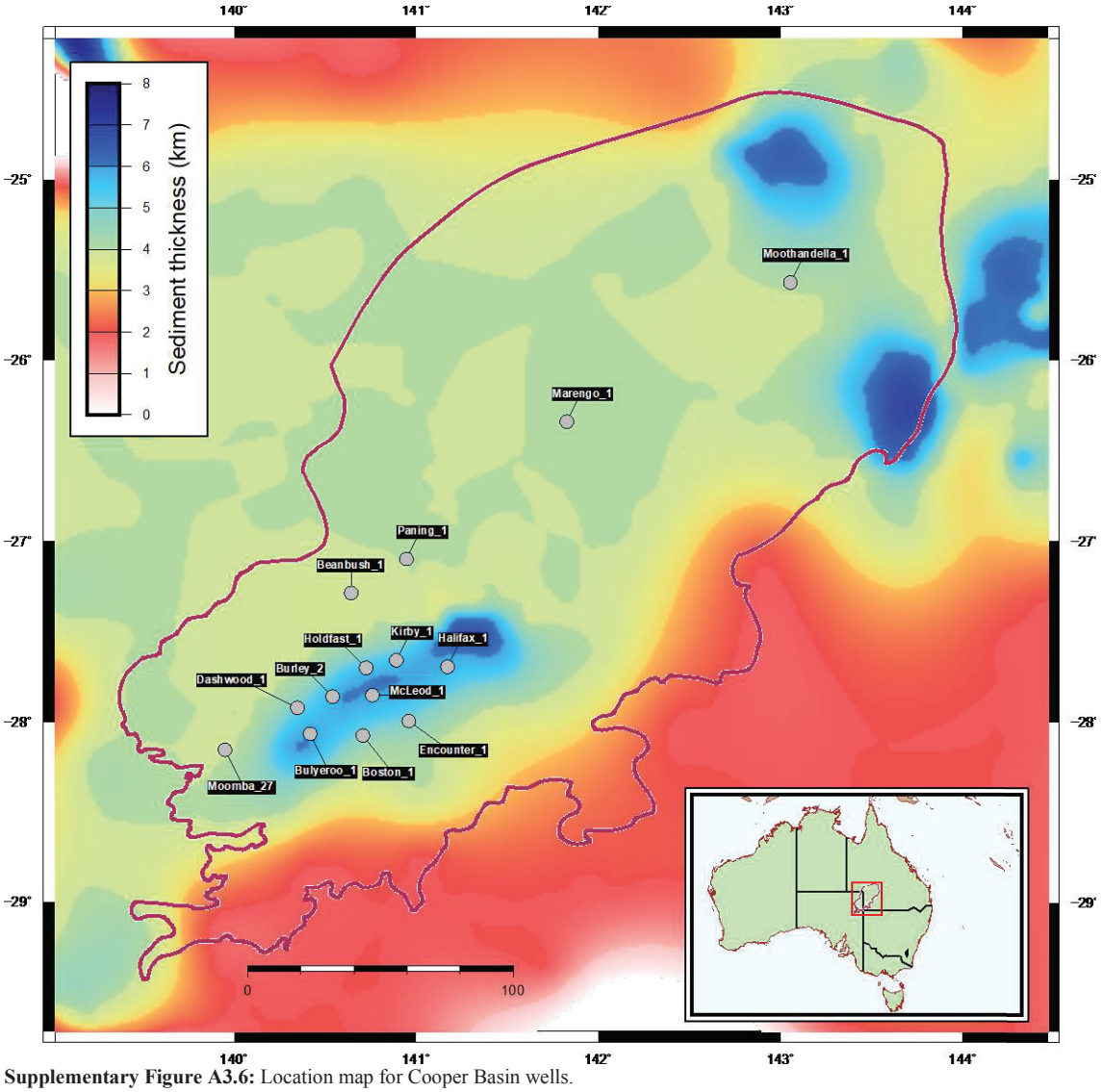

Supplementary Figure A3.6: Location map for Cooper Basin wells.

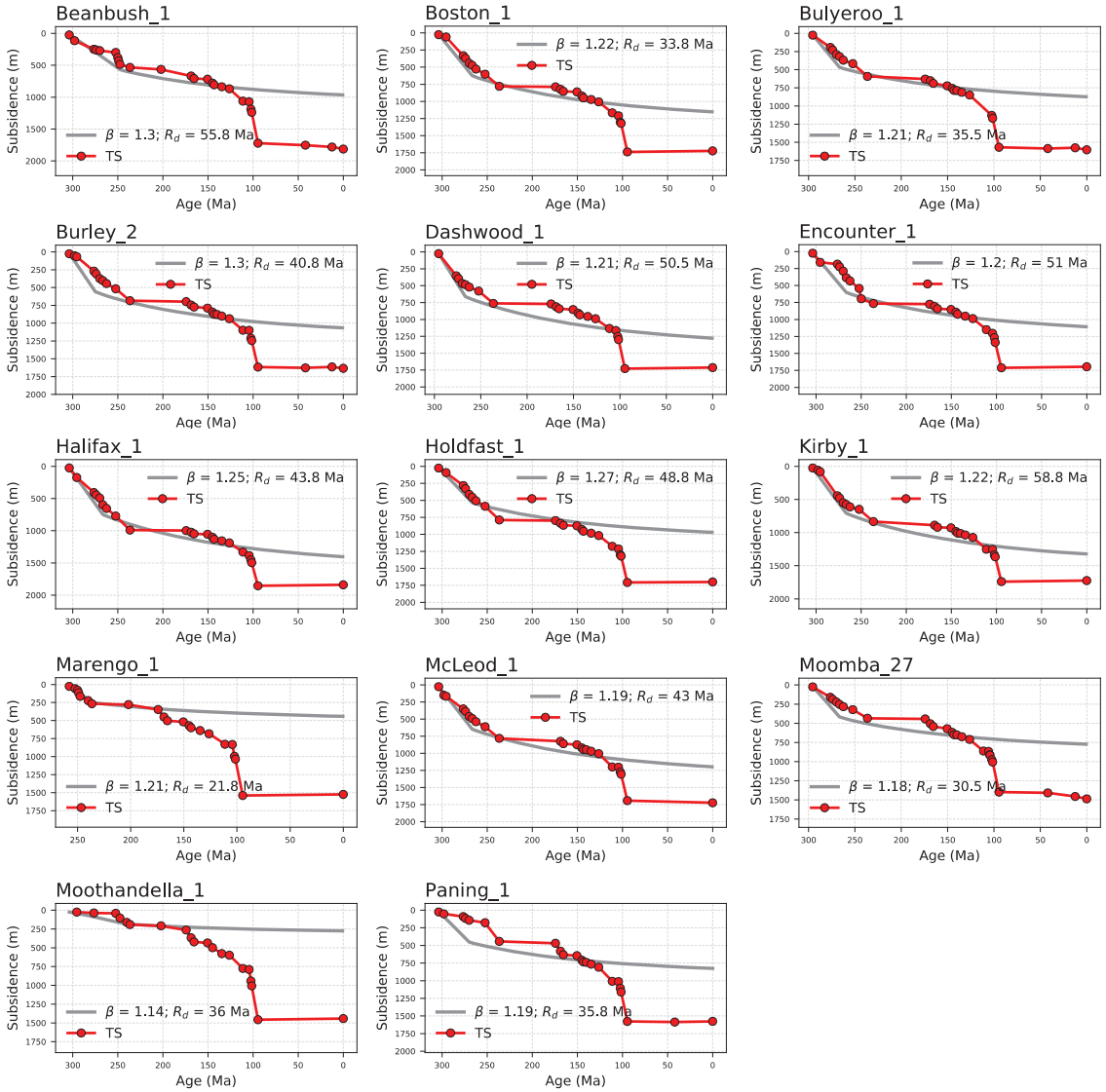

Supplementary Figure A3.7: Backstripped, water-loaded tectonic subsidence curve for wells in the Cooper Basin (red line and uncertainty envelope) and forward modelled best-fit tectonic subsidence (grey line) for stretching factor β and rift duration R_d.

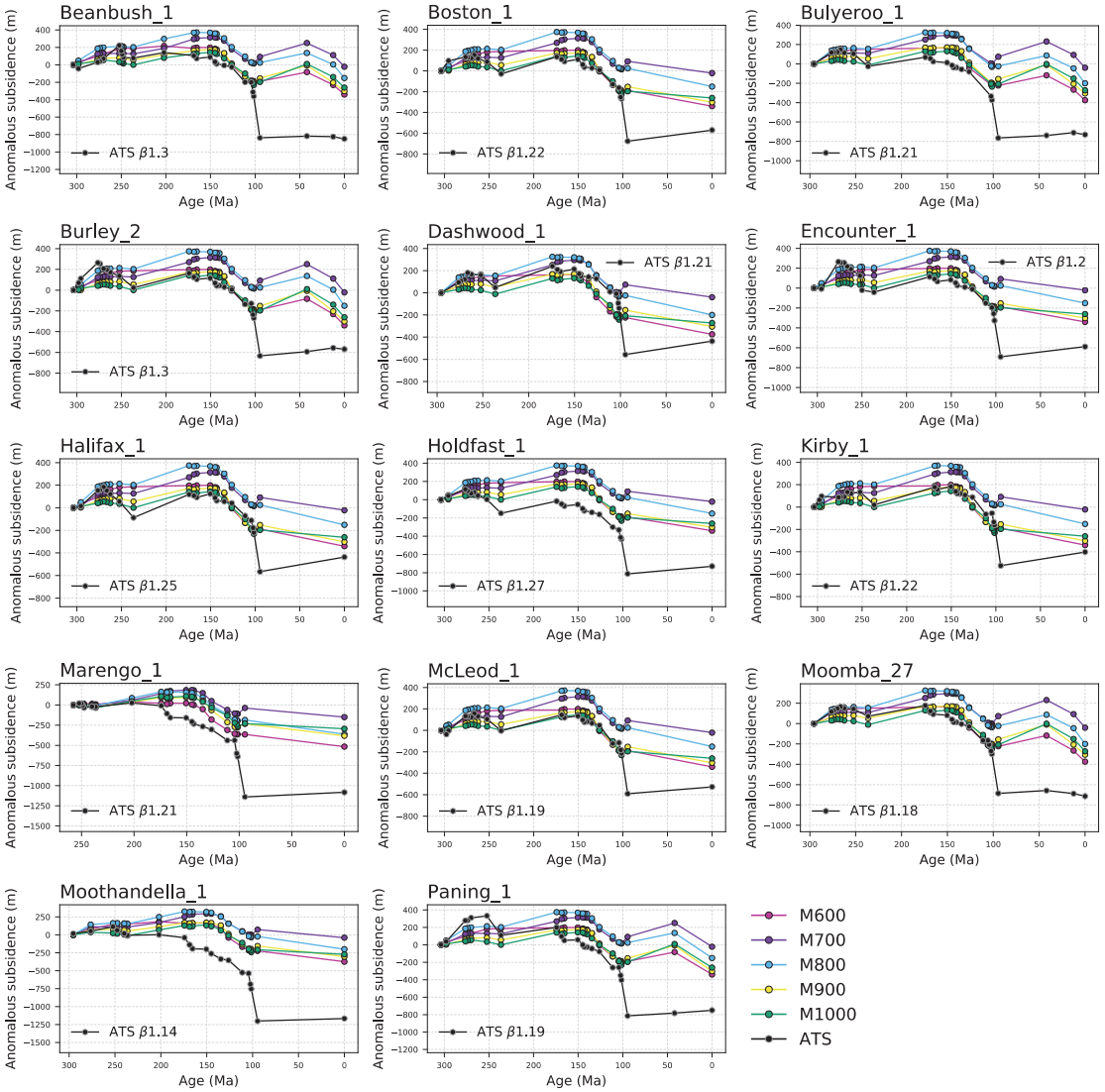

Supplementary Figure A3.8: Dynamic topography for flow models M600–M1000 and anomalous vertical motion (black line) for wells in the Cooper Basin. Anomalous vertical motion is the difference between the backstripped tectonic subsidence and the forward modelled subsidence. Positive values represent anomalous uplift and negative values indicate anomalous subsidence.

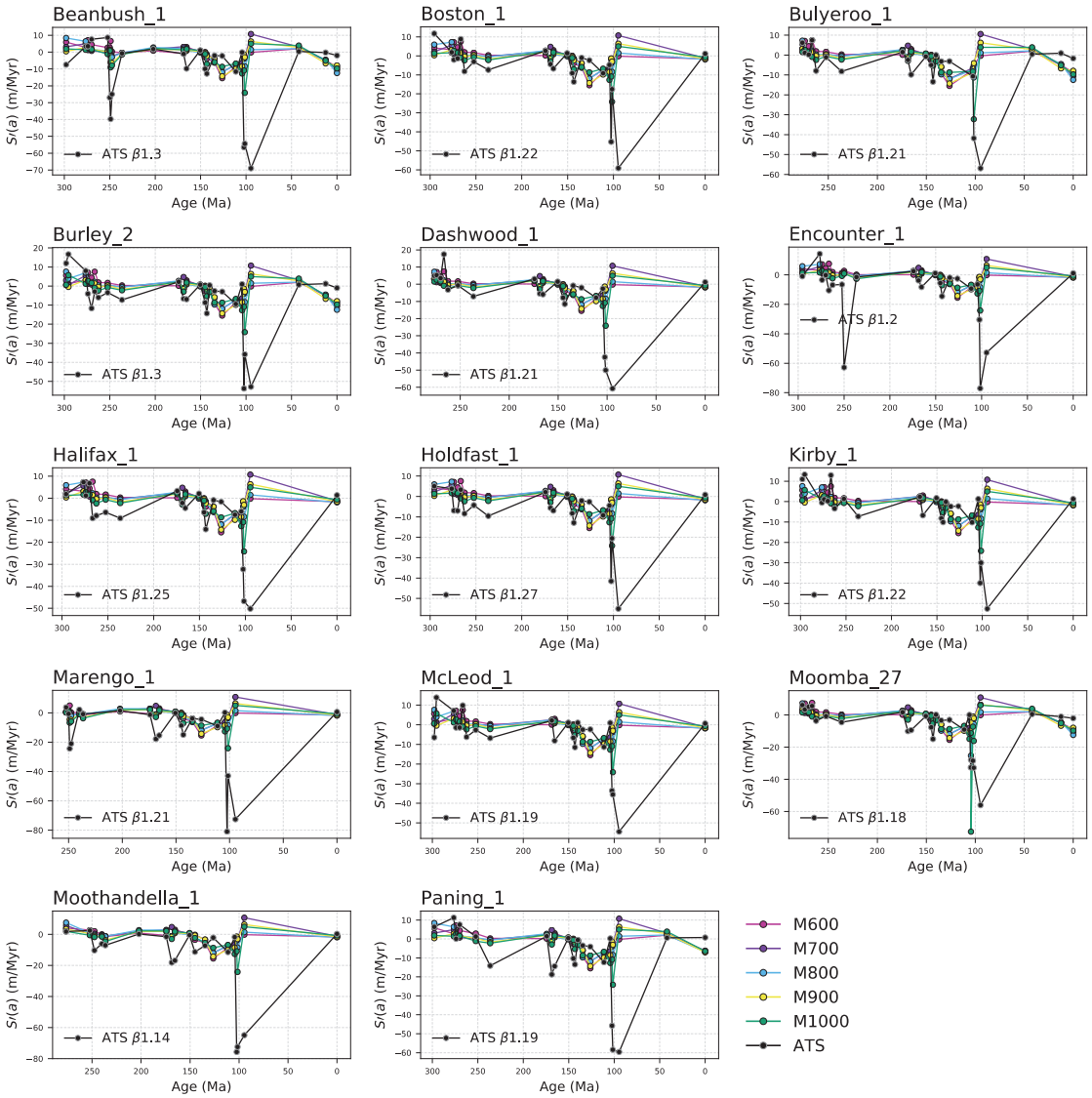

Supplementary Figure A3.9: First derivatives of dynamic topography for each case M600–M1000 in the Cooper Basin (coloured lines) and of anomalous vertical motions (black line). Positive values indicate uplift and negative values indicate subsidence.

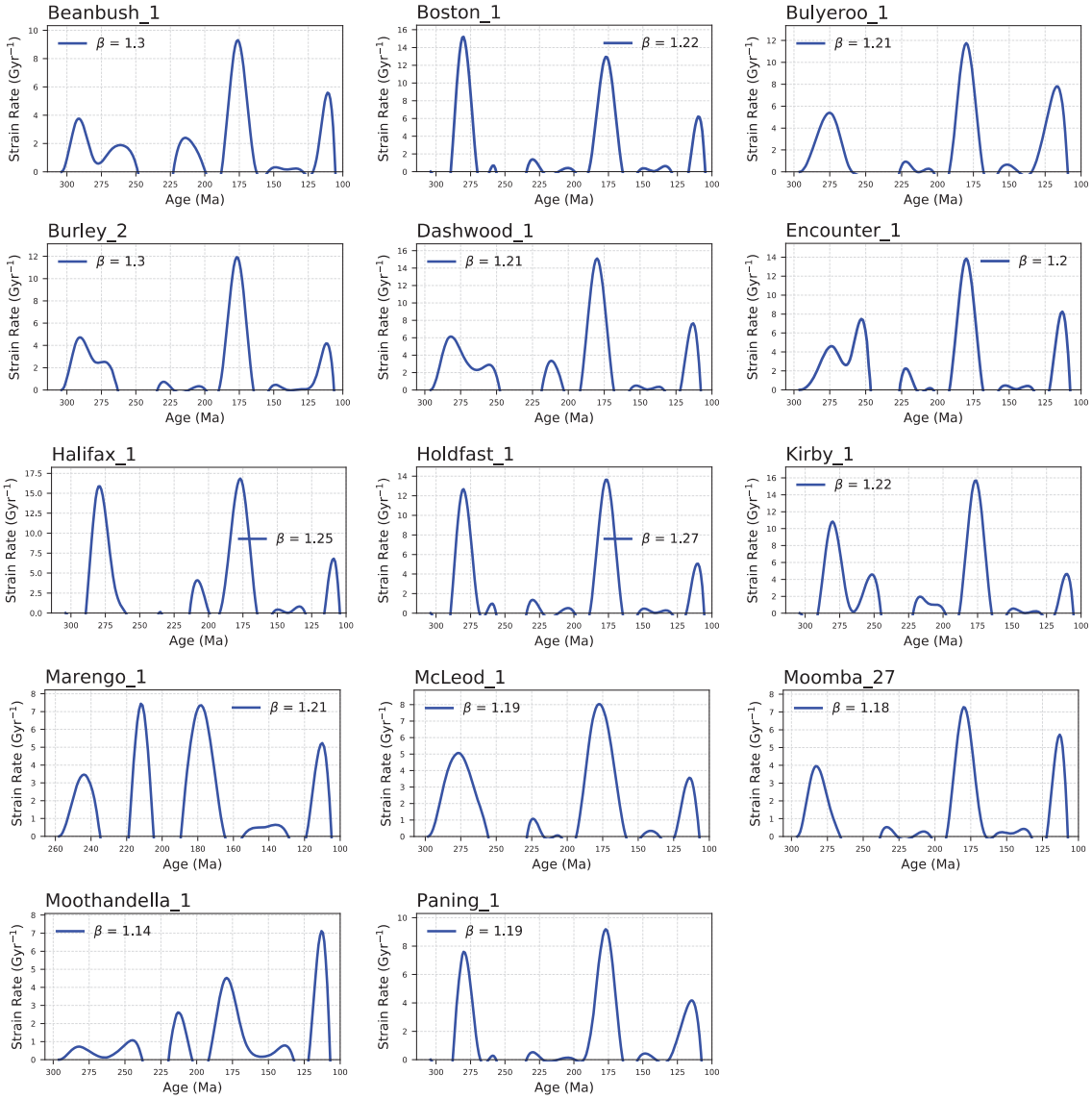

Supplementary Figure A3.10: Strain rate inversion results for wells in the Cooper Basin. Note: we do not show anything younger than 100 Ma since there is limited/no data for these times.

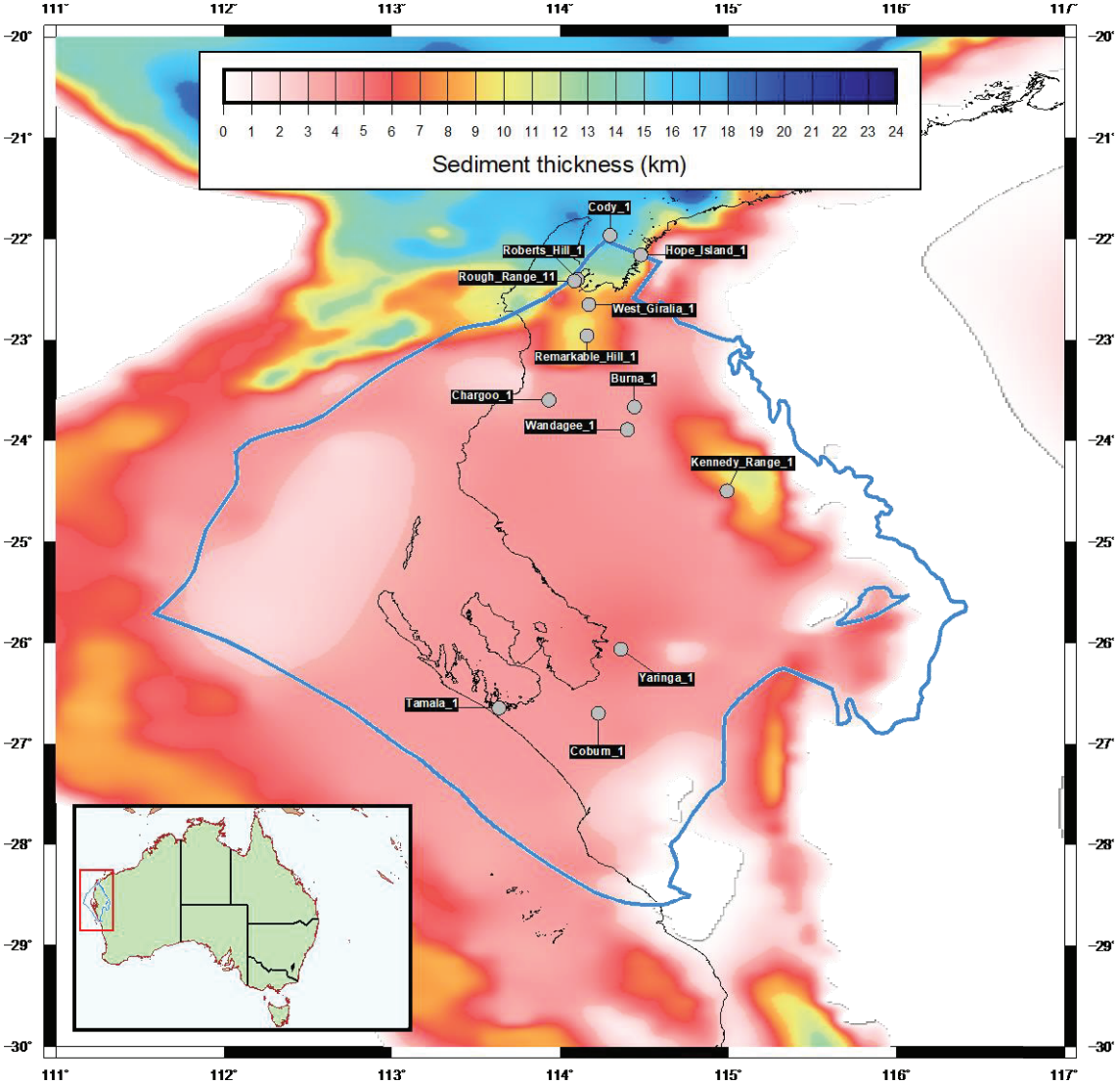

Supplementary Figure A3.11: Location map for Southern Carnarvon Basin wells.

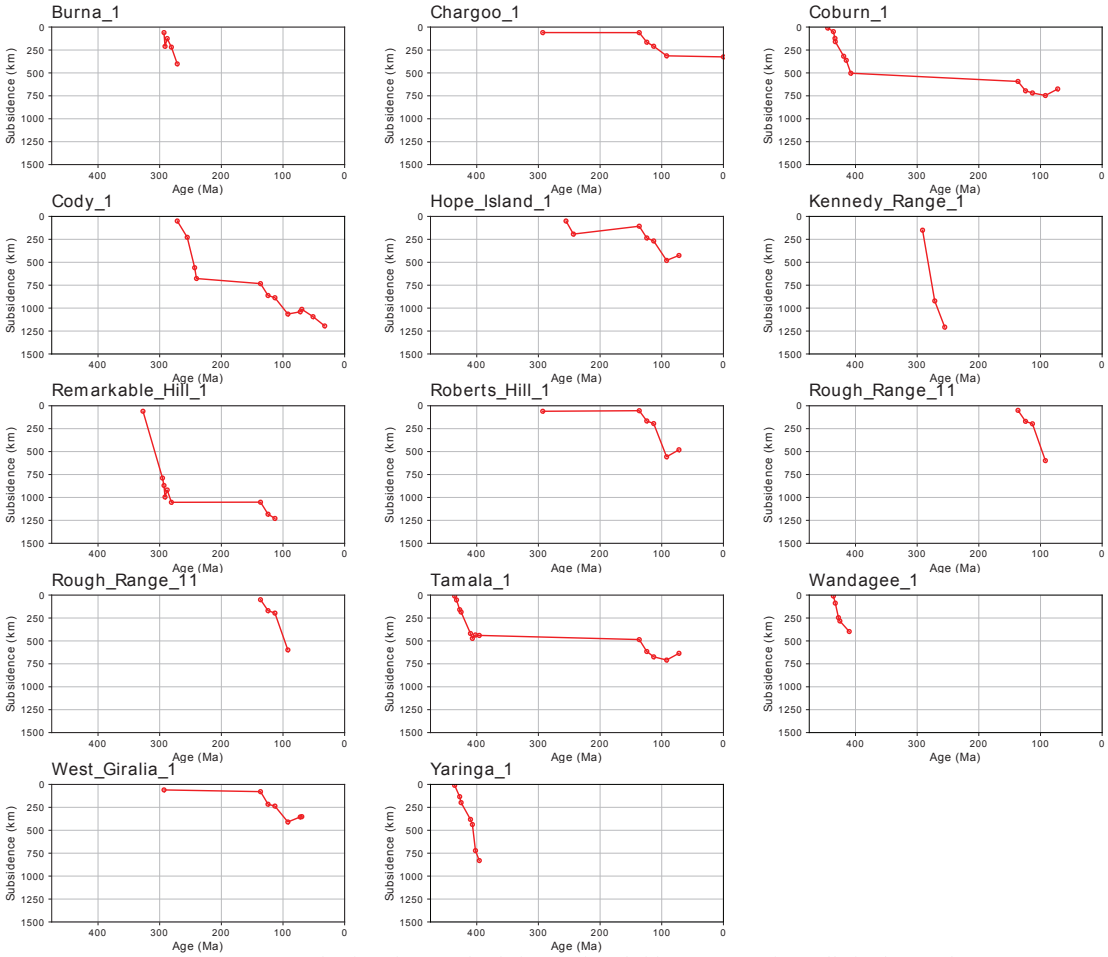

Supplementary Figure A3.12: Backstripped, water-loaded tectonic subsidence curves for wells in the Southern Carnarvon Basin (red line and uncertainty envelope).

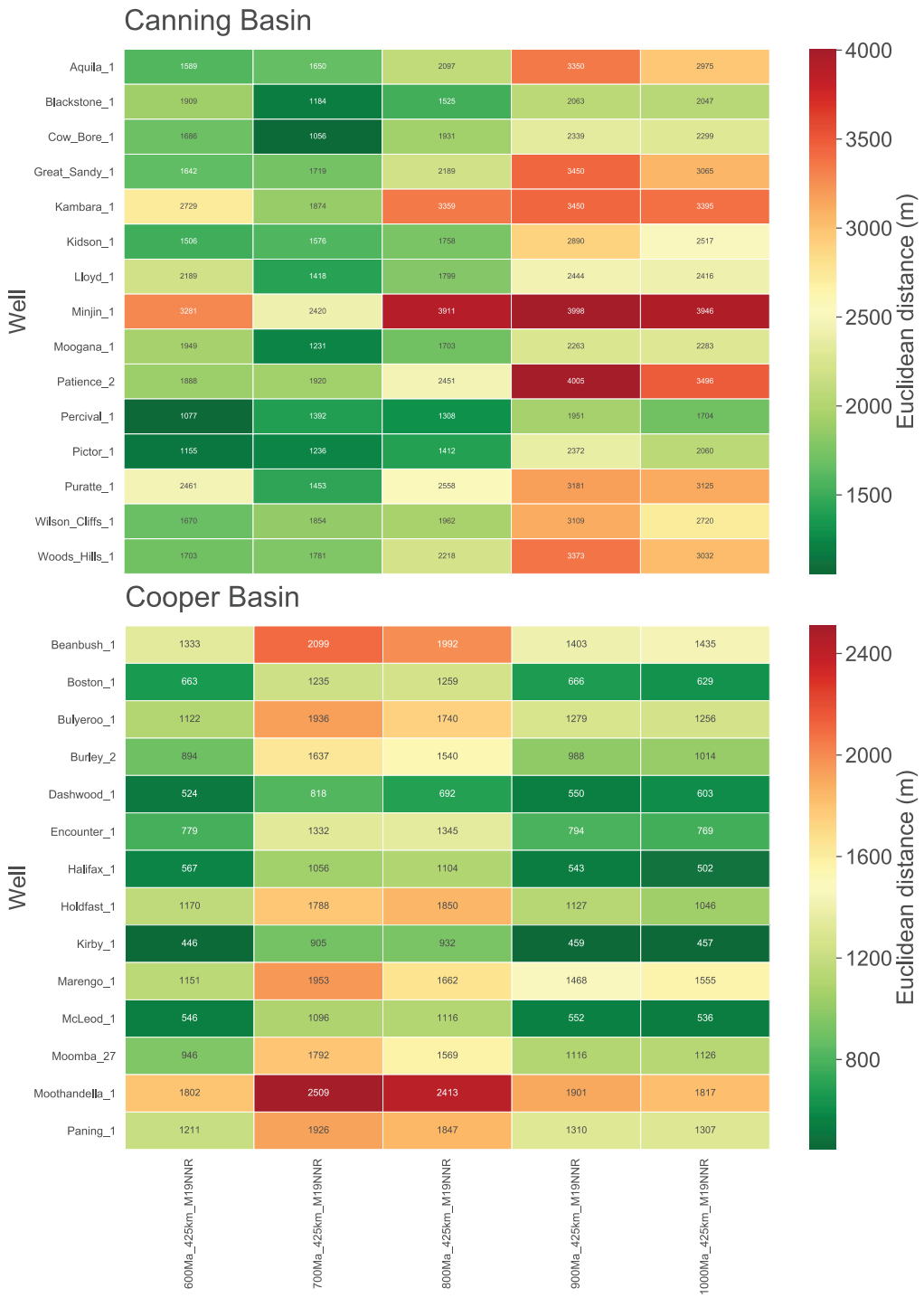

Supplementary Figure A3.13: Euclidean distance calculated between anomalous vertical motion curves and dynamic topography predicted by model cases M600-M1000 for Canning (top) and Cooper (bottom) Basin wells.

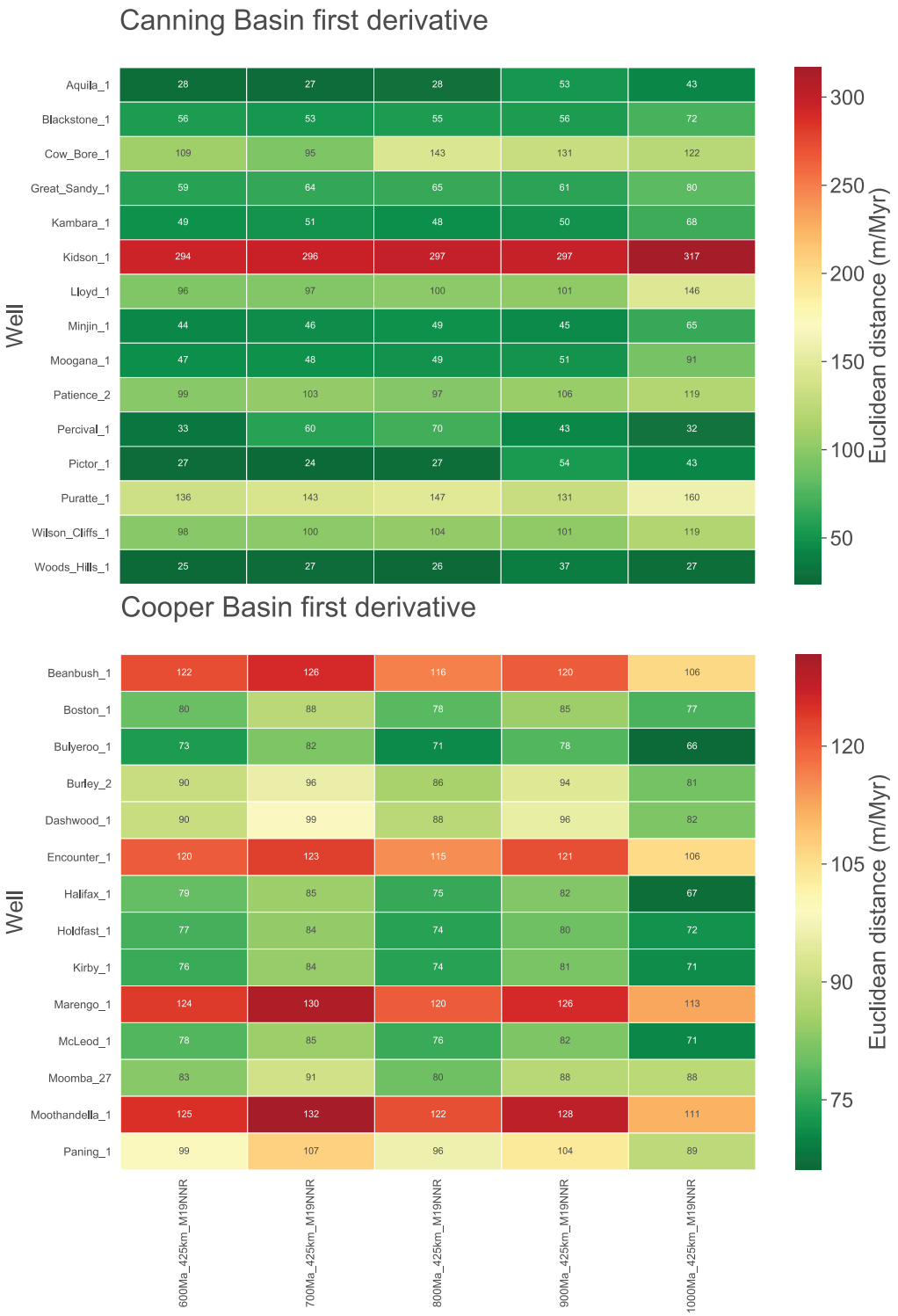

Supplementary Figure A3.14: Euclidean distance calculated between first derivatives curves of anomalous vertical motion and first derivatives of dynamic topography predicted by model cases M600-M1000 for Canning (top) and Cooper (bottom) Basin wells.